

University of Denver

Digital Commons @ DU

Electronic Theses and Dissertations

Graduate Studies

1-1-2014

Fabrication and Application of a Polymer Neuromorphic Circuitry Based on Polymer Memristive Devices and Polymer Transistors

Robert A. Nawrocki
University of Denver

Follow this and additional works at: <https://digitalcommons.du.edu/etd>



Part of the [Computer Engineering Commons](#), and the [Electrical and Computer Engineering Commons](#)

Recommended Citation

Nawrocki, Robert A., "Fabrication and Application of a Polymer Neuromorphic Circuitry Based on Polymer Memristive Devices and Polymer Transistors" (2014). *Electronic Theses and Dissertations*. 470.
<https://digitalcommons.du.edu/etd/470>

This Dissertation is brought to you for free and open access by the Graduate Studies at Digital Commons @ DU. It has been accepted for inclusion in Electronic Theses and Dissertations by an authorized administrator of Digital Commons @ DU. For more information, please contact jennifer.cox@du.edu, dig-commons@du.edu.

Fabrication And Application Of A Polymer Neuromorphic Circuitry Based
On Polymer Memristive Devices And Polymer Transistors

A Dissertation

Presented to

the Faculty of the Daniel Felix Ritchie School of Engineering and

Computer Science

University of Denver

In Partial Fulfillment

of the Requirements for the Degree

Doctor of Philosophy

by

Robert A. Nawrocki

March 2014

Advisors: Prof. Richard M. Voyles

Prof. Sean E. Shaheen

©Copyright by Robert A. Nawrocki 2014

All Rights Reserved

Author: Robert A. Nawrocki
Title: Fabrication And Application Of A Polymer Neuromorphic Circuitry
Based On Polymer Memristive Devices And Polymer Transistors
Advisors: Prof. Richard M. Voyles, Prof. Sean E. Shaheen
Degree Date: March 2014

Abstract

Neuromorphic engineering is a discipline that aims to address the shortcomings of today's serial computers, namely large power consumption, susceptibility to physical damage, as well as the need for explicit programming, by applying biologically-inspired principles to develop neural systems with applications such as machine learning and perception, autonomous robotics and generic artificial intelligence.

This doctoral dissertation presents work performed fabricating a previously developed type of polymer neuromorphic architecture, termed Polymer Neuromorphic Circuitry (PNC), inspired by the McCulloch-Pitts model of an artificial neuron. The major contribution of this dissertation is a development of processing techniques necessary to realize the Polymer Neuromorphic Circuitry, which required a development of individual polymer electronics elements, as well as customization of fabrication processes necessary for the realization of the circuitry on separate substrates as well as on a single substrate. This is the first demonstration of a fabrication of an entire neuron, and more importantly, a network of such neurons, that includes both the weighting functionality of a synapse and the somatic summing, all realized with polymer electronics technology.

Polymer electronics is a new branch of electronics that is based on conductive and semi-conductive polymers. These new elements hold a great advantage over the conventional, inorganic electronics in the form of physical flexibility, low cost and ease of fabrication, manufacturing compatibility with many substrate materials, as well as

greater biological compatibility. These advantages were the primary motivation for the choice to fabricate all of the electrical components required to realize the PNC, namely polymer transistors, polymer memristive devices, and polymer resistors, with polymer electronics components.

The efficacy of this design is validated by demonstrating that the activation function of a single neuron approximates the sigmoidal function commonly employed by artificial neural networks. The utility of the neuromorphic circuitry is further corroborated by illustrating that a network of such neurons, and even a single neuron, are capable of performing linear classification for a real-life problem.

Acknowledgements

First of all, I would like to express my gratitude to both of my advisors, Professor Richard M. Voyles (Associate Dean of Research at Purdue University) and Professor Sean E. Shaheen (Professor at University of Colorado), for their guidance, insights and patience.

I also thank Professor Wenzhong “David” Gao, Professor Mohammad H. Mahoor and Professor Martin F. Quigley for serving as the committee members in my final oral examination. Additionally, I would like to thank Professor Nancy M. Lorenzon for all her help in my research.

I thank all my colleagues and collaborators, in both the Computer Engineering Department and the Physics Department at University of Denver, especially Erin M. Galiger, Justin Huff, Yanzhe Cui, Jade Irizarry-Swordy, Xiaoting Yang, Tony Nava, Joshua Lane, Arash Hajjam, Robert Whitman, Gerald Edelstein, and Jon Buckley; at National Renewable Energy Laboratory in Golden, Colorado, Alexander M. Nardes, Brian A. Bailey, and Ajaya Sidel; at University of Colorado, Boulder, David Ostrowski, Zefram Marks, Tzu-Min Oo, Ryan R. Brow, Jan Van Zeghbroeck, Jacob Friedlein, Robert R. McLeod and Nikolaus Correll; Michael Chabinyk from University of California, Santa Barbara; Hsi-Wen Tung, Famin Qiu, Dominic R. Frutiger, Bradley J. Nelson from ETH Zürich and Giacomo Indiveri from INI Zürich, Switzerland.

Last but not least, my family, Katarzyna Nawrocki and Lech Nawrocki, Monika Neal and Tom Neal, and Raphael Balkanski and Nina Neal. I thank you all.

The work was sponsored in part by NSF under grants DMR-1006930, OISE-1053249 and IIS-0923518 with additional support from the NSF SSRRC as well as the NNIN Grant ECS-0335765.

Table of Contents

CHAPTER 1: INTRODUCTION.....	1
1.1 MOTIVATION.....	1
1.2 DISSERTATION OVERVIEW.....	2
1.3 REVIEW OF LITERATURE	3
1.4 BACKGROUND.....	9
CHAPTER 2: DESIGN OF A POLYMER NEURON.....	14
2.1 SYNAPSE.....	17
2.2 SOMA	22
2.3 SINGLE NEURON OPERATION AND ACTIVATION.....	23
2.4 LEARNING VERSUS PROGRAMMING.....	29
CHAPTER 3: INDIVIDUAL COMPONENTS.....	30
3.1 ORGANIC ELECTRONICS	30
3.1.1 Background.....	30
3.1.2 Organic Electronic Circuit Elements.....	35
3.1.3 Advantages and Disadvantages.....	37
3.2 ORGANIC MEMRISTIVE DEVICE	43
3.2.1 General Operation.....	43
3.2.2 Switching Behavior.....	45
3.2.3 Device Configurations.....	51
3.2.4 Switching Mechanisms.....	53
3.2.4.1 Electromigration of Metal Into the Active Layer	53
3.2.4.2 Formation of Conductive Filaments through Redox Behavior ..	54
3.2.4.3 Charge Trapping	54
3.2.4.4 The Ferroelectric Effect	55
3.2.5 OM-PROM For Synthetic Synapse.....	56
3.2.5.1 Device Operation	59
3.2.5.2 Manufacturing.....	71
3.3 ORGANIC FIELD EFFECT TRANSISTOR	74
3.3.1 Basic Concepts.....	75
3.3.2 OFET For Synthetic Soma.....	85
3.3.2.1 Device Configuration, Materials, and Procedures	85
3.3.2.2 Fabricating Considerations	91
3.3.2.3 Physically Flexible OFETs	99
3.4 ORGANIC RESISTOR.....	102
3.4.1 PEDOT:PSS - Conductive Polymer.....	103
3.4.2 PEDOT:PSS for Neuronal Resistors.....	104
CHAPTER 4: PNC FABRICATION.....	110
4.1 SEPARATE SUBSTRATES NEURON	111
4.1.1 Spin Coating.....	112
4.1.2 Fabrication.....	113
4.2 COMMON SUBSTRATE NEURON.....	117
4.2.1 Blade Coating.....	118
4.2.2 Fabrication.....	124
CHAPTER 5: PNC FOR LINEAR CLASSIFICATION.....	136
5.1 SINGLE NEURON CLASSIFICATION.....	139
5.2 NETWORK OF NEURONS CLASSIFICATION.....	146
CHAPTER 6: PNC APPLICATION.....	149
6.1 STRUCTURED COMPUTATIONAL POLYMERS.....	149

6.2 PAPERBOTS	157
CHAPTER 7: SUMMARY AND FUTURE WORK.....	166
7.1 FUTURE WORK.....	167
REFERENCES.....	173
APPENDIX A: LIST OF PUBLICATIONS.....	190
APPENDIX B: PNC SIMULATION.....	192
APPENDIX C: MANUFACTURING PROCESS.....	198
APPENDIX D: LIST OF EQUIPMENT USED.....	205
APPENDIX E: MANUFACTURING EQUIPMENT.....	206

List of Figures

- Figure 1. Schematic diagram of a single neuron with two inputs, denoted by V_{IN1} and V_{IN2} , and one output, marked V_{OUT} . (a) Organic memristive devices, R_{MEM1} and R_{MEM2} , provide the synaptic weights while a tuned organic field effect transistor (OFET) provides the sigmoidal activation that bounds the output as a function of the sum of the weighted inputs. (b) Circuit that replaces an individual memristive device with two resistors and a switch, as illustrated in Figure 3. 15
- Figure 2. (a) Biological neuron with input signal received at a synapse while soma adds the input signal and produces appropriate output (original image from Wikipedia.org). (b) Graphical representation of operation of a single artificial neural, with mathematical expression being shown in Equation 1: Artificial synapse (connection weight) weights the input signal while the soma produces proportional output (activation function) that is the sum of all of the input signals. 17
- Figure 3. Bistable memristive device: (a) electrical symbol - used in Figure 1(a); (b) representation in a form of two resistors, R_{ON} (low resistance) and R_{OFF} (high resistance), and a switch - used in Figure 1(b). 18
- Figure 4. I - V characteristics of a bistable memristive device with reversible switching, analogous to OM-RAM devices: (a) ideal operation, (b) real device. 19
- Figure 5. I - V characteristics of a bistable memristive device with irreversible switching, analogous to OM-PROM devices: (a) ideal operation, (b) real device. 21
- Figure 6. The activation function of a two-input polymer neuron, with large V_G , resulting in circuit behavior akin to linear amplifier, independent of the OFET but dependent on R_{BASE} and R_{MEM} . 25
- Figure 7. The activation function of a two-input polymer neuron, fabricated using the separate-substrate approach, indicated in Figure 51(a), with each input assigned binary weighting. The graph was obtained with the inputs (shown in Figure 1) being tied together. 27
- Figure 8. The activation function of a two-input polymer neuron, fabricated using the common-substrate approach, indicated in Figure 51(b). 28
- Figure 9. An example of a conjugated polymer chain built around an organic small molecule. (a) Thiophene ring (C_4H_4S), (b) polythiophene $(C_4H_4S)_n$ and (c) poly(3-hexylthiophene), a thiophene derivative (polymerized thiophene), with C_6H_{13} side

chains being attached to one of the carbon atoms of an individual thiophene ring. The 100% regioregularity is achieved by having all of the top and bottom side chains aligned. (d) P-type semiconducting thiophene derivative poly(3,3'''-dialkylquaterthiophene) (PQT-12) and (e) insulating poly(4-vinyl phenol) (PVP or P4VP). 32

Figure 10. Bonding in conducting conjugated polymers. (a) The sp^2 hybrid orbitals are shown in light and dark blue, and the unhybridized p_z orbitals shown in gray. Electrons are represented by the dots. The two sp^2 hybrid orbitals on the side extend in and out of the plane of the page. (b) An example of a backbone of conjugated polymers. 34

Figure 11. Example of manufacturing equipment used for deposition of organic electronics materials; (a) spin coater, (b) printing solution dispenser (courtesy of SonoPlot, Inc.), (c) blade coater, and (d) laminating press. 40

Figure 12. Physically flexible organic light emitting diode (OLED) shown, (a) being flexed and, (b) lit-up. 42

Figure 13. Industrial scale roll-to-roll fabrication of physically flexible printed electronics (courtesy of PolyIC GmbH & Co.). 42

Figure 14. Operational I - V characteristics of the two general types of OM-RAM devices, bipolar and polar. (a) For a bipolar OM-RAM, the device is either in the OFF state (R_{OFF} - high resistance, red or dark in gray scale) or ON state (R_{ON} - low resistance, green or light in grayscale) depending on past voltage. Gray, dashed arrows represent switching either to the ON or OFF state. The element can be turned ON by increasing the input voltage above the positive threshold value. Analogously, it can be turned OFF by decreasing the input voltage below the negative threshold value. (b) In a polar OM-RAM, both of the ON and OFF transitions occur for the same input voltage polarity, either positive or negative. 46

Figure 15. Operational I - V characteristics of two types of OM-PROM devices: (a) device originally in OFF state (R_{OFF} - high resistance, red or dark in gray scale) permanently changes state to ON state (R_{ON} - low resistance, green or light in gray scale), and (b) device originally in ON state irreversibly changes to OFF state. Gray, dashed arrows represent switching either to the ON or OFF state. 49

Figure 16. I - V relationship of a memory transistor. Two different drain-source currents (I_{DS}) can be measured depending on the sweeping direction of the gate-source voltage (V_{GS}). 50

Figure 17. Two general device configurations are common to most of organic devices. (a) Traditional configuration; the current flows from the bottom to the top of the device. b)

Inverted configuration, the current flows from the top to the bottom of the device. The top and bottom electrodes (TE, BE) are typically made from a thin layer of metal. The active layer (AL), which may itself consist of multiple layers or materials, is responsible for the electrical switching of the device. The hole or electron injection layers are often included to overcome energetic barriers at the interfaces or to increase the adhesion. Typically the TE serves as the cathode, and electrons flow from the TE to the BE.

52

Figure 18. *I*-*V* characteristics curve demonstrating the operation of an OM-RAM device with glass/ITO/PMMA+ZnO NPs/Al configuration.

57

Figure 19. Device configuration of PEDOT:PSS-based memristive device utilized for the multiplicative functionality of a synapse. An array of six memristive devices (3 x 2) can be seen with an individual device, formed at an intersection of BE (ITO) and TE (Ag/Ag₂O), clearly marked.

59

Figure 20. The c-AFM images, topography (left) and current (right), of PEDOT:PSS film indicating filamentary peaks being formed due to voltage application. (a) Initial 0-volt scan indicating OFF state with no current. (b) 2-volt scan indicating OFF state with no current. (c) Final 3-volt scan showing resistive change to ON state facilitated by a dramatic increase of recorded current. (Images by David Ostrowski).

61

Figure 21. (a) The c-AFM of PEDOT:PSS film indicating filamentary peaks being formed due to voltage application. (b) Topography line trace. (Images by David Ostrowski).

63

Figure 22. Two sets of memristive devices (with device configuration being shown in Figure 19) with two types of pulses applied; 5-ms pulse with 10-volt amplitude (black and light blue lines) and 10-ms pulse with 5-volt amplitude (light green and dark red lines). The total number of electrons transferred is roughly equal for both types of pulses, with 1.82×10^{20} electrons for 5-ms pulse and 1.92×10^{20} for 10-ms pulse, indicating that the switching is charge driven.

63

Figure 23. Band diagrams of forward (a) and reverse (b) biased PEDOT:PSS-based OM-PROM devices.

65

Figure 24. *I*-*V* relationship of a PEDOT:PSS-based memristive device, with configuration shown in Figure 19. A resistive change of less than 1 volt can be clearly seen. However, the change is permanent resulting in OM-PROM classification of the device.

66

Figure 25. *I*-*V* relationship of a PEDOT:PSS-based memristive device with (black circles) without (red crosses) PMMA

layer resulting in device indicating Ohmic (with PMMA layer) and non-Ohmic (without PMMA layer) relationship.	68
Figure 26. <i>I-V</i> characteristics of a PEDOT:PSS-based memristive device illustrating the effect of varying thicknesses of PMMA layer. BE made from ITO and Al are shown illustrating markedly higher current of the Al devices due to increased sheet conductivity of metal electrodes compared to ITO.	68
Figure 27. Performance of two PEDOT:PSS-based OM-PROM devices (one in the ON-state, one is the OFF-state) over a period of twenty months with storage in air. The current is shown for a read voltage of 0.5 V. <i>I-V</i> curves taken at several intervals for the device tested in the ON-state are shown in the inset. After twenty months, the device in the ON-state was refreshed by applying a voltage sweep with limits of ± 2.0 V.	69
Figure 28. <i>I-V</i> characteristics curve of an OM-PROM device with a high turn ON voltage of ~ 18 V.	71
Figure 29. (a) An example of a shadow mask used to define the area of a metal electrode obtained through metal evaporation. (b) An example of an organic memristive device with metal electrodes obtained by evaporation of metal through a shadow mask. An array of six devices formed at the intersection BEs and TEs can be seen.	74
Figure 30. Four individual OFET arrangements that depend on the location of the gate and source and drain (contact) electrodes: (a) top-gate-top-contact, (b) top-gate-bottom-contact, (c) bottom-gate-bottom-contact, and (d) bottom-gate-bottom-contact.	77
Figure 31. Interdigitated pattern of source and drain "fingers" aiming to maximize the channel width at a given area. (a) schematics, (b) picture of source and drain patterned electrodes.	78
Figure 32. (a) Application of voltage bias at the gate electrode induces charges at the insulator-semiconductor interface allowing for the formation of a conducting channel and a subsequent charge path between source and drain electrodes. (b) Application of greater voltage bias at the gate electrode produces greater drain current for the same drain-source voltage bias, due to greater amount of charges being induced at the insulator-semiconductor interface.	80
Figure 33. Cross section of an OFET indicating the shape of channel inversion charge depending on the magnitude of drain-source voltage in relation to the gate-source voltage bias, and a subsequent change of the OFET's <i>I-V</i> characteristics curve transitioning from linear to saturation regime.	83

Figure 34. Family of I_D versus V_{DS} curves showing the effect of channel length modulation producing a finite output resistance. The intersection of the sloped saturation region curves with the horizontal axis allows for a graphical extraction of the channel-length modulation parameter λ according to Equation 13.	85
Figure 35. Top-gate-bottom-contact configuration of an OFET used to function as a synthetic soma. The configuration was inspired by (Baeg, et al., 2011).	86
Figure 36. I - V characteristic curve of a typical, PQT-12-based OFET, with top-gate-bottom-contact configuration shown in Figure 35.	87
Figure 37. Snapshot of thickness measurement of (a) PQT-12 and (b) PVP + PQT-12, with (c) snapshot of scratches on the surface of the sample with a polymeric film.	89
Figure 38. (a) Zoomed picture of source and drain electrode trenches, made with a negative photoresist NR71, visible on glass substrate. (b) Source and drain electrodes on glass substrate, obtained through metal evaporation and photoresist liftoff, with channel length of approximately 5 μm . (c) An array of OFETs, with three probe tips connected to source, drain, and gate electrodes clearly visible. The probe tips were used to scratch through the PQT-12 (semiconductor) and PVP (insulator) layers in order to make a good contact with the metal electrodes underneath.	91
Figure 39. An AFM image, (a) top view and (b) side view, of PEDOT:PSS film that was obtained from insufficiently mixed solution with IPA wetting agent, leaving bold spots. (Images by Tony Nava). (c) SEM image of the same film.	93
Figure 40. Examples of damaged OFETs due to high gate voltage being applied and a resulting melting of the insulating layer due to the generated heat.	95
Figure 41. Comparison of, (a) fast cool down rate of a PQT-12 film and (b) slow cool down rate of the semiconducting material. It can be seen that film that is quickly cooled down produces a high number of large holes with a subsequent reduction of the drain current of an OFET.	97
Figure 42. An example of an early OFET, with saturating drain current of tens of nanoamperes, created without optimized parameters, such as the anneal temperature and ramp down as well as annealing in stream of N_2 .	98
Figure 43. Comparison of freshly created OFET lacking saturating features (marked with solid lines), and treated OFET showing saturating characteristic (dashed lines).	99

Figure 44. Physically flexible OFETs fabricated according to the device layout shown in Figure 35.	101
Figure 45. <i>I-V</i> characteristics curves of physically flexible OFETs, shown in Figure 44, (a) before bending, and (b) after bending. It can be seen that the physical flexion did not negatively affect the operation of the device.	102
Figure 46. Cartoon representation of a planar morphology of thin film of PEDOT:PSS particles, surrounded by a thin PSS-rich surface layer (left) along with chemical structure of PSS (top right) and PEDOT (bottom right). (image reproduced from (de Kok et al., 2006)).	103
Figure 47. (a) <i>I-V</i> characteristics curve of a family of polymer resistors based on PEDOT:PSS, an electrically conducting polymer. Five different resistors are demonstrated, created by varying the separation of metal electrodes. (b) Near-linear relation between resistance and the electrode separation.	105
Figure 48. Two distinct polymer resistor layouts: (a) planar and (b) stacked.	106
Figure 49. Because spin casting and blade casting indiscriminately cover the entirety of the substrate, individual resistors are obtain by isolating specific electrodes by manual removal of PEDOT:PSS.	108
Figure 50. Polymer resistors, with PEDOT:PSS used as conductive polymer material, deposited using; (a) blade casting, and (b) plotting process.	109
Figure 51. Two alternative fabrication approaches needed to fabricate an entire polymer neuron made from different electrical devices: (a) "separate substrates" where all of the devices are fabricated on separate substrates and are subsequently connected according to the circuit diagram, and (b) "common substrate" with all of the devices fabricated on a common substrate with the inter-element wiring fabricated on the chip.	111
Figure 52. Polymer neuron fabricated using separate-substrate approach. (a) A large view of the setup with the memristive devices and resistors clearly visible, along with a microscope and a network analyzer; (b) a zoomed view of two memristive devices along with micromanipulators used to connect to the resistor chip; (c) individual substrate with a 2 x 3 array of organic memristive devices (OM-PROMs); (d) individual substrate with PEDOT:PSS-based organic resistors; (e) individual substrate with organic transistors; (f) a zoomed view of an individual organic transistor, seen through a microscope-mounted camera, displayed on an overhead monitor.	116

- Figure 53. Diagram of blade coating technique with stationary substrate and moveable blade. 119
- Figure 54. Laboratory-scale blade coater with stationary substrate and moveable blade. The metal substrate, that the sample is placed atop, can be heated, allowing for better film morphology. 120
- Figure 55. An advantage of blade coating demonstrated by the ability to cover a portion of a substrate leaving clean portions for the deposition of another type of polymeric film. 123
- Figure 56. An example of two films bladed on the same substrate, with dashed arrows indicating the direction of blade movement. The overlap indicates a removal of previously applied film due to improperly chosen non-orthogonal solvents. 124
- Figure 57. Common-substrate PNC configuration with three distinct regions shown from left to right: OM-PROMs, Resistors, and OFETs. (a) Design for Bottom Electrode (BE - gray), obtained through photolithographic process, and Top Electrode (TE - yellow and black chequered), obtained from thermal evaporation of metal through a shadow mask. The PNC design features three-neuron network (individual neurons are color-coded with network design shown in Figure 58), with inputs, output, and three individual neurons shown. Via holes are used to send the (electrical) signal from the output of hidden neurons (BE of OFET) to the inputs of the output neuron (TE of OM-PROMs). (b) BE design indicating individual regions occupied by OM-PROMs, resistors, and OFETs. (c) BE and TE design indicating areas covered by individual polymeric films, such as PEDOT:PSS covering both the OM-PROM and resistor regions, along with device configurations of all of the electrical elements aligned with their respective regions. 126
- Figure 58. Three-layered neural network implemented in the PNC design shown in Figure 57, with individual neurons color-coded: red, indicating hidden neuron 1; green, indicating hidden neuron 2; and blue, indicating a single output neuron. (a) Conceptual design of the neural network indicating three distinct neural "layers": input, hidden, and output. (b) Circuit diagram of the neural network, shown in Figure 57, based on the individual neural design shown in Figure 1, with three separate color-coded neurons shown. 128
- Figure 59. Pictures of a glass substrates with Polymer Neuromorphic Circuitry fabricated based on a common-substrate paradigm, the first demonstration of neuromorphic circuit fabricated with organic electronics element. (a) Cr/Ag/Au BE on glass. (b) A single PNC chip inside a circular container. (c) An array of glass chips with only

BE (left) and fully-functioning PNC chips (right). A red-colored glass substrate, OFET area, is clearly seen on the left side of the chip. Immediately to the right of the red-covered area, there is a clear area, about 5 mm in width, used for the via-holes, with no polymeric materials deposited.

130

Figure 60. Laboratory setup used to characterize the Polymer Neuromorphic Circuitry fabricated on a single, glass substrate. Five individual micromanipulators can be seen used to provide $Input_1$, $Input_2$, OFET's V_G , Ground, and Output connections.

135

Figure 61. (a) A diagram of active tether, powered by water hammer phenomenon, with individual elements outlined. (b) Prototype of the active tether.

138

Figure 62. Water hammer phenomenon, indicating a force acting on the end of the hose. The red (solid) arrow indicates the direction of propulsion, (a) up and (b) down, while the blue (dashed) arrows correspond to the flow of the liquid with their length being indicative of the liquid pressure and the effect on the direction (shape closer to the end has a greater effect on the direction of propulsion).

139

Figure 63. Pictorial representation of ten shapes used for active tether classification, with their corresponding direction (angle) of propulsion marked. Shape (a) represents a reference value where the hose is propelled along the horizontal axis, with output voltage being ~ 0 V. Images from (Yang, 2010).

145

Figure 64. Examples of highly engineered, smart materials: (a) liquid terminator from the movie Terminator 2 (image from Wikipedia.org), (b) concept of smart material used as an elbow brace or a glove (image from Nick Dragotta).

150

Figure 65. Concept of a prototype of Structured Computational Polymers. (a) Proposed concept of the design. (b-g) Small scale implementation of the prototype. The prototype features sensing functionality in a form of three, custom-made pressure sensors placed inside separate cells. Two conventional LEDs, protruding on a side of the prototype, are serving as the outputs. Information processing, implemented using conventional, inorganic electronics components connected according to the PNC layout, is embedded inside the material.

156

Figure 66. A prototype of a foldable design, termed PaperBot, inspired by an arthropod locomotion.

159

Figure 67. A physically flexible sheet of PEN, with a fabricated array of organic transistors, used to create a prototype of smart material, shown in Figure 69(c).

160

- Figure 68. Structure of a smart material used for foldable PaperBots. Physically flexible PEN, with organic electronics fabricated on, is sandwiched between two sheets of paper. Cuts in the paper, performed with a laser cutter before the lamination step, are used as hinges of the PaperBot. 160
- Figure 69. Step-by-step process of a prototype of a smart material, with embedded physically flexible organic electronics, used to manufacture a foldable, rapidly prototyped hexapod, termed PaperBot. 163
- Figure 70. Inexperienced high school students are guided in the assembly process of rapidly prototyped PaperBots. 165
- Figure 71. (a) Proposed neural circuit to realize the neuronal activation with the soma being realized by an organic operational amplifier (O-OpAmp). (b) Activation function of the O-OpAmp-based neuronal circuit with four memristive synaptic functionalities. The "ON & OFF" and "OFF & ON" cases produced two different curves by utilizing different *Mem1* and *Mem2* resistances. 169
- Figure 72. Example of *I-V* characteristics scan of an OM-RAM device fabricated based on insulating copolymer PS-*b*-PMMA doped with conductive C₆₀. 170
- Figure 73. *I-V* characteristics scan of an analog memristive device that could be used as a spiking synapse in a spiking neural network. 171

List of Equations

Equation 1. Mathematical representation of the output of an artificial neuron.....	15
Equation 2. Mathematical representation of the output of an artificial neural circuit shown in Figure 1.....	16
Equation 3. Expression for the summed, n scaled input weights, which are then used as the input to the somatic transistor.....	22
Equation 4. Expression that describes the circuit behavior, shown in Figure 1, when the transistor operates in <i>linear</i> regime.....	24
Equation 5. Expression that describes the circuit behavior, shown in Figure 1, when the transistor operates in <i>saturation</i> regime.....	24
Equation 6. Simplification of Equation 4, when $V_G \gg V_{OUT}$	24
Equation 7. Expression that describes neural circuit behavior in transistor's linear regime, for large value of V_G , resulting in simplified Equation 4, with behavior shown in Figure 6.....	24
Equation 8. Simplification of Equation 4, when $V_G \rightarrow 0$	25
Equation 9. Expression that describes neural circuit behavior in transistor's linear regime for small value of V_G , resulting in simplified Equation 4.....	26
Equation 10. OFET drain current calculated for linear region.....	84
Equation 11. OFET drain current calculated for saturation region without the channel-length modulation parameter, resulting in a completely flat curve.....	84
Equation 12. Carrier mobility calculation.....	84
Equation 13. Equation used to calculate the channel length modulation parameter.....	84
Equation 14. Calculation of OFET's drain current including the channel-length modulation parameter, resulting in a sloped curve.....	84
Equation 15. Calculation of the output resistance with the channel length modulation parameter.....	85

List of Tables

Table 1. Single simulated neuron trained to perform the simple binary classification associated with water hammer effect).....	146
Table 2. Single polymer neuron trained to perform the simple binary classification associated with water hammer effect, shown in Figure 63(a-e).....	146
Table 3. Configuration of memristive synapses, often termed connection weights, used in a network shown in Figure 58, to perform the active tether classification.....	147
Table 4. A small network of neurons trained to perform the simple classification associated with water hammer effect, shown in Figure 63(a-j).....	148
Table 5. A truth table of the SCP prototype with three pressure/bend sensors acting as neuronal inputs, and two LEDs functioning as neuronal outputs, as shown in Figure 65(b).....	157

List of Acronyms

<i>2ME</i>	2-methoxyethanol
<i>AL</i>	Active Layer
<i>ANN</i>	Artificial Neural Network
<i>BD</i>	Bistable Device
<i>BE</i>	Bottom Electrode
<i>BOM</i>	Bistable Organic Memory
<i>DMF</i>	Dimethylformamide
<i>DU</i>	University of Denver
<i>EIL</i>	Electron Injection Layer
<i>HIL</i>	Hole Injection Layer
<i>HNN</i>	Hardware Neural Network
<i>ITO</i>	Indium Tin Oxide
<i>IPA</i>	Isopropyl Alcohol
<i>MEA</i>	Monoethanolamine
<i>NP</i>	Nanoparticle
<i>OBD</i>	Organic Bistable Device
<i>OBMD</i>	Organic Bistable Memory Device
<i>OFET</i>	Organic Field Effect Transistor
<i>OLED</i>	Organic Light Emitting Diode
<i>OM-PROM</i>	Organic Memristive Programmable Read Only Memory
<i>OM-RAM</i>	Organic Memristive Random Access Memory
<i>ONVM</i>	Organic Non-Volatile Memory
<i>OPV</i>	Organic Photovoltaics
<i>OTFT</i>	Organic Thin Film Transistor
<i>PEDOT</i>	Poly(3,4-ethylenedioxythiophene)
<i>PEDT</i>	Poly(3,4-ethylenedioxythiophene)
<i>PEN</i>	Polyethylene Naphthalene
<i>PES</i>	Polyethersulfone
<i>PET</i>	Polyethylene Terephthalate
<i>PMMA</i>	Poly(methyl methacrylate)
<i>PNC</i>	Polymer Neuromorphic Circuitry
<i>PQT-12</i>	Poly(3,3''' dialkylquaterthiophene)
<i>PS-b-PMMA</i>	copolymer of Polystyrene and Poly(methyl methacrylate)
<i>PSS</i>	Polystyrene sulfonate
<i>PTFT</i>	Polymer Thin Film Transistor

<i>PVP</i>	Poly(4-vinylphenol)
<i>RPM</i>	Rapid Prototyping Machine
<i>RR</i>	Regioregular
<i>SCP</i>	Structured Computational Polymer
<i>SNN</i>	Synthetic Neural Network
<i>STD</i>	Short-term Depression
<i>STP</i>	Short-term Potentiation
<i>TE</i>	Top Electrode
<i>TEM</i>	Transmission Electron Microscopy
<i>WORM</i>	Write Once Read Many times
<i>ZnO</i>	Zinc Oxide

Chapter 1: Introduction

1.1 Motivation

Majority of today's computers are built according to a concept first outlined by Alan Turing in 1937 (Cragon, 2000). They are founded on the idea of universal computation of serial instructions with macro separation of information and information processing. This paradigm has proven to be greatly successful, with computers found to augment just about every aspect of humans' lives. However, built around the principle of transistors operating in saturation regime with deterministic computational approach, these computers are power hungry, primarily serial in execution, susceptible to physical damage, and have to be explicitly programmed for specific tasks (Sharad, Augustine, Panagopoulos, & Roy, 2012). Furthermore, even though the AI has made spectacular progress in the last few years, it is still largely limited to specific applications such as automated phone services, intelligent personal assistance, such as Apple's SIRI, or on-line health advices (Diller, 2010; Jackson, 2013).

Compared to conventional supercomputers that consume megawatts of power and take minutes or even hours to compute parallel and complex tasks, a brain of a fruit fly consumes microwatts of power while performing such intricate and disparate tasks as flight control, path planning, predator avoidance, and food and mate search (Fox, 2009). As

such, an attempt to build small mechanical devices with embedded intelligence cannot rely on conventional microprocessor-based information processing, but requires a paradigm shift.

Neuromorphic engineering is a concept that was first coined by Carver Mead in 1990 (Mead, 1990). It attempts to apply biologically inspired computing to concepts such as machine learning, machine perception, and autonomous robotics. It is generally believed that its ultra-low power consumption, resilience against damage, as well as the generic artificial intelligence are due to the massively parallel nature of the information processing of relatively simple information processing elements (Boahen, 2005).

1.2 Dissertation Overview

Given the limitation of the serially emulated neuromorphic systems, the desire to build low-power generic information processing for small-size robots coupled with the shortcomings or complexities of the currently available hardware neuromorphic systems, the potential of biologically inspired neuromorphic architectures to build machines that can learn and reason, and my personal interest in biologically inspired computing, I decided to investigate the possibility of developing a simple parallel information processing system that would be truly distributed, could be employed for a wide variety of tasks, easy to manufacture and based on a type of information processing akin to the type of processing observed in nature.

The primary contributions of this doctoral dissertation include: development of a new technique for localized blade coating that allows for customization of polymeric film characteristics for different devices on the same substrate; adaptation and verification of bio-

inspired architecture necessary to realize the Polymer Neuromorphic Circuitry; development of a novel polymer memristive device that enabled the realization of synaptic memories with tunable characteristics; development of a collection of polymer electronic "primitives" to enable rapid prototyping of analogue and digital polymer neuromorphic circuitry

This dissertation is organized as follows. First I present a review of the state of the art in neuromorphic circuits proposals and implementations followed by a background of the discovery of my own architecture. Next, I will demonstrate my own neuromorphic proposal of a single neuron, with the emphasis on the simplicity of this design. Chapter Three will provide a background information on organic electronics as well electrical elements required for the implementation of my neuromorphic circuit. Chapter Four is dedicated to manufacturing complexities and compromises necessary for creation of individual organic electronics elements as well manufacturing of disparate organic electronics elements on a single substrate. In Chapter Five I will show that a single polymer neuron is capable of simple linear classification. I will also demonstrate the functioning of a small network of polymer neurons validating the claim of their cascading ability. Chapter Six is dedicated to the application of the PNC in a form of a smart material that could be used in manufacturing of soft robots. Finally in Chapter 7 I will summarize the work as well as present the future directions of the research.

1.3 Review of Literature

The bulk of the current research in neuromorphic circuitry aims at approximating spiking biological neuron behavior. Their primary goal

is to more accurately model large-scale biological networks for the purposes of understanding the brain. Furthermore, with their complexities largely due to a hefty number of electrical elements used, these circuits are primarily designed to be implemented in silicon. With the Hodgkin-Huxley model (Hodgkin & Huxley, 1952) regarded as an accurate model of the biological neuron, the examples include a piecewise-linear circuit approximation of the Hodgkin-Huxley model (Storace, Julian, & Parodi, 2001), the above threshold Hodgkin-Huxley circuit that offers the ability to selectively tune individual parameters of the Hodgkin-Huxley model (Renaud, Tomas, Bornat, Daouzli, & Saighi, 2007), or the sub-threshold Hodgkin-Huxley circuit that integrates a biophysical network of Hodgkin-Huxley neurons and conductance-based synapses with programmable kinetics of channel gating parameters (Yu & Cauwenberghs, 2010). Other models that mimic the behavior of a spiking biological neuron, including the Axon-Hillock circuit (Mead, 1989), the Integrate & Fire neuron (van Schaik, 2001), "Bernoulli-Cell" (Drakakis, Payne, & Toumazou, 1997), "Tau-Cell" (Edwards & Cauwenberghs, 2000), or log-domain low-pass filter model (Arthur & Boahen, 2004), have been proposed and realized. To date, the majority of these neural circuits have been implemented using inorganic (primarily silicon-based) electronics components (Indiveri et al., 2011).

A number of large-scale projects have been undertaken, that attempt to simulate, or emulate, biological brains with greater or lesser degree of biological realism. A programmable neuromorphic chip, termed Neurogrid, was created at Stanford University with the goal of powering an affordable supercomputer designed to explore various hypothesis about the inner workings of a mammalian cortex (Gao,

Benjamin, & Boahen, 2012; Silver, Boahen, Grillner, Kopell, & Olsen, 2007). Neurogrid is based on highly interconnected silicon neurons emulated with an eight-transistors-per-soma circuit with a limited degree of biological realism.

SPIking Neural Network Architecture (SpiNNaker) is a massively parallel, low power, neuromorphic supercomputer currently under construction at Manchester University (Sharp, Galluppi, Rast, & Furber, 2012). Its main aim is to model large, biologically realistic networks of spiking neurons. The supercomputer will consist of 65,536, 18-core processors, each with their own on-board routers and 128 MB of memory used to store synaptic weights. SpiNNaker is intended to be a hardware platform that will allow for different neural algorithms, such as simulation of visual cortex or the cerebellum, to be implemented.

Systems of Neuromorphic Adaptive Plastic Scalable Electronics (SyNAPSE) is a DARPA-funded program aiming to develop neuromorphic system technology that would be capable to scale to biological levels (DARPA, 2013; HRL, 2013; IBM, 2013). The ultimate goal of this project is the ability to build robots with intelligence, size, and power consumption comparable to small mammals, such as mice or cats. The project, primarily contracted to IBM and HRL (formerly Hughes Research Laboratories), aims to create a system consisting of 10 billion neurons with 100 trillion synapses, consume one kilowatt of power, and occupy less than two cubic decimeters. The implementation will likely be based on CMOS technology with neuromorphic architecture that employs memristive synapses (Ananthanarayanan, Esser, Simon, & Modha, 2009; K. H. Kim et al., 2012; Seo et al., 2011).

The Blue Brain Project is an attempt to reverse engineer the human brain and recreate it at the cellular level, inside a computer

simulation (EPFL, 2013). The main goal of this École Polytechnique Fédérale de Lausanne (EPFL) based and European Union funded project, conducted with the greatest degree of biological realism, is to gain a complete understanding of the human brain with the intention of better and faster understanding of various neurological disorders and their respective treatments (Maass, Legenstein, & Markram, 2002; Reimann et al., 2013). The research involves studying individual slices of living brain tissue, by means of optical microscopy and patch clamp electrodes, from various brain regions of the cerebral cortex. The simulation of approximately one million neurons with one billion synapses, is conducted on IBM-built Blue Gene supercomputer (hence the "Blue Brain" project name) fit with 4,096 quad-core PowerPC RISC processors.

Other proposals aim at more compact designs, typically implementing non-spiking neural models, with more conventional applications in mind, such mobile robot control, autonomous vehicle control or visual obstacle tracking. For instance Deshmukh et al. (Deshmukh, Morghade, Khera, & Bajaj, 2005) suggested realizing the functionality of a neuron via a conventional CMOS technology. In simulation, they constructed a network of binary logic discrete neurons, with a single neuron based on the operation of a transistor in its saturation region. A single neuron was based on a weighter circuit, constructed with two flip flops, one XOR and one NAND gate, used to perform the connection weight functionality, with an additional NOR gate used as an output of all weighter circuits. Two-phase clocking with no overlap was used to ensure that the weights were shifted without corruption. They demonstrated a network consisting of three

layers, each fit with five neurons, capable of performing a task of simple pattern recognition.

Gupta and Bhat (Gupta & Bhat, 2005) proposed a design aiming at realizing the sigmoidal activation function, as well as its derivative, commonly used with neural networks (Haykin, 1998). This design was based on asymmetry of individual transistors, operating in their linear regions, connected as cross-coupled differential pairs. This proposal used an external signal to obtain either the sigmoidal or the derivative of sigmoidal activation function from the same circuit. It featured fifteen transistors, cross-coupled and operating in their subthreshold regions, as well as four current sources. The authors demonstrated a proof-of-concept neuron capable of generating both tansigmoidal (bounded between ± 10 volts) and logsigmoidal (bounded between 0 and 20 volts) activation functions as well as the bell-shaped derivative (with a peak at around 4.5 volts). Additionally, experimental results showing family of outputs with various saturation levels of the sigmoidal shape curve, along with their derivatives were shown. The difference between the positive saturation (1st quadrant) and negative saturation (3rd quadrant) authors determined to be up to 200%.

A number of companies, including Intel, IBM, AMD, Hitachi, Siemens and Samsung, to name just a few, offer or have offered commercial chips that, to a various extent (degree of precision, including or excluding learning ability, various network architecture), realized the functionality of neural networks (Dias, Antunes, & Mota, 2004). Hitachi, for instance, offered neural chips with either Hopfield or Backpropagation learning functions with up to 574 neurons and 32k synapses. IBM developed a number of chips that employed radial basis function (RBF) architecture and could use up to 36 neurons per chip

with a maximum of 64 synapses per neuron. Intel offered chips that did (NI1000, via restricted coulomb energy, and probabilistic neural network, algorithms) and did not (Electrically Trainable Analog Neural Network) possess learning capabilities. A chip with no learning paradigm requires having its weights imported after an external neural network has been trained (for instance using software such as MATLAB's ANN Toolbox).

On a much smaller scale, a single device made of molecules and nanoparticles, termed Nanoparticle Organic Memory Field-Effect Transistor, or NOMFET (Alibart et al., 2010), was shown to exhibit a facilitating (STP, or short-term potentiation) and depressing (STD, or short-term depression) behavior of a biological spiking synapse. The same device was shown to exhibit both, the STP and STD functions commonly found in biological brains: By applying positive or negative gate voltage, while holding source and drain contacts grounded, facilitating or depressing behavior can be programmed respectively. This device makes the use of the charge storage capability of nanoparticles embedded in an insulating material that is sandwiched between source and drain electrodes of the transistor. Applying voltage repeatedly results in steadily increasing or decreasing voltage response of the NOMFET due to individual charges being continuously and cumulatively retained by gold nanoparticles. The transconductance gain of the transistor is used to dynamically tune the amount of charge stored by the nanoparticles. That, in effect, makes the device mimic the short-term plasticity of a biological synapse.

1.4 Background

The memristor is a two-terminal, passive device considered to be the fourth fundamental electrical element alongside the resistor, the capacitor, and the inductor (Chua, 1971; Strukov, Snider, Stewart, & Williams, 2008). Theoretically, the memristor relates flux to charge, but practically it behaves like a variable resistor with a non-volatile memory that retains its last value.

It should be noted that at present there appears to be a lack of agreement on the definition of a memristor (Marks, 2012; Meuffels & Schroeder, 2011; Meuffels & Soni, 2012). Memristor is defined as a device that relates flux to charge. However, most of the fabricated inorganic and organic devices are bistable resistors rather than continuously variable devices. As such, I will refer to these devices as "memristive devices".

The first proposal to employ memristive devices to realize synaptic weighting functionality was suggested by Likharev *et al.* (Likharev, Mayr, Muckra, & Turel, 2003; Strukov & Likharev, 2012). Their CMOL (CMOS/nanowire/MOLecular/nanodevice) was a proposed design that aimed at combining the existing CMOS technology with the ultra-high-area density, two-terminal devices to form a neuromorphic implementation. This nanoscale hybrid semiconductor / nanodevice integrated circuit with a neuromorphic architecture, would be created from CMOS op-amps acting as somas, and synapses from two-terminal, bistable memristive nanodevices formed at intersections of nanoscale axonic and dendritic wires. The arrangement of these devices would produce a system with a behavior similar to that of a neural network. Via simulation, CMOL was demonstrated to perform functions such as

image recognition and pattern classification (J. H. Lee & Likharev, 2007; Türel, Lee, Ma, & Likharev, 2004).

Subsequently, with the overwhelmingly positive response, in both academia and commercial industry, to the announcement of the “discovery” of a memristor, other research groups have suggested the use, or in very few cases demonstrated the advantages, of memristive synapses (Chen, Li, Wang, & Duan, 2013; Hui, Hai, & Pino, 2012; B. Liu et al., 2013; Rose, Pino, & Qing, 2011; Serrano-Gotarredona, Masquelier, Prodromakis, Indiveri, & Linares-Barranco, 2013). However, because of the manufacturing or circuit complexities, these systems tend to concentrate only on a specific aspect of neural functionality, namely the synaptic functionality, without addressing the neural soma.

A memristor emulator, built from inexpensive off-the-shelf components, was demonstrated at the University of South Carolina (Pershin & Di Ventra, 2010). The device, consisting of a digital potentiometer, analog-to-digital converter and a microcontroller, was shown to have the ability to realize the synaptic properties by exhibiting the formation of associative memory in a simple, three-neuron-two-synapse network.

A group at University of Michigan has demonstrated the possibility of employing a silicon-based memristor to realize the time-dependent characteristics of a biological spiking synapse (Gaba, Sheridan, Zhou, Choi, & Lu, 2013; S. H. Jo et al., 2010). Their realized design utilized conventional CMOS neurons and silicon-based memristive devices acting as artificial synapses and performing both potentiating (increasing) and depressing (decreasing) functions commonly associated with spike timing dependent plasticity, STP or STD, observed in biological neural networks. In their design, memristors

were arranged into a cross-bar with pre- and post-synaptic neurons being located on adjacent sides of the cross-bar. This allowed every post-synaptic neuron to receive a signal from every pre-synaptic neuron. The use of memristive synapses resulted in neural behavior akin to spiking, biological neurons.

Recently a new proposal for integrating memristive devices with previously proposed synaptic circuit, was made (Indiveri, Linares-Barranco, Legenstein, Deligeorgis, & Prodromakis, 2013). A Differential Pair Integrator circuit (Bartolozzi & Indiveri, 2007), that can produce both linear dynamics with biologically plausible time constants as well as non-linear short-term plasticity effects commonly associated with biological synapses, was augmented to incorporate memristive devices. This hybrid memristor-CMOS neuromorphic synapse circuit was demonstrated in simulation to emulate the same detailed synaptic biophysics while theoretically achieving power and space savings. The memristive circuit allowed for individual memristors acting as independent neural weights but with the same temporal dynamics, allowing for each memristor to represent either a full synaptic contact or an individual ion channel in the synaptic cleft.

As already stated, the proposed or demonstrated memristive synaptic circuits are primarily based on inorganic memristive devices first demonstrated by Strukov et al. (Strukov, et al., 2008).

Organic electronics is a branch of electronics that is based on conducting and semiconducting polymers and molecules. It relies on the electronic properties of π -conjugated molecules that derive their electronic conduction from alternating sequences of single and double carbon-carbon bonds along their main chain. Manufacturing of inorganic electronics requires clean environments and vacuum deposition processes

that lead to high production costs. In contrast, organic (polymer) electronics can be manufactured using low-cost, roll-to-roll atmospheric processing methods such as inkjet, blade-coating, and lamination (R. Nawrocki, Voyles, & Shaheen, 2012; So, 2010; Sun & Dalton, 2008).

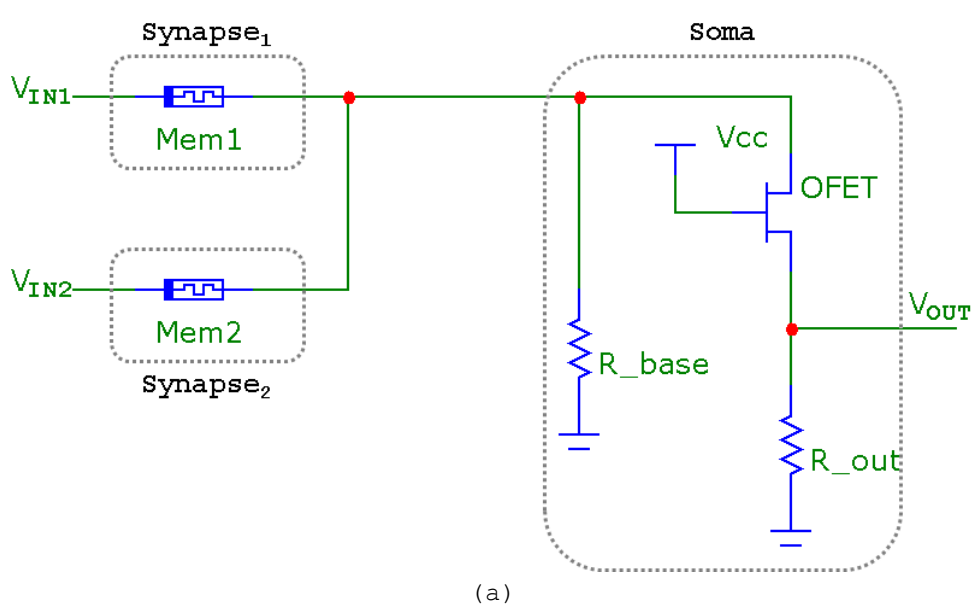
With the motivation of developing neuromorphic circuitry that takes advantage of the attractive features of organic electronics materials, I have proposed a low-complexity neuromorphic architecture, inspired by the McCulloch-Pitts model of an artificial neuron, based on a novel, single Organic Field Effect Transistor (OFET) neuronal circuit that uses an organic memristive device to realize the programmable weighting (multiplicative) property of a synapse (R. A. Nawrocki, Shaheen, & Voyles, 2011). This is the first demonstration of a fabrication of an entire neuron, and a network of such neurons, that includes both the weighting functionality of a synapse and the somatic summing. All of the neurons, and the network of such neurons, were manufactured using polymer electronics devices. This focus on organic electronics is a key strength of my approach as essentially all of the proposed or implemented neuromorphic circuits to date have relied on conventional, inorganic components.

I will demonstrate that the activation function of the neuron approximates that of a sigmoid. I acknowledge that the use of a single transistor soma results in the activation that is more akin to a non-linear amplifier rather than a standard sigmoidal activation function. However, a prudent choice of circuit parameters minimizes the discrepancy. I will also validate the utility of the proposed neuromorphic circuitry by demonstrating that a network of such neurons,

and even a single neuron, are capable of performing linear classification for a real-life problem.

Chapter 2: Design of a Polymer Neuron

I have developed a simple, single-transistor, single-memristive-device-per-input circuit, shown in Figure 1, which produces a suitable approximation to neural synapses and the soma (R. A. Nawrocki, Shaheen, et al., 2011), while exhibiting significant immunity to low yield during device fabrication. The circuit nominally produces a linear behavior, but I will show later how a nonlinear behavior can be achieved as well.



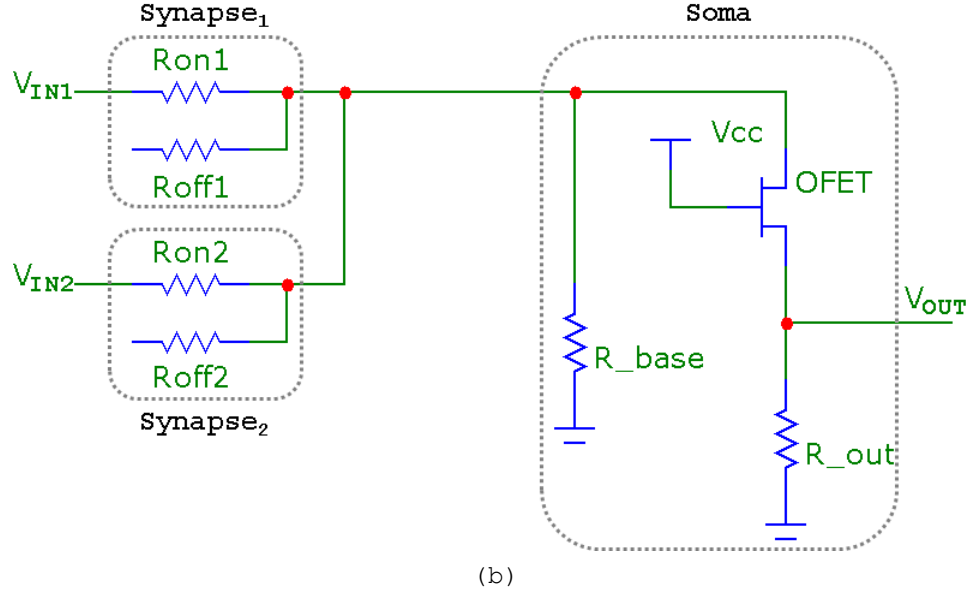


Figure 1. Schematic diagram of a single neuron with two inputs, denoted by V_{IN1} and V_{IN2} , and one output, marked V_{OUT} . (a) Organic memristive devices, R_{MEM1} and R_{MEM2} , provide the synaptic weights while a tuned organic field effect transistor (OFET) provides the sigmoidal activation that bounds the output as a function of the sum of the weighted inputs. (b) Circuit that replaces an individual memristive device with two resistors and a switch, as illustrated in Figure 3.

The McCulloch-Pitts neuron capabilities I am trying to capture are codified in the algorithmic expression:

$$y = \varphi \left(\sum_{i=1}^n (w_i x_i) \right)$$

Equation 1. Mathematical representation of the output of an artificial neuron.

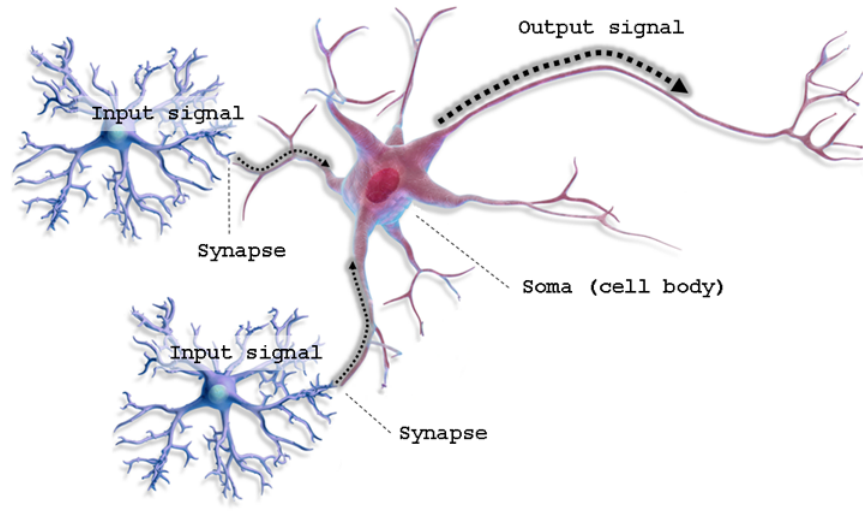
Here, each input, x_i , is scaled by the corresponding connection weight, w_i , summed and then mapped to an output, y , by the activation function, φ . (A threshold can be included as an additional input tied high or low.) In Figure 1, V_{INi} corresponds to x_i and V_{OUT} corresponds to y . The scaling of the input value is accomplished with the use of memristive devices and is described in more details later. Equation 2 represents the output of a single artificial neural circuit shown in Figure 1,

with the relationship of R_{fixed} and R_{weight} in the circuit operation described later in text.

$$V_{OUT} = \varphi \left(\sum_{i=1}^n \left(\frac{R_{fixed}}{(R_{weight_i} + R_{fixed})} \right) V_{IN_i} \right)$$

Equation 2. Mathematical representation of the output of an artificial neural circuit shown in Figure 1.

It has been shown that linear activation functions have limited usefulness (Haykin, 1998) for classifying complex patterns, hence a nonlinear activation, such as a sigmoid, is my ultimate goal. Figure 2(a) depicts a biological neuron while Figure 2(b) is a graphical representation of the McCulloch-Pitts neuron shown in Equation 1.



(a)

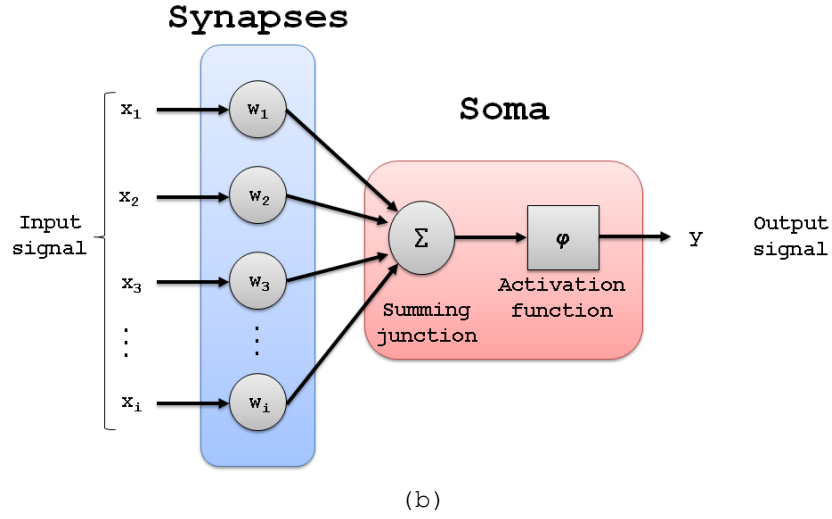


Figure 2. (a) Biological neuron with input signal received at a synapse while soma adds the input signal and produces appropriate output (original image from Wikipedia.org). (b) Graphical representation of operation of a single artificial neural, with mathematical expression being shown in Equation 1: Artificial synapse (connection weight) weights the input signal while the soma produces proportional output (activation function) that is the sum of all of the input signals.

2.1 Synapse

From the computational perspective, in biological neurons, the synapse provides both the multiplicative weighting capability and the ability to store programmable weights, w_i . The circuit in Figure 1 achieves multiplicative weighting with voltage dividers formed by R_{MEMi} and R_{BASE} and achieves programmable weights by instantiating R_{MEMi} with bistable memristive devices. In Figure 1, R_{MEMi} corresponds to w_i in Equation 1. In its most basic form, a bistable memristive device can be thought of as a two-terminal memory element modeled with two resistors (high and low) and a switch, as shown in Figure 3 (R. Nawrocki, et al., 2012). Initially, it is in the OFF state represented by the high resistance, R_{OFF} . The switch is flipped into the ON state by applying a high positive voltage to the device in excess of the positive threshold

(the positive programming voltage). Likewise, the switch is flipped back into the OFF state by applying a negative voltage in excess of the negative threshold (the negative programming voltage).

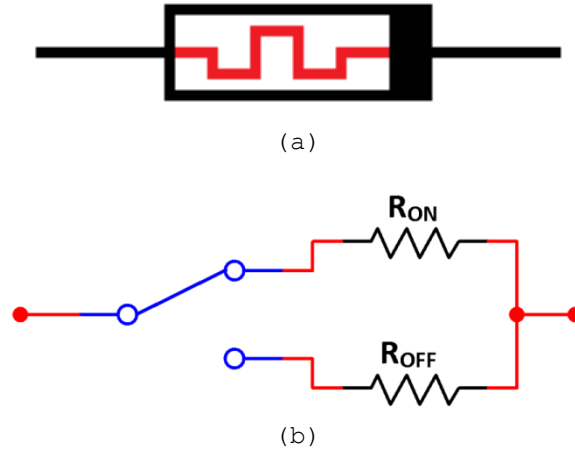
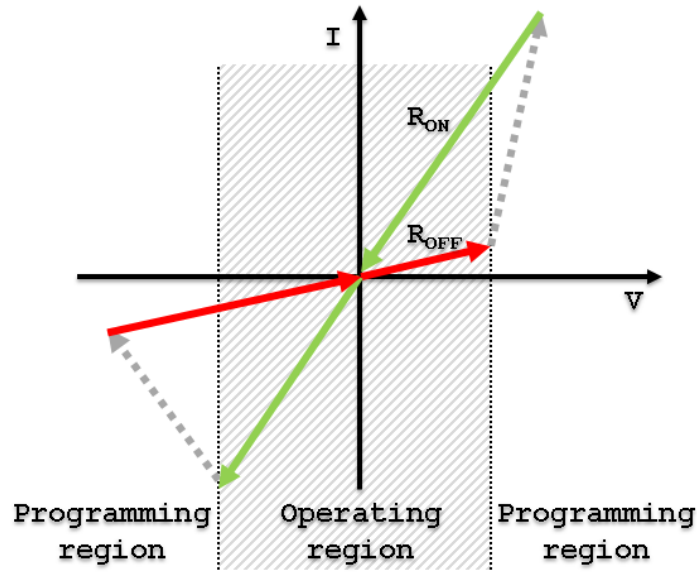
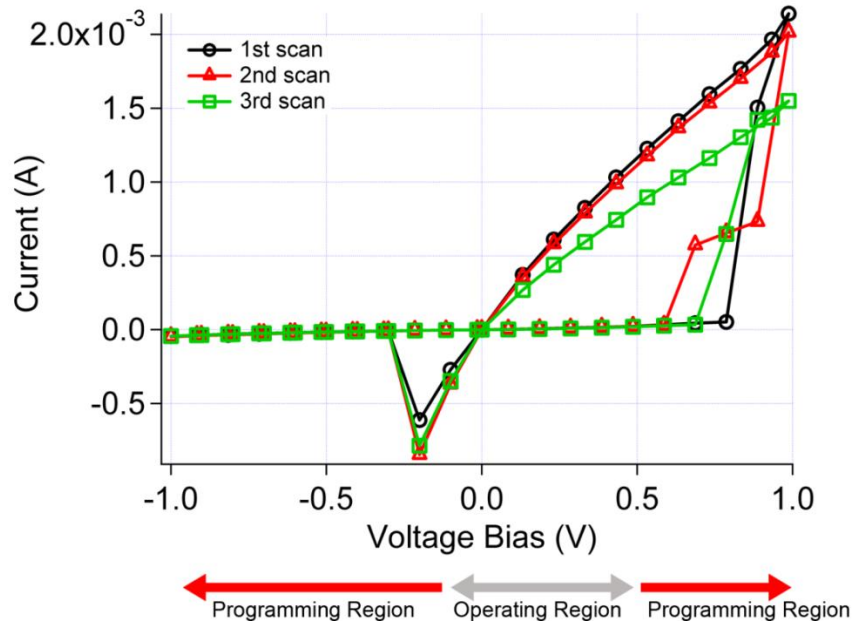


Figure 3. Bistable memristive device: (a) electrical symbol - used in Figure 1(a); (b) representation in a form of two resistors, R_{ON} (low resistance) and R_{OFF} (high resistance), and a switch - used in Figure 1(b).

A bistable memristive device that exhibits the ability to repeatedly switch between ON and OFF states is analogous to a random access memory and will be referred to here as Memristive Random Access Memory (M-RAM). The novelty of my work is in the use of those devices realized from organic materials, which I refer to as Organic Memristive Random Access Memory (OM-RAM), to function as organic synapses. Figure 4(a) portrays an idealized diagram while Figure 4(b) shows I - V characteristics of an OM-RAM device created in my laboratory. The near-linear portions of the I - V curves, resulting from the distinct ON and OFF resistances (R_{ON} of $\sim 500 \, \Omega$ and R_{OFF} of $\sim 22 \, k\Omega$ respectively), are clearly visible as the input voltage is scanned three times from 0 V to +1 V to -1 V and back to 0 V, with the device switching states at ~ 0.7 V.



(a)

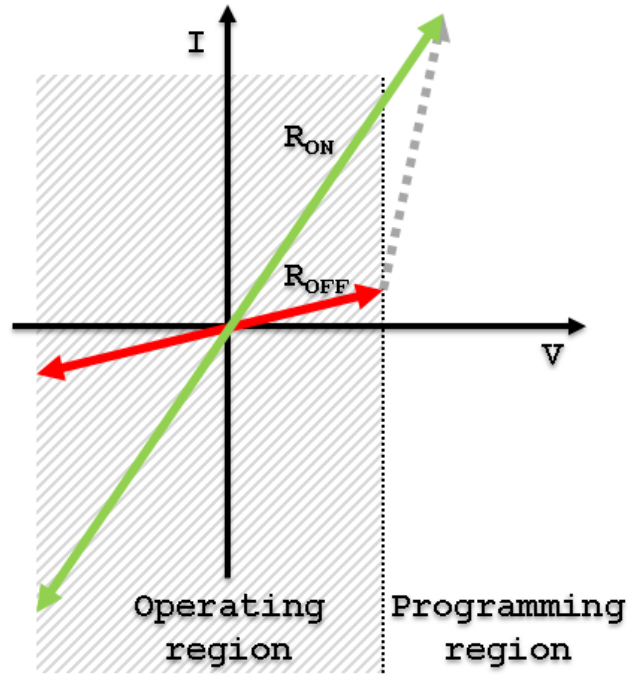


(b)

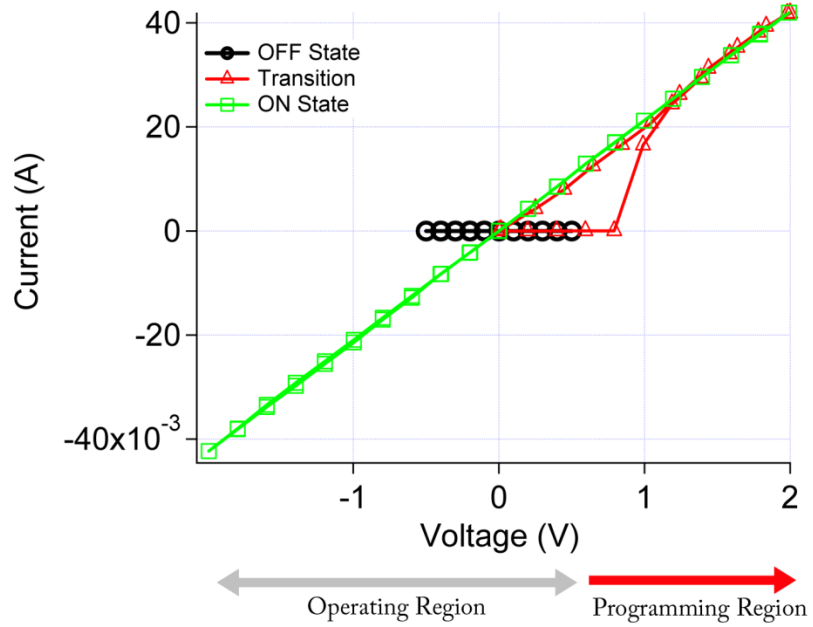
Figure 4. I - V characteristics of a bistable memristive device with reversible switching, analogous to OM-RAM devices: (a) ideal operation, (b) real device.

There also exists a subset of organic memristive devices where the change of state is irreversible. As such, this device is analogous to a programmable read only memory, and I will refer to it as an

Organic Memristive Programmable Read Only Memory (OM-PROM) device. Figure 5(a) shows a schematic graph while Figure 5(b) demonstrates the I - V relationship of an OM-PROM device created in my laboratory. It can be seen that the device is in an OFF state (with $R_{OFF} = \sim 560 \text{ k}\Omega$, corresponding to a synaptic value of "0"), with a linear resistance, until a threshold voltage is reached. Once the device turns ON (with $R_{ON} = \sim 50 \text{ }\Omega$, corresponding to a synaptic value of "1"), the state is permanently retained. The value of the threshold voltage (of $\sim 0.8 \text{ V}$ in Figure 5(b)), of either OM-RAM or OM-PROM, dictates the boundary between the operating region and the programming region. During programming, the applied voltage needs to exceed the appropriate threshold voltage to affect the storage of a desired value. Likewise, during operation, the applied inputs must not exceed the synaptic threshold voltage, otherwise an OFF synapse will undesirably turn ON and produce unpredictable results. Fortunately, this is one of the purposes of the activation function: bounding the output of neurons so cascading values cannot exceed input parameters.



(a)



(b)

Figure 5. I - V characteristics of a bistable memristive device with irreversible switching, analogous to OM-PROM devices: (a) ideal operation, (b) real device.

Furthermore, as described above, an OM-RAM's and an OM-PROM's value, or state, are electrically programmed (analogous to modifying the value of connection weight during the neural network training) with minimal additional circuitry. Only a programming voltage beyond the threshold voltage is needed and the ability to route it appropriately. It is this input weighting capability, and electrical programmability, that make such a memristive device a natural choice to realize the functionality of a polymer synapse. However, it should be noted that biological synapses can be either excitatory (analogous to positive connection weights) or inhibitory (negative connection weights) (Kandel, Schwartz, & Jessell, 2000). The use of a memristive device in a voltage divider as an artificial synapse only allows for positive connection weights.

2.2 Soma

The soma performs two functions: i) summation of the arbitrary number of inputs and ii) mapping of the summed-input signal to the bounded output signal through the activation function. The circuit in Figure 1 sums the n scaled input values at the intermediate point labeled V_X (with $n = 2$ in the figure) according to the formula:

$$V_X = \sum \left(\left(\frac{R_{BASE}}{(R_{MEM_i} + R_{BASE})} \right) V_{IN_i} \right)$$

Equation 3. Expression for the summed, n scaled input weights, which are then used as the input to the somatic transistor.

where R_{MEM_i} is the "programmed" resistance value setting the synaptic weight, w_i , on the i^{th} input, V_{IN_i} . Equation 3 ignores the impedance of the OFET in Figure 1, assuming it is large compared to R_{BASE} .

The activation function that maps V_X to V_{OUT} requires deeper consideration and will be explained more carefully in the next section. It is well-known that a non-linear activation function is necessary for complex, non-linear classification in a multi-layer perceptron (Haykin, 1998). A sigmoidal activation function is a popular choice and I manipulate the characteristic I - V curve of the OFET (shown in section 3.3.2 *OFET For Synthetic Soma*), to approximate such a function.

Careful selection of both the OFET device fabrication parameters and V_G allows achieving tantalizingly close approximations of sigmoidal behavior of the artificial neuron with a very simple circuit. The simplicity and robustness of the circuit is important to achieve large-scale (multi-neuron), full-connectivity networks with meaningful behavior despite the relatively low yields that typify organic electronics at this time.

2.3 Single Neuron Operation and Activation

While the I - V characteristics of the fabricated OFET holds the key to the output behavior of the neuronal circuit, it does not tell the entire story. The circuit of Figure 1 is essentially a linear amplifier configuration. However, by balancing the linear and saturation regions of the OFET, a valuable approximation to the sigmoid can be achieved.

Equation 4 and Equation 5, below, predict the behavior of the circuit in Figure 1 with Equation 4 modeling the behavior in the transistor's linear region, while Equation 5 models the transistor's saturation region (Gburek & Wagner, 2010; Horowitz, 2010b; Neamen, 2009; Tinivella, Shen, Pirola, Ghione, & Camarchia, 2010). Because the

impedance of the OFET is several orders of magnitude larger than R_{BASE} , Equation 3 holds.

$$V_{OUT}^2 - \left(\frac{(-V_G + V_{OUT})^{-\gamma}}{1/2 \mu_0 C_x W/L R_{OUT}} + 2V_G \right) V_{OUT} - \left(\left(\frac{R_{BASE}}{R_{BASE} + R_{MEM}} V_{IN} \right)^2 - 2V_G \left(\frac{R_{BASE}}{R_{BASE} + R_{MEM}} V_{IN} \right) \right) = 0$$

Equation 4. Expression that describes the circuit behavior, shown in Figure 1, when the transistor operates in *linear* regime.

$$\lambda V_{OUT}^3 - \left(1 + \lambda \frac{R_{BASE}}{R_{BASE} + R_{MEM}} V_{IN} + 2\lambda V_G \right) V_{OUT}^2 + \left[\frac{(-V_G + V_{OUT})^{-\gamma}}{1/2 \mu_0 C_x W/L R_{OUT}} + 2V_G \right. \\ \left. + 2\lambda V_G \frac{R_{BASE}}{R_{BASE} + R_{MEM}} V_{IN} + \lambda V_G^2 \right] V_{OUT} - (V_G^2 + \lambda V_G^2 \frac{R_{BASE}}{R_{BASE} + R_{MEM}} V_{IN}) = 0$$

Equation 5. Expression that describes the circuit behavior, shown in Figure 1, when the transistor operates in *saturation* regime.

OFET's I - V characteristics function (such as the one shown in Figure 36) suggests that to achieve sigmoidal behavior in our artificial soma, large negative values of V_G are beneficial. However, in the linear region (Equation 4), we see that when $V_G \gg V_{OUT}$, the second term with $V_G \times V_{OUT}$ dominates both, the first term, V_{OUT}^2 , and the third term, V_{IN}^2 . This effectively simplifies Equation 4 to:

$$V_{OUT} \left(\cancel{\frac{V_{OUT}}{V_G}} - \left(\cancel{\frac{(-V_G + V_{OUT})^{-\gamma}}{(1/2 \mu_0 C_x W/L R_{OUT}) V_G}} + 2 \right) \right) - \left(\left(\cancel{\frac{R_{BASE}}{R_{BASE} + R_{MEM}} V_{IN}^2} \right) - 2 \left(\cancel{\frac{R_{BASE}}{R_{BASE} + R_{MEM}} V_{IN}} \right) \right) = 0$$

Equation 6. Simplification of Equation 4, when $V_G \gg V_{OUT}$.

$$V_{OUT} = \left(\frac{R_{BASE}}{R_{BASE} + R_{MEM}} \right) V_{IN}$$

Equation 7. Expression that describes neural circuit behavior in transistor's linear regime, for large value of V_G , resulting in simplified Equation 4, with behavior shown in Figure 6.

which represents a linear amplifier with no sensitivity to individual parameters of the OFET. Indeed, we have verified this experimentally, with Figure 6 showing the neural circuit output indicating a linear transfer function only dependent on R_{BASE} and R_{MEM} : Increasing the number

of neuronal inputs only increases the near-linear slope of the function.

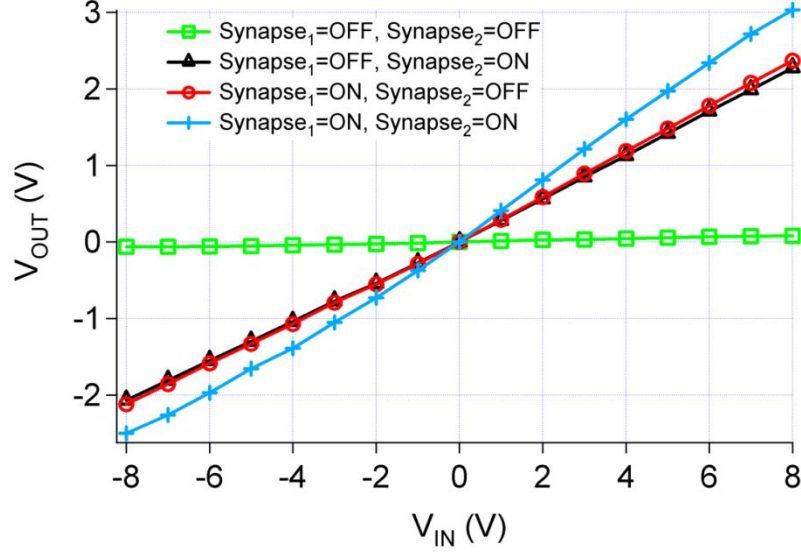


Figure 6. The activation function of a two-input polymer neuron, with large V_G , resulting in circuit behavior akin to linear amplifier, independent of the OFET but dependent on R_{BASE} and R_{MEM} .

When V_G is small, such that $V_G \rightarrow 0$, the first term, V_{OUT}^2 , and the third term, V_{IN}^2 , both dominate, while the second term is reduced to $V_{OUT}^{1-\gamma}$, and the fourth term with $V_G \times V_{IN}$ disappears. This simplifies to Equation 9 and produces the flattening or saturating effect, which is the basis of the sigmoidal behavior of the neural circuit shown in Figure 1. This trend is shown in Figure 7 and Figure 8.

$$V_{OUT}^2 - \left(\frac{(-V_G + V_{OUT})^{-\gamma}}{1/2\mu_0 C_x W/L R_{OUT}} + 2V_G \right) V_{OUT} - \left(\left(\frac{R_{BASE}}{R_{BASE} + R_{MEM}} V_{IN} \right)^2 - 2V_G \left(\frac{R_{BASE}}{R_{BASE} + R_{MEM}} V_{IN} \right) \right) = 0$$

Equation 8. Simplification of Equation 4, when $V_G \rightarrow 0$.

$$V_{OUT} \left(\frac{1}{\frac{1}{2} \mu_0 C_x \frac{W}{L} R_{OUT} V_{OUT}^\gamma} - V_{OUT} \right) = \left(\frac{R_{BASE}}{R_{BASE} + R_{MEM}} \right)^2 V_{IN}^2$$

Equation 9. Expression that describes neural circuit behavior in transistor's linear regime for small value of V_G , resulting in simplified Equation 4.

Equation 5 describes the circuit's behavior when transistor operates in a saturation regime. In an ideal device, the drain current is independent of the drain-to-source voltage and produces a familiar horizontal behavior. However, in real devices, the drain current does depend on the drain-to-source voltage producing a curve with a non-zero slope (Neamen, 2009). Equation 5 includes a λ term, typically obtained from the slope of the OFET curves in the saturation regime, which accounts for this dependence.

Analysis of Equation 5 reveals that parameter λ has a great effect on the circuit behavior. For a very small value, such that $\lambda \rightarrow 0$, V_{OUT} is independent of V_{IN} producing a completely flat curve. However, for larger values of λ , V_{OUT} is dependent on V_{IN} and requires further investigation. When V_G is small, such that $V_G \rightarrow 0$, the second term, $V_{IN} \times V_{OUT}^2$ starts to weakly influence otherwise independent V_{OUT} , producing a curve with a small slope. When V_G is large, it influences most of the terms, resulting in greater influence of V_{IN} on V_{OUT} , for instance the third term $V_G \times V_{IN}$, and the fourth term $V_G^2 \times V_{IN}$, producing a curve with a much steeper slope.

Figure 7 demonstrates the activation (transfer) function of a single polymer neuron, constructed with two inputs, with binary connection weight (a single memristive device per input), and a single output, connected according to Figure 1, with a separate-substrate fabrication approach outlined in Figure 51(a). The inputs were tied

together to demonstrate the summing effect of the neuron. The neuron was made with all organic electronic components described in the previous sections, namely OM-PROMs, OFET, and polymer resistors.

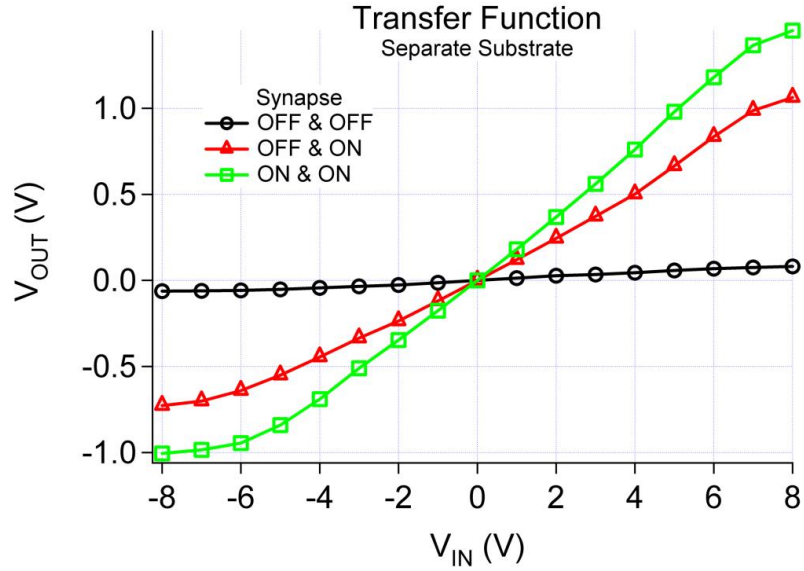


Figure 7. The activation function of a two-input polymer neuron, fabricated using the separate-substrate approach, indicated in Figure 51(a), with each input assigned binary weighting. The graph was obtained with the inputs (shown in Figure 1) being tied together.

Figure 8 displays activation function of a single neuron fabricated according to common-substrate method shown in Figure 51(b).

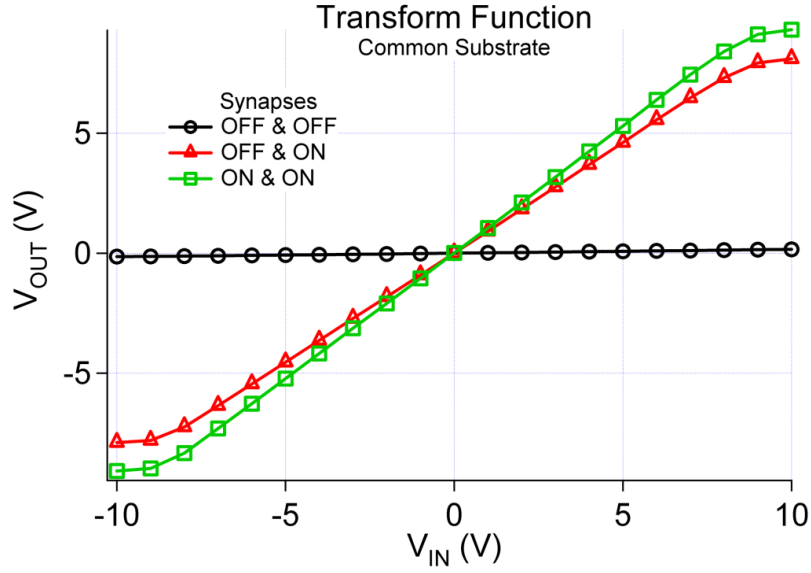


Figure 8. The activation function of a two-input polymer neuron, fabricated using the common-substrate approach, indicated in Figure 51(b).

Ideally, the transfer function of a neuron with a synapse in OFF state (equivalent to being equal to "0") would be zero. However, it can be seen that the output of a polymer neuron is small but non-zero. This is due to the fact that the R_{MEMi} of the OFF synapse has a high, but non-infinite resistance, resulting in a small, but non-zero current, computed with the voltage divider shown in Equation 3. Furthermore, in a standard perceptron the activation function boundary is fixed (usually between ± 1) and the synaptic states only affect the slope of the function. In the neuron presented here the output's leveling off is proportional to the number of inputs used as well as the value of the synaptic states. For instance in Figure 7(a) the output levels off at approximately -0.7 and 1 volt when only one synapse is in ON state but flattens around -1 and 1.5 volt with both synapses are turned ON; in Figure 7(b) the output reaches -5.7 and 6.5 volts with only one synapse

in the ON state, and -7.7 and 8.7 with both synapses in the ON state. As such, the activation function of the polymer neuron presented here is not truly sigmoidal but rather more akin to a non-linear amplifier. However, as illustrated in *Chapter 5: PNC For Linear Classification*, the neuron is able to perform useful function approximation in real-life applications with a prudent choice of parameters in Equation 4 and Equation 5.

2.4 Learning versus Programming

At present, the circuit does not incorporate any training functionalities. Instead, determining the desired configuration of weights is conducted off-line, in software, where the activation function and quantization level of the connection weights are customized to reflect the electrical characteristics of the elements used. The training can be performed in any software environment that allows customization of the activation function. Additionally, because the memristive synapses can only have positive resistive values, the software needs to explicitly restrict the values of computed connection weights. For this study, Emergent Neural Network Simulation System (Aisa, Mingus, & O'Reilly, 2008) and Matlab Neural Network (Mathworks, 2013) were used as the training software. The connection weights were then manually exported by selective programming (turning to an ON state) of the appropriate memristive synapses.

Chapter 3: Individual Components

This chapter provides background information on organic electronics followed by in-depth discussion of individual electronics elements, namely memristive devices, transistors, as well as resistors, concentrating on their respective fabrication constraints and complexities.

3.1 Organic Electronics

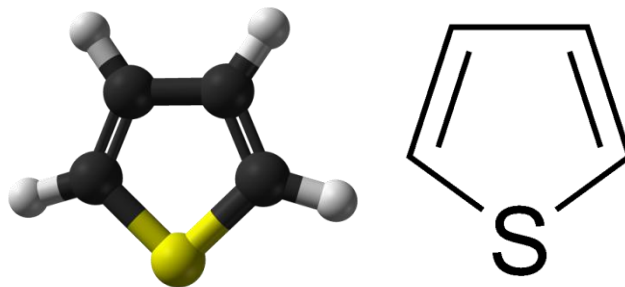
Organic electronics is a branch of electronics that is based on conducting and semiconducting polymers and molecules (R. Nawrocki, et al., 2012; So, 2010; Sun & Dalton, 2008). It relies on the electronic properties of π -conjugated molecules that derive their electronic conduction from alternating sequences of single and double carbon-carbon bonds along their main chain.

The field of organic electronics has been the focus of fundamental research for several decades and is now to the point of commercial application. Intense research and development continues in the area with the goal of realizing novel, next generation electronics for a multitude of applications that utilize the intrinsic tunability, low cost, and ease of processing that the materials have to offer.

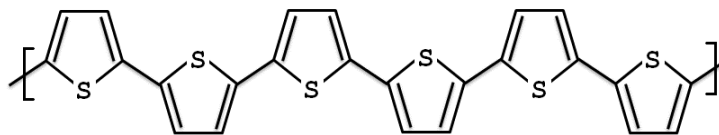
3.1.1 Background

Figure 9 displays diagrams of organic molecules illustrating how larger chains are built from smaller molecules. Figure 9(a) shows a

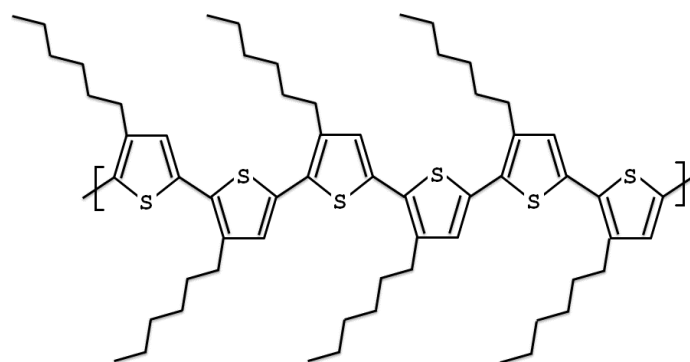
thiophene ring with a chemical formula of C_4H_4S , while Figure 9(b) displays polythiophene, with a chemical formula of $(C_4H_4S)_n$. Figure 9(c) shows poly(3-hexylthiophene) (P3HT), an organic semiconductor, built around the polythiophene chain, with C_6H_{13} side chains attached. The figure displays an example of the P3HT molecule with 100% regioregularity (RR), an alignment of the top and bottom side chains. A general characteristic of the molecules is the presence of double bonds alternating with single bonds along the polymer chain, which results in delocalization of π -conjugated electrons along the polymer backbone. Figure 9(d) shows an example of poly(3,3'''-dialkylquaterthiophene) (PQT-12), also an organic semiconductor built around the polythiophene chain, with $C_{12}H_{25}$ side chains attached, while Figure 9(e) demonstrates insulating poly(4-vinyl phenol) (PVP or P4VP).



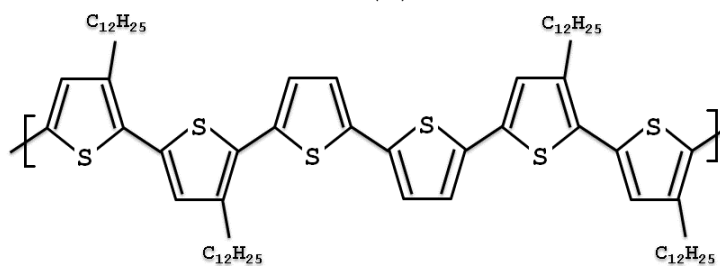
(a)



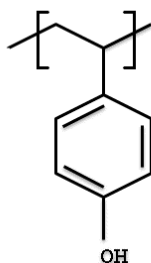
(b)



(c)



(d)

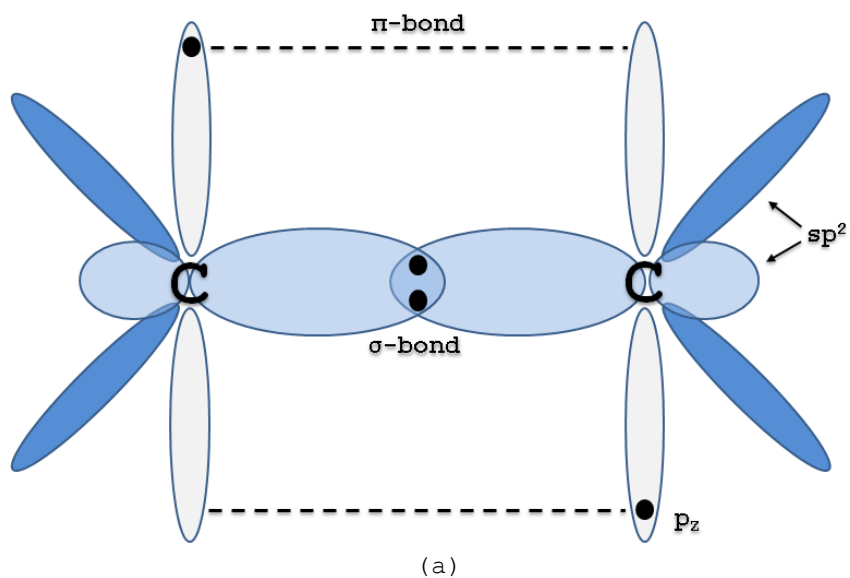


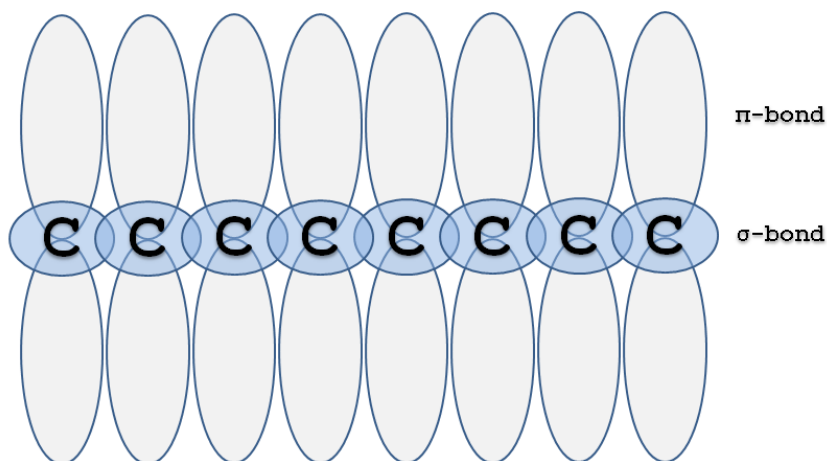
(e)

Figure 9. An example of a conjugated polymer chain built around an organic small molecule. (a) Thiophene ring (C_4H_4S), (b) polythiophene $(C_4H_4S)_n$ and (c) poly(3-hexylthiophene), a thiophene derivative (polymerized thiophene), with C_6H_{13} side chains being attached to one of the carbon atoms of an individual thiophene ring. The 100% regioregularity is achieved by having all of the top and bottom side chains aligned. (d) P-type semiconducting thiophene derivative poly(3,3''-dialkylquaterthiophene) (PQT-12) and (e) insulating poly(4-vinyl phenol) (PVP or P4VP).

The electron configuration of the six electrons in a carbon atom, in its ground state, is $1s^2 2s^2 2p^2$. The electrons in the core orbitals do not contribute to the chemical bonding. In a carbon atom, four valence

electrons, in the $2s^2 2p^2$, are used to form covalent bonds. The s and p orbitals combine to form hybrid orbitals, which give rise to single, double, or triple bonds. In conjugated polymers, one $2s$ orbital pairs with the two $2p$ orbitals to form 3 sp^2 hybrid orbitals, leaving one p orbital unhybridized. Two of the sp^2 orbitals on each carbon atom form covalent bonds with neighboring carbons, the third generally forms a covalent bond with a hydrogen or side group. This is called a σ -bond, which is any bond with cylindrical symmetry around the internuclear axis (Skotheim, Elsenbaumer, & Reynolds, 1998). The unhybridized p_z orbital overlaps with the unhybridized p_z orbital on the neighboring carbon. This is called a π -bond which arises from electrons approaching side by side, off the internuclear axis. Figure 10 illustrates the concept (Nardes, 2007; So, 2010).





(b)

Figure 10. Bonding in conducting conjugated polymers. (a) The sp^2 hybrid orbitals are shown in light and dark blue, and the unhybridized p_z orbitals shown in gray. Electrons are represented by the dots. The two sp^2 hybrid orbitals on the side extend in and out of the plane of the page. (b) An example of a backbone of conjugated polymers.

The electrons in the π -bonds are weakly bound, and are relatively easily delocalized. These delocalized π electrons are the conduction electrons in these organic materials. The sp^2 hybridization in conducting polymers is important because this leaves one p electron per atom to form its own bond. Under the assumption that the single and double bonds have the same length, Bloch theory (Kittel, 1996) states that solids formed from atoms or molecules with half-filled shells have partially filled bands with metallic transport properties. However, the length of the single and double bonds are not identical and the Peierls instability (the C-C bonds are longer than the C=C bonds) (Peierls, 1955) splits this simple band into 2 sub-bands, a completely filled valence band (highest occupied molecular orbital or HOMO level) and an empty conduction band (lowest unoccupied molecular orbital or LUMO level), separated by an energy gap, making the material a semiconductor.

Through the process of doping, the conductivity of original (undoped) π -conjugated polymers can be changed from insulating to conducting, with the conductivity increasing as the doping level increases (Skotheim, et al., 1998). Both *n*-type (electron donating) and *p*-type (electron accepting) dopants have been used to induce an insulator to semiconductor to conductor transition in electronic polymers. Similar to the inorganic semiconductors, these dopants remove or add charges to the polymers, but the details are very different. Unlike substitutional doping that occurs for inorganic semiconductors, the dopant atomic or molecular ions are positioned interstitially between chains in π -conjugated polymers, and donate charges to or accept charges from the polymer backbone. The counter ion is not covalently bound to the polymer, but only attracted to it by the Coulomb force. In some cases called self-doping, these dopants are covalently bound to the polymer backbone (Nalwa, 1997).

The physical flexibility of organic electronics devices is largely due to the fact that polymeric and other organic materials are held together by relatively weak intermolecular bonds (σ -bond), as opposed to crystalline structure in inorganic electronics, and bending does not critically affect their mechanical integrity or charge transport properties.

3.1.2 Organic Electronic Circuit Elements

Prior to 1970's, polymers were generally restricted to use as insulators. It was not until 1977 when scientists at the University of Pennsylvania demonstrated that treating polyacetylene with halogen compounds increased its electrical conductivity to values comparable to metals (Chiang et al., 1977), a work that has earned them the Nobel

Prize in 2000. Subsequently, work on polymeric conductors and semiconductors evolved over the next several decades. Today, most electronic circuit components commonly fabricated with inorganic elements, such as silicon or germanium, have already been demonstrated at some level in the polymer electronics field. All-polymer capacitors have been reported as early as the 1970's (Walles, 1972) and are currently available commercially. The first organic thin film transistor was reported in 1983 (Ebisawa, Kurokawa, & Nara, 1983), followed by the first all-polymer thin film transistor reported circa 1990 (Garnier, Horowitz, Peng, & Fichou, 1990).

Entire electric circuits made from all-polymer components have been demonstrated, including D flip-flops (Yoo et al., 2006), shift registers (McGimpsey, Samaniego, Chen, & Wang, 1998), and ring oscillators (Herlogsson, Coelle, Tierney, Crispin, & Berggren, 2010). A 128-bit organic RFID transponder chip with Ethernet-style encoding and wireless anti-collision protocol was demonstrated (Myny et al., 2009). Complete circuits that allow for hardware-based cryptography for the use with RFID tags were also shown (David, Ranasinghe, & Larsen, 2011). In early 2011, researchers at IMEC in Belgium have reported a 4000-organic-transistor, 8-bit logic, physically flexible processor fabricated on a 25 μm thin plastic foil. Capable of executing about six hard coded instructions per second, the processor was developed with the use in RFID tags in mind (Calamia, 2011).

Organic Light Emitting Diodes (OLEDs) were reported as early as 1990 (Burroughes et al., 1990) and became commercially available around 2004. Currently, stand-alone OLED indicators are commercially available, as are consumer electronic products that incorporate larger

format OLED technology such as smart phones, television sets, and portable games. Organic Photovoltaic devices (OPVs) offer the promise of low production cost in high volumes (Brabec, Scherf, & Dyakonov, 2008; Shaheen, Ginley, & Jabbour, 2005). Niche commercial products, such OPV-based solar computer cases and backpacks, are also currently available.

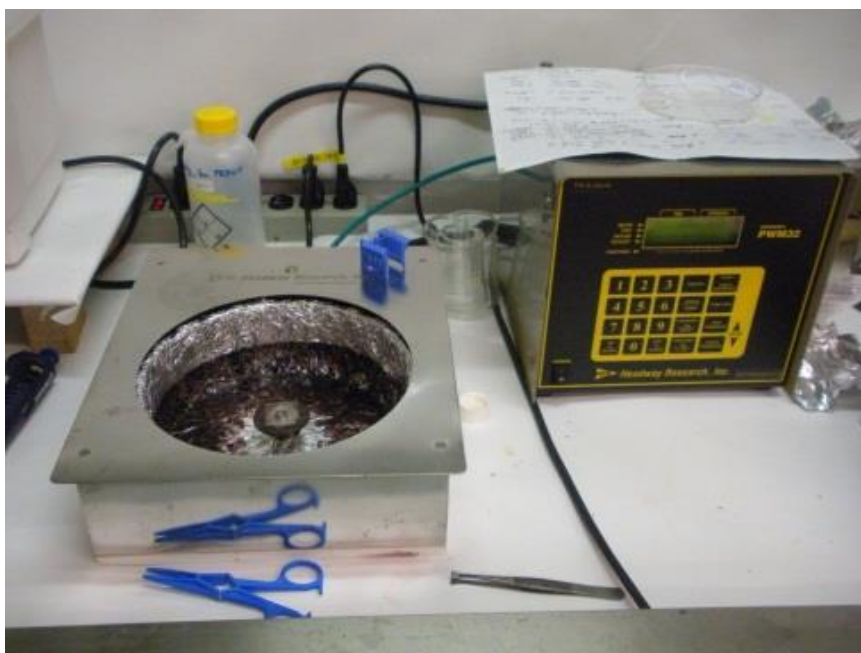
Organic Memristive Random Access Memory (in physics literature commonly referred to as Organic Bistable Devices, or OBDs) (Heremans et al., 2011) are not yet available commercially. Their most widely cited applications include their ability to function as a memory element and are intended as a replacement for either hard-drives or Random Access Memory (Kuang et al., 2010); logic operations, such as their ability to perform the implication logic often regarded as the foundation of the conventional approach to Artificial Intelligence (Lehtonen, Poikonen, & Laiho, 2010); and the use as artificial synapses in neuromorphic systems (R. Nawrocki, et al., 2012; Snider, 2007).

3.1.3 Advantages and Disadvantages

Manufacturing inorganic electronics requires high temperatures, typically 400 °C to 1400 °C, high-vacuum, and very clean environments. These can result in very high production costs. In the research and development phase, organic electronics are also typically fabricated in clean room facilities. However, organic electronics tend to be more tolerant to particulate contamination. It is therefore anticipated that the production stage will not require full clean room facilities, but rather that the local environment, in the vicinity of the substrate, be kept within acceptable particulate levels. This is expected to have a direct effect on lowering the cost. Additionally, the substrate

temperatures required for fabrication of organic devices are much lower and thus more compatible with manufacturing processes of plastic substrates. This should enable new, low cost integration of devices with plastics used in everyday consumer items. Finally, the organic nature of the materials used makes them intrinsically more biologically compatible allowing for future integration with biological organs or organisms (Owens & Malliaras, 2010).

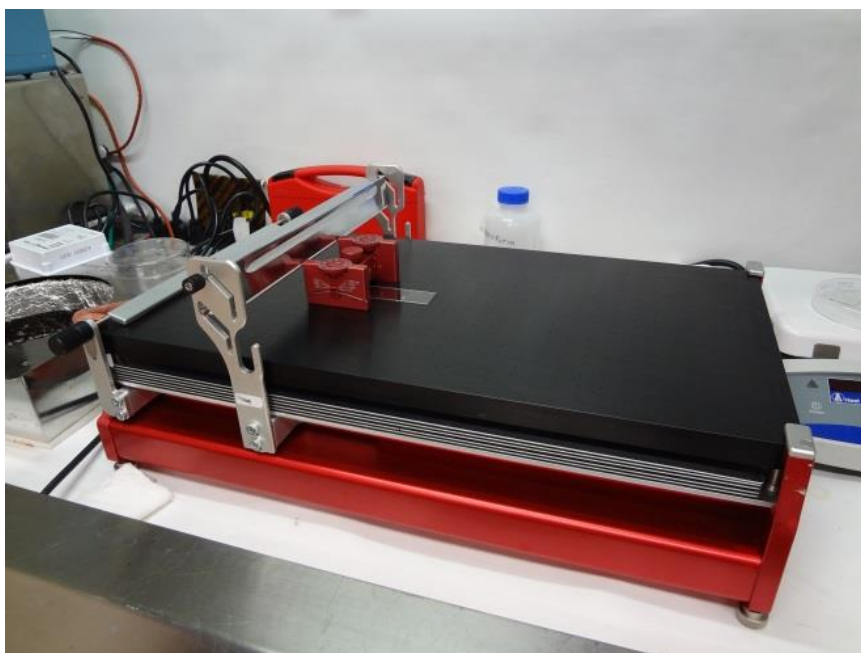
Solution processing of polymer electronics in particular is a key enabler of both low costs and rapid prototyping and fabrication. For laboratory research and development, spin coating (Figure 11(a)) is often the technique of choice due to its simplicity and the good uniformity of thin films that it can produce. For larger scale fabrication, direct write printing methods such as inkjet printing (Figure 11(b)), spray coating, slot die printing, or flexographic printing are possible (Krebs, Gevorgyan, & Alstrup, 2009). Printing has been used to produce electronic elements such as capacitors (Y. Liu, Cui, & Varahramyan, 2003), transistors (Sekitani, Noguchi, Zschieschang, Klauk, & Someya, 2008), OPVs (Green et al., 2008; Shaheen, Radspinner, Peyghambarian, & Jabbour, 2001), and OLEDs (Lopez, Sanchez, & Estrada, 2008). Other examples of solution processing include blade coating (Figure 11(c)) (F. Padinger, C.J. Brabec, T. Fromherz, J.C. Hummelen, & N.S. Sariciftci, 2000) and laminating (Figure 11(d)) (Bailey, Reese, Olson, Shaheen, & Kopidakis, 2011).



(a)



(b)



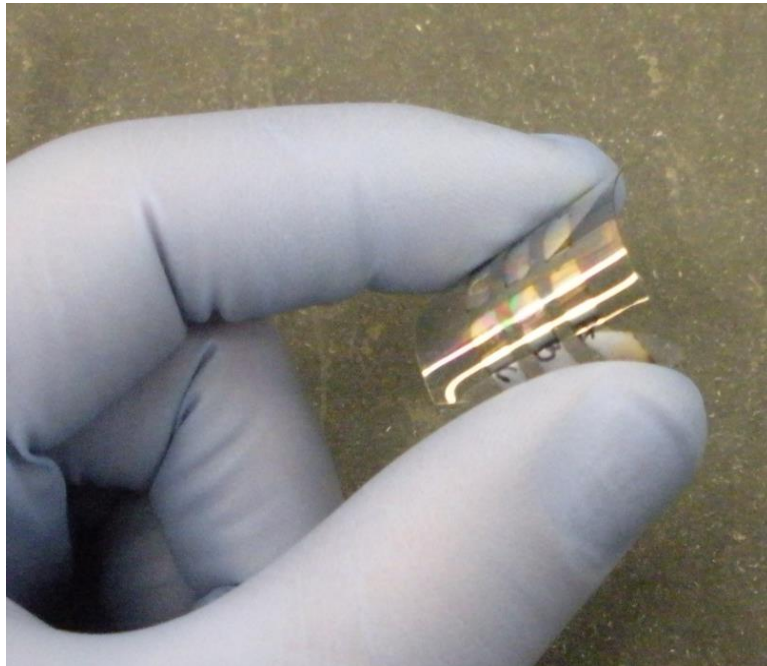
(c)



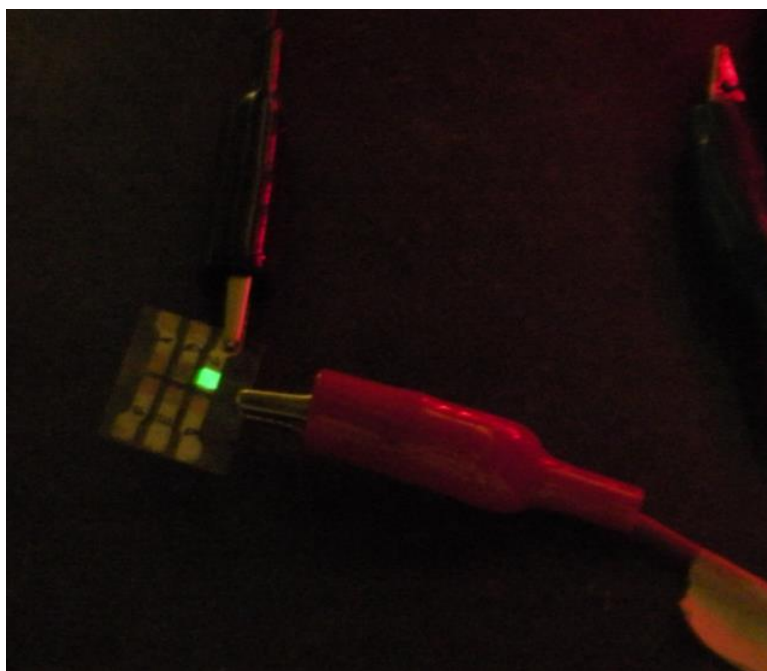
(d)

Figure 11. Example of manufacturing equipment used for deposition of organic electronics materials; (a) spin coater, (b) printing solution dispenser (courtesy of SonoPlot, Inc.), (c) blade coater, and (d) laminating press.

The use of flexible substrates for organic electronics is advantageous both for production and for application (Figure 12(a) and (b)). Transistors (J. Zhang et al., 2007), capacitors (B. C. Kim, Too, Kwon, Bo, & Wallace, 2011), OPVs (Kushto, Kim, & Kafafi, 2005), OLEDs (D. Zhang et al., 2006), and OM-RAMs (Son et al., 2010) have all been demonstrated on flexible substrates. Figure 13 shows an example of roll-to-roll (Sondergaard, Hosel, & Krebs, 2013) printing of organic transistor circuits on industrial scale.



(a)



(b)

Figure 12. Physically flexible organic light emitting diode (OLED) shown, (a) being flexed and, (b) lit-up.



Figure 13. Industrial scale roll-to-roll fabrication of physically flexible printed electronics (courtesy of PolyIC GmbH & Co.).

There are however several challenges and disadvantages that are characteristic of organic electronic materials and devices. With

regards to organic circuits, the price paid for ease of processing comes in the form of the operating bandwidth of the devices. Since carrier mobilities in organic semiconductors are typically orders of magnitude lower than in inorganic semiconductors, transistors and other devices are limited to much slower speeds. Also, solution processing of nanoscale devices with length scales approaching those of today's IC devices (10 - 20 nm regime) is challenging and will require advancements in techniques such as nanoimprint lithography (Ro et al., 2011).

3.2 Organic Memristive Device

3.2.1 General Operation

A bistable device is a device that can stably exist in one of two states. An example of such a device might be a strip of a magnetic tape that can be magnetized in one of two possible directions, for instance up or down, that represent the two states. One apparent application of such a device is a memory element. A number of different technologies that exhibit bistable behavior, based on both inorganic and organic elements, have emerged over the years. One example is an optically bistable device. Such a device relies on optical characteristics of materials with two resonant transmission states that result in two different power outputs for the same input power (Almeida & Lipson, 2004). Another example is a phase-change memory (Salinga & Wuttig, 2011), in which the material can be in two possible morphological states: a crystalline phase with low resistance and an amorphous phase with high resistance.

An Organic Memristive Random Access Memory (OM-RAM) is an electrically bistable, non-volatile, two-terminal device that relies on organic or organic-inorganic hybrid materials in its active layer. OM-RAM's are referred to by several different monikers in the literature, including Organic Bistable Memory Device, Bistable Organic Memory, or Organic Non-Volatile Memory. For the purposes of this dissertation, the term Organic Memristive Random Access Memory, or OM-RAM, will be used.

The earliest publications of electrical switching behavior in thin-film devices were reported over three decades ago (Potember, Poehler, & Cowan, 1979). An OM-RAM was first reported in 2002 (L. P. Ma, Liu, & Yang, 2002), when a thin metal layer was embedded within an organic active medium to induce the two-state behavior.

The memristor is another example of a two-terminal device that undergoes a change of state. Since the first publication in 2008 claiming demonstration of a fully functioning memristor, based on TiO_2 film undergoing resistive change due to the shift of oxygen atoms upon the application of voltage bias (Strukov, et al., 2008), a number of groups have claimed to have demonstrated fabricating of memristors using both inorganic (Gergel-Hackett et al., 2009) and organic compounds (Islam et al., 2010).

As already mentioned, currently there is a lack of agreement in the scientific community on the definition of a memristor (Marks, 2012; Meuffels & Schroeder, 2011; Meuffels & Soni, 2012). As defined by Chua (Chua, 1971), memristor is a device that relates flux to charge. However, overwhelming majority of the fabricated devices, including the devices that I have fabricated, do not undergo such a change. Instead, they experience morphological changes, or other types of physical or

electrical changes (discussed in further details in section 3.2.4 *Switching Mechanisms*) that result in change of resistivity. Therefore, I will refer to such devices as memristive devices.

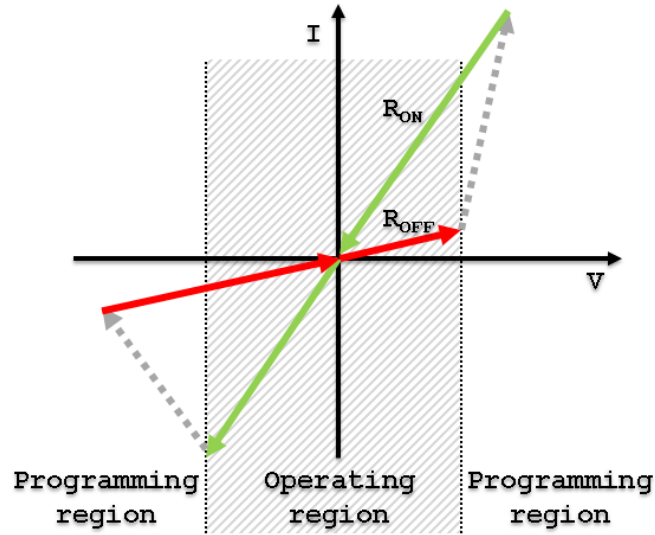
The memristive devices can be roughly grouped into two categories: analog memristive devices with their continuously varying resistances (Wang, Sun, Gao, & Greenham, 2010) and digital memristive devices that demonstrate two distinctive resistive states (Erokhin et al., 2010). Because of the ubiquity of the digital memristive devices compared to the relative scarcity of analog memristive devices, as well as the bistable nature of memristive devices utilized in my neuromorphic circuit, this section is dedicated to the digital organic memristive devices.

3.2.2 Switching Behavior

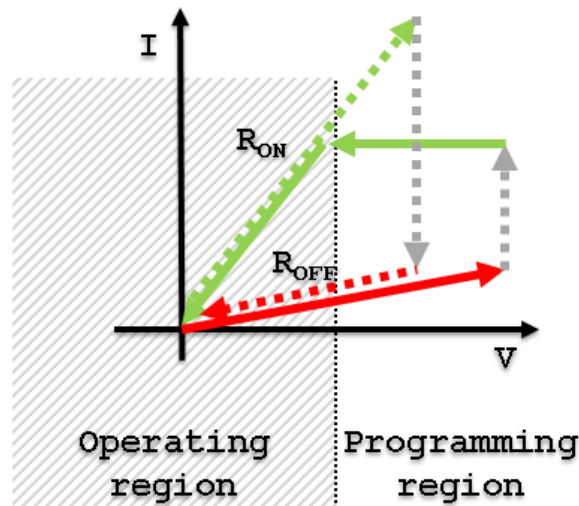
There are two types of switching behaviors observed in OM-RAMs, bipolar and unipolar, as depicted in Figure 14(a) and Figure 14(b) respectively (Heremans, et al., 2011). With the vast majority of the fabricating devices exhibiting bipolar switching, their operation can be summarized as follows. The device is in the OFF state (high resistance) until the input voltage is increased past a positive threshold voltage, for instance +1 V. It remains in the ON state (low resistance) until the voltage is reduced below a negative threshold voltage, for instance -1 V. The positive and negative threshold voltages do not have to be of the same magnitude.

The polar switching OM-RAM, depicted in Figure 14(b), operates in a very similar manner to the bipolar switching device. Here, both the ON and OFF transitions occur for the same polarity of the input voltage. The magnitude of the OFF threshold can be higher or lower than

the ON threshold. The polar switching can occur for either the positive or the negative voltage.



(a)



(b)

Figure 14. Operational I - V characteristics of the two general types of OM-RAM devices, bipolar and polar. (a) For a bipolar OM-RAM, the device is either in the OFF state (R_{OFF} - high resistance, red or dark in gray scale) or ON state (R_{ON} - low resistance, green or light in grayscale) depending on past voltage. Gray, dashed arrows represent switching either to the ON or OFF state. The element can be turned ON by increasing the input voltage above the positive threshold value. Analogously, it can be turned OFF by decreasing the input voltage below the negative threshold value. (b) In a polar OM-RAM, both of the ON and OFF transitions

occur for the same input voltage polarity, either positive or negative.

For both the polar and bipolar switching OM-RAMs, when the input voltage is kept in the operating region ($V_{OFF} < V_{IN} < V_{ON}$), the device will stay in its current state (either ON or OFF). Setting the input voltage past a threshold value, the device enters into the programming region, ($V_{IN} > |V_{ON}| \text{ \& \; } |V_{OFF}|$), with a subsequent change of its state (ON to OFF, or OFF to ON).

One of the main characteristic of an OM-RAM is the ON/OFF ratio, which is the difference between the ON and OFF currents, typically illustrated in log-linear plot to magnify the difference between the ON and OFF currents. Values as high as seven orders of magnitude have been reported. The retention time of OM-RAMs has been reported as high as 10^5 seconds with 10^5 read/write cycles (Son et al., 2011).

An Organic Memristive Programmable Read Only Memory (OM-PROM) is a device that can be considered as a sub-class of OM-RAMs. Such a device is sometimes referred to in the literature as Write-Once-Read-Many, or WORM. The difference between an OM-PROM and an OM-RAM is that in an OM-PROM the change of state, to either ON or OFF, is permanent; no amount of forward or reverse voltage will result in the device switching back to its original state. This point is illustrated in Figure 15, in which two types of OM-PROM devices can be distinguished. In the first type, shown in Figure 15(a), when the device is first created, it is in the OFF state. It can then be permanently set to an ON state (Mamo, Machado, van Otterlo, Coville, & Huemmelgen, 2010). In the second type, Figure 15(b), the device is first in an ON state, but can then be permanently switched OFF (Wang et al., 2011). For many

applications, the permanent nature of OM-PROM is a limitation. However, there are certain applications, such as RFID tags, where it is desirable to have a permanent, non-erasable type of memory.

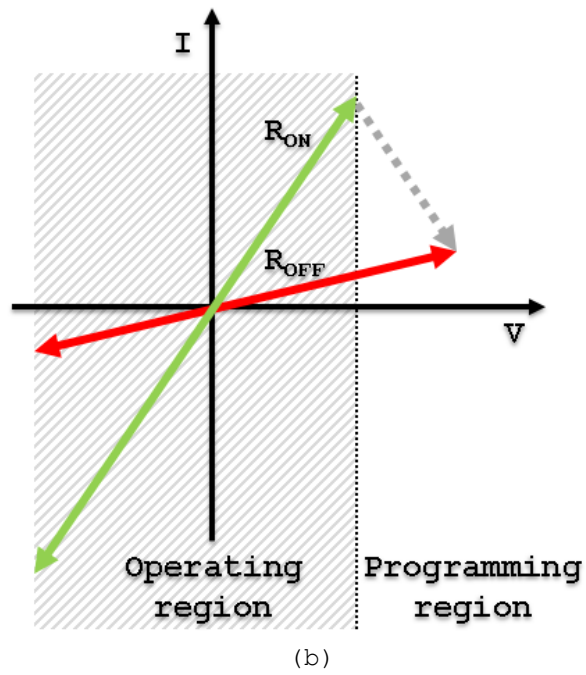
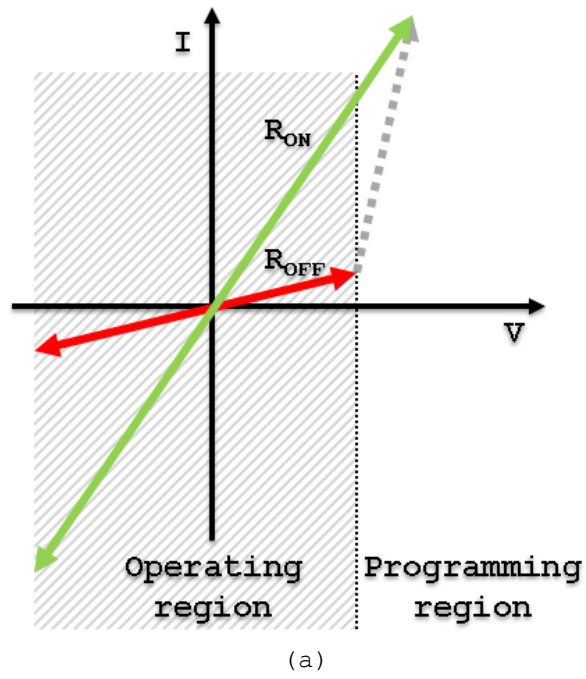


Figure 15. Operational I - V characteristics of two types of OM-PROM devices: (a) device originally in OFF state (R_{OFF} - high resistance, red or dark in gray scale) permanently changes state to ON state (R_{ON} - low resistance, green or light in gray scale), and (b) device originally in ON state irreversibly changes to OFF state. Gray, dashed arrows represent switching either to the ON or OFF state.

There also exists a class of three-terminal, organic electrical devices that exhibit hysteretic behavior; a memory transistor. In memory OFETs, reported as early as 2001 (Velu et al., 2001), for a single gate-source voltage (V_{GS}) two different drain-source current (I_{DS}) values can be measured depending on the sweeping direction. Their I - V characteristic curve is similar to that of a Schmitt trigger, albeit the current is always positive. The operation of an ideal memory transistor is illustrated in Figure 16. OFETs rely on the semiconducting properties of polymer thin films. In a memory OFET, the polymer semiconductor changes state depending on the direction of the voltage sweep. The physics of this resistive change is similar to that observed in two-terminal OM-RAMs, which are described in more details in the following section. Devices in which the memory effect is photoinduced have also been reported (C.-J. Kim et al., 2011). The difference in I_{DS} between the ON and OFF states has been reported as high as almost four orders of magnitude (Das & Appenzeller, 2011).

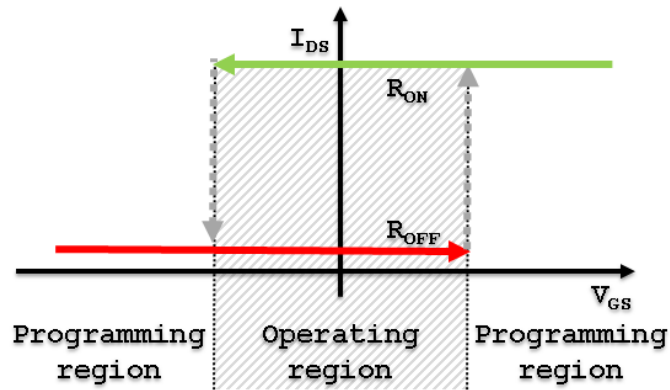


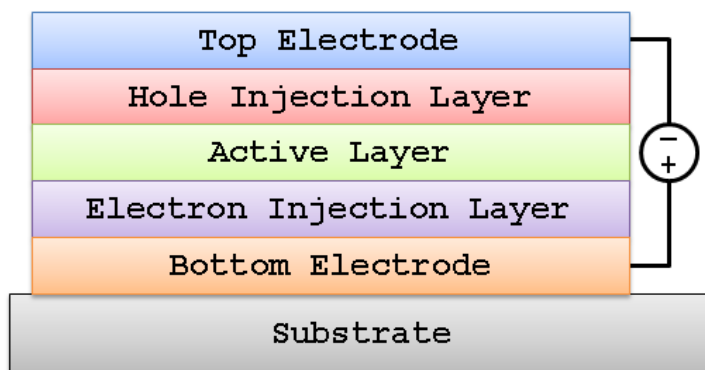
Figure 16. I - V relationship of a memory transistor. Two different drain-source currents (I_{DS}) can be measured depending on the sweeping direction of the gate-source voltage (V_{GS}).

3.2.3 Device Configurations

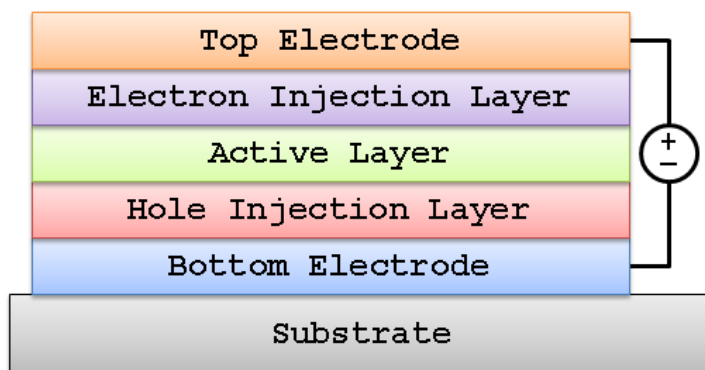
In an OM-RAM devices the electrical bistability is enacted by a physical or chemical change to the device. This change depends on the types of materials used. Two general configurations for an OM-RAM device are demonstrated in Figure 17. In a traditional configuration, Figure 17(a), the current flows from the bottom to the top of the device. In organic electronics this configuration typically results in devices with better performance (higher current). However, these devices suffer from lesser air stability. In an inverted configuration, Figure 17(b), the current flows from the top to the bottom of the device. This configuration benefits from better air stability though it typically suffers from worse performance compared to devices constructed with a traditional configuration.

Any OM-RAM device has a minimum of three layers: top electrode (TE), bottom electrode (BE), and active layer (AL). The TE and BE are primarily used as device contacts, although in some cases they can also play a role in the switching mechanism. However, the AL is the layer that is usually where the physical or chemical changes occur and therefore responsible for the electrical bistability. It can be either a single material layer, a single material layer doped with other materials, such as nanoparticles (NPs), or it can be comprised of several layers or materials. In any type of polymer or organic electronics devices, a crucial factor is the interface between organic (i.e., polymer) and inorganic (e.g., metal) materials. Interface engineering is of great importance as it affects the functionality, effectiveness and stability of organic electronics devices (H. Ma, Yip, Huang, & Jen, 2010). It involves alignment of surface energy and work

functions that play a significant role in the molecular morphology and energetics that dictate the rates of charge injection (J. Lee, Hong, & Lee, 2011; C. W. Lin et al., 2011). As a result some devices incorporate additional layers, such as an electron injection layer (EIL) or a hole injection layer (HIL) to optimize the injection characteristics. Electronically, these layers can also act to block the opposite type of charge carrier from being transported through the device. Mechanically, these layers can also act to increase wettability or adhesion between the AL and the electrodes.



(a)



(b)

Figure 17. Two general device configurations are common to most of organic devices. (a) Traditional configuration; the current flows from the bottom to the top of the device. b) Inverted configuration, the current flows from the top to the bottom of the device. The top and bottom electrodes (TE, BE) are typically made from a thin layer of metal. The active layer (AL), which may

itself consist of multiple layers or materials, is responsible for the electrical switching of the device. The hole or electron injection layers are often included to overcome energetic barriers at the interfaces or to increase the adhesion. Typically the TE serves as the cathode, and electrons flow from the TE to the BE.

3.2.4 Switching Mechanisms

When the input voltage of an OM-RAM is kept below the threshold voltage, the device can often be approximated as operating as a linear resistor. Therefore, to simplify the analysis and reduce its computational complexity in a circuit design, the device can be replaced by two resistors and a switch, as illustrated in Figure 2(b) and Figure 3. The switch determines whether high or low resistance, corresponding to either the OFF and the ON state, should be used in the analysis.

When the input voltage exceeds the threshold value, however, the device momentarily exhibits a highly non-linear behavior and switches between states. There are multiple physical mechanisms by which the switching process can occur and the state is stored in the OM-RAM. These rely on processes such as charge trapping in the organic layer, field dependent charge carrier mobility, and charge injection from the electrodes (Houili, Tutis, & Izquierdo, 2010). A given device may rely on one or more such mechanisms, and it can occur that in the literature a device is reported without full understanding of which mechanism(s) are responsible. Four of the most common mechanisms are discussed next.

3.2.4.1 Electromigration of Metal Into the Active Layer

The first such mechanism is electromigration of metal ions into organic active layer (L. P. Ma, Xu, & Yang, 2004). In a metal-

insulator-metal (MIM) sandwich, the device is initially in the OFF state (high resistance). However, when the potential exceeds threshold, small amounts of metal ions are injected from the anode into the polymer insulator sandwiched between two metal electrodes. This ionic migration, due to the high electric stress at the tip of a fine conducting filament, acts to decrease the physical separation of the two electrodes. This reduces the total resistance and changes the state from OFF to ON (Dearnaley, Morgan, & Stoneham, 1970). When a reverse potential is applied the impurities are extracted from the insulator back to the metal contact thereby increasing the total resistance across the polymer, switching from ON to OFF.

3.2.4.2 Formation of Conductive Filaments through

Redox Behavior

Another mechanism that is invoked is based on oxidation-reduction behavior (Heonjun & Ohyun, 2010) of a conducting polymer such as PEDOT:PSS. When a voltage is applied to the electrode, the polymer chains are oxidized to PEDOT^+ by the injected carriers. Facile pathways for current flow form along the PEDOT^+ chains, and the device switches from the OFF to the ON state (high resistance to low resistance). The PEDOT^+ chains are reduced to neutral PEDOT^0 chains by injection of carriers when a voltage is applied in the opposite direction. The current paths are then destroyed, and the device switches from the ON to the OFF state.

3.2.4.3 Charge Trapping

Another mechanism employed to explain the electrical bistability is based on charge trapping in a semiconducting polymer whose carrier

mobility is dependent upon the charge carrier concentration (Son, You, Kim, Jung, & Kim, 2009). In this scenario, the polymer is embedded with conductive nanoparticles (NPs). At first, when the device is created and tested, the resistance is high. However, when the voltage potential exceeds a critical limit, electrons become trapped in the NPs. Subsequently the embedded electrons form a conductive path and allow the current to flow more freely (ON state). This results from the carrier concentration dependence of the mobility in organic semiconductors, which is well established (Blom, Smit, Haverkort, & Wolter, 1993; Coehoorn, Pasveer, Bobbert, & Michels, 2005). A higher concentration of carriers increases the carrier mobility, and hence the conductivity, by filling trap states that would otherwise impede carrier transport. The excess carriers also increase the dielectric constant that changes the activation energy for carrier transport (Gregg, Chen, & Branz, 2004). Reversing the voltage polarity has the effect of pulling the electrons out of the NPs and switches the device back to the OFF state. The polarity of the device is determined by an asymmetry in the work functions of the electrodes. Such a trap filling mechanism has been analyzed with a Space Charge Limited Current (SCLS) model (Lampert & Mark, 1970), where it was found that the ON/OFF ratio of the device increased with increasing trap depth and resulting density of trapped electrons (Jung & Kim, 2011; H.-T. Lin, Pei, & Chan, 2007).

3.2.4.4 The Ferroelectric Effect

Ferroelectric polymers, whose electric dipole can be modified by the application of external electric field, have also been successfully utilized for the switching mechanism in OM-RAM devices. These polymers,

which are typically insulating, can be blended with semiconducting polymers to enable the working OM-RAM device. The switching mechanism in this case is due to changes at one of the electrode/semiconductor interfaces. Initially, an energetic barrier at the interface results in injection limited current in the device. Then, as the device is biased, polarization charges generated in the ferroelectric polymer are compensated by charges from the metal electrode. A portion of the compensated charges also occupies the semiconducting polymer, leading to band bending that reduces the energetic barrier at the interface. As a result, the current in the device increases to form the ON state and becomes space charge limited as opposed to injection limited in its functional form. The other electrode interface is typically engineered to avoid this effect. What results overall is a rectifying behavior in the device with the current modified by the ferroelectric polarization (Naber, Asadi, Blom, de Leeuw, & de Boer, 2010).

3.2.5 OM-PROM For Synthetic Synapse

This section outlines the details of the fabrication processes used in creating the organic memristive device employed to perform the functionalities of a synthetic synapse in Polymer Neuromorphic Circuitry presented here.

A number of device configurations were investigated. The first such device was inspired by Son *et al.* (Son, et al., 2009). In these devices, created according to traditional configuration (Figure 17(a)), conductive zinc oxide nanoparticles (ZnO NPs) were embedded inside an otherwise insulating layer of poly(methyl methacrylate) (PMMA), sandwiched between two electrodes made from indium tin oxide (ITO) and aluminum (Al), or glass/ITO/PMMA+ZnO NPs/Al. The bistable operation of

these devices was attributed to charges being trapped by the conductive ZnO NPs upon application of a voltage bias (see 3.2.4.3 *Charge Trapping* section for explanation of the mechanism). A reversal of the voltage bias would subsequent remove the charges with a consequent reduction of the conductivity. The benefit of this configuration was its simplicity, although the ZnO NPs had to be synthesized. However, even though some success was achieved with these devices, they largely failed in their reproducibility as well as long-term stability. Figure 18 illustrates an *I-V* characteristic scan of one of such devices.

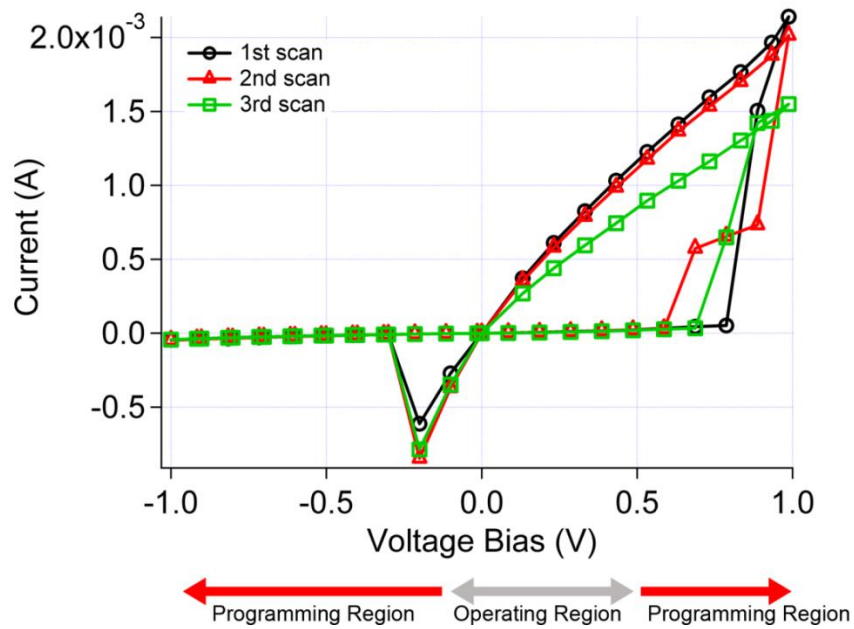


Figure 18. *I-V* characteristics curve demonstrating the operation of an OM-RAM device with glass/ITO/PMMA+ZnO NPs/Al configuration.

The lack of stability of the ZnO NP-based device prompted a modification of its configuration. Two additional layers were inserted along with a subsequent modification of the top and bottom electrodes. The ITO was initially retained as the choice for the bottom electrode; however, the top electrode was obtained from silver. This change had a

number of benefits. First, silver is much more air stable, which should result in devices with much better air stability (discussed later). Next, silver has a higher work function compared to aluminum (5.1 eV compared to 4.3 eV) which resulted in a device with an inverted configuration, or TE being a positive electrode and BE being a negative electrode (Figure 17(a)). Finally, from the manufacturing perspective, because at present the metal electrode is still obtained through thermal evaporation of a metal, silver is much easier to deposit compared to aluminum.

A layer of thin film of zinc oxide (ZnO) was introduced between the insulating PMMA (without ZnO nanoparticles) and conducting ITO. ZnO is a hole-blocking layer that is typically used in organic photovoltaics (OPVs) with the intent to allow the generated electrons to be collected at only one electrode (Bailey, et al., 2011). In a memristive device, it provides for a rectifying behavior.

A thin layer of PEDOT:PSS was inserted between the PMMA layer and the silver TE. Because of its high conductivity, PEDOT:PSS is often used as an electrode (Crispin et al., 2006; Lim et al., 2006; Mu, Li, Jones, Steckl, & Klotzkin, 2007). However, as already outlined in section 3.2.4.2 *Formation of Conductive Filaments through Redox Behavior*, oxidation of PEDOT:PSS can lead to chemical changes and a subsequent modification of its conductance (Heonjun & Ohyun, 2010). Therefore, with the following configuration, glass/ITO/ZnO/PMMA/PEDOT:PSS/Ag, PEDOT:PSS was used as the active layer, meaning the layer responsible for resistive switching of the device. Figure 19 graphically depicts the configuration of the

PEDOT:PSS-based device investigated for the purposes of functioning as a synthetic synapse.

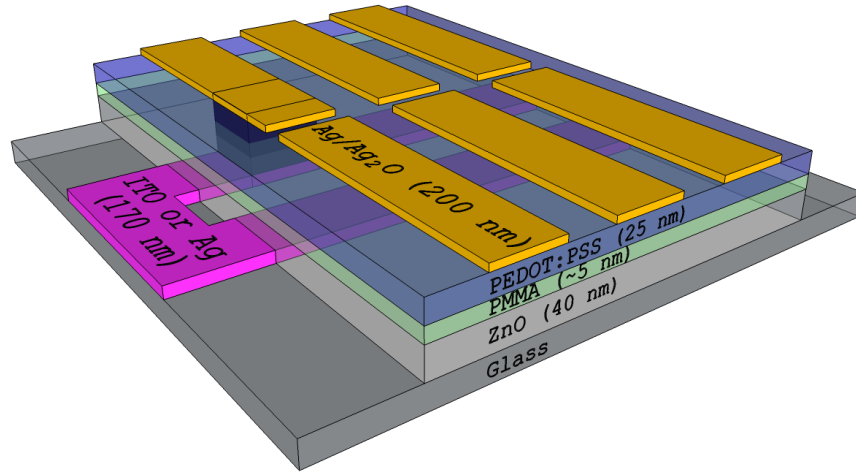


Figure 19. Device configuration of PEDOT:PSS-based memristive device utilized for the multiplicative functionality of a synapse. An array of six memristive devices (3 x 2) can be seen with an individual device, formed at an intersection of BE (ITO) and TE (Ag/Ag₂O), clearly marked.

3.2.5.1 Device Operation

The fundamental switching behavior of this OM-PROM device is attributed to changes of the doping level of the PEDOT:PSS layer, as described as the underlying mechanism for electrical switching in earlier work (Moller, Perlov, Jackson, Taussig, & Forrest, 2003; Wang, et al., 2011). However, importantly, these devices undergo a transition from the OFF (low current) to the ON (high current) states, once the turn ON voltage has been exceeded. This is in contrast to the previously published work that demonstrated transitions from ON to OFF due to reversible reduction of $\text{PEDOT}^+ \rightarrow \text{PEDOT}^0$. This *de-doping* occurred upon injection of electrons from the aluminum contact, which functioned as a negative electrode. The devices presented here have several distinctions that result in the opposite behavior. First, a low-

conductivity formulation of PEDOT:PSS (Clevios P VP AI 4083) was used, such that the intrinsic doping level is low, and the de-doping pathway is largely inhibited. Second, use of the Ag/Ag₂O top contact as a positive electrode results in efficient hole injection into the PEDOT:PSS and subsequent oxidative *doping* of PEDOT⁺ → PEDOT⁺. This pathway was ascribed previously as the turn ON mechanism for a reversible switch in which ITO was used as the positive electrode (Ha & Kim, 2008). An additional piece of information corroborating the doping mechanism of PEDOT is that annealing of the PEDOT:PSS films in dry nitrogen just prior to vacuum deposition of the top electrode was necessary in order for the devices to function. Otherwise, exposure to ambient conditions prior to metal deposition typically resulted in the devices already being in the ON state upon initial *I*-*V* scans. This is attributed to uptake of water, which has been found to result in ionic conduction and subsequent increase of conductivity in PEDOT:PSS of approximately one order-of-magnitude (Nardes et al., 2008). Furthermore, devices fabricated with PEDOT:PSS treated with ethylene glycol have also resulted in devices bypassing the OFF state which is attributed to PEDOT being doped by ethylene glycol (Jianyong Ouyang et al., 2004).

To further verify the switching mechanism, conductive Atomic Force Microscopy (c-AFM) study was conducted, where the conductive tip was used as the top electrode in the glass/ITO/ZnO/PEDOT:PSS device. A number of consecutive scans revealed that the device experienced a localized resistive change indicating that the effect is definitely not due to metallic filament formation due to electromigration of metal atoms from the electrode, but rather due to PEDOT doping via

electrically injected charges that form filamentary pathways, as indicated in the Figure 20.

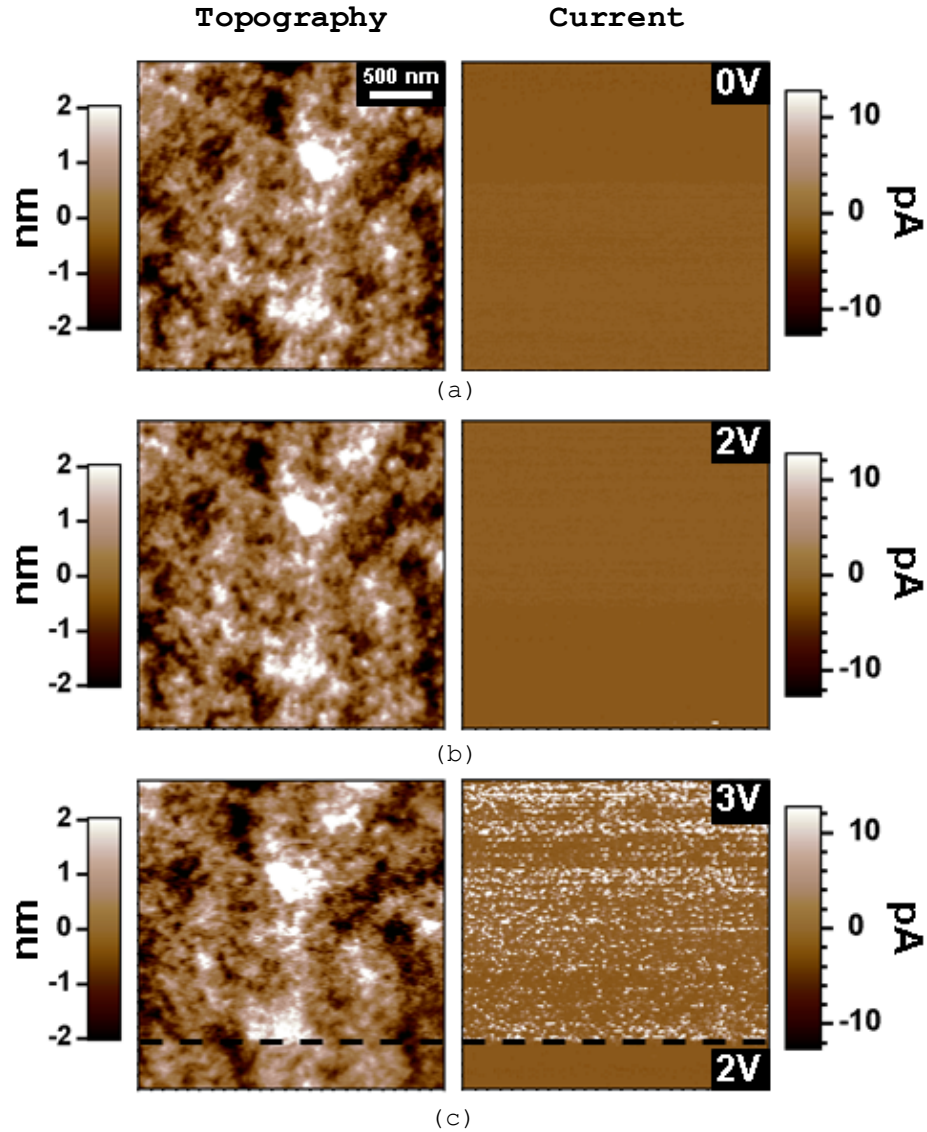
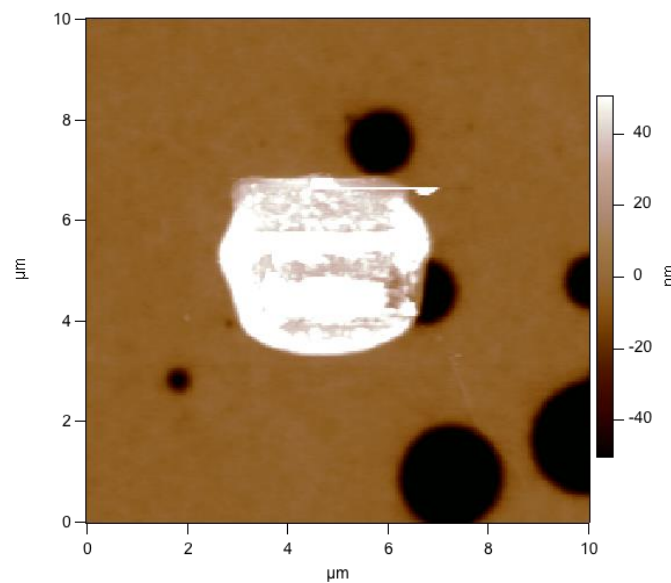


Figure 20. The c-AFM images, topography (left) and current (right), of PEDOT:PSS film indicating filamentary peaks being formed due to voltage application. (a) Initial 0-volt scan indicating OFF state with no current. (b) 2-volt scan indicating OFF state with no current. (c) Final 3-volt scan showing resistive change to ON state facilitated by a dramatic increase of recorded current. (Images by David Ostrowski).

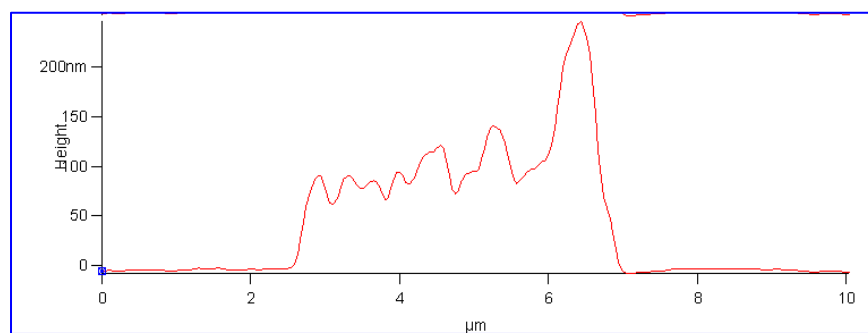
It was also observed that the area with applied voltage has experienced a noticeable swelling, shown in Figure 21(a) and Figure

21(b). The swelling is most likely due to uptake of water vapor and removal of ions with a subsequent repulsion of molecules due to their Coulombic interaction, as reported in (Charrier, Janssen, & Kemerink, 2010).

It has been shown that oxidized PEDOT undergoes a change of light absorbance (Coskun, Cirpan, & Toppare, 2007). A number of measurements were conducted, including UV-VIS and Raman spectroscopy, with the hope of showing such a change. However, none of the attempts proved successful, likely due to the extremely localized nature of the filamentary pathways.



(a)



(b)

Figure 21. (a) The c-AFM of PEDOT:PSS film indicating filamentary peaks being formed due to voltage application. (b) Topography line trace. (Images by David Ostrowski).

The application of pulse signals of various voltage magnitudes and fixed duration indicated that devices would switch states within 5 ms. Also a simple estimate revealed that switching requires roughly equal number of electrons injected indicating that the switching mechanism is charge driven. Figure 22 shows an example of 5-volt signal applied for duration of 10 ms and 10-volt signal applied for duration of 5 ms. It can be seen that the total number of charges, crudely equal to 2×10^{20} , (area under the curve) is roughly equal in both of the cases.

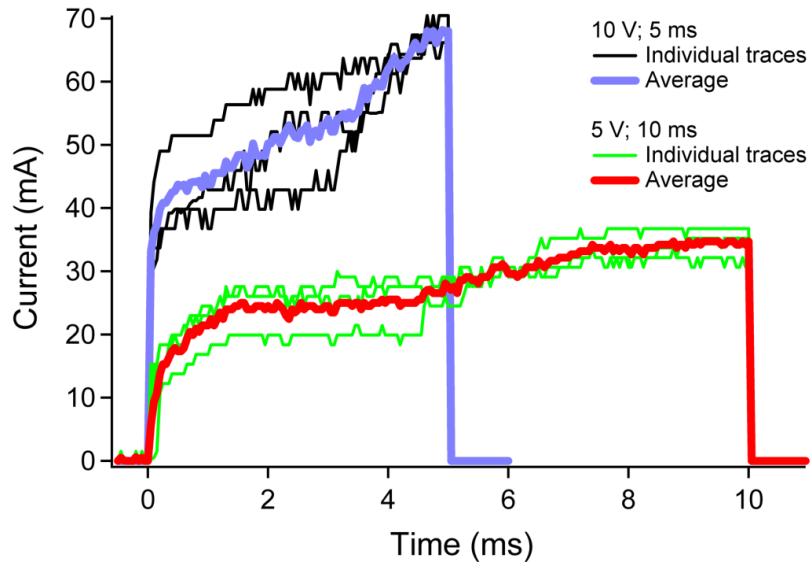
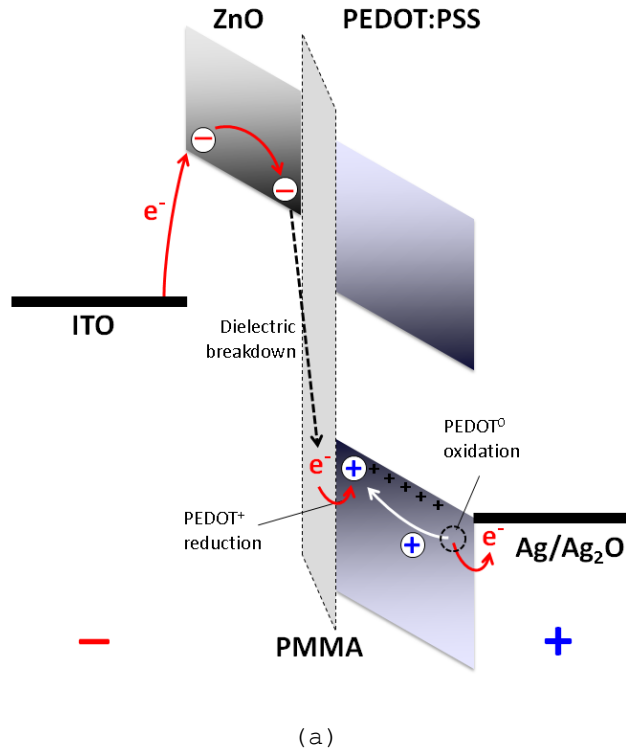


Figure 22. Two sets of memristive devices (with device configuration being shown in Figure 19) with two types of pulses applied; 5-ms pulse with 10-volt amplitude (black and light blue lines) and 10-ms pulse with 5-volt amplitude (light green and dark red lines). The total number of electrons transferred is roughly equal for both types of pulses, with 1.82×10^{20} electrons for 5-ms pulse and 1.92×10^{20} for 10-ms pulse, indicating that the switching is charge driven.

In a forward biased device, as illustrated in Figure 23(a), electrons are injected from BE into the hole-blocking ZnO layer and then across the insulating PMMA layer. At the interface between electron-blocking PEDOT:PSS and TE, neutral PEDOT⁰, through a process of oxidation, splits into an electron that will be extracted at the TE and PEDOT⁺ that will travel towards the PMMA/PEDOT:PSS to recombine with electron from the BE in a process of PEDOT reduction. In a reverse biased device, shown in Figure 23(b), at the PMMA/PEDOT:PSS interface, a neutral PEDOT⁰, will split into an electron and a conductive PEDOT⁺. That electron will jump across an insulating layer of PMMA and a hole-blocking ZnO layer to be extracted at the BE. The conductive PEDOT⁺ will recombine with an electron at the PEDOT:PSS/TE interface.



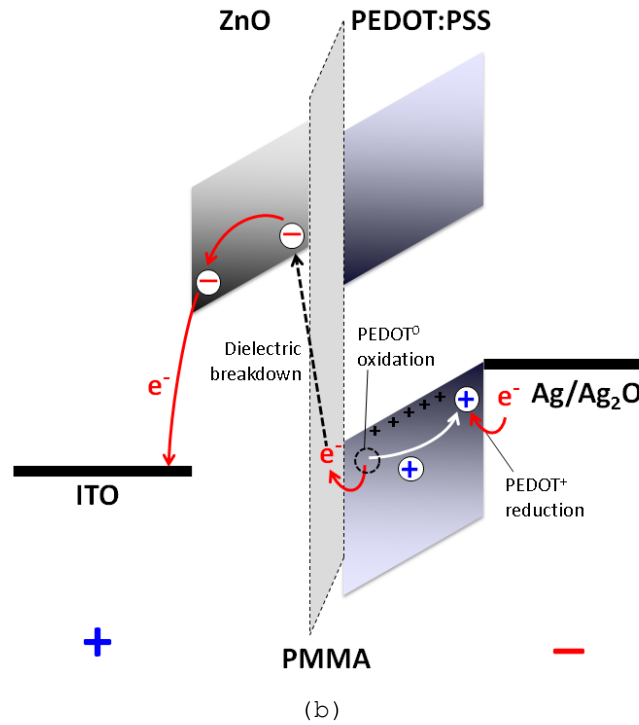


Figure 23. Band diagrams of forward (a) and reverse (b) biased PEDOT:PSS-based OM-PROM devices.

Introduction of PEDOT:PSS layer proved to be instrumental in obtaining a fully functioning memristive device (R. A. Nawrocki et al., 2013). Figure 24 illustrates I - V relationship of PEDOT:PSS based device with resistive change at ~ 1 V clearly visible. However, even though some of previously published work on PEDOT:PSS-based memristive devices clearly show the possibility of state reversibility (Jeong, Kim, Yoon, & Choi, 2010; M. Kim, Park, & Kim, 2009), the OFF to ON state change in this device configuration is permanent.

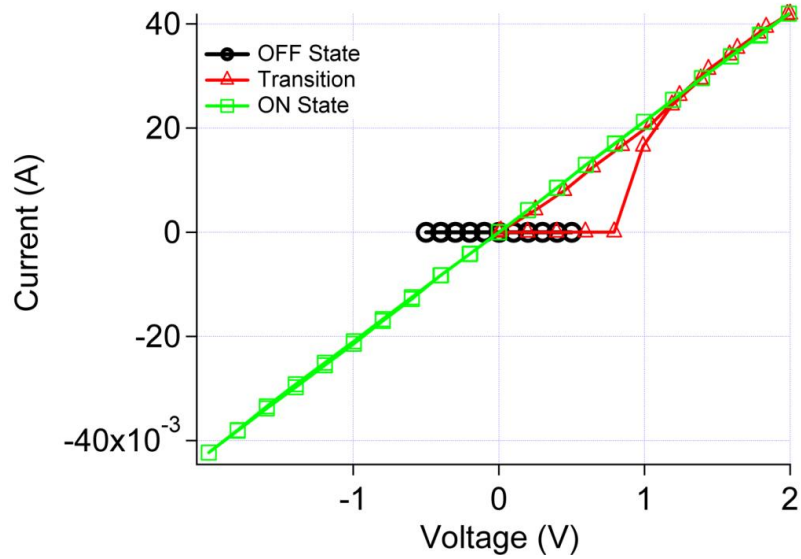


Figure 24. I - V relationship of a PEDOT:PSS-based memristive device, with configuration shown in Figure 19. A resistive change of less than 1 volt can be clearly seen. However, the change is permanent resulting in OM-PROM classification of the device.

Initial successes of this configuration have prompted further investigation of individual layers as well as device alternatives. Because of the eventual need to fabricate an entire neuron on a single substrate, a metal alternative to ITO electrode was investigated. Various metals were considered, including aluminum, copper, silver, and gold with aluminum and gold being clearly the most favorable (see section on 4.2 *Common Substrate Neuron* for further explanation).

Investigation of the effects of PMMA layer was also carried out. A removal of this insulating layer resulted in a device with a clearly non-Ohmic characteristic attributed to a partial removal of ZnO layer by the acidic PEDOT:PSS, as seen in Figure 25. More importantly, it was also revealed that changing the thickness of the PMMA layer had an effect on the boundary between the operating region and programming region (change of the threshold voltage) as well as the ON/OFF ratio.

As illustrated in Figure 26, devices with PMMA of 5, 10, 15, and 25 nm resulted in devices with turn ON voltage of approximately 0.5, 0.8, 1.1, and 1.4 V respectively. Also, the difference between the ON and OFF currents can be seen as approximately 10^3 , 5×10^3 , 10^5 , and 10^8 respectively.

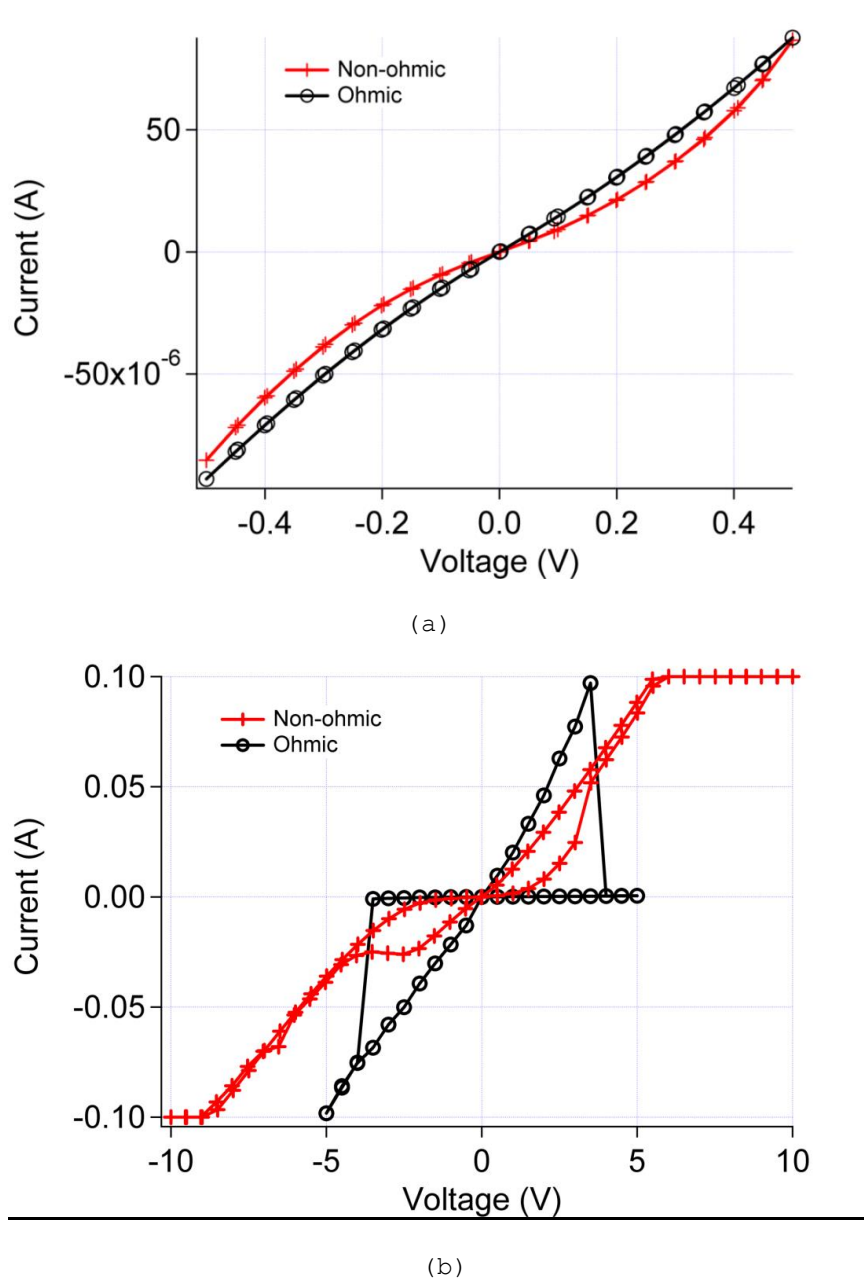


Figure 25. I - V relationship of a PEDOT:PSS-based memristive device with (black circles) without (red crosses) PMMA layer resulting in device indicating Ohmic (with PMMA layer) and non-Ohmic (without PMMA layer) relationship.

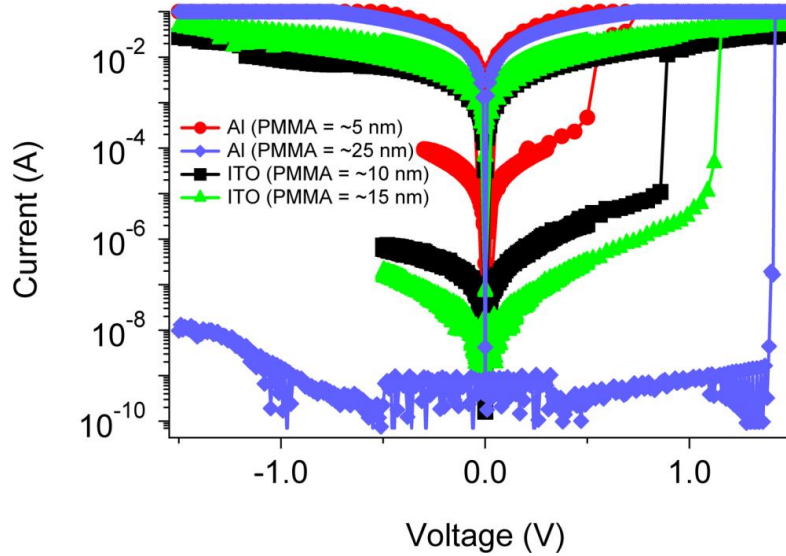


Figure 26. I - V characteristics of a PEDOT:PSS-based memristive device illustrating the effect of varying thicknesses of PMMA layer. BE made from ITO and Al are shown illustrating markedly higher current of the Al devices due to increased sheet conductivity of metal electrodes compared to ITO.

Motivated by long lifetimes seen in organic photovoltaic devices induced with the inherent air-stability of the inverted geometry, a study of the ability of the devices to preserve their state, and hence store data over an extended time bases, was conducted. For the study, the devices were stored in ambient conditions in the dark. The 200 nm thick silver electrode used in the device geometry is beneficial for protecting the PEDOT:PSS active layer from oxygen and water molecules (Lloyd et al., 2009). Because in OM-PROM devices the data storage is permanent, two sets of devices were used: one in OFF-state and one in ON-state. Figure 27 shows a typical retention time graph, with the measurement spanning almost two years (approximately 600 days). It can

be seen that the ON-current was reduced by about a factor of four. However, because the OFF-current is also decreasing, the ON/OFF ratio can be still seen as being over three orders of magnitude. The inset of Figure 27 shows I - V relationship of a single device, originally in OFF-state, but then turned to ON-state, and a subsequent decrease of the output current from day 1, through day 10, 120, 330, and 600. The OFF-current was measured from devices fabricated on the same substrate, after verifying that all of the devices had a similar ON and OFF-currents. Such encouraging retention time is attributed to the device's inverted configuration. It was further verified that the devices retain their switching ability from the original OFF-state, even after being stored for twenty months. Additionally, it can be seen that devices stored in the ON-state can be refreshed (black arrow marked "Refresh" in the figure) close to their original ON-current, by applying a voltage sweep to the device, as shown in Figure 27.

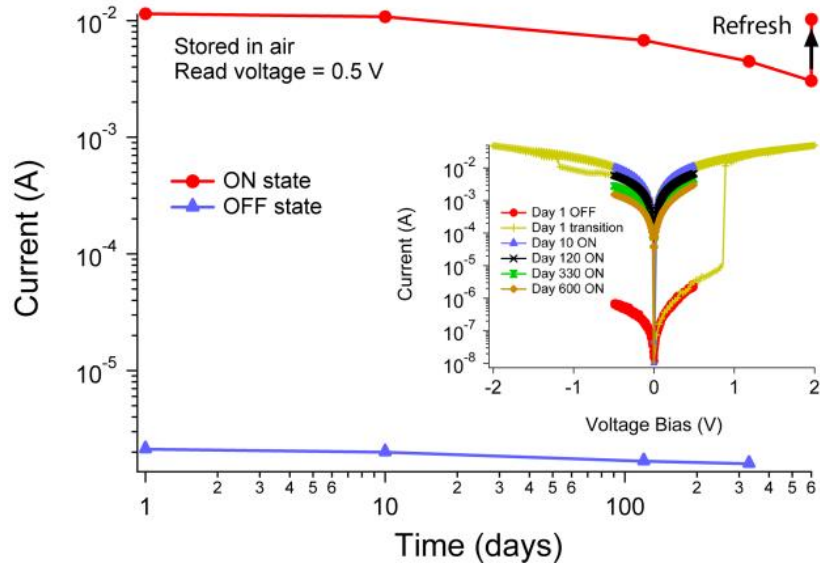


Figure 27. Performance of two PEDOT:PSS-based OM-PROM devices (one in the ON-state, one is the OFF-state) over a period of twenty months with storage in air. The current is shown for a

read voltage of 0.5 V. *I-V* curves taken at several intervals for the device tested in the ON-state are shown in the inset. After twenty months, the device in the ON-state was refreshed by applying a voltage sweep with limits of ± 2.0 V.

As previously illustrated, the turn ON threshold is largely dictated by the thickness of the PMMA layer. The devices shown in Figure 26 all exhibit a very low turn ON voltage of less than 1.5 volts. However, as already discussed, this voltage also determines the boundary between the neuron's operating region and programming region. Because of the markedly lower operating bandwidth of organic electronic devices, specifically organic transistors (discussed in 3.3.2 *OFET For Synthetic Soma*), is it generally desired to have the programming region extending at least up to 10 volts. As such investigations of PEDOT:PSS-based memristive devices with a thick PMMA layer was carried out.

Figure 28 demonstrates *I-V* relationship of an OM-PROM device fabricated with a significantly thicker layer of PMMA, of over 50 nm. It can be seen that the device switches at a much higher voltage of approximately 18 volts. However, while in the devices with much thinner PMMA layer the switching was attributed to PEDOT doping via electrically injected charges that form filamentary pathways (R. A. Nawrocki, et al., 2013), in the thick PMMA devices the switching is likely due to catastrophic localized "short" due to the application of a very high voltage bias.

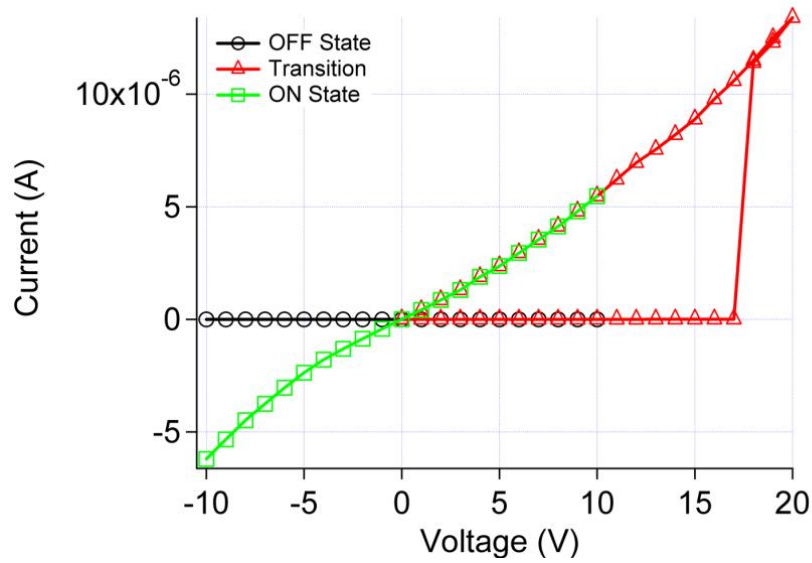


Figure 28. *I*-*V* characteristics curve of an OM-PROM device with a high turn ON voltage of ~18 V.

3.2.5.2 Manufacturing

This section outlines the details of the fabrication processes used to create the devices. The device structure for this experiment, outlined in Figure 19, was glass/ITO/ZnO/PMMA/PEDOT:PSS/Ag or Al/ZnO/PMMA/PEDOT:PSS/Ag. Zinc acetate (ZnAc), used as the precursor for the ZnO layer, and PMMA (MW ~996,000) were used as received from Sigma-Aldrich. Clevios P VP AI 4083 was used as the PEDOT:PSS layer. This low-conductivity version was found to perform best over several other formulations (PH 500 and P). All of the solvents, except for isopropyl alcohol (IPA), namely dimethylformamide (DMF), toluene, 2-methoxyethanol (2ME), and monoethanolamine (MEA), were anhydrous and used as received from Sigma-Aldrich. ITO substrates were cleaned by ultrasonication in acetone and IPA for 10 minutes each.

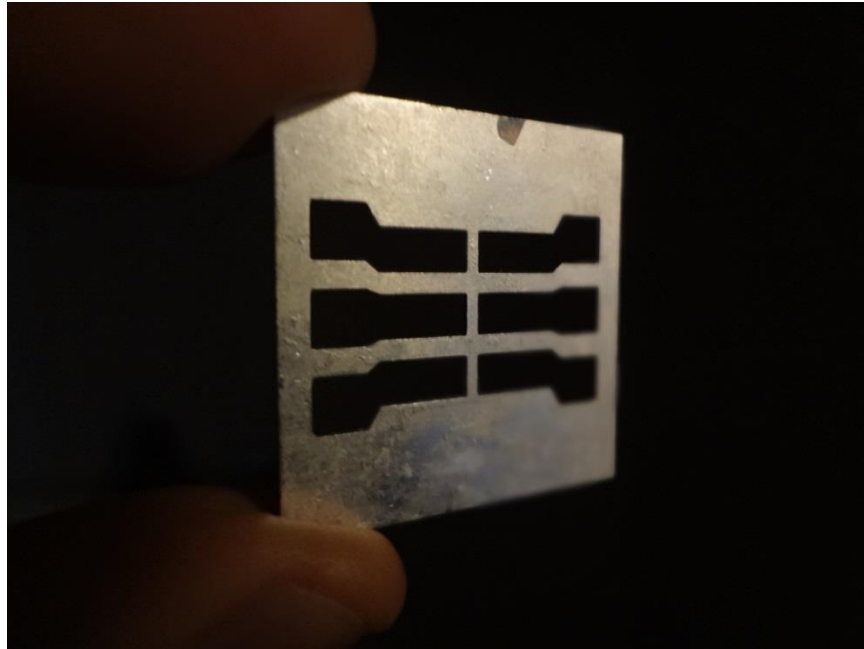
For ZnO layer deposition, ZnAc powder was first dehydrated by placing it on a hot plate at 120 °C for 10 minutes. It was then

immediately placed in a nitrogen-flow desiccator to cool and for the condensation to evaporate. This dehydration process was repeated if water condensation was apparent. The solution was obtained by dissolving 140 mg of ZnAc in 1 mL of 2-methoxyethanol and 45 μ L of monoethanoamine at 60 °C for about 8 hours. For deposition, the cooled solution was filtered through a polyethersulfone (PES) filter (VWR) with a pore size of 0.45 μ m before spin-coating at 2000 rpm for 60 seconds, or blade-coating at 60 °C at 15 mm/s. The sample was then placed on a hot plate preheated to 300 °C in air for 10 minutes. After removal and cooling, the sample was rinsed, to remove organic residue, in deionized H₂O, acetone, ethanol, and IPA for 10 seconds each and then dried on a hotplate in air for 10 minutes at 200 °C. The resulting ZnO films were approximately 40 nm thick.

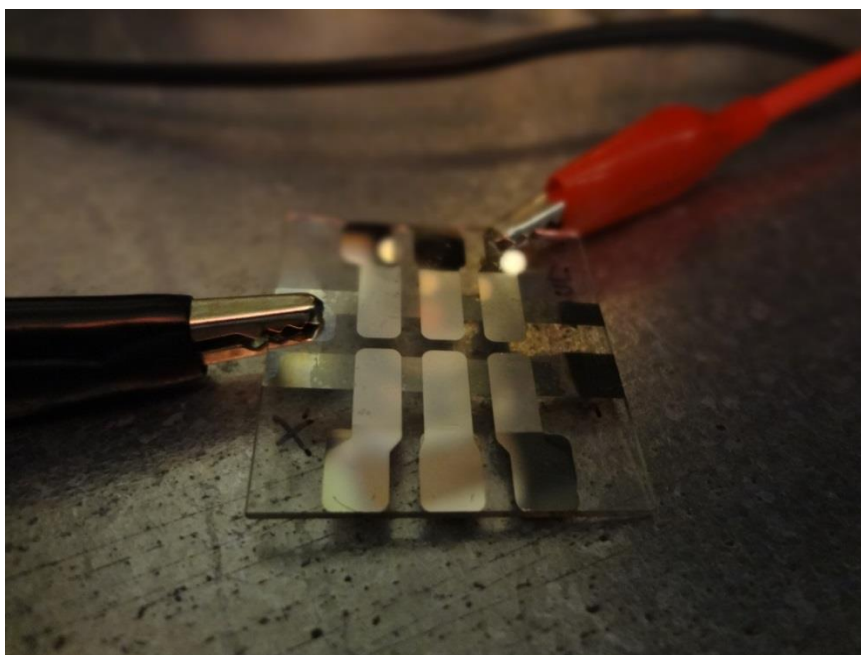
PMMA layers of various thicknesses in the range of ~0-50 nanometers were obtained by dissolving PMMA (MW ~996,000) in DMF with concentrations ranging from 3.5 mg/mL to 30 mg/mL. A layer of the material was deposited by spin-coating with a speed of 1000 to 4000 rpm for 60 seconds, or blade-coating at 60 °C at 15 mm/s. Subsequently the device was annealed at 120 °C for 10 minutes in a stream of N₂. PEDOT:PSS layers with a thickness of 25 nm were obtained by first diluting with IPA (1:1) and mixed overnight on a room-temperature stir-plate to ensure uniform mixing. The solution was then filtered using 0.45 μ m PES filter and subsequently spin-coated for 60 seconds at 4000 rpm, or blade-coating at 20 °C at 15 mm/s (the blade-coating temperature was reduced below the boiling point of IPA). The sample was annealed at 120 °C for 10 minutes in a stream of N₂. Blade-coated films

were deposited using either a BYK-Gardner manual film applicator or a Zehntner ZAA 2300 Automatic Film Applicator Coater.

Immediately preceding vacuum deposition of the top electrode, the devices were placed on a hotplate at 120 °C (105 °C for common-substrate devices with PQT-12 layer already on, see section 4.2.2 *Fabrication*) for 10 minutes under nitrogen in order to dehydrate the PEDOT:PSS layer. Silver top electrodes with a thickness of 200 nm were thermally evaporated at a base pressure of $\sim 2 \times 10^{-6}$ Torr and a rate of ~ 5 Å/s. A shadow mask, such as the one shown in Figure 29(a), was used to define devices. *I-V* measurements were performed with a Keithley 237 unit with a delay of 20 ms between voltage steps. The thicknesses of individual layers were measured with surface profiler Dektak 3030.



(a)



(b)

Figure 29. (a) An example of a shadow mask used to define the area of a metal electrode obtained through metal evaporation. (b) An example of an organic memristive device with metal electrodes obtained by evaporation of metal through a shadow mask. An array of six devices formed at the intersection BEs and TEs can be seen.

3.3 Organic Field Effect Transistor

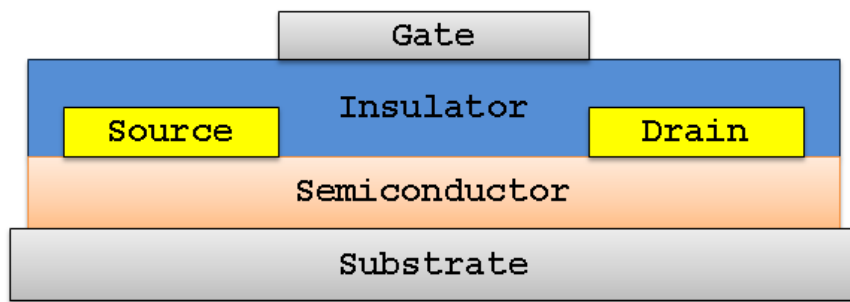
Organic Field Effect Transistor, or OFET, sometimes referred to as Organic Thin Film Transistor, or OTFT, is a type of a field effect transistor that uses an organic semiconductor in its active channel. Organic transistors can be prepared by either vacuum deposition of small organic molecules, such as fullerenes, by solution-casting of polymers or small molecules, or by mechanical transfer of a peeled single-crystalline organic layer. Primarily OFETs are fabricated using planar or layered approach; individual materials, such as electrodes, semiconductor, insulator, are deposited sequentially, atop one another.

OFETs have been developed to realize low-cost, large-area and biodegradable electronics.

3.3.1 Basic Concepts

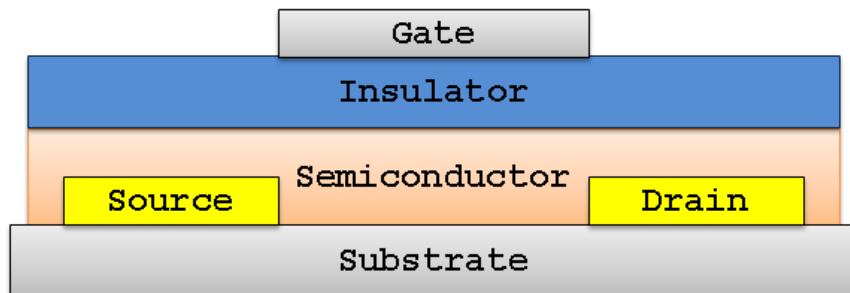
A thin film transistor can be analyzed as a parallel plate capacitor, with gate electrode acting as one of the plates while the other plate is made from the semiconducting medium along with the source and drain electrodes. The function of the source and drain electrodes is to inject and retrieve charges from the semiconductor while the gate electrode modulates that current (Bao & Locklin, 2007; Horowitz, 2010a; Sze & Ng, 2006).

Depending on the location of the gate electrode, as well as the source and drain (contact) electrodes, four distinctive arrangements have been conceived: top-gate-top-contact, top-gate-bottom-contact, bottom-gate-top-contact, and bottom-gate-bottom-contacts. These four possibilities are illustrated in Figure 30(a-d). From a fabricating perspective, given a finite amount of area dedicated to an individual transistor, an interdigitated source-drain "finger" pattern is often employed to maximize the channel width between the drain and source electrodes. This concept is illustrated in Figure 31(a) with the channel area being chequered-pattern marked. Figure 31(b) demonstrates a snapshot of the source and drain electrodes manufactured on a glass substrate through the process of photolithography.



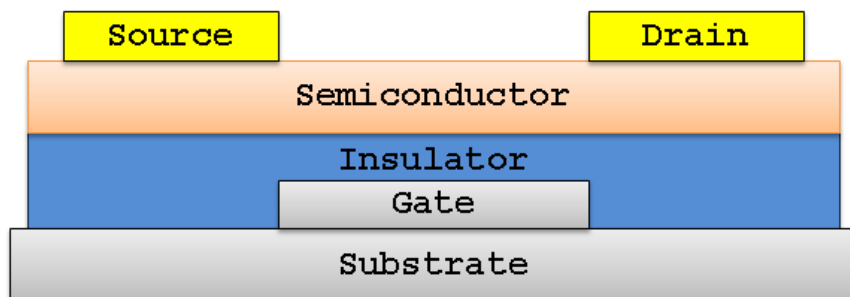
Top gate, top contacts

(a)



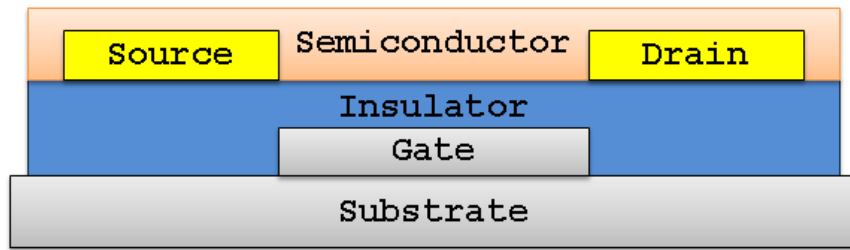
Top gate, bottom contacts

(b)



Bottom gate, top contacts

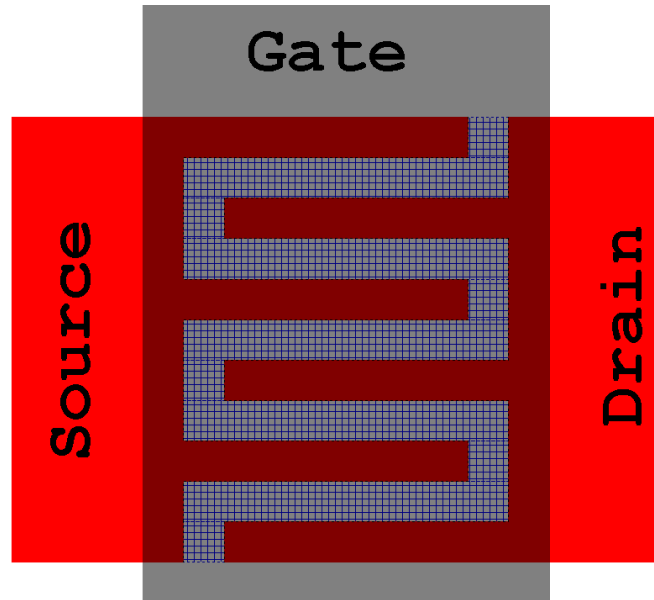
(c)



Bottom gate, bottom contacts

(d)

Figure 30. Four individual OFET arrangements that depend on the location of the gate and source and drain (contact) electrodes: (a) top-gate-top-contact, (b) top-gate-bottom-contact, (c) bottom-gate-bottom-contact, and (d) bottom-gate-bottom-contact.



(a)



(b)

Figure 31. Interdigitated pattern of source and drain “fingers” aiming to maximize the channel width at a given area. (a) Schematics, (b) picture of source and drain patterned electrodes.

An OFET is essentially made of three components: a dielectric, a semiconductor, and three electrodes. The generic device geometry, with all of the aforementioned components, is shown in Figure 32 in a bottom-gate-top-electrode configuration. Electrically, organic semiconductor is an insulator due to the fact that the density of thermally induced free carriers is very low. Therefore, in the absence of gate electrode and gate voltage V_G , no current will flow between the drain and source electrodes regardless of their potential difference. Practically, because of the presence of dark carriers in organic semiconductors¹, all OFETs experience some amount of leakage current even when $V_G = 0$ V.

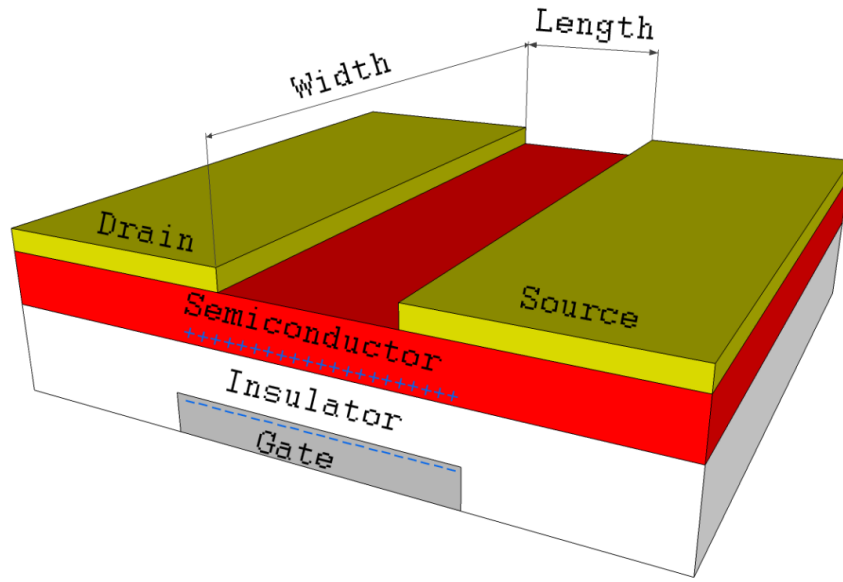
¹ Presence of dark carriers in organic semiconductors is mainly attributed to impurities, such as oxygen or water vapor, being introduced to the organic semiconductor film during synthesis process or device manufacturing (Ferguson, Kopidakis, Shaheen, & Rumbles, 2011).

Because majority² of currently available organic semiconductors are good hole transporters (p-type semiconductors), most fabricated organic transistors are classified as p-channel OFETs. Therefore, the explanation of device operation will concentrate on p-channel OFET operation. However, except for the sign of the charge, the explanation is pertinent to both p- and n-channel transistors.

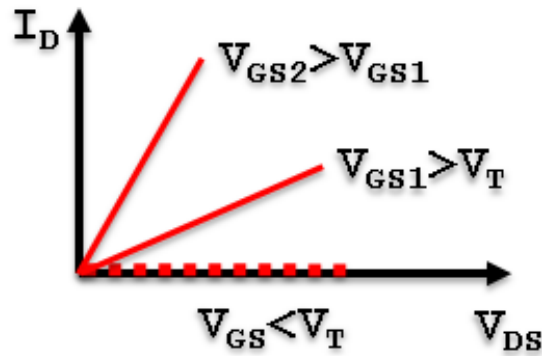
When a (negative) voltage bias is applied to the gate electrode it induces a (negative) charge-buildup at the gate side of the dielectric and the opposite (or positive) charge-buildup at the insulator-semiconductor interface forming a conductive channel³. As a result, the normally non-conductive semiconductor becomes conductive allowing for the transport of charges (holes). The "thickness" of the channel is directly proportional to the magnitude of the voltage bias applied at the gate electrode. If the bias is greater than a threshold value, $V_{GS} > V_T$, the resulting channel is sufficiently dense to continuously carry charges between drain and source electrodes resulting in drain current I_D . The concept is illustrated in Figure 32. The magnitude of the current is proportional to the magnitude of the gate bias with subsequently increasing current slope, as indicated Figure 32(b).

² Until recently fullerenes, molecules composed entirely of carbon atoms, such as C_{60} commonly referred to as buckyball or buckminsterfullerene, or C_{61} also known as [6,6]-phenyl-C61-butyric acid methyl ester or PCBM, were the only n-type organic semiconductors for the use in OFETs (Hwang, Murari, & Jenekhe, 2013).

³ The conductive channel is actually being induced inside the semiconducting film and is believed to be typically just few angstroms thick.



(a)

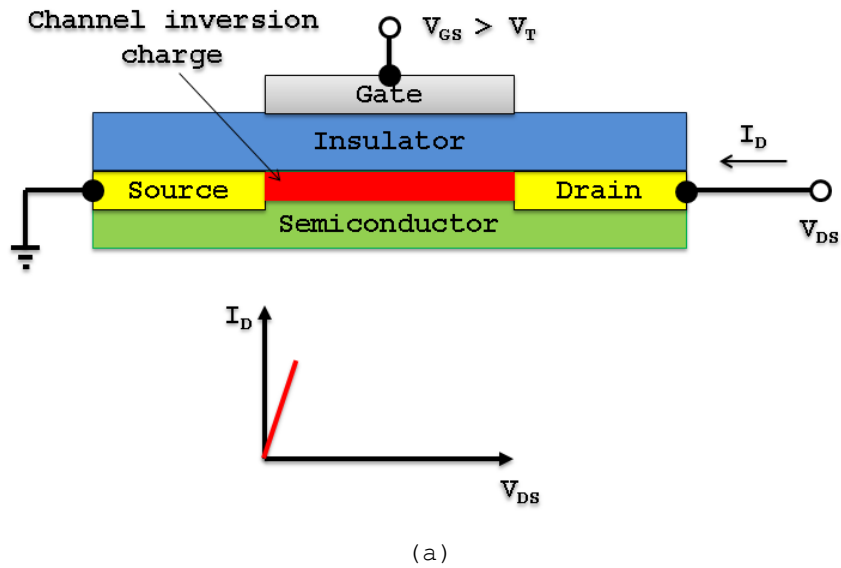


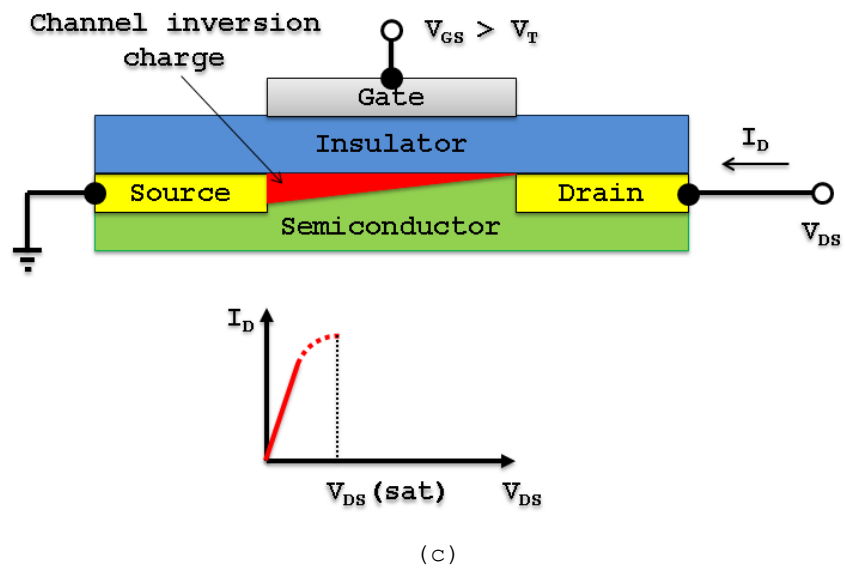
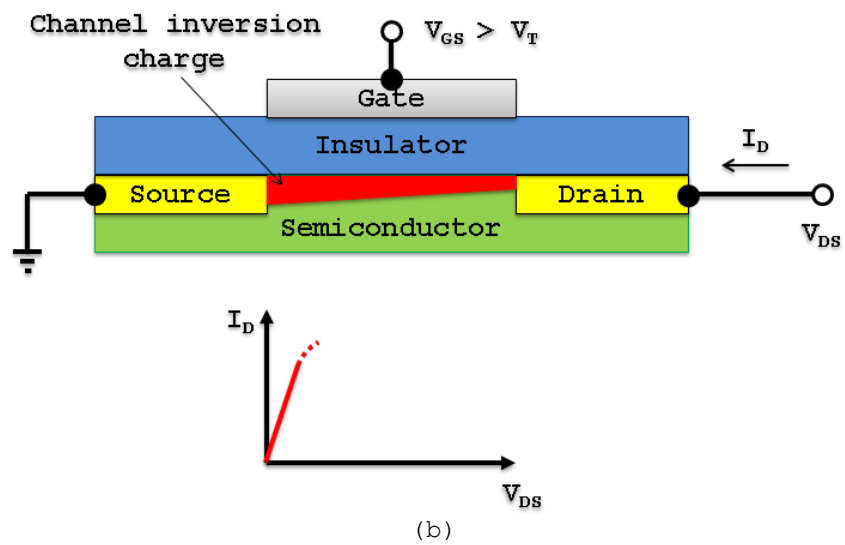
(b)

Figure 32. (a) Application of voltage bias at the gate electrode induces charges at the insulator-semiconductor interface allowing for the formation of a conducting channel and a subsequent charge path between source and drain electrodes. (b) Application of greater voltage bias at the gate electrode produces greater drain current for the same drain-source voltage bias, due to greater amount of charges being induced at the insulator-semiconductor interface.

Slow increase of the V_{DS} results in slow increase of the drain current, Figure 33(a). As the drain voltage increases, the voltage drop across the drain-source voltage increases resulting in decrease of the induced charge density near the drain electrode, Figure 33(b). The

incremental conductance of the channel at the drain then decreases, which causes the slope of the I_D curve to decrease. When V_{DS} approaches the value of V_{GS} , the induced inversion charge density at the drain terminal reaches zero, occurring at the so-called *pinch off* point. Because the potential at the pinch of point remains equal to $V_G - V_T$, the drain current becomes independent of the drain voltage and further increases of the V_{DS} do not result in increase of the I_D and the slope of the current remains flat, Figure 33(c-d). From a practical consideration, however, increase of V_{DS} beyond the pinch off point is typically accompanied by an increase of I_D due to shortening of the length of the channel and a subsequent reduction of the output resistance (discussed in more details later in this section), and is often referred to as channel length modulation.





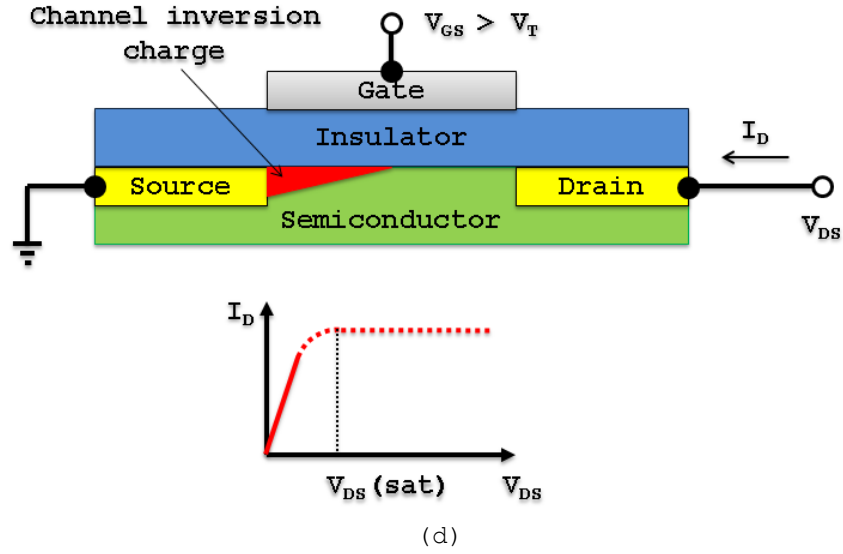


Figure 33. Cross section of an OFET indicating the shape of channel inversion charge depending on the magnitude of drain-source voltage in relation to the gate-source voltage bias, and a subsequent change of the OFET's I - V characteristics curve transitioning from linear to saturation regime.

Equation 10 and Equation 11 demonstrate standard relationship between transistor parameters and the current for two cases, linear and saturation regimes, while Equation 12 represents the relation between transistor's parameters and the carrier mobility μ (Neamen, 2009; Tinivella, et al., 2010). Inspection of Equation 11 reveals that the equation for the saturation region does not include a V_{DS} term, with the only variable being the gate voltage, resulting in the drain current being independent of the drain-to-source voltage. This has the effect of producing a flat curve and is characterized by an infinite output resistance r_o . However, as already discussed, in most realized transistors, the drain current is not independent of that voltage and an increase of the drain-to-source voltage bias results in increase of the drain current due to a finite output resistance. To account for this discrepancy, the equation for the saturation region of a transistor can include another term, $(1 - \lambda V_{DS})$. λ is called the channel

length modulation parameter and can be extracted graphically, as shown in Figure 34, and calculated according to Equation 13. Equation 14 demonstrates the OFET's I - V relationship that includes the channel-length modulation functionality with channel length modulation factor.

$$I_D = \mu C_x \frac{W}{L} \left(V_{GS} - V_T - \frac{V_{DS}}{2} \right) V_{DS}$$

Equation 10. OFET drain current calculated for linear region.

$$I_D = \mu C_x \frac{W}{L} \frac{(V_{GS} - V_T)^2}{2}$$

Equation 11. OFET drain current calculated for saturation region without the channel-length modulation parameter, resulting in a completely flat curve.

$$\mu = \mu_0 (-V_{GS} + V_T)^\gamma$$

Equation 12. Carrier mobility calculation.

$$V_A = \frac{1}{\lambda}$$

Equation 13. Equation used to calculate the channel length modulation parameter.

$$I_D = \mu C_x \frac{W}{L} \frac{(V_{GS} - V_T)^2}{2} (1 + \lambda V_{DS})$$

Equation 14. Calculation of OFET's drain current including the channel-length modulation parameter, resulting in a sloped curve.

Figure 34 depicts an example of an OFET curve with a non-zero channel length modulation parameter. The extrapolated curve intersects the voltage axis at a point $V_A = 27.5$ volts, resulting in the parameter $\lambda = 0.0364$. With $V_{DS} = -15$ V and $I_D = 2.62 \times 10^{-7}$ A, according to the Shichman-Hodges model (Sansen, 2007), Equation 15 indicates that the output resistance $r_0 = 162$ M Ω , which is high but

non-infinite, and produces the relatively high slope of the drain current in the OFET's saturation regime.

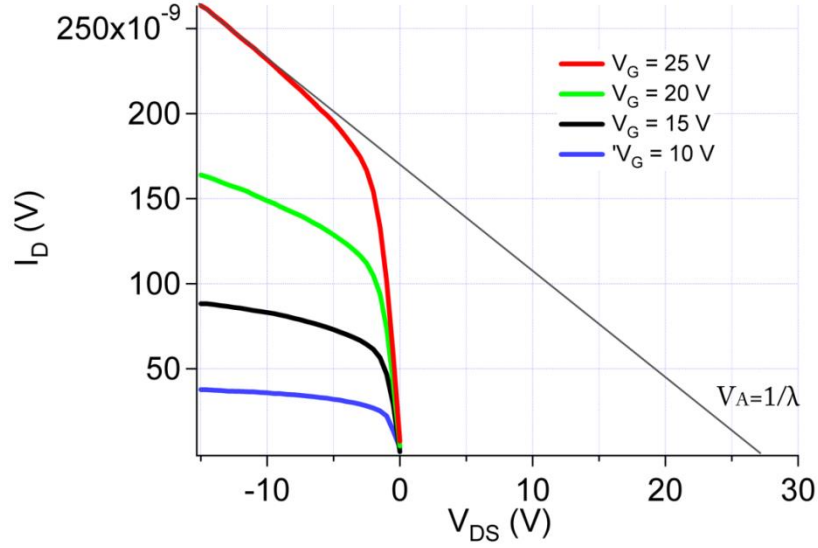


Figure 34. Family of I_D versus V_{DS} curves showing the effect of channel length modulation producing a finite output resistance. The intersection of the sloped saturation region curves with the horizontal axis allows for a graphical extraction of the channel-length modulation parameter λ according to Equation 13.

$$r_0 = \frac{1/\lambda + V_{DS}}{I_D}$$

Equation 15. Calculation of the output resistance with the channel length modulation parameter.

3.3.2 OFET For Synthetic Soma

This section outlines the details of the fabricating processes used in creating organic transistors presented in this work.

3.3.2.1 Device Configuration, Materials, and Procedures

As discussed, Organic Field Effect Transistor (OFET) relies on electrical properties of a thin film of organic or polymer

semiconductor in its channel. Many exotic semiconducting and insulating materials with multitude of process steps have been presented in the literature. However, my choice of the OFET configuration was primarily driven by the need of simplicity and ease of processing. Figure 35 demonstrates the configuration of the top-gate-bottom-electrode OFET created in my laboratory, inspired by (Baeg et al., 2011), including the choice of individual materials and their respective thicknesses, while Figure 36 shows an example of a typical I - V characteristic curve of such a device (Figure 9(d) and Figure 9(e) illustrate chemical structures of the organic semiconductor and organic insulator used).

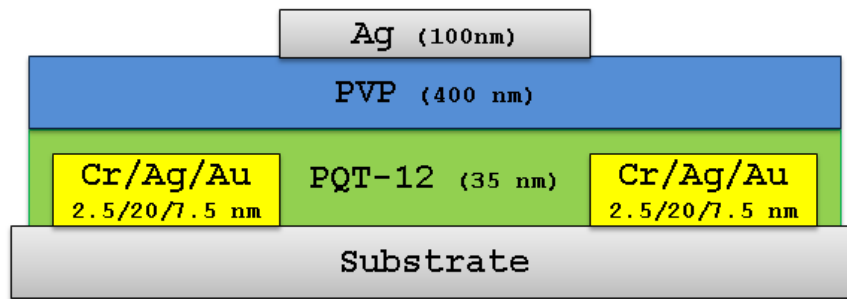


Figure 35. Top-gate-bottom-contact configuration of an OFET used to function as a synthetic soma. The configuration was inspired by (Baeg, et al., 2011).

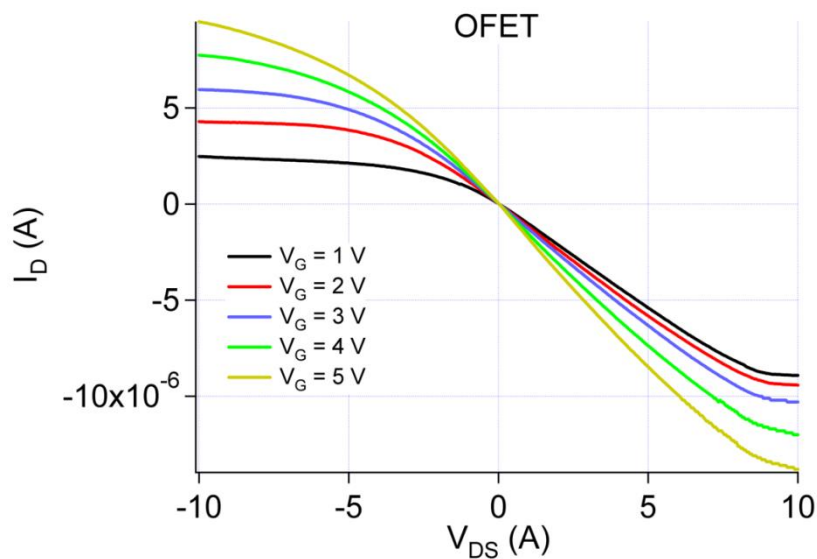
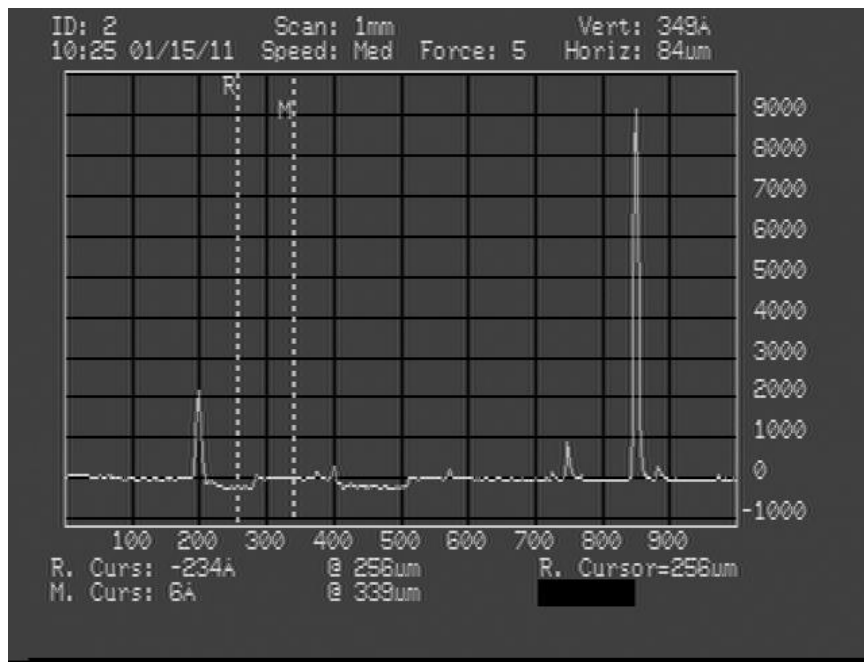


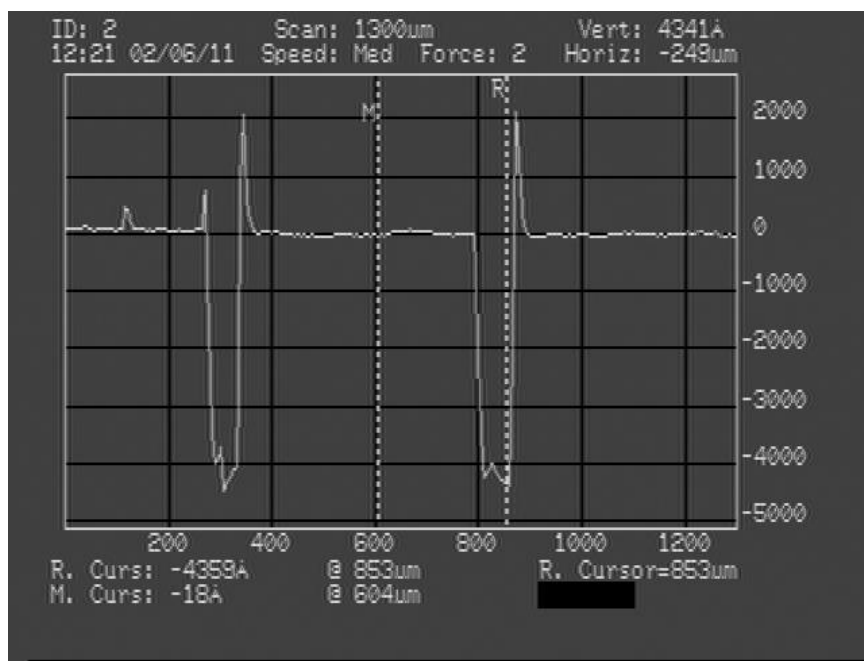
Figure 36. *I*-*V* characteristic curve of a typical, PQT-12-based OFET, with top-gate-bottom-contact configuration shown in Figure 35.

The following outlines the OFET's fabrication procedure. First, glass substrates of approximately 1" x 1" were ultrasonically cleaned in acetone and IPA for 10 minutes each, followed by oxygen plasma treatment for two minutes. A photolithographic process, based on a negative photoresist NR71 (Futurrex, 2013; Sigma-Aldrich, 2013), was used to obtain the drain and source electrode pattern providing for a channel length of 5 μm . Next, three metals, chromium (Cr - good adhesion to glass and polymer substrate), silver (Ag - good electrical conductance and low cost), and gold (Au - good carrier injection into organic semiconducting medium as well as low oxidation) were thermally evaporated with thicknesses of 2.5 nm, 20 nm, and 7.5 nm respectively. The source and drain electrode trenches were obtained by a subsequent lift off procedure by submersing the substrate in acetone and sonicating for approximately 20 seconds (an example of the source and drain electrodes, fabricated on glass substrate, is illustrated in Figure 31(b)). The choice of the semiconductor was poly(3,3'''-dialkyl- quaterthiophene) (PQT-12), which was deposited from a solution in chlorobenzene (CB) with a concentration of 8 mg/mL, preceded by filtering with PES filter, either by spin coating at 2000 rpm, or blade coating 15 mm/s with substrate temperature of 60 °C, followed by annealing at 145 °C for 10 minutes in stream of N_2 , before the stream of N_2 was removed and the hot plate was allowed to slowly cool down to about 80 °C followed by removal of the sample. Poly(4-vinyl phenol) (PVP), dissolved in 1-butanol (BuOH) with a concentration of 80 mg/mL, was used as the dielectric material with the same processing steps as

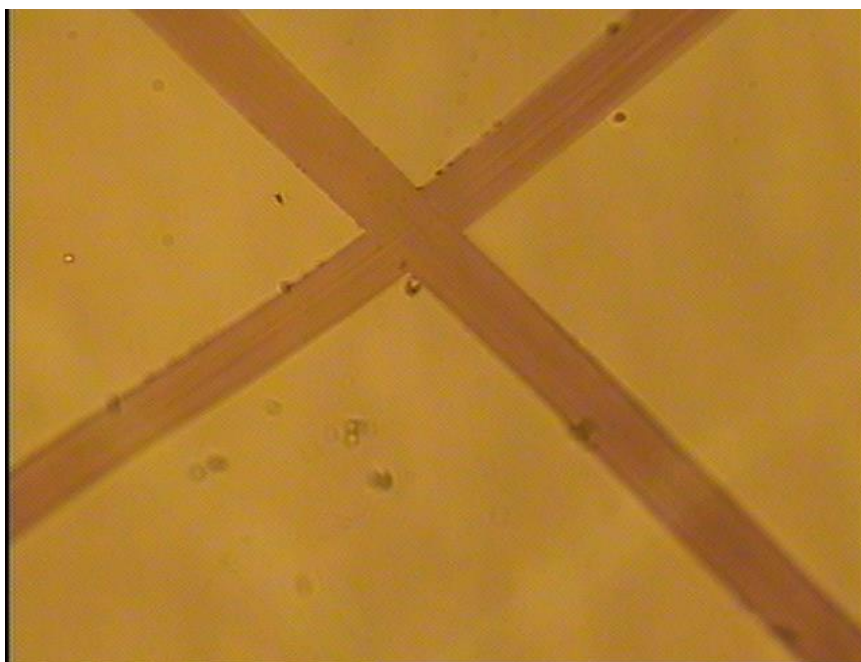
the semiconductor except for the annealing temperature of 105 °C. The thicknesses of the polymeric films were determined to be about 35 nm and 400 nm respectively. The gate electrode was formed from a thin film of silver that was thermally evaporated through a shadow mask. Figure 38(a) illustrates a zoomed picture of source and drain electrode trenches obtained through process of photolithography, while Figure 38(b) demonstrates the source and drain electrodes obtained through process of metal evaporation and photoresist liftoff. Figure 38(c) shows an array of organic transistors with three probe tips connected to source, drain, and gate electrodes.



(a)

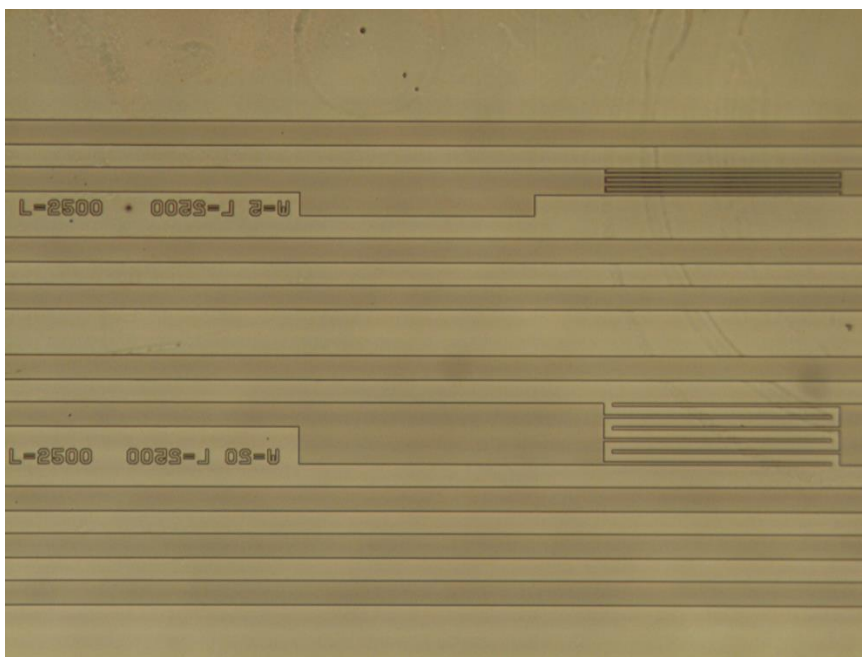


(b)

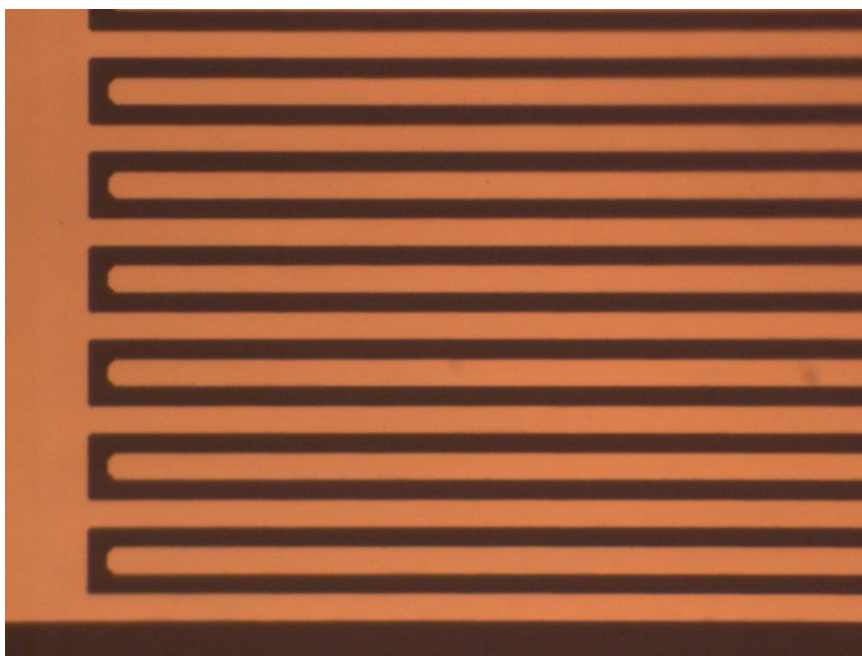


(c)

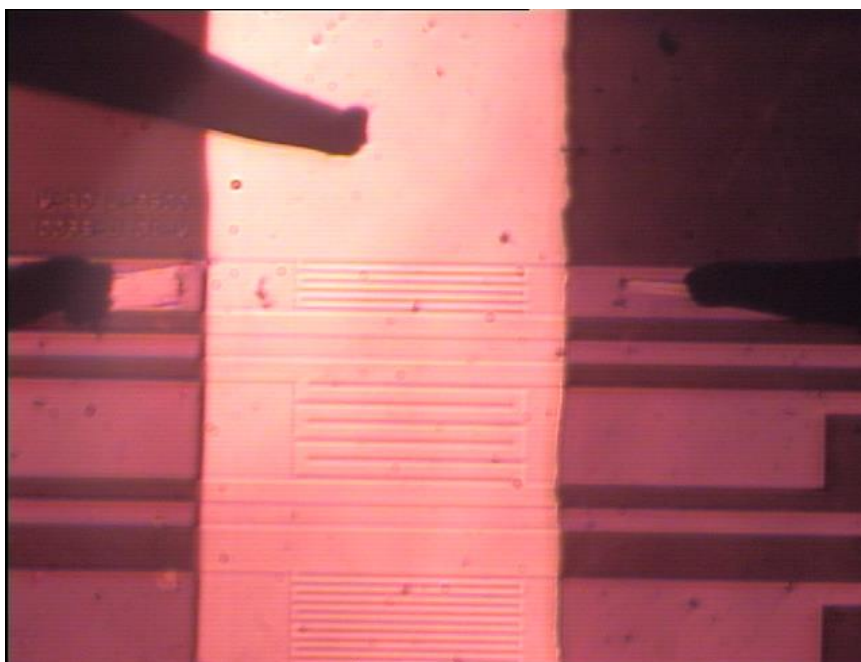
Figure 37. Snapshot of thickness measurement of (a) PQT-12 and (b) PVP + PQT-12, with (c) snapshot of scratches on the surface of the sample with a polymeric film.



(a)



(b)



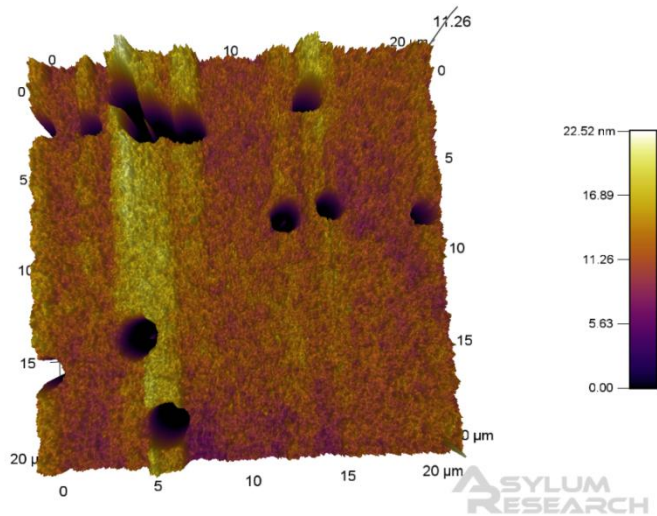
(c)

Figure 38. (a) Zoomed picture of source and drain electrode trenches, made with a negative photoresist NR71, visible on glass substrate. (b) Source and drain electrodes on glass substrate, obtained through metal evaporation and photoresist liftoff, with channel length of approximately 5 μm . (c) An array of OFETs, with three probe tips connected to source, drain, and gate electrodes clearly visible. The probe tips were used to scratch through the PQT-12 (semiconductor) and PVP (insulator) layers in order to make a good contact with the metal electrodes underneath.

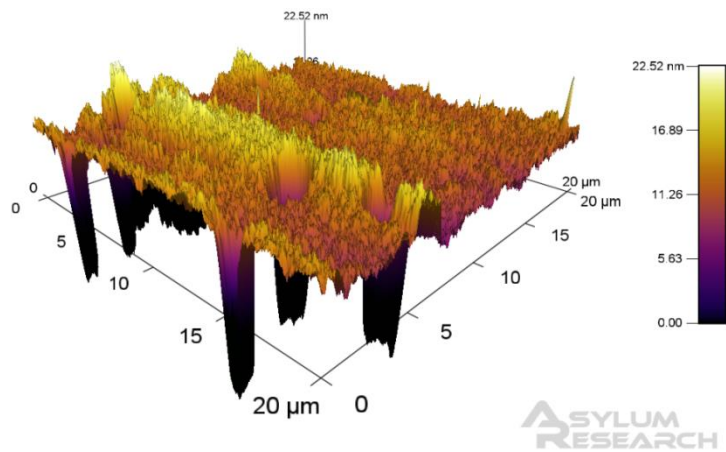
3.3.2.2 Fabricating Considerations

Throughout the development of the process recipe, a number of important details were observed, specifically relating to intrinsic chemical or physical properties of organic electronics. As seen in Equation 10 and Equation 11 an insulating material with a high capacitance per unit area, C_x , is commonly desired as it results in higher drain current (Ortiz, Facchetti, & Marks, 2010). However, in a layered structure of organic electronics, the choice of adjacent material is often facilitated by their respective polarities; when depositing material B on top of material A, one needs to ensure that a

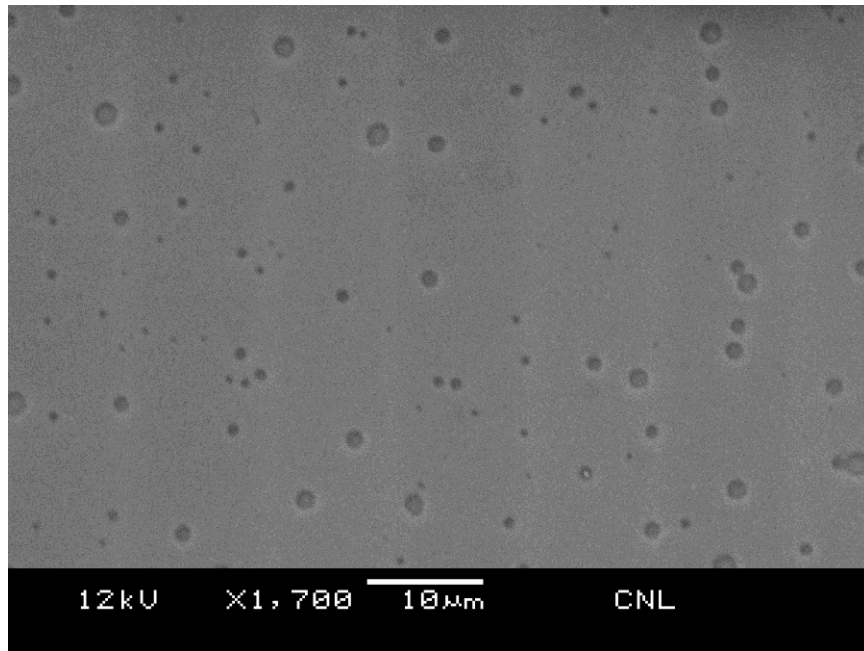
solvent used with material B will not also dissolve material A, otherwise material A will be removed by the deposition of material B (Baeg, et al., 2011), as illustrated in Figure 56. This concept is known as orthogonal solvent requirement and necessitates proper consideration. Another issue of consideration is the surface tension, especially its relation to hydrophobicity and hydrophilicity; incompatible materials will not wet their respective surfaces leaving patches, or bold spots, as illustrated in Figure 39.



(a)



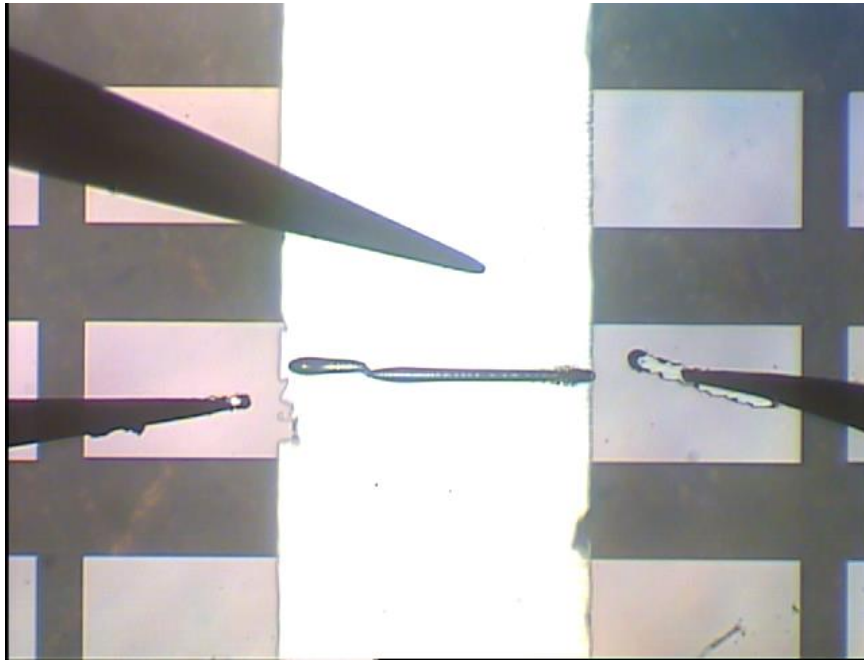
(b)



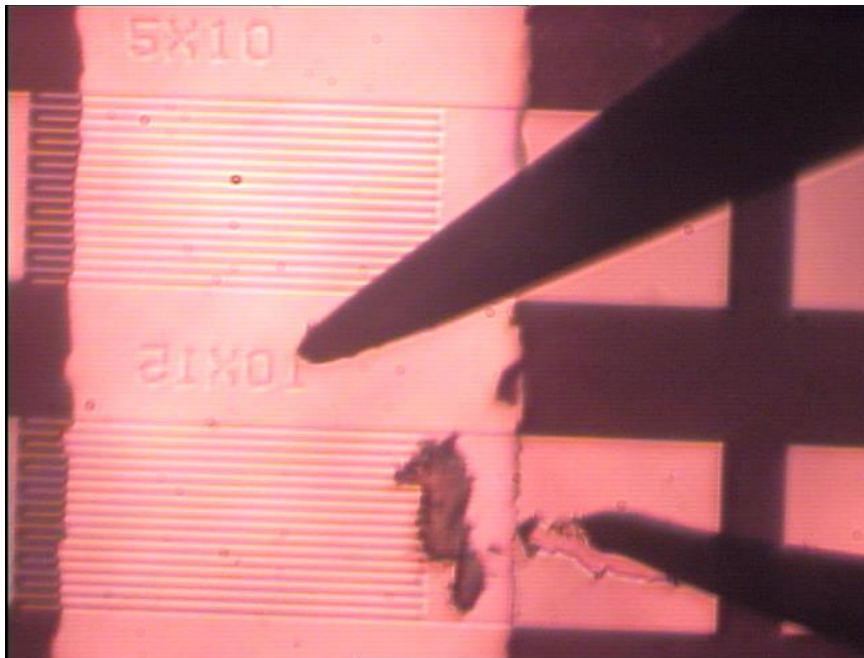
(c)

Figure 39. An AFM image, (a) top view and (b) side view, of PEDOT:PSS film that was obtained from insufficiently mixed solution with IPA wetting agent, leaving bold spots. (Images by Tony Nava). (c) SEM image of the same film.

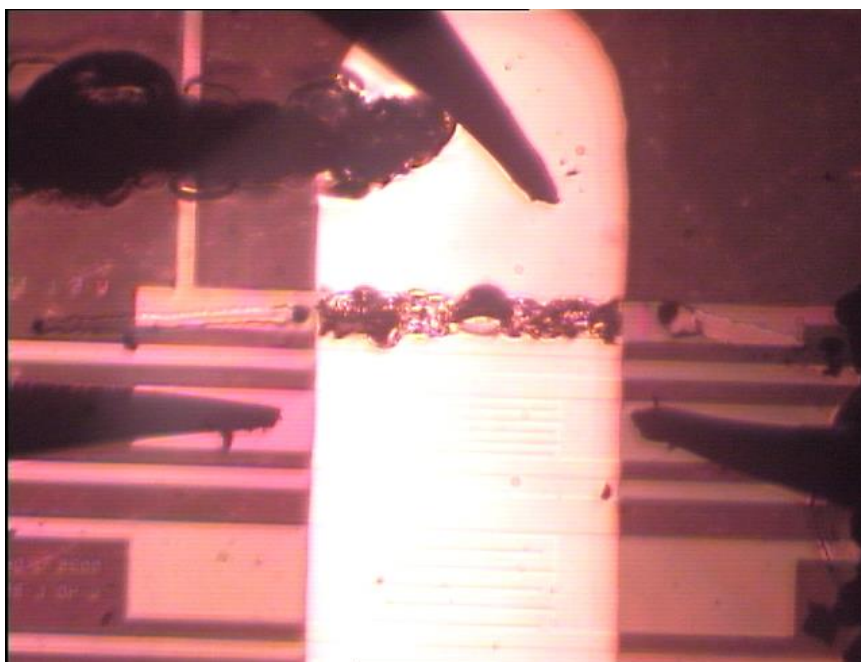
In a field effect transistor the thickness of the insulating material determines the magnitude of the gate voltage needed to induce the conducting channel in the semiconducting layer; thinner insulating later requires lower gate voltage, however higher gate voltage produces higher density of charges in the channel resulting in higher drain current. Figure 40 demonstrates examples of a damaged OFETs resulting from the gate voltage being too high (too thin dielectric layer) with a subsequent melting of the dielectric layer and catastrophic removal of the gate electrode.



(a)



(b)

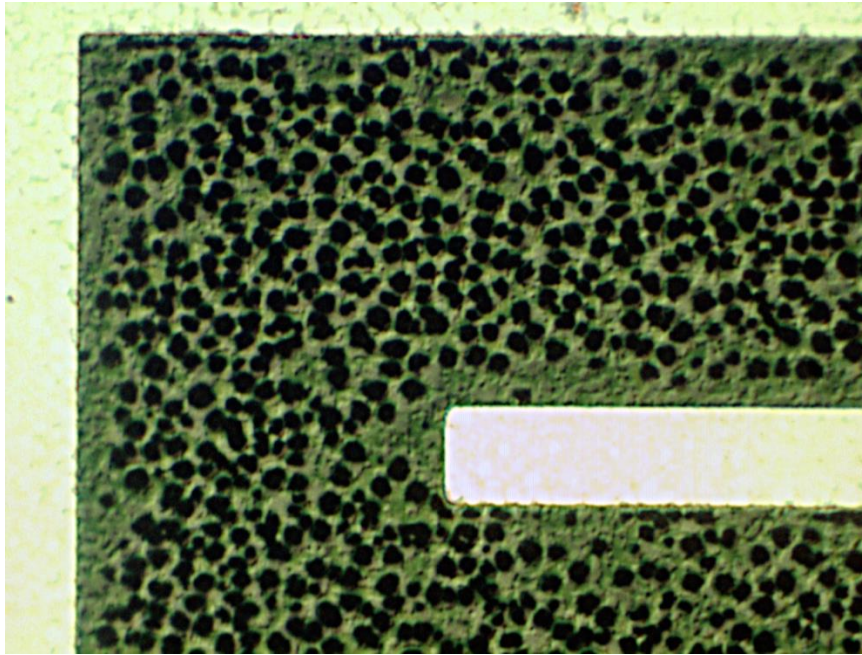


(c)

Figure 40. Examples of damaged OFETs due to high gate voltage being applied and a resulting melting of the insulating layer due to the generated heat.

The importance of the correct annealing temperature of an organic film is a well-known fact. Too low temperature will result in unfavorable crystalline formation (the carrier mobilities, and subsequently the drain current, relate directly to the semiconductor crystallinity); however, too high temperature often results in crystallites that are too large leading to pinholes and a very rough surface. Much less is known about the effects of the cool-down rate. It was observed that drastic and expedient reduction of substrate temperature, after the PQT-12 was annealed, would produce transistors with significantly reduced drain current. However, slow reduction of the temperature, from 145 °C to 80 °C over the course of about 30 minutes, would result in a significantly higher drain current. As a result, following the annealing of PQT-12, the

subsequent materials were annealed at 105 °C in order to avoid affecting the crystallinity of the semiconducting film. Optical microscopy revealed that the cool down rate has a significant effect on the formation of the crystalline structure of PQT-12 with fast cool down rate producing holed film, as shown in Figure 41.



(a)



(b)

Figure 41. Comparison of, (a) fast cool down rate of a PQT-12 film and (b) slow cool down rate of the semiconducting material. It can be seen that film that is quickly cooled down produces a high number of large holes with a subsequent reduction of the drain current of an OFET.

Throughout the recipe development process it was also determined that the need to anneal the PQT-12 material in a stream of N_2 was crucial. Devices annealed in oxygen were shown to exhibit a significant decrease in drain current, more than one order of magnitude, compared to devices annealed in a stream of nitrogen gas. It is generally believed that this is due to the trapping of oxygen atoms in the polycrystalline structure of PQT-12, resulting in greater difficulty of the charges hopping across individual molecules.

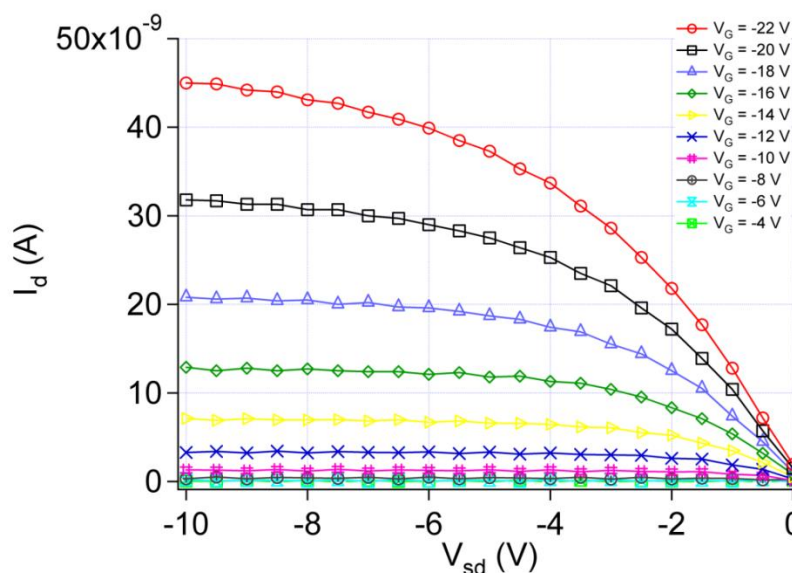


Figure 42. An example of an early OFET, with saturating drain current of tens of nanoamperes, created without optimized parameters, such as the anneal temperature and ramp down as well as annealing in stream of N_2 .

It was also determined that the PQT-12 cool down process should be carried in oxygen as opposed to the stream of N_2 , as in the latter devices the insulator solution would fail to completely wet the surface of the semiconductor leaving a number of bold spots (pin holes) with a subsequent shortening of the gate electrode. This was attributed the formation of a few monolayers of H_2O upon exposure of the PQT-12 to the atmosphere.

Transistors are associated with having two distinctive regions of operation: linear and saturation. In organic transistors the saturation region is often not very "flat" (discussed in section 3.3.1 *Basic Concepts*). Furthermore, it has been observed that OFETs with smaller channel width to channel length ratios result in devices with much "flatter" saturation current as compared to devices with larger channel widths. Throughout this study, it was observed that in devices with

very long channel length of 30 mm, the newly fabricated devices failed to produce the flattening saturation current. However, an annealing treatment at 30 °C for 40 minutes in air, resulted in the desired characteristics of two distinct operation regions; linear and saturation. This can most likely be attributed to moisture being trapped in the film resulting in separation of the molecules and a slight swelling of the film. Figure 43 demonstrates the change with solid lines representing I - V scan of a freshly created transistor while dashed lines are used to denote a treated OFET.

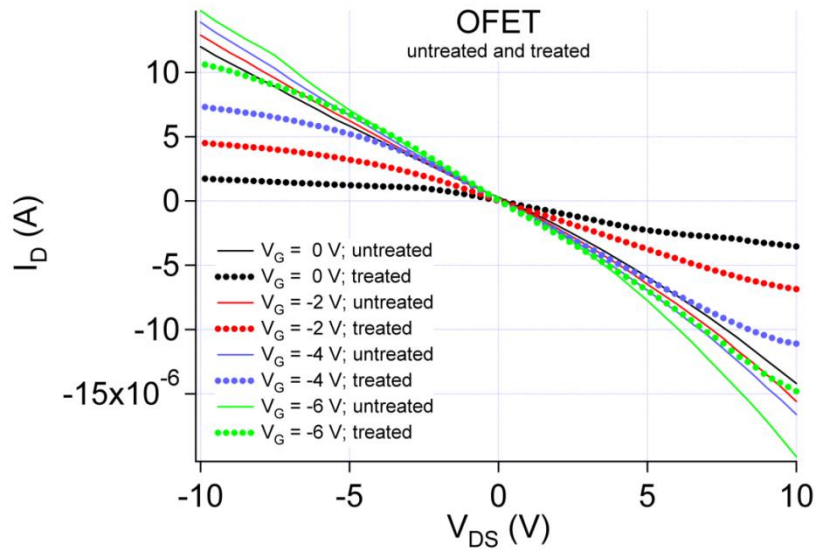


Figure 43. Comparison of freshly created OFET lacking saturating features (marked with solid lines), and treated OFET showing saturating characteristic (dashed lines).

3.3.2.3 Physically Flexible OFETs

Because of the lower cost and ease of fabrication, the majority of the presented organic electronics devices were fabricated on glass

substrate. However, glass is also thick, inflexible, and brittle⁴. As such, new substrate medium was investigated.

Poly(ethylene 2,6-naphthalate) (PEN) is a new type of polymer designed to replace the ubiquitous polyethylene terephthalate (PET) because of its reduced reactivity with many common solvents (Ghai, 2013; Teijin, 2013). An array of physically flexible organic transistors was fabricated on PEN according to the configuration outlined in Figure 35. The source and drain electrodes were fabricated using a standard photolithographic technique with channel length of approximately 5 μm . The semiconducting and dielectric PQT-12 and PVP films were deposited using either spin or blade casting techniques. The gate electrode was obtained from thermally evaporated silver through a shadow mask. Figure 44(a) displays a 1" x 1" PEN substrate with only source and drain electrodes, while Figure 44(b) demonstrates an array of the entire organic transistors respectively. Figure 45(a) and Figure 45(b) illustrate the pre- and post-flexed OFET I - V characteristics curve demonstrating that bending this 120 μm -thick substrate, to a 90° angle, with an approximate radius of less than 1 cm, does not result in a destruction of the device. The post-bend devices present a slightly improved I - V characteristics likely due to improved morphological alignment of the semiconducting PQT-12 molecules.

⁴ In 2012 Corning Inc. has introduced Willow Glass, or Gorilla Glass, a physically flexible sheet of glass, about 100 microns thick (Corning, 2013).

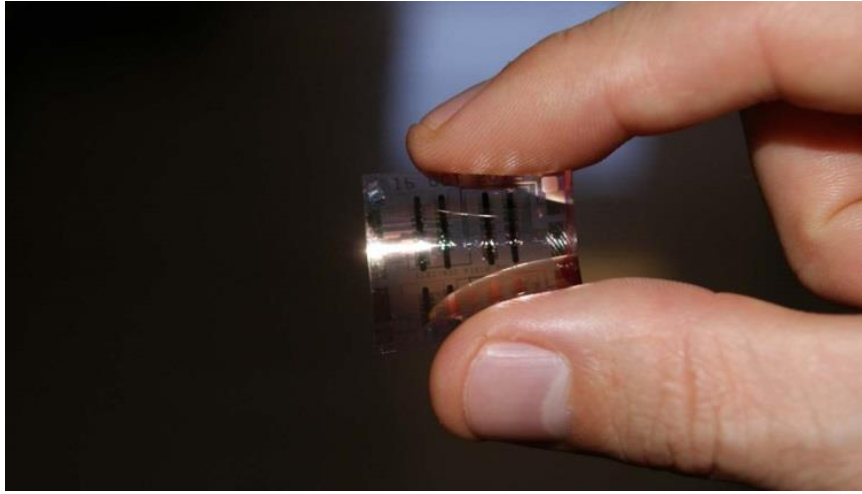
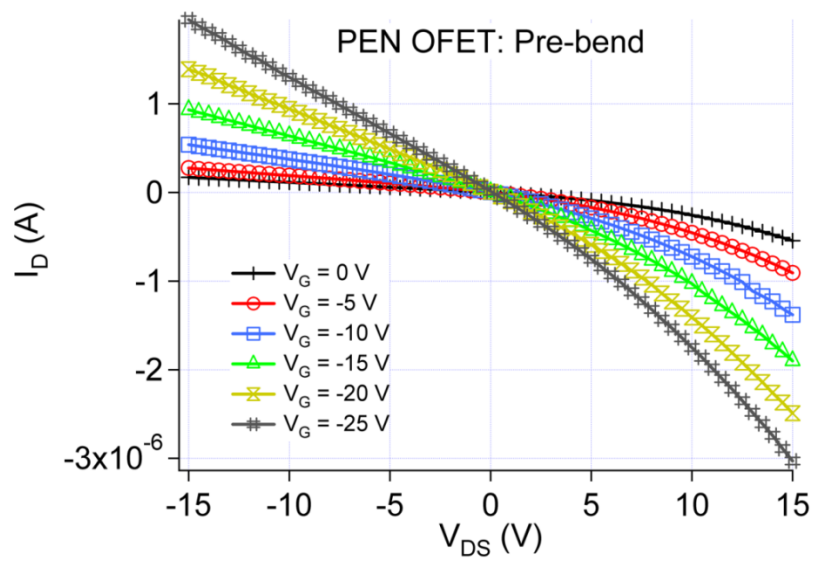


Figure 44. Physically flexible OFETs fabricated according to the device layout shown in Figure 35.



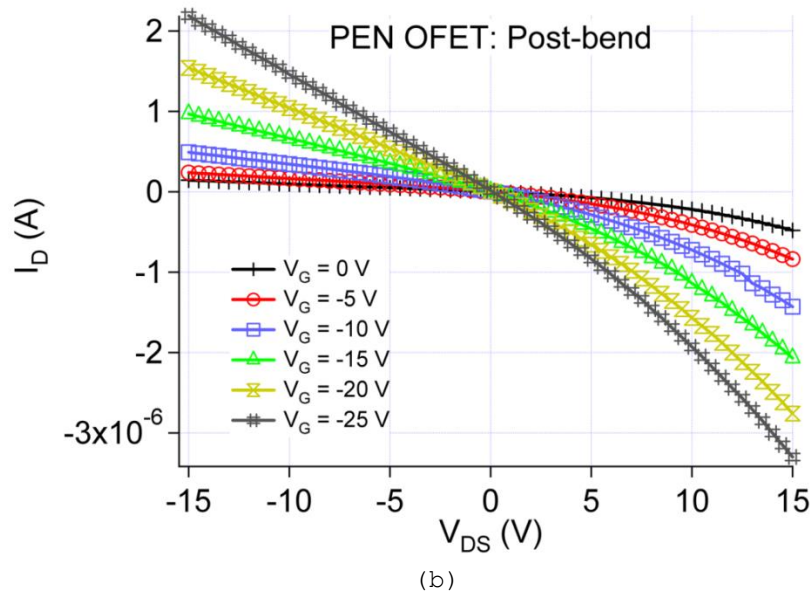


Figure 45. I - V characteristics curves of physically flexible OFETs, shown in Figure 44, (a) before bending, and (b) after bending. It can be seen that the physical flexion did not negatively affect the operation of the device.

3.4 Organic Resistor

Resistor is perhaps the simplest of the four fundamental, two-terminal electrical elements. It relies on a linear relationship between voltage and current that holds in its operation region. As such, it requires the use of a conductive material that fits this description. A number of conductive polymeric materials have been synthesized over the years, and they can be classified into three main groups: no heteroatom group, nitrogen-containing group, and sulfur-containing group (Naarmann, 2000). Examples of the no heteroatom group include poly(fluorine)s, polypyrenes, poly(acetylene)s (PAC), and poly(p-phenylene vinylene) (PPV). The nitrogen-containing group includes poly(pyrrole)s (PPY), polycarbazoles, polyindoles, and polyanilines (PANI). The sulfur-containing group is made up of

poly(thiophene)s (PT), poly(p-phenylene sulfide) (PPS), and poly(3,4-ethylenedioxythiophene) (PEDOT). Perhaps the most widely used conductive polymer is the last listed material, namely PEDOT.

3.4.1 PEDOT:PSS – Conductive Polymer

Poly(3,4-ethylenedioxythiophene) or PEDOT, or sometimes even PEDT, is a conducting polymer based on 3,4-ethylenedioxythiophene monomer. Advantages of this blue polymer include optical transparency in its conducting state, high stability, electrochromism, moderate band gap and low redox potential. As most other polymers, PEDOT itself is an insoluble material. However, when it is synthesized in the presence of poly(4-styrenesulfonate) (PSS), it can form an aqueous dispersion that can later be cast into thin films (Nardes, 2007; Nardes, et al., 2008). Therefore most materials presented in the literature is PEDOT:PSS mixture even though it may be referred to as simply PEDOT. Figure 46 demonstrates a cartoon representation of a planar arrangement of the PEDOT:PSS mixture along with chemical structure of both PEDOT and PSS.

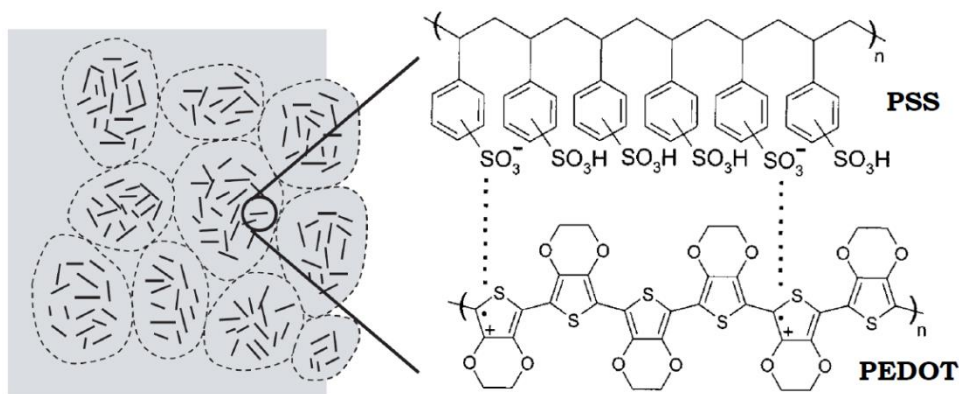


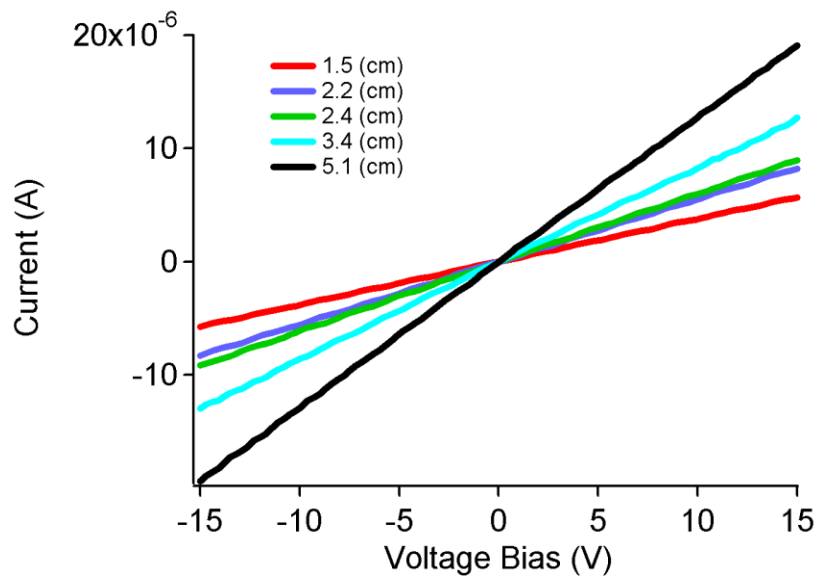
Figure 46. Cartoon representation of a planar morphology of thin film of PEDOT:PSS particles, surrounded by a thin PSS-rich surface layer (left) along with chemical structure of PSS (top right) and PEDOT (bottom right). (image reproduced from (de Kok et al., 2006)).

Different formulations of PEDOT:PSS can be commercially obtained, each with varying electrical conductivities, ranging from ultra-low conductive Clevios P VP CH 8000 ($5 \times 10^4 - 3 \times 10^5 \Omega\text{cm}$), to mid-grade conductivity P VP AI 4083 (500 - 5000 Ωcm), and high-conductivity PH 500 (300 S/cm). Inkjet formulation, such as Clevios P Jet HC (30 - 90 S/cm), synthesized to alleviate the issue of nozzle clogging, are also available (Clevios, 2013).

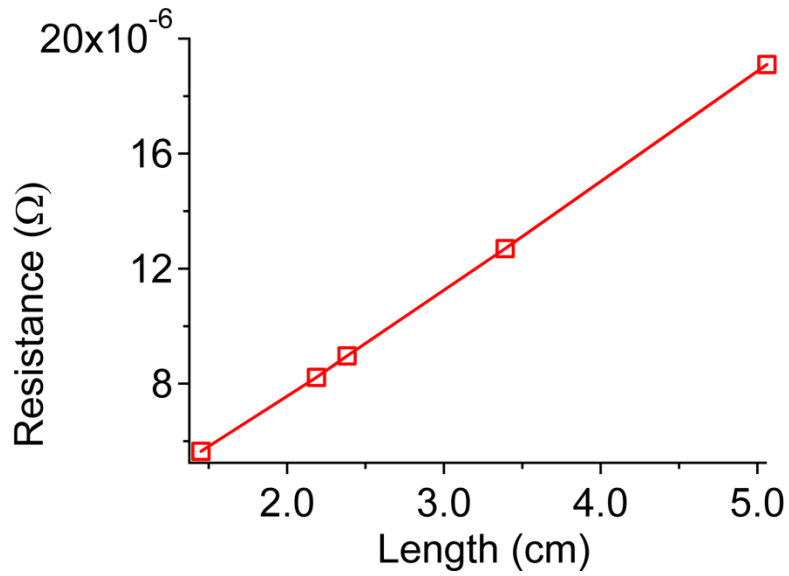
The conductivity of PEDOT:PSS can be further increased, sometimes by even three orders of magnitude, by a post-treatment with various compounds, such as ethylene glycol, dimethyl sulfoxide (DMSO), salts, sugars, zwitterions, cosolvents, and acids (Nardes, et al., 2008; J. Ouyang, Chu, Chen, Xu, & Yang, 2005; Y. Xia & J. Ouyang, 2010; Y. Xia, Zhang, & Ouyang, 2010; Y. J. Xia & Ouyang, 2009; Y. J. Xia & J. Y. Ouyang, 2010).

3.4.2 PEDOT:PSS for Neuronal Resistors

The choice to use PEDOT:PSS as the conductive polymer in polymer resistor was not solely driven by the ease of processing but also by the constraint of the fabrication of an entire polymer neuron on a single substrate. Because PEDOT:PSS was already used in the fabrication of a synthetic synapse, the choice for the polymer resistor was obvious. Figure 47(a) indicates linear I - V relationship of a family of polymer resistors while Figure 47(b) demonstrates that the overall resistance increases linearly with increasing electrode separation.



(a)



(b)

Figure 47. (a) I - V characteristics curve of a family of polymer resistors based on PEDOT:PSS, an electrically conducting polymer. Five different resistors are demonstrated, created by varying the separation of metal electrodes. (b) Near-linear relation between resistance and the electrode separation.

At least two different resistor layouts can be conceived; planar and stacked. In a planar arrangement, Figure 48(a), both electrodes are deposited on a substrate with a conductive film deposited in between.

In this layout electrode separation can be from few micrometers to few millimeters with resistances in the range of 10^6 to $10^{12} \Omega$. In stacked or layered design, Figure 48(b), one of the electrodes is deposited on a substrate (bottom electrode, or BE) while the other is deposited on top of it (top electrode, or TE), with the conducting polymer separating the electrodes. A cross-bar arrangement, with two electrodes deposited at 90° angle with respect to one another, is perhaps the most common example. In this layout, electrode separation is due to the thickness of the conducting film and can vary from few to few hundred nanometers with resistances in the range of 10^1 to $10^4 \Omega$.

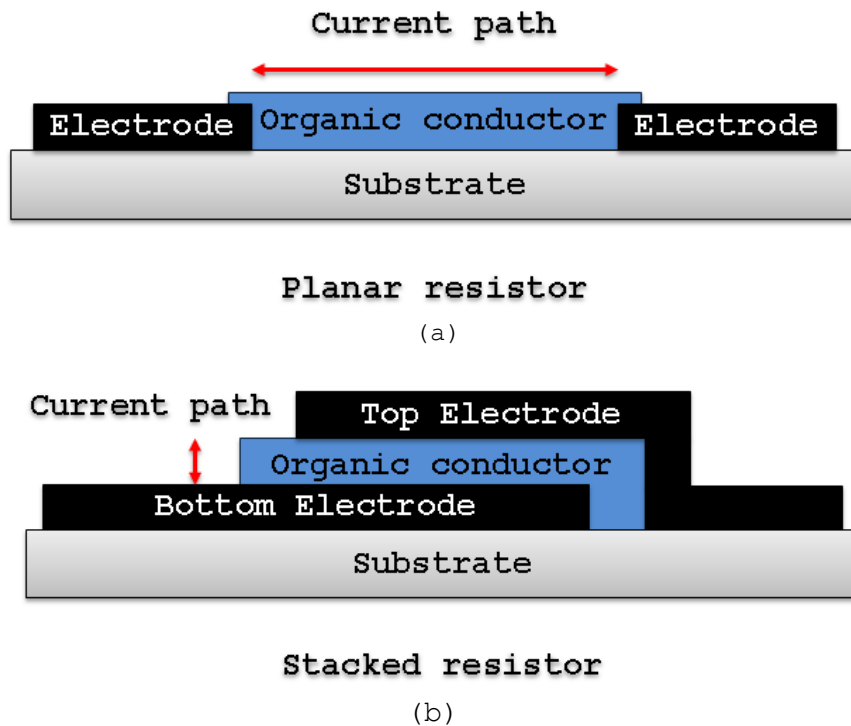
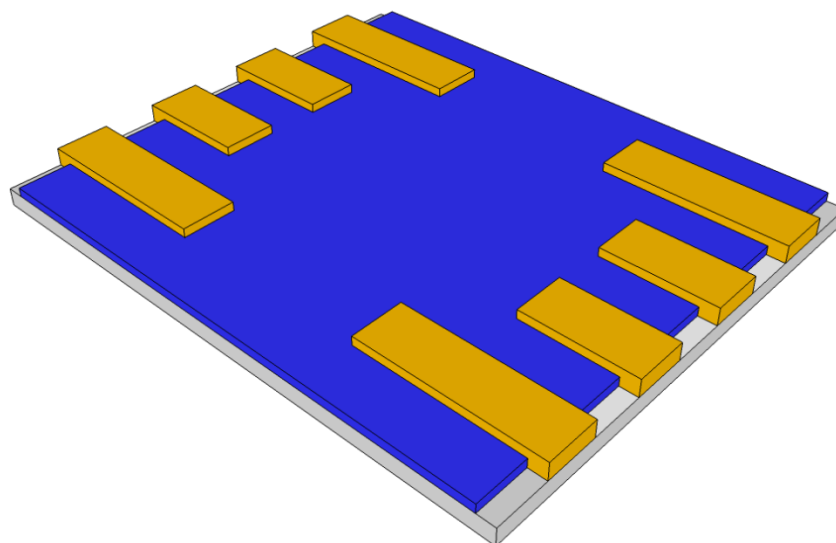


Figure 48. Two distinct polymer resistor layouts: (a) planar and (b) stacked.

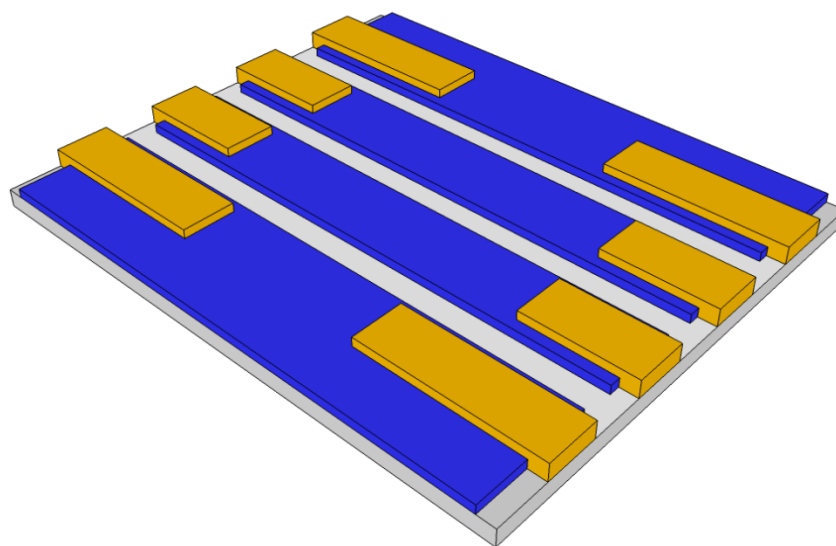
Polymer resistors, used in the neural circuit, were fabricated using either spin casting, blade casting or plotting techniques, with

spin casted devices used in circuit where all of the electrical elements were fabricated on separate chips (see separate-substrate section 4.1 *Separate Substrates Neuron*), while blade casting and plotting were used when the entire neuron was fabricated on a single chip (see common-substrate section 4.2 *Common Substrate Neuron*), with constraints being elaborated further in a subsequent chapter. The planar resistor layout, Figure 48(a), was used with metal lines deposited on a glass substrate using a standard photolithography with a well-defined electrode separation. Because both spin casting and blade casting cover the entirety of the substrate indiscriminately⁵, the individual resistors were obtained by selectively removing PEDOT:PSS film around the electrodes, to avoid the current flowing between “wrong” electrodes, as illustrated in Figure 49. However, during automation of the process, this step could be performed either by laser ablation, patterning, such as what was demonstrated in (Schaefer, Holtkamp, & Gillner, 2011), or direct printing or plotting. Figure 50(a) demonstrates R_{BASE} resistor, with two electrodes clearly visible, fabricated using blade casting process followed by manual removal of PEDOT:PSS film. Figure 50(b) depicts R_{BASE} resistor made with PEDOT:PSS film plotted using Sonoplot liquid dispenser (Sonoplot, 2013).

⁵ As it will be addressed in more details later, the blade casting procedure can be used to cover only a portion of a chip.

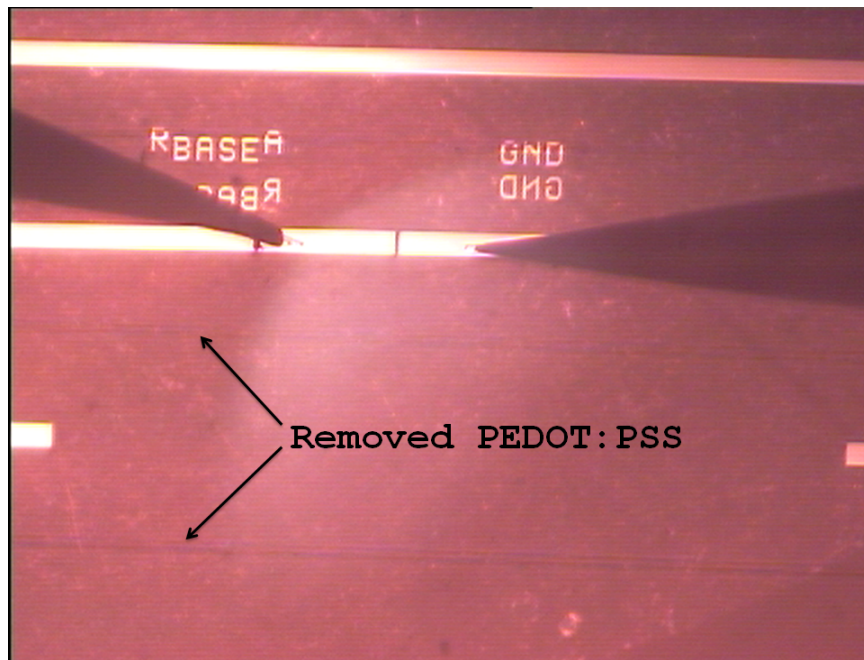


(a)

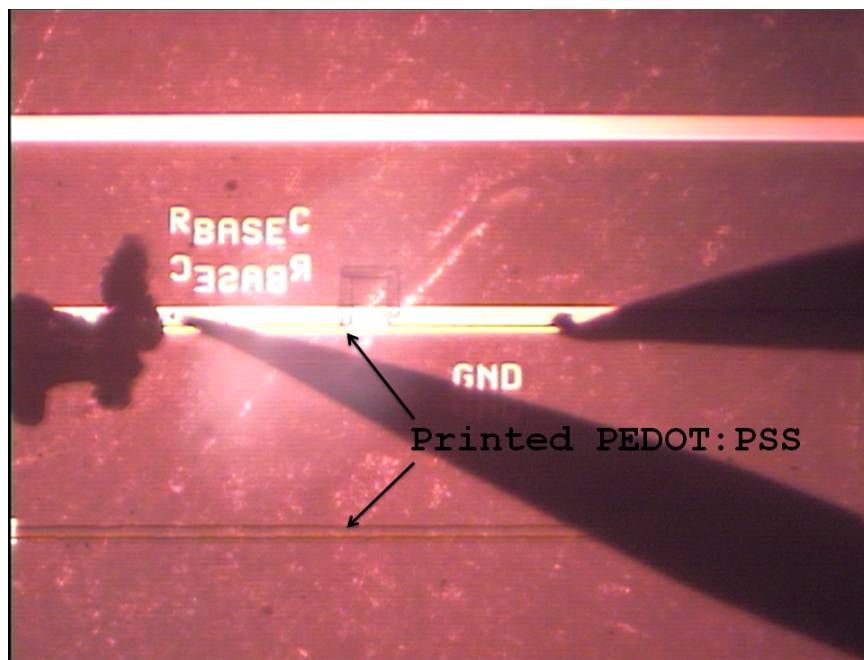


(b)

Figure 49. Because spin casting and blade casting indiscriminately cover the entirety of the substrate, individual resistors are obtained by isolating specific electrodes by manual removal of PEDOT:PSS.



(a)



(b)

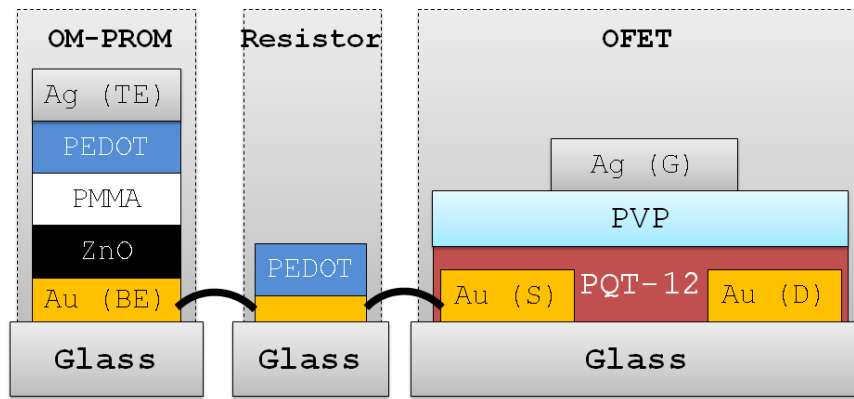
Figure 50. Polymer resistors, with PEDOT:PSS used as conductive polymer material, deposited using; (a) blade casting, and (b) plotting process.

Chapter 4: PNC Fabrication

From a processing standpoint, there are two possibilities of fabricating a circuit that incorporates disparate components, such as OM-PROMs and OFETs, on the same substrate (Apte, Bottoms, Chen, & Scalise, 2011; Senturia, 2001). The easier of the two alternatives centers on creating all of the devices on separate substrates and then connecting them externally. The main advantage of this approach is the ease of manufacturing of individual components. However, the price paid is the need to connect individual elements on the disparate chips, which can be prohibitively complex for circuitry that requires a large number of devices (connections). This "separate substrates" approach is depicted in Figure 51(a) and is discussed in the next section.

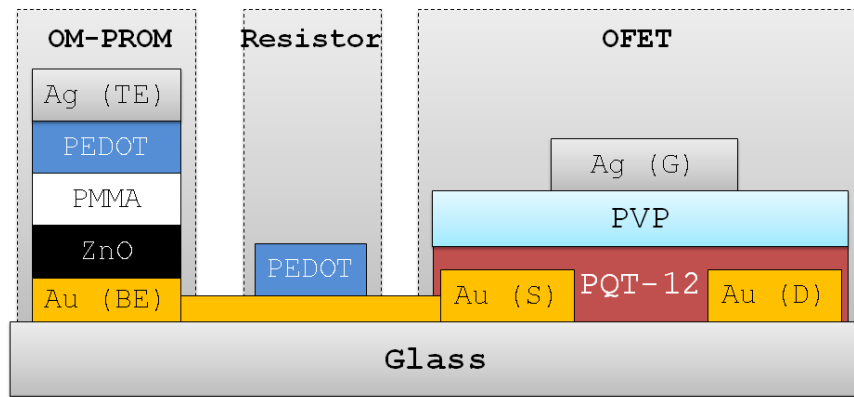
In an alternative method all of the dissimilar elements are made on the same chip. In this methodology, there is no need for external inter-element connections. However, the drawback stems from the exponential increase in fabricating complexity with the number of disparate elements made. The "common substrate" approach is depicted in Figure 51(b) and is discussed in the subsequent section.

Separate Substrates



(a)

Common Substrate



(b)

Figure 51. Two alternative fabrication approaches needed to fabricate an entire polymer neuron made from different electrical devices: (a) "separate substrates" where all of the devices are fabricated on separate substrates and are subsequently connected according to the circuit diagram, and (b) "common substrate" with all of the devices fabricated on a common substrate with the inter-element wiring fabricated on the chip.

4.1 Separate Substrates Neuron

There is a wealth of knowledge in processing of inorganic electronics stemming from many decades of experience about materials and chemicals required for multi-layered manufacturing. In contrast,

organic electronics is a much younger field with less extensive database of production and integration processes (So, 2010). Therefore, in the first attempt to build a synthetic neuron, all of the polymer components, namely the memristive devices, the transistors, and the resistors, were fabricated on separate chips and were later connected manually to reflect the neuronal architecture presented in Figure 1.

4.1.1 Spin Coating

Spin coating is one of the oldest processing techniques used in microfabrication of electronics elements. The process involves deposition of a small quantity of liquid material, typically at the center of a substrate, and then spinning the substrate at high speeds, normally in the range of 600 - 6000 rpm. The centripetal force will cause the liquid to spread out, leaving a thin and ultra-uniform film throughout the entirety of the substrate. After the film deposition, the sample is usually placed on a hot plate to evaporate the solvent but also to aid in molecular alignment of the molecules. The final film thickness largely depends on the spin speed as well as the viscosity of the liquid. Thicknesses ranging from few nanometers to tens of micrometers can be achieved. Figure 11(a) shows an example of a typical spin coater.

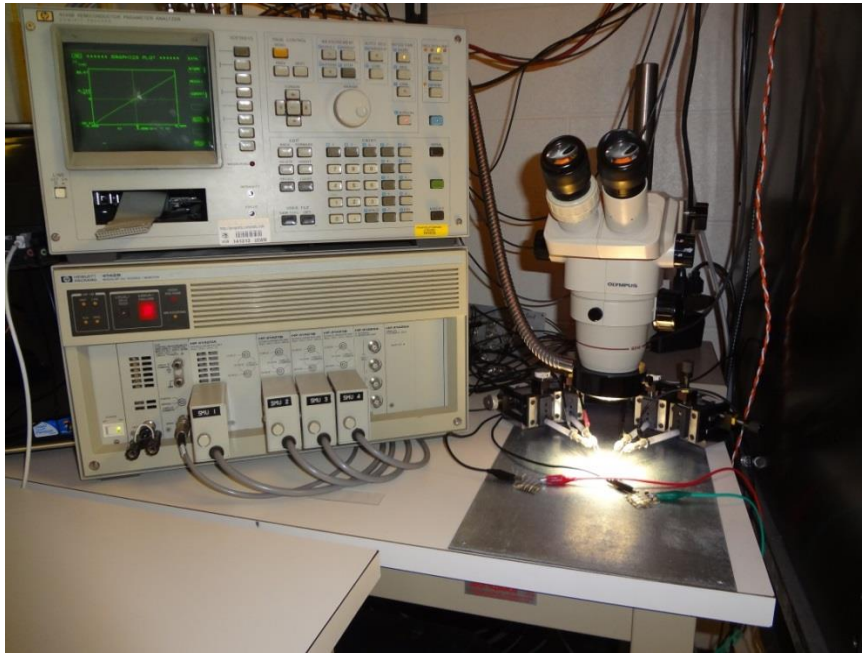
Organic electronics devices are primarily characterized by their layered layout, as demonstrated in Figure 51. As such, individual layers are deposited, for instance via spin coating, sequentially. Therefore special care must be taken to ensure that adjacent materials require different solvent, otherwise deposition of the next material will dissolve the previously deposited film. This concept, known as

orthogonal solvents, is one of the major stumbling blocks in multimaterial fabrication of organic electronics (see section 3.3.2.1 *Device Configuration, Materials, and Procedures*).

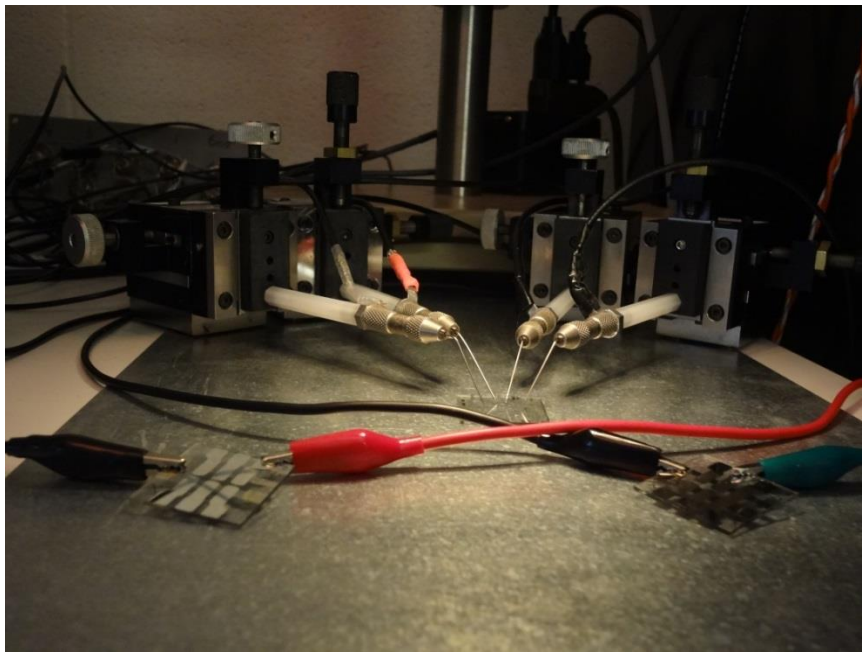
4.1.2 Fabrication

At the commercial level, the separate-substrate fabrication is followed by the assembly of the individual components, or chips, on a common substrate, oftentimes with individual chips glued on top of other chips, with external wiring connecting individual chips. Such an approach, however, can be very time consuming, costly, and introduce new sources of fabrication failure. Therefore, in this study, the approach pursued concentrated on fabricating individual elements on separate chips, which were subsequently manually connected using external wiring.

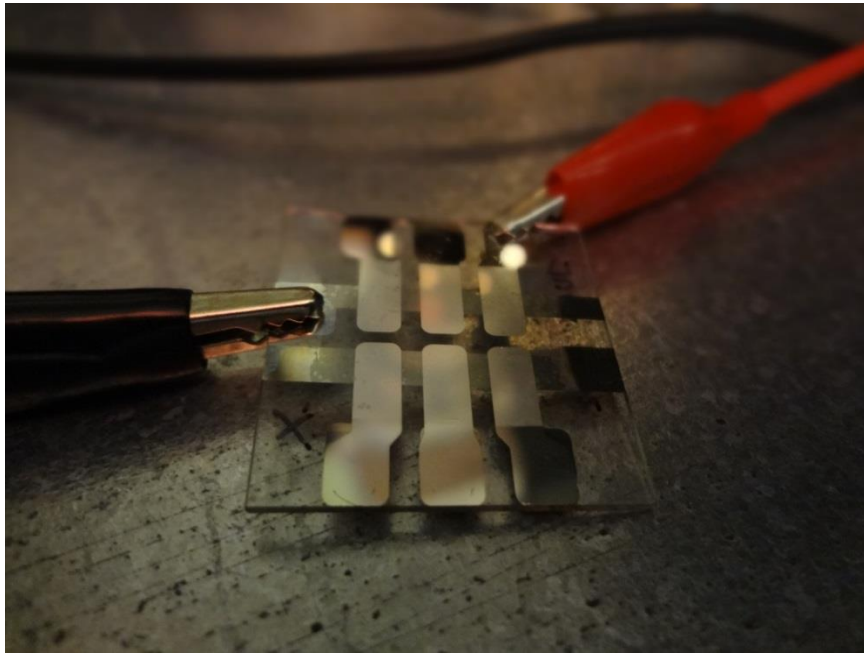
Figure 52 illustrates the setup based on separate substrates approach used to fabricate the polymer neuron. Figure 52(a) shows a large view of the setup with the memristive devices and resistors clearly visible, along with a microscope and a network analyzer. Figure 52(b) shows a zoomed view of the two memristive devices along with micromanipulators used to connect to the resistor chip, while individual substrates with memristive device, resistors, and transistors, are shown in Figure 52(c), Figure 52(d), and Figure 52(e) respectively. Figure 52(f) illustrates a zoomed view of an individual organic transistor, seen through a microscope-mounted camera, displayed on an overhead monitor.



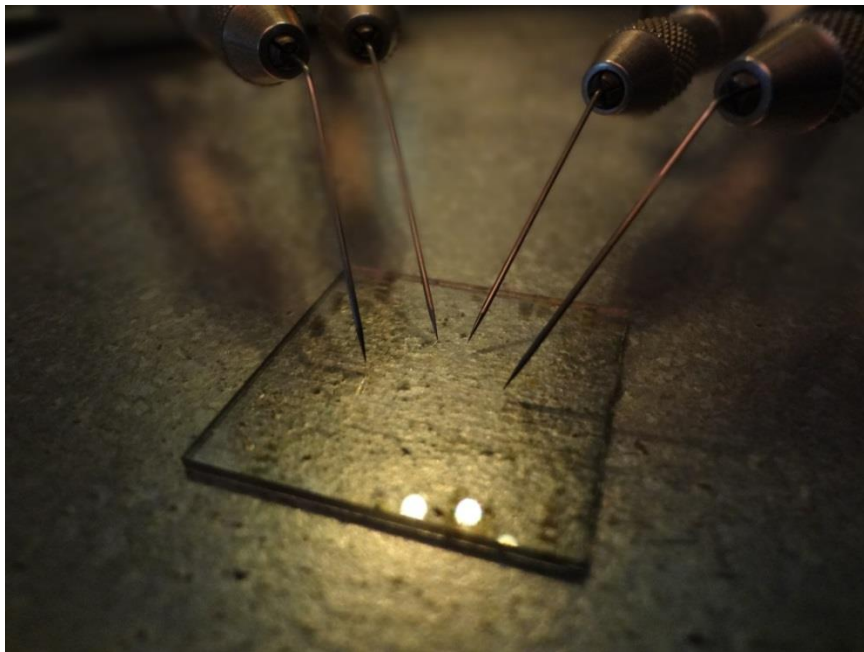
(a)



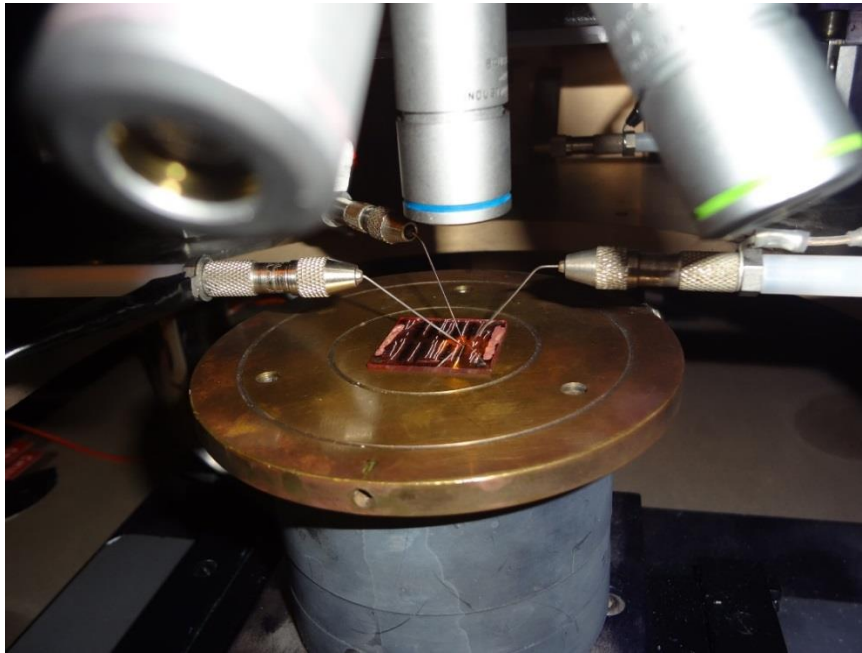
(b)



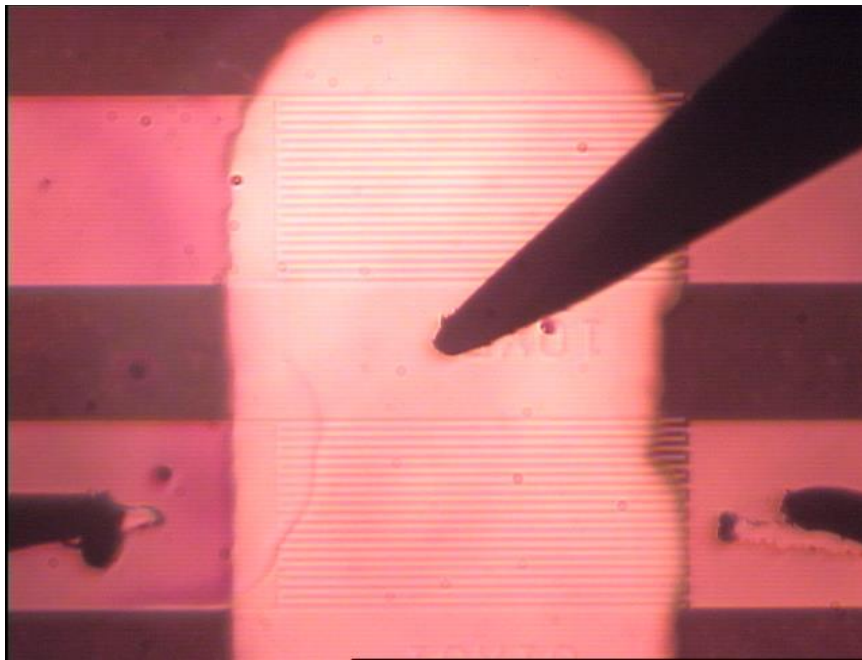
(c)



(d)



(e)



(f)

Figure 52. Polymer neuron fabricated using separate-substrate approach. (a) A large view of the setup with the memristive devices and resistors clearly visible, along with a microscope and a network analyzer; (b) a zoomed view of two memristive devices along with micromanipulators used to connect to the resistor chip; (c) individual substrate with a 2 x 3 array of

organic memristive devices (OM-PROMs); (d) individual substrate with PEDOT:PSS-based organic resistors; (e) individual substrate with organic transistors; (f) a zoomed view of an individual organic transistor, seen through a microscope-mounted camera, displayed on an overhead monitor.

In the separate-substrates technique, all of the organic materials or the devices, namely memristive devices, resistors, and transistors, were fabricated using spin coating technique. The metal contact electrodes were fabricated using a standard thermal evaporation process using either shadow mask, for features larger than one millimeter (i.e. OFET's gate electrodes), or photolithography, for features smaller than 100 micrometers (i.e. OFET's source and drain electrodes). Figure 7 demonstrates the activation function of a single neuron fabricated using the separate substrates approach. The details of individual elements' fabrication are discussed in sections 3.2.5 *OM-PROM For Synthetic Synapse*, 3.3.2 *OFET For Synthetic Soma* and 3.4.2 *PEDOT:PSS for Neuronal Resistors*, while the effectiveness of this separate-substrate neuron is illustrated in the next chapter, in section 5.1 *Single Neuron Classification*.

4.2 Common Substrate Neuron

The separate-substrates approach to fabricate an individual neuron is only feasible for small-scale, testing purposes. However, development of a fully functioning, large-scale neuromorphic circuitry would require an alternative approach, such as the aforementioned common-substrate methodology. Constrained by the need to fabricate three disparate electrical elements, each one based on different organic or polymeric films, I have decided to investigate the ability

to fabricate individual organic electronics elements using a blade coating technique.

Perhaps two main advantages of spin coating are its low cost and ease of fabrication. However, spin coating indiscriminately covers the entirety of the substrate. Therefore, when attempting to fabricate disparate electrical components, made from different chemical solutions, on the same substrate, alternative means of coating needed to be investigated.

4.2.1 Blade Coating

Blade coating, often referred to as blade casting, doctor blading coating, or tape casting, is one of the widely used techniques for producing thin and uniform films on large area surfaces (Berni, Mennig, & Schmidt, 2004). This casting process was originally developed in the 1940's for depositing thin sheets of piezoelectric materials and capacitors (Howatt, Breckenridge, & Brownlow, 1947). In this technique, a liquid is deposited on a substrate, either from a reservoir or from a liquid dispenser, such as a pipette, followed by a relative blade movement with respect to the substrate. The thickness of the film is controlled by the height of the blade, the relative speed of the blade, as well as the viscosity of the solution. Blade coating has been demonstrated to fabricate various organic electronics elements, including OPVs (F. Padinger, C. J. Brabec, T. Fromherz, J. C. Hummelen, & N. S. Sariciftci, 2000), OLEDs (Kopola, Tuomikoski, Suhonen, & Maaninen, 2009), OFETs (Manuelli, Knobloch, Berndt, & Clemens, 2002) and OM-PROMs (R. A. Nawrocki, et al., 2013).

Two types of designs can be conceived. In the first possibility, the substrate is stationary while the blade moves, as shown in Figure 53. While this approach typically allows for samples below one meter in length, the film uniformity as well as its morphology is typically much better. In the alternative design, the blade is fixed while the substrate is being pulled, or rolled. Because the substrate can come from a roll, this approach benefits from the enormity of the possible device area (as illustrated in Figure 13). However, the price paid is in a lesser uniformity of the deposited film due to the physical motion of the substrate.

Figure 54 illustrates an example of a laboratory-scale blade coater with stationary substrate and freestanding blade being pushed by an arm attached to a motor.

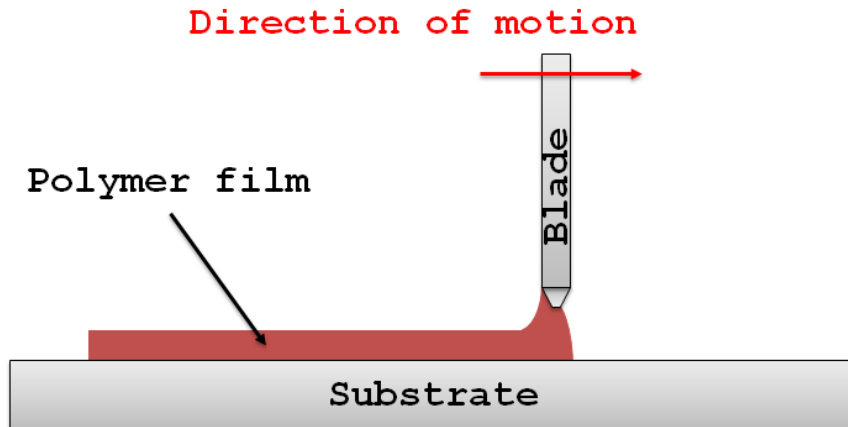


Figure 53. Diagram of blade coating technique with stationary substrate and moveable blade.

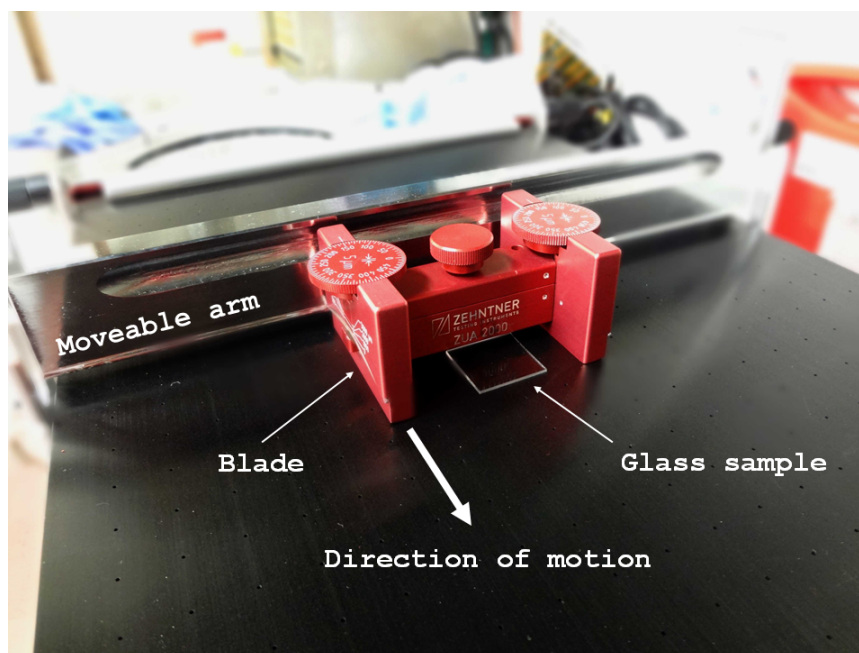
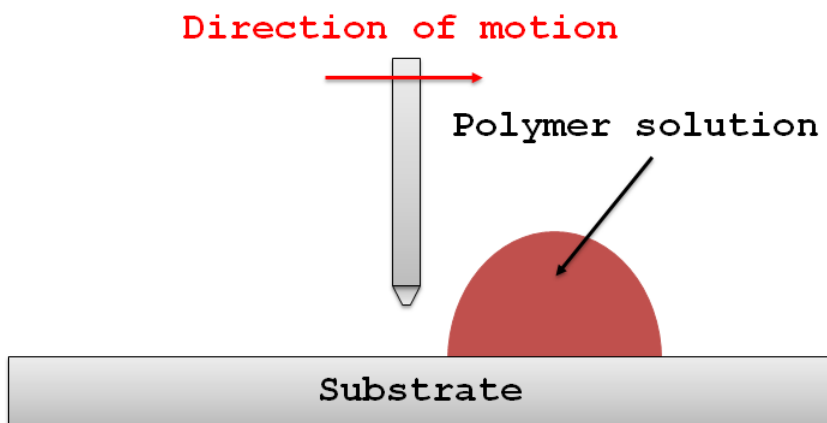


Figure 54. Laboratory-scale blade coater with stationary substrate and moveable blade. The metal substrate, that the sample is placed atop, can be heated, allowing for better film morphology.

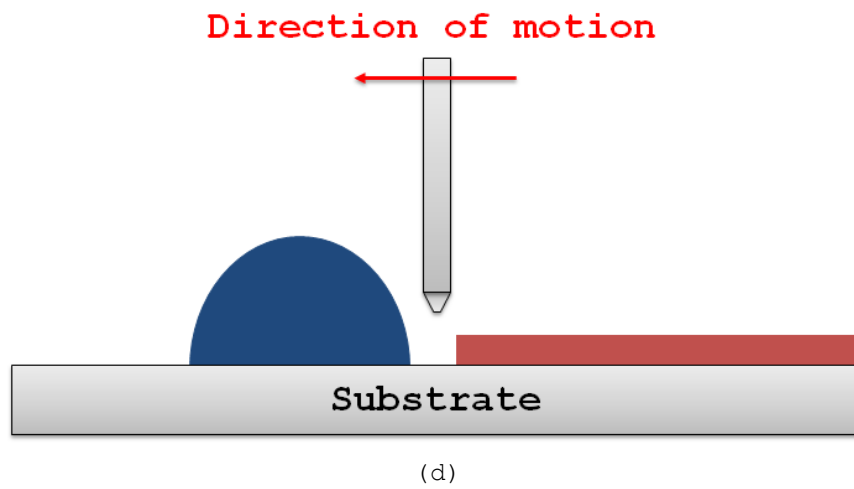
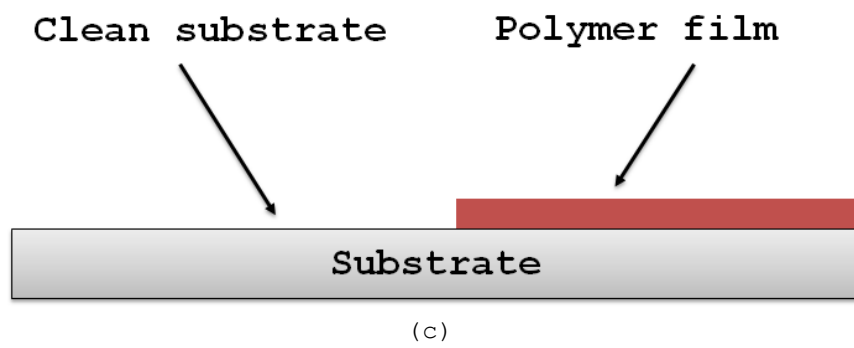
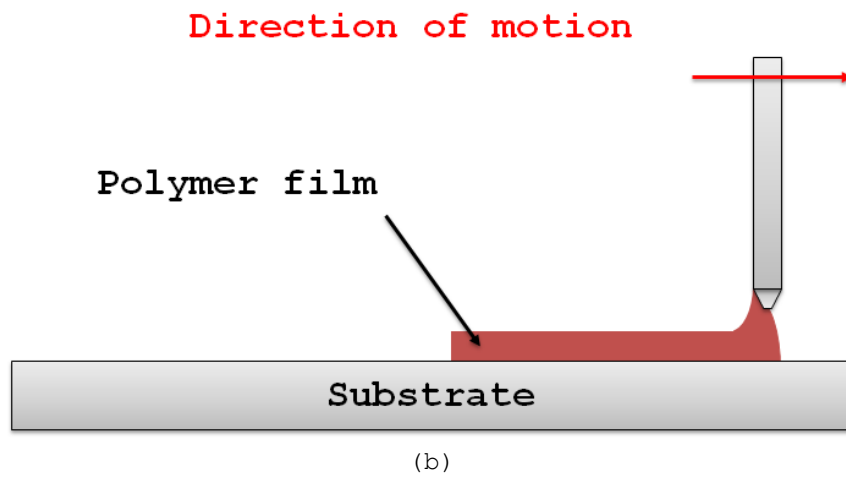
Blade coating technique holds many advantages over standard spin coating technique. One such advantage is the ability to coat large surfaces; the substrate dimensions are primarily limited by the width of the blade, for instance 2 meters, as the length of the substrate is limited by the length of the roll (for instance few hundred meters).

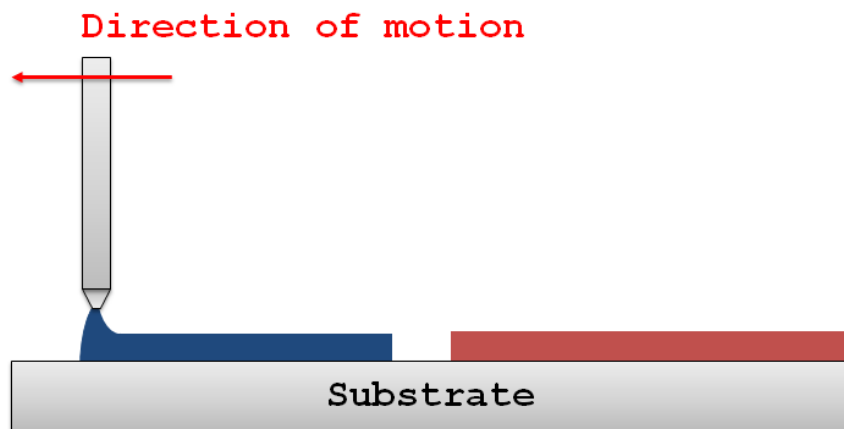
Another advantage of blade coating is the ability to control the substrate temperature. The electrical properties of organic electronics films are influenced by the film morphology, the three-dimensional arrangement of the molecules, of the polymeric film. The substrate temperature, during film deposition, can have an effect on the film as well as the surface morphology (surface roughness) of the resulting polymeric thin film.

Finally, as already stated, spin coating covers the entirety of the substrate that a solution is deposited on. In contrast, blade coating allows for only a partial coverage of a substrate; positioning a blade in the middle of a substrate will result in coverage of only a half of that substrate, leaving the other half clean for the deposition of other polymeric solutions, as illustrated in Figure 55. Figure 56 shows an example of two films, PQT-12 (dark red, left side of substrate) and octafluoro zinc phthalocyanine (F8ZnPc, light green, right side of substrate) (Kuhnle, 2009), bladed on the same substrate, with the substrate rotated approximately 45° in order to more acutely demonstrate the concept. The overlap region shows a partial removal of PQT-12, deposited first, by the subsequent application of P8ZnPc due to the improper choice of non-orthogonal solvents (both materials were dissolved in chlorobenzene).

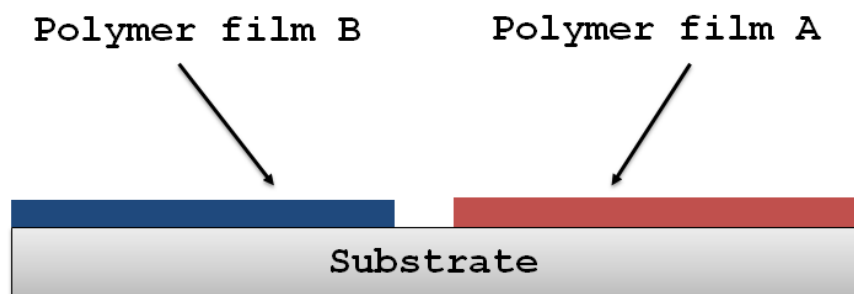


(a)





(e)



(f)

Figure 55. An advantage of blade coating demonstrated by the ability to cover a portion of a substrate leaving clean portions for the deposition of another type of polymeric film.

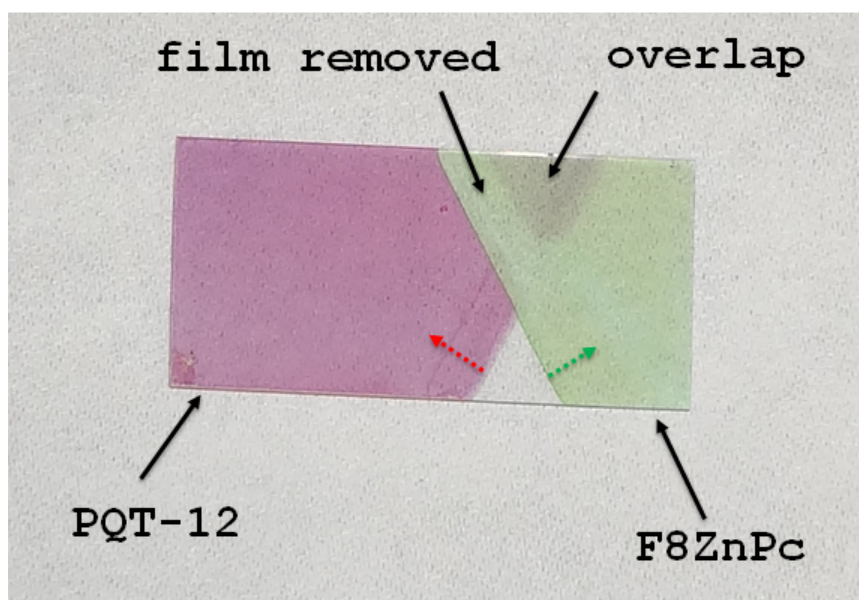
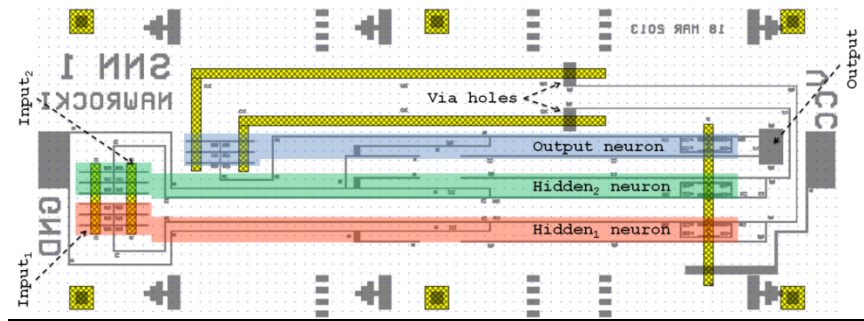


Figure 56. An example of two films bladed on the same substrate, with dashed arrows indicating the direction of blade movement. The overlap indicates a removal of previously applied film due to improperly chosen non-orthogonal solvents.

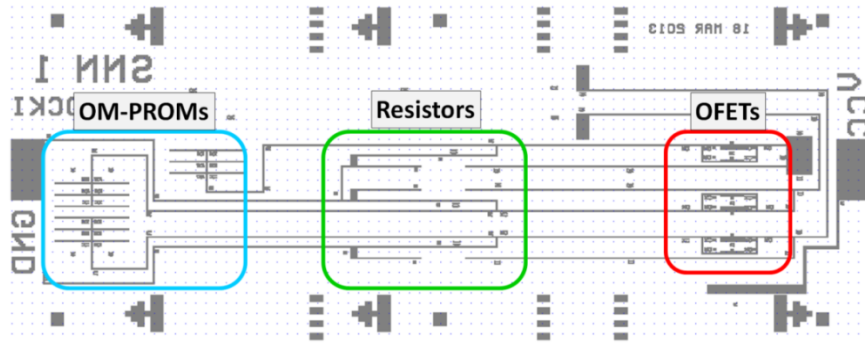
4.2.2 Fabrication

The neural circuitry of Polymer Neuromorphic Circuitry requires three separate electrical elements; memristive devices, transistors, and resistors. As demonstrated in sections 3.2.5 *OM-PROM For Synthetic Synapse* and 3.3.2 *OFET For Synthetic Soma*, memristive devices and transistors are fabricated using different materials. However, OM-PROM utilizes conductive polymer PEDOT:PSS that could be used in fabricating of an organic resistor (3.4 *Organic Resistor*). Such redundancy would greatly simplify the common-substrate fabrication process requiring only two-separate film deposition regions, one for transistors and one for memristive devices, with third (middle) region reserved for the resistors. Figure 51 demonstrates the possible fabrication outline with individual materials shown.

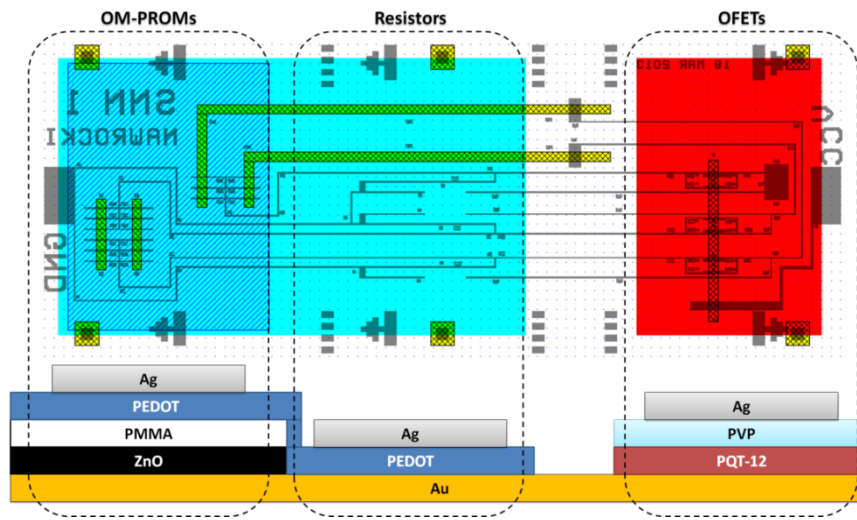
Figure 57 depicts a common-substrate PNC configuration of a network of three neurons, benefitting from the PEDOT:PSS redundancy, with three distinct regions shown from left to right: OM-PROMs, Resistors, and OFETs. Figure 57(a) shows a Bottom Electrode (BE) and Top Electrode (TE) designs. The BE (gray in the figure), common to all of the elements, as well as serving as connections between individual components, is obtained through a photolithographic process as outlined in section 3.3.2 *OFET For Synthetic Soma*. The TE, used for individual elements as well as connections between individual neurons, known as via holes (described in more details next), was obtained from thermally evaporated metal through a shadow mask. Figure 57(b) shows only the BE design indicating individual regions occupied by OM-PROMs, resistors, and OFETs, while Figure 57(c) depicts both the BE and the TE design indicating areas covered by individual polymeric films, such as common PEDOT:PSS, along with device configurations of all of the electrical elements aligned with their respective regions.



(a)



(b)



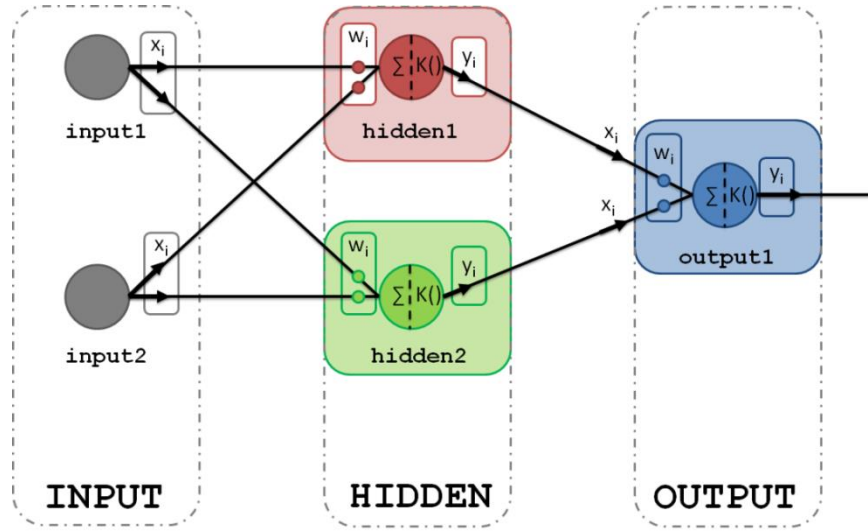
(c)

Figure 57. Common-substrate PNC configuration with three distinct regions shown from left to right: OM-PROMs, Resistors, and OFETs. (a) Design for Bottom Electrode (BE - gray), obtained through photolithographic process, and Top Electrode (TE - yellow and black chequered), obtained from thermal evaporation of metal through a shadow mask. The PNC design features three-neuron network (individual neurons are color-coded with network design shown in Figure 58), with inputs, output, and three individual neurons shown. Via holes are used to send the (electrical) signal from the output of hidden neurons (BE of OFET) to the inputs of the output neuron (TE of OM-PROMs). (b) BE design indicating individual regions occupied by OM-PROMs, resistors, and OFETs. (c) BE and TE design indicating areas covered by individual polymeric films, such as PEDOT:PSS covering both the OM-PROM and resistor regions, along with device configurations of all of the electrical elements aligned with their respective regions.

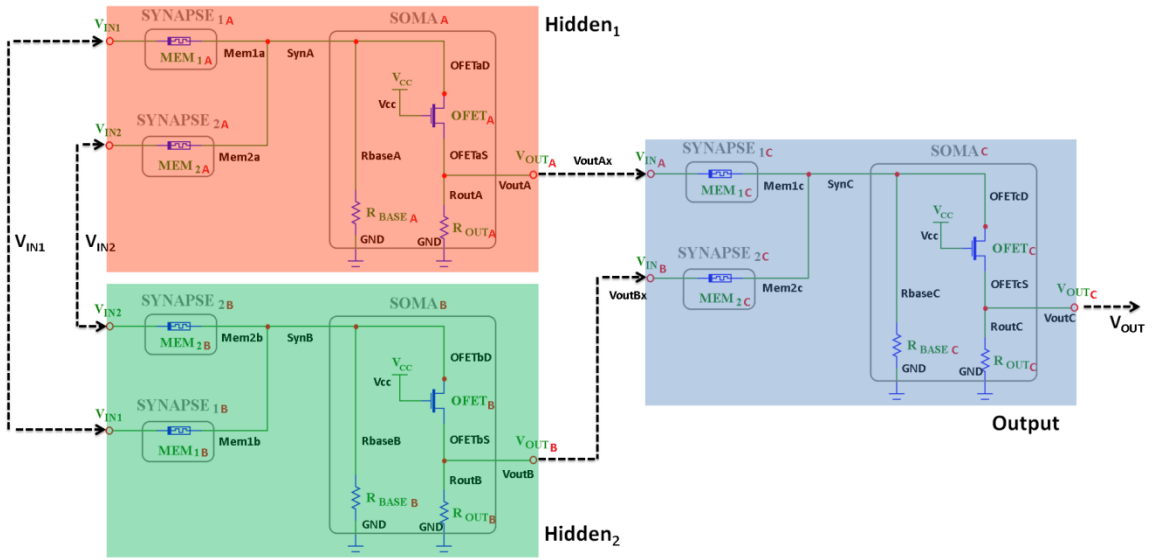
A neural network typically requires three types of cells; input cells, hidden cells, and output cells (Haykin, 1998). Output cells

provide output signal and thus can often be connected to external actuators. Hidden cells, along with output cells, are responsible for computing the pattern classification that the network is trained to recognize. Input cells are used to relay the information between the outside world and the neural network. As such, the input cells are purely conceptual and, in a hardware implementation, are implemented with wires or connectors.

The PNC design, shown in Figure 57, features three distinct neurons connected according to the neural configuration presented in Figure 58(a). Figure 58(b) illustrates a circuit diagram of a three-neuron network, with individual neurons connected according to the circuit design shown in Figure 1. Individual neurons, *Hidden₁* (red), *Hidden₂* (green), and *Output* (blue), are color-coded. Figure 58(c) shows PNC design of the three-neuron network, with inputs, output, and three individual neurons clearly marked by the colored boxes used in Figure 58(b). Via holes are used to send the signal from the output of individual hidden neurons (BEs of individual OFETs) to the inputs of the output neuron (TEs of individual OM-PROMs).



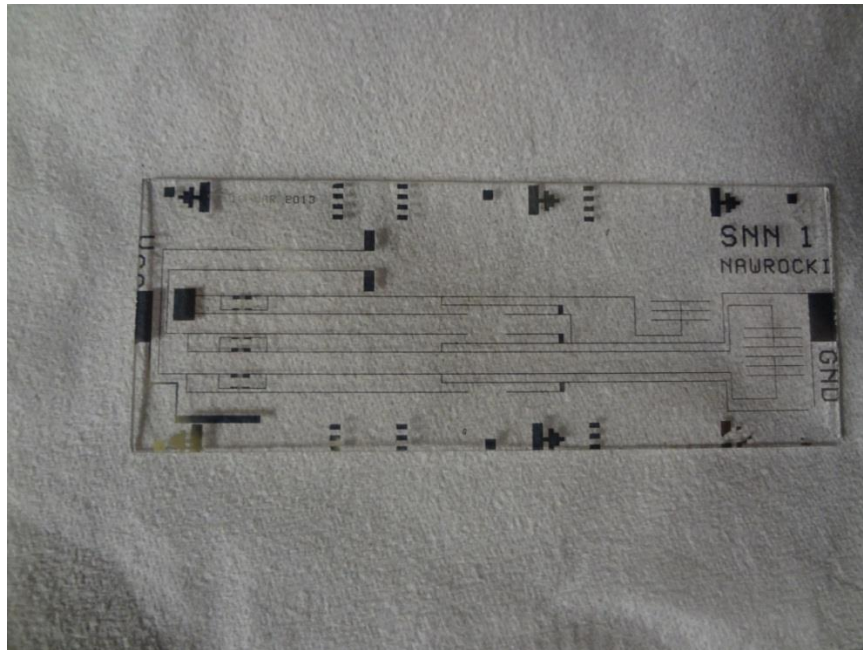
(a)



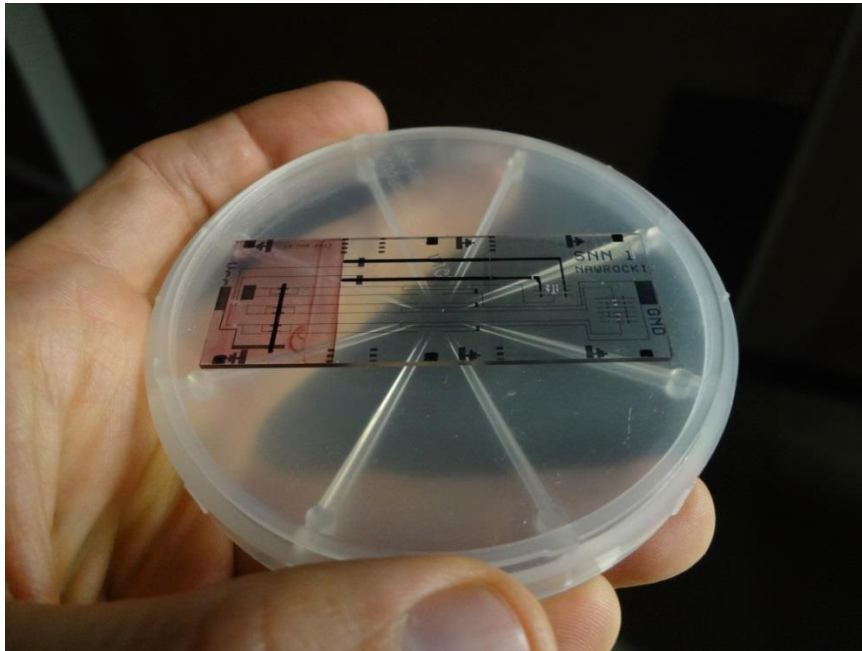
(b)

Figure 58. Three-layered neural network implemented in the PNC design shown in Figure 57, with individual neurons color-coded: red, indicating hidden neuron 1; green, indicating hidden neuron 2; and blue, indicating a single output neuron. (a) Conceptual design of the neural network indicating three distinct neural "layers": input, hidden, and output. (b) Circuit diagram of the neural network, shown in Figure 57, based on the individual neural design shown in Figure 1, with three separate color-coded neurons shown.

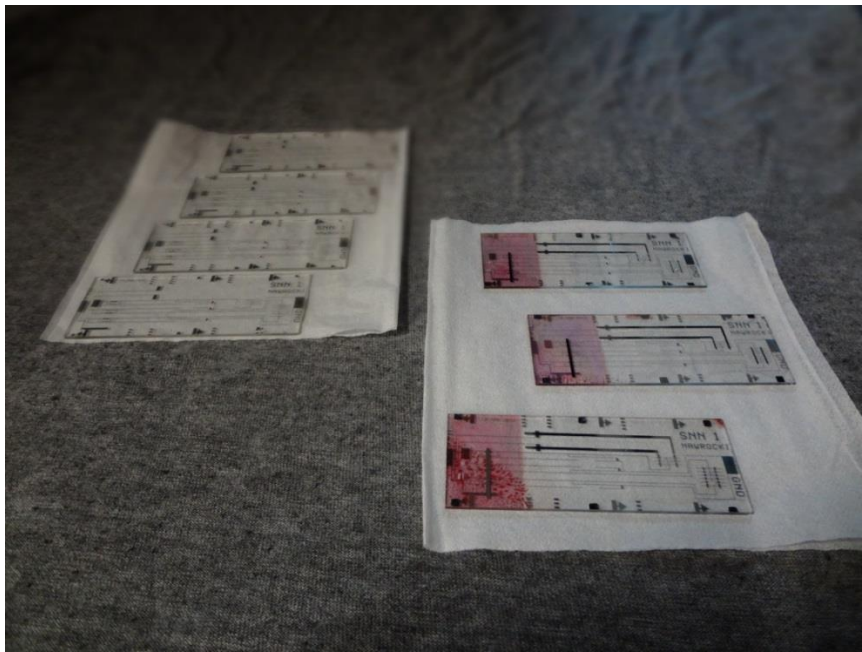
Figure 59(a) displays a picture of a 3" x 1" glass substrate, with BE configuration of Polymer Neuromorphic Circuitry fabricated according to the arrangement presented in Figure 58, while Figure 59(b) shows a chip with a fully functioning network of polymer neurons. Three areas dedicated to individual electrical elements can be seen, with the left-most area (red, due to the organic semiconductor PQT-12) occupied by transistors, the right-most area dedicated to memristive devices, and resistors fabricated in middle area (lightly blue, from PEDOT:PSS). A clear strip, located directly adjacent to the transistor area, is deliberately left free of polymeric films to allow for the via holes. The four dots located at the top of the chip, also matched by three dots located on the bottom of the chip, are used for the manual alignment of the blade during film deposition.



(a)



(b)



(c)

Figure 59. Pictures of a glass substrates with Polymer Neuromorphic Circuitry fabricated based on a common-substrate paradigm, the first demonstration of neuromorphic circuit fabricated with organic electronics element. (a) Cr/Ag/Au BE on glass. (b) A single PNC chip inside a circular container. (c) An array of glass chips with only BE (left) and fully-functioning

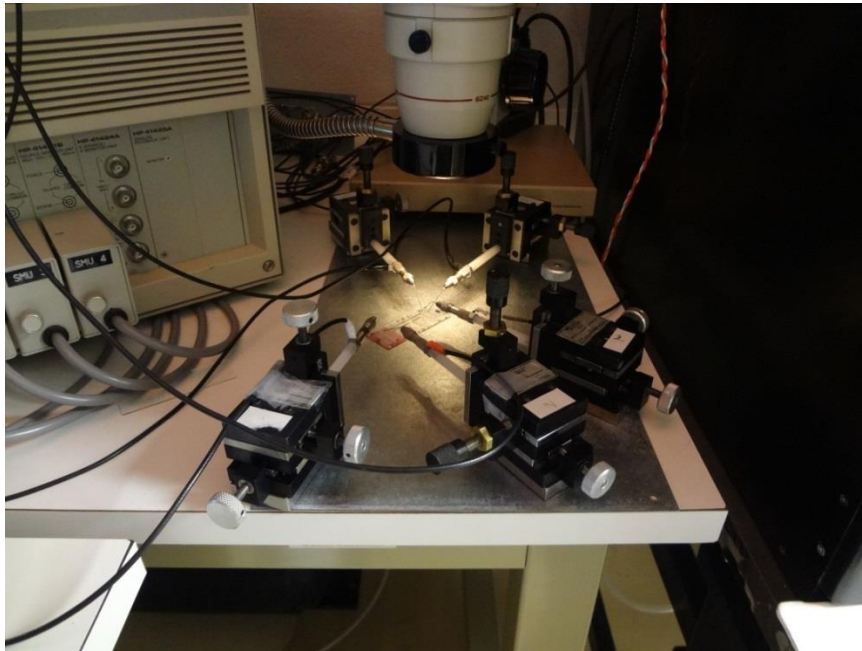
PNC chips (right). A red-colored glass substrate, OFET area, is clearly seen on the left side of the chip. Immediately to the right of the red-covered area, there is a clear area, about 5 mm in width, used for the via-holes, with no polymeric materials deposited.

The sequence of the film deposition of the individual organic materials had to be design in such a fashion as to adhere to their specific individual requirements. The process commenced with fabricating the bottom electrodes through the photolithographic process. Because the zinc oxide film is obtained from high-temperature annealing of zinc acetate solution, this layer was deposited first. Since the carrier mobility of the organic transistor is greatly affected by the imperfections and impurities of the source-drain electrodes, the semiconducting PQT-12 film was deposited next, with thermal annealing at 145 °C in a stream of N₂, with a slow cool-down procedure. The insulating PVP was subsequently deposited on top of the PQT-12 film followed by annealing at 105 °C, which is below the crystalline transition temperature of the PQT-12 (see 3.3.2 *OFET For Synthetic Soma* section for explanation). Next, a layer of PMMA was deposited over the OM-PROM specific area, followed by thermal annealing at 105 °C. PEDOT:PSS was bladed on both, the resistor and memristive devices area (for devices with plotted polymer resistors, PEDOT:PSS was only bladed across the OM-PROM specific region), followed by thermal annealing at 105 °C in a stream of N₂ (the importance of annealing PEDOT:PSS in oxygen-free atmosphere is discussed in section 3.2.5 *OM-PROM For Synthetic Synapse*). Finally, the top electrodes for OFETs and OM-PROMs were obtained from thermally evaporated silver through a shadow mask that was manually aligned using the six alignment markers located at the periphery of the design. Prior to the device

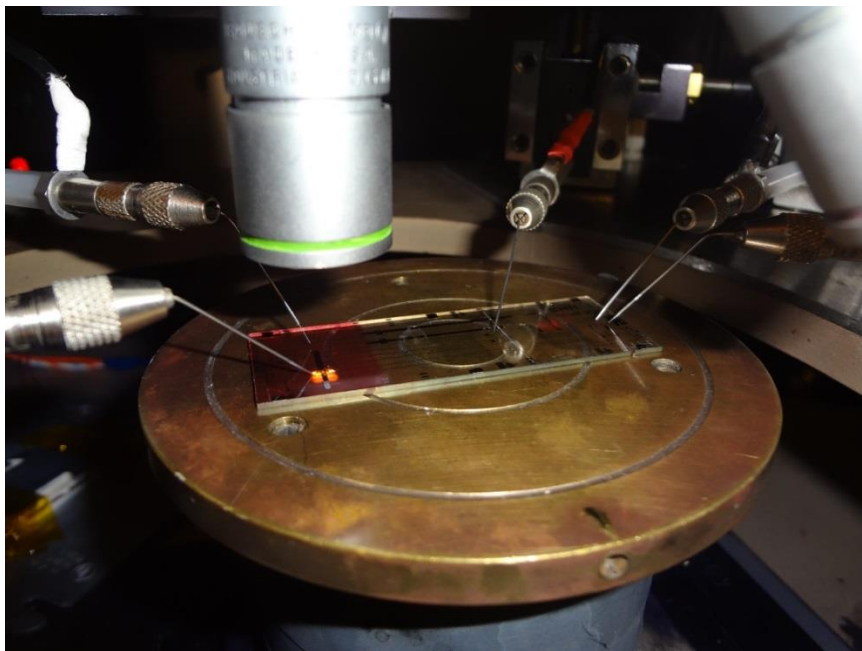
characterization, individual resistors were obtained by manual patterning of the PEDOT:PSS film by selective removal of the film to define individual resistor areas, as outlined in section 3.4.2 *PEDOT:PSS for Neuronal Resistors*.

The film deposition alignment markers, the shadow mask alignment markers, and a step-by-step fabrication process, including the photolithographic step, the polymeric solutions steps, and the thermal evaporation step, are all illustrated in details in *Appendix C: Manufacturing Process*.

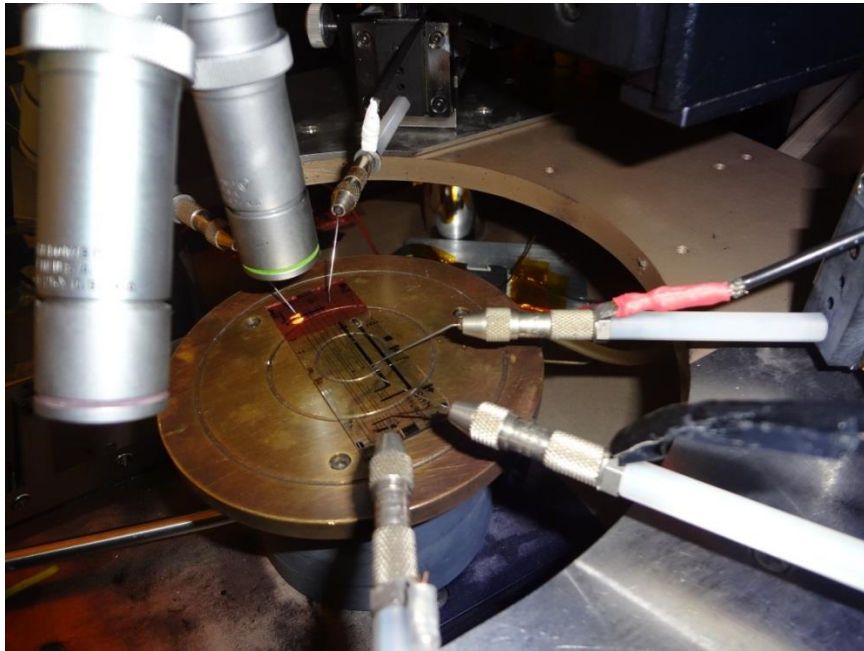
Figure 60 presents the laboratory setup used to characterize the Polymer Neuromorphic Circuitry fabricated on a single, glass substrate. The glass chip is seen inside a black box housing a probe station. Five individual micromanipulators are used to provide for five necessary connections required to provide two circuit inputs and a single output, the power to transistors' gate electrode, as well as the ground: *Input₁*, *Input₂*, *Output*, OFET's V_G , and *Ground* connections. Figure 8 demonstrates the activation function of a single neuron obtained using the common substrate approach, while the functionality and the effectiveness of this common-substrate neuromorphic circuitry is illustrated in the next chapter, in section 5.2 *Network of Neurons Classification*.



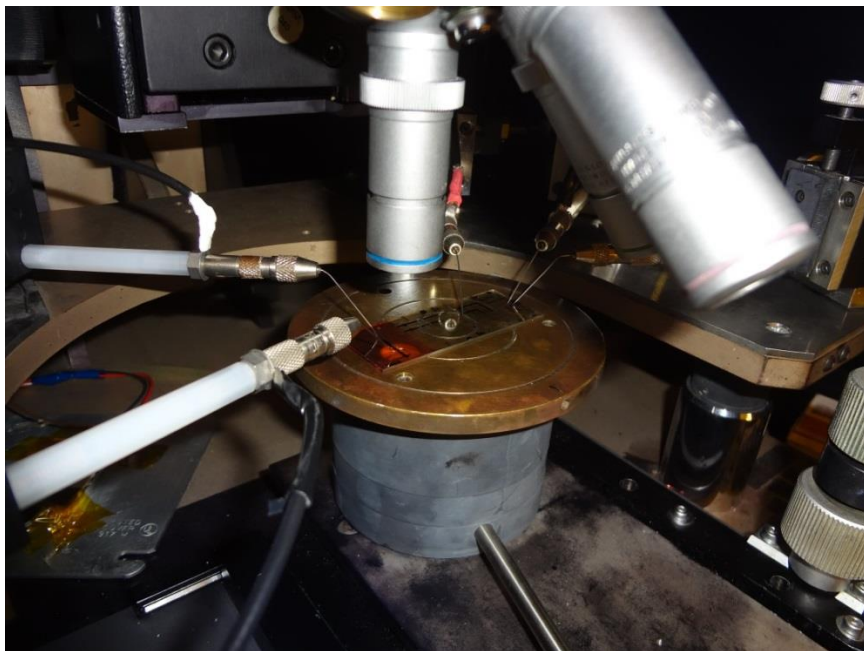
(a)



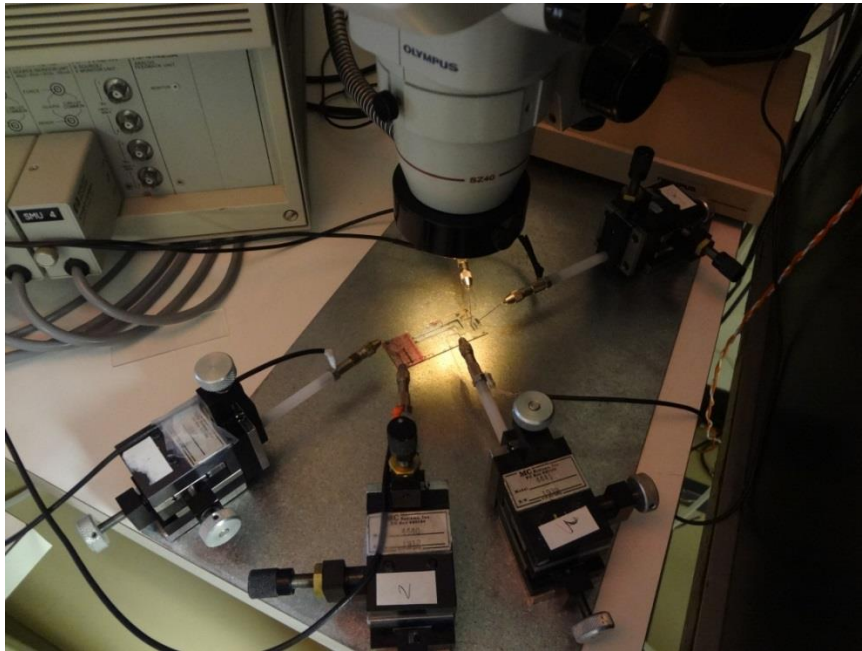
(b)



(c)



(d)



(e)

Figure 60. Laboratory setup used to characterize the Polymer Neuromorphic Circuitry fabricated on a single, glass substrate. Five individual micromanipulators can be seen used to provide $Input_1$, $Input_2$, OFET's V_G , Ground, and $Output$ connections.

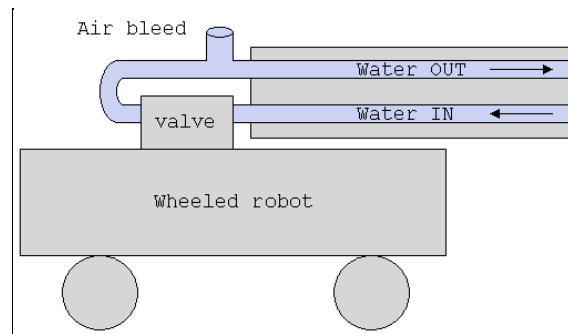
Chapter 5: PNC For Linear Classification

To elucidate the effectiveness of the polymer neuron to perform pattern classification I have chosen a simple example where the shape of an active tether dictates the direction of a propulsive impulse imparted to a front mounted robot or other device (R. A. Nawrocki, Shaheen, Yang, & Voyles, 2009; Perrin, Know, & Howel, 2004).

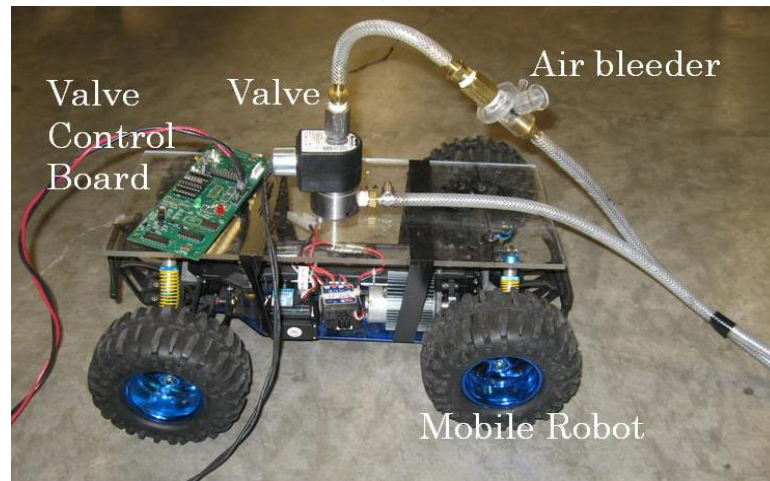
In the experiment, when water traveling through a hose experiences a rapid and sharp change in pressure, for instance facilitated by a fast closure of a valve, the increased pressure, due to the continuous motion of the flowing liquid, results in a force impacted at the point of the closure. This phenomenon is known as a water hammer effect. When the hose is fixed and rigid, it can often result in pipe destruction. However, when the hose is not permanently attached to a stationary medium, it experiences a jerky motion, such as the observed shaking of a gas hose at a gas station.

Perrin *et al.* have realized the possibility of the use of this effect as a source of propulsion of a wheeled robot, attached at the end of the hose with a valve, (Perrin, *et al.*, 2004), as illustrated in Figure 61. At the Collaborative Mechatronics Laboratory (CML) at the

University of Denver (DU) we have extended on the idea by investigating and verifying the hypothesis that a shape of the hose can affect the direction of the propulsion force (Yang, Voyles, Kang, & Povilus, 2009). Affecting such an active tether, the use of water hammer effect would result in controlled directional propulsion. We have also verified that the shape closest to the front of the hose has a significantly greater impact on the direction than points further away (R. A. Nawrocki, Xiaoting, Shaheen, & Voyles, 2011). Figure 62 illustrates the water hammer concept, with the length of the dashed arrows indicating the water pressure and its effect on the direction of propulsion.



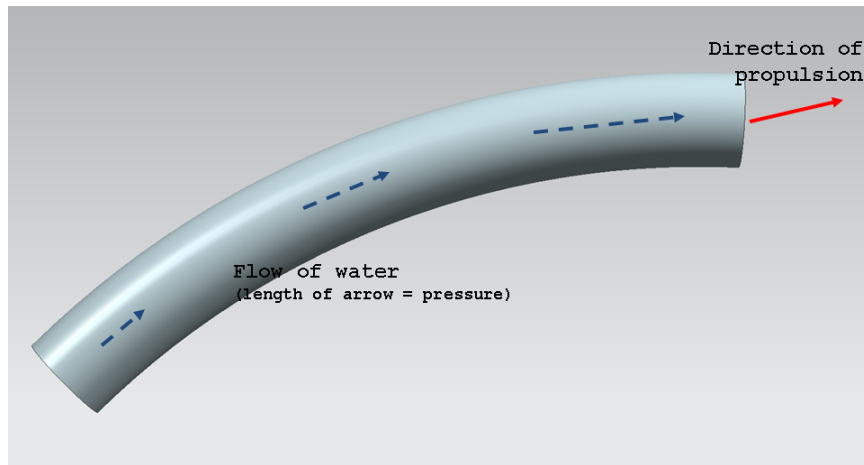
(a)



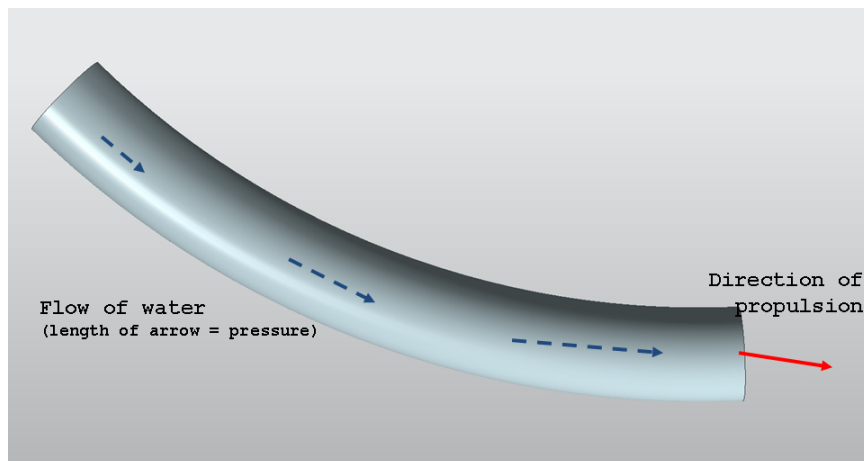
(b)

Figure 61. (a) A diagram of active tether, powered by water hammer phenomenon, with individual elements outlined. (b) Prototype of the active tether.

It was previously demonstrated, via simulation and emulation, that a network of synthetic neurons is capable of accurately correlating the shape-of-the-hose (neural input) to the direction of propulsion (neural output) relationship (R. A. Nawrocki, Xiaoting, et al., 2011). The network consisted of four input neurons, four hidden neurons, and a single output neuron.



(a)



(b)

Figure 62. Water hammer phenomenon, indicating a force acting on the end of the hose. The red (solid) arrow indicates the direction of propulsion, (a) up and (b) down, while the blue (dashed) arrows correspond to the flow of the liquid with their length being indicative of the liquid pressure and the effect on the direction (shape closer to the end has a greater effect on the direction of propulsion).

5.1 Single Neuron Classification

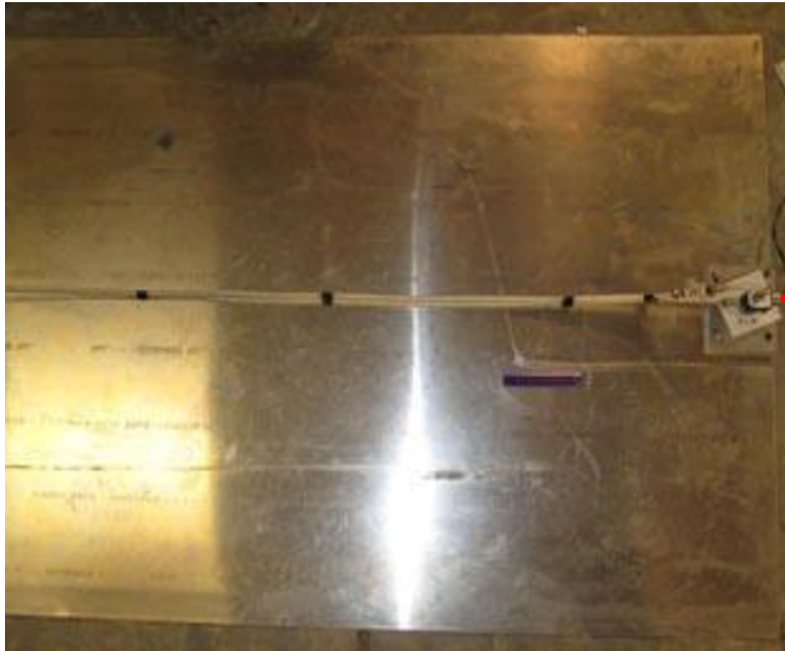
Having verified that a simulated and an emulated network of synthetic neurons are both capable of predicting the direction of propulsion, I have repeated the active tether pattern classification experiment but with only a single polymer neuron performing the classification. Two coordinate values, x and y , were used to represent a single point on the hose used as a two-dimensional input vector with the angle of propulsion used as a one dimensional output value. The neuron was fit with two inputs while each synapse contained three (n) OM-PROMs, each with different resistances, allowing for eight (2^n) possible synaptic states. The neuron was constructed according to the separate-substrate configuration shown in Figure 51(a), while Figure 52 illustrates the setup used to characterize the neuron.

Figure 63(a-e) illustrates a sample of five shapes of the active tether, used for neural classification purposes. It can be seen that shapes closer to a straight (horizontal) line correspond to a more straight (smaller magnitude of the angle) direction of propulsion, as indicated by the red arrow. Furthermore, more curved shapes result in a higher angle of the propulsion. While the previously demonstrated simulated and emulated networks consisted of a larger number of input and output neurons, as well as a larger number of classified shapes (R.

A. Nawrocki, Xiaoting, et al., 2011), the single neuron was only used to classify a small subset of shapes.

Table 1 lists output voltages ("OUT" column) from a single simulated neuron constructed with the same electrical characteristics of the polymer electrical elements performing classification of four shapes shown in Figure 63.

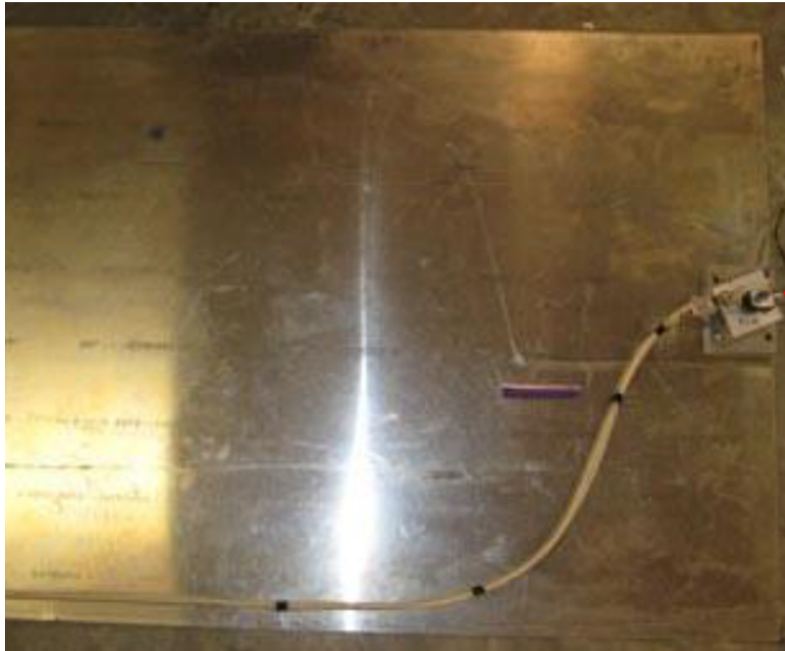
Table 2 shows measured output voltages of a single, separate-substrate polymer neuron, with activation function shown in Figure 7, performing the same, five sample active tether classification. The " θ_{actual} " is the experimentally observed direction of propulsion of the active tether (shown in Figure 63), while " $\theta_{simulated}$ ", and " θ_{PNCI} ", represent the simulated neuron and the tangible polymer neuron output respectively. The full-scale error was computed assuming the maximum output value of $\pm 50^\circ$. The maximum error of the polymer neuron was recorded as 0.05 with the average error computed as 0.026.



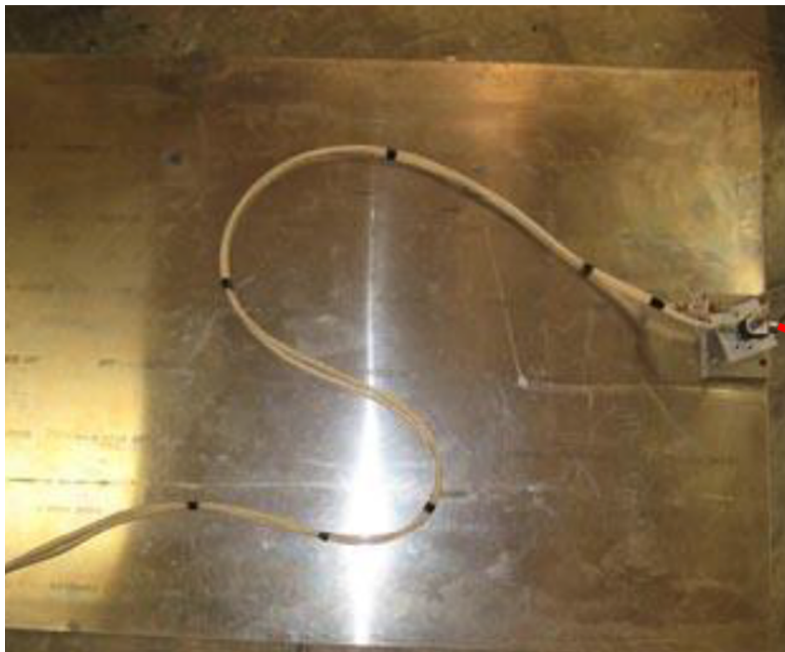
(a)



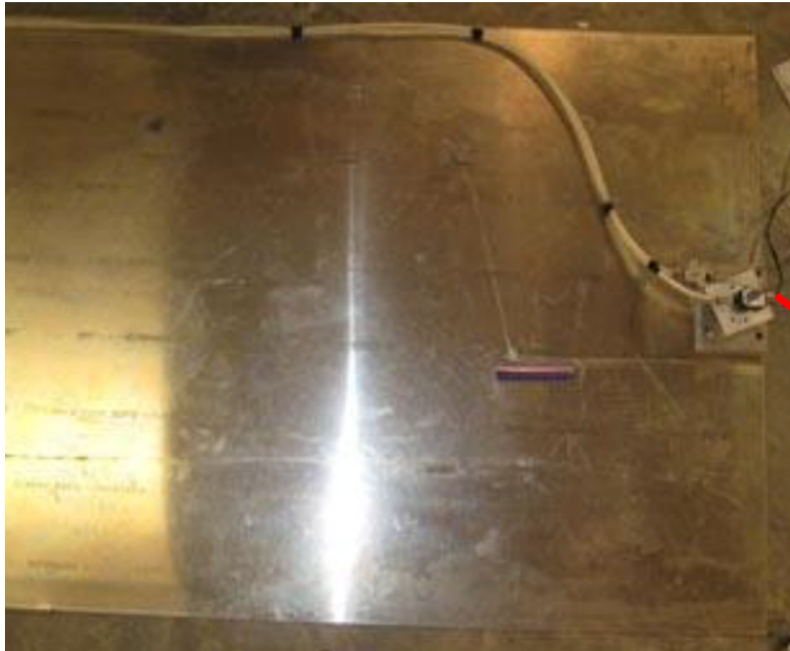
(b)



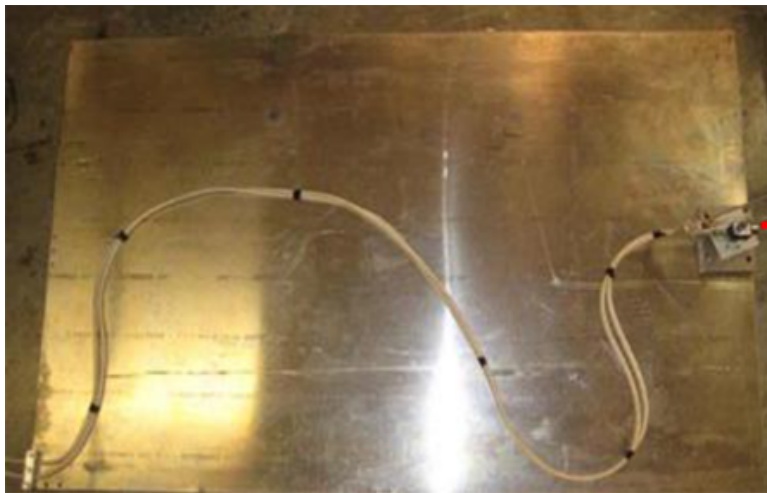
(c)



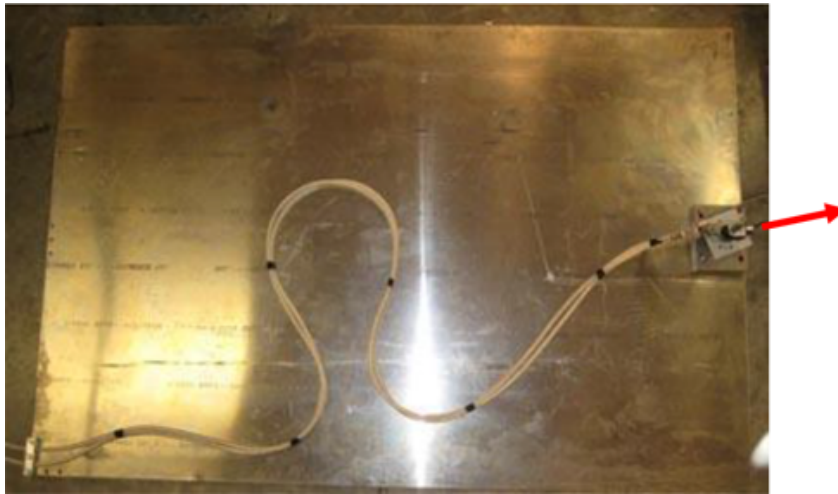
(d)



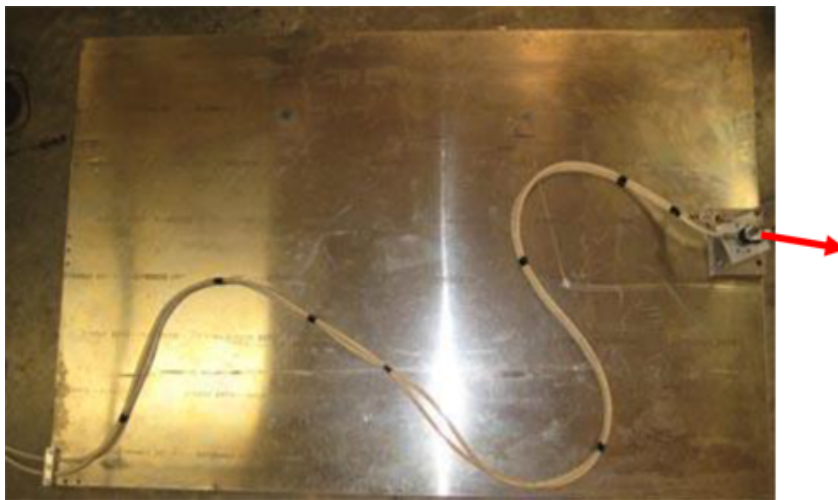
(e)



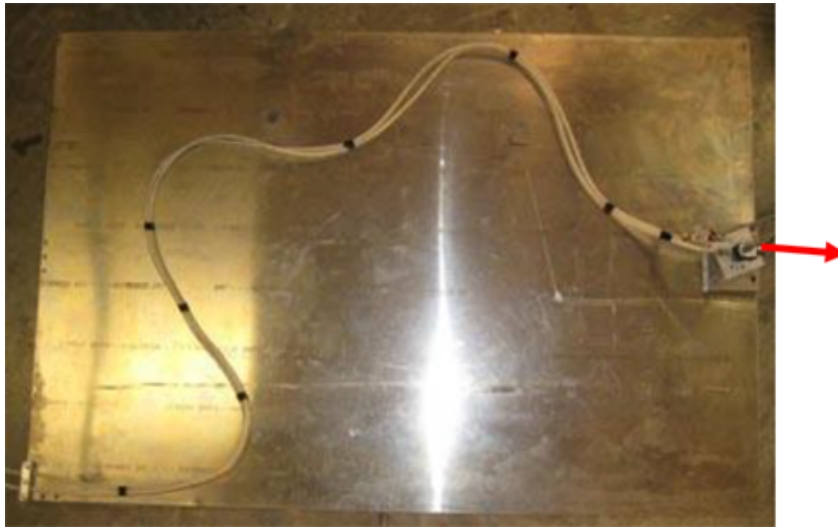
(f)



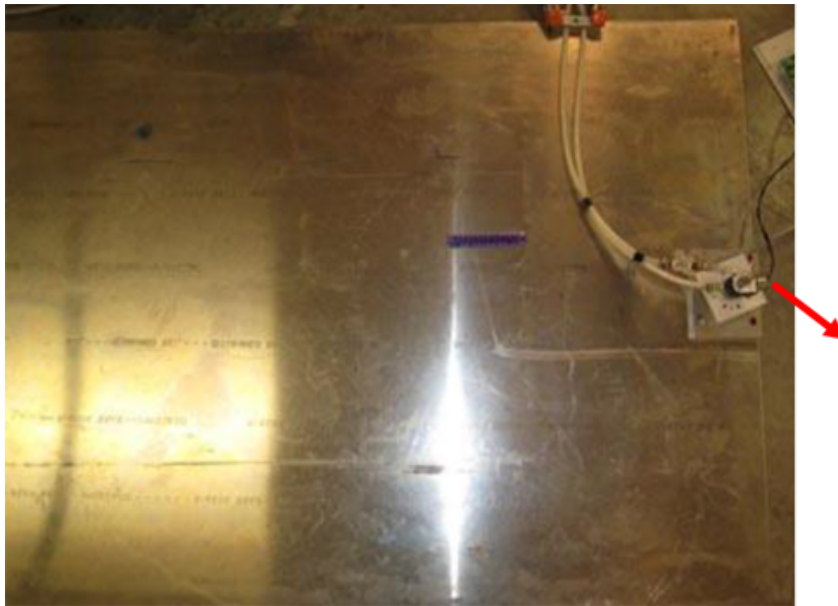
(g)



(h)



(i)



(j)

Figure 63. Pictorial representation of ten shapes used for active tether classification, with their corresponding direction (angle) of propulsion marked. Shape (a) represents a reference value where the hose is propelled along the horizontal axis, with output voltage being ~ 0 V. Images from (Yang, 2010).

Shape	$\theta_{\text{actual}} (^{\circ})$	$\theta_{\text{simulated}} (^{\circ})$	OUT (V)	Error
a	-1	0	-0.01	0.01
b	-45	-50	-0.31	0.05
c	-18	-22	-0.18	0.04
d	10	11	0.16	0.01
e	17	20	0.18	0.03

Table 1. Single simulated neuron trained to perform the simple binary classification associated with water hammer effect).

Shape	$\theta_{\text{actual}} (^{\circ})$	$\theta_{\text{PNC1}} (^{\circ})$	OUT (V)	Error
a	-1	0	-0.01	0.01
b	-45	-50	-0.3	0.05
c	-18	-21	-0.19	0.03
d	10	11	0.16	0.01
e	17	18	0.19	0.01

Table 2. Single polymer neuron trained to perform the simple binary classification associated with water hammer effect, shown in Figure 63(a-e).

5.2 Network of Neurons Classification

The ability of a single synthetic neuron to perform a simple pattern classification can be easily extended to the ability of a network of neurons to perform a more complex classification (Haykin, 1998). What has not been shown is the neuron's cascading ability, meaning the ability of a group of neurons to form a network, with individual neurons receiving input signal from other neurons instead of an external power supply.

To verify the ability of the PNC to cascade I have chosen the same pattern matching of the active tether, described in the previous section *5.1 Single Neuron Classification*, with a more complex function resulting from an increased number of samples used. The PNC was trained on ten samples, shown in Figure 63(a-j).

Figure 58(a) illustrates the configuration of the fully-connected network used, with two input, two hidden, and one output neuron, shown

in Figure 59(b), with the measurement setup shown in Figure 60, connected according to the common-substrate fabrication paradigm shown in Figure 51(b), with synaptic resistances shown in Table 3.

Table 4 shows measured output voltages of the common-substrate network of polymer neurons, with the activation function of a single neuron shown in Figure 8. The " θ_{actual} " is the experimentally observed direction of propulsion of the active tether (shown in Figure 63(a-j)), while " θ_{PNC2} " represent the value predicted by the PNC. As in the previous experiment, the full-scale error was computed assuming the maximum output value of $\pm 50^\circ$, with the maximum error recorded as 0.05 and the average error computed as 0.018. This validates the claim that such a simple PNC presented here, consisting of only three neurons, is capable of performing a simple pattern classification as well cascading the signal to function as a network.

Hidden 1			Hidden 2			Output		
Input 1	Mem1A1	ON	Input 1	Mem1B1	ON	Hidden 1	Mem1C1	ON
	Mem1A2	ON		Mem1B2	OFF		Mem1C2	ON
	Mem1A3	OFF		Mem1B3	OFF		Mem1C3	OFF
Input 2	Mem2A1	ON	Input 2	Mem2B1	ON	Hidden 2	Mem2C1	ON
	Mem2A2	ON		Mem2B2	ON		Mem2C2	ON
	Mem2A3	OFF		Mem2B3	OFF		Mem2C3	OFF

Table 3. Configuration of memristive synapses, often termed connection weights, used in a network shown in Figure 58, to perform the active tether classification

Shape	θ_{actual} ($^\circ$)	θ_{PNC2} ($^\circ$)	OUT (V)	Error
a	-1	0	-0.02	0.01
b	-45	-49	-6.11	0.04
c	-18	-20	-3.78	0.02
d	10	11	3.18	0.01
e	17	18	3.84	0.01
f	-4	0	-2.02	0.04
g	-5	-4	-2.38	0.01
h	8	9	2.70	0.01
i	6	7	2.31	0.01
j	45	50	6.14	0.05

Table 4. A small network of neurons trained to perform the simple classification associated with water hammer effect, shown in Figure 63(a-j).

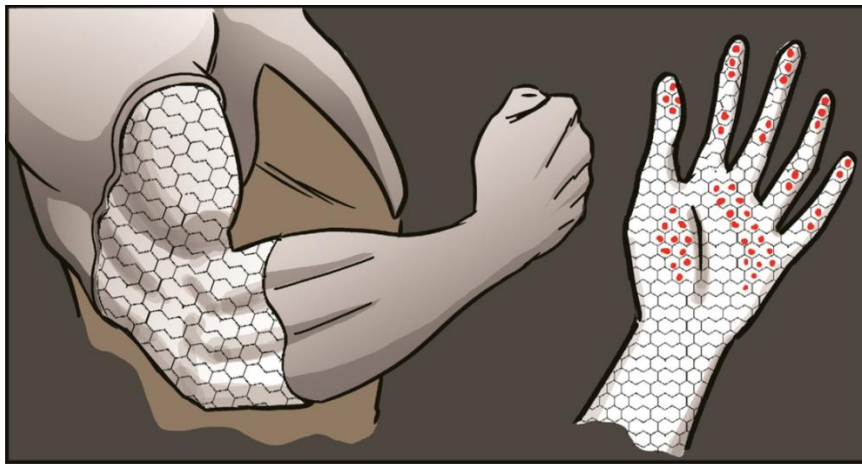
Chapter 6: PNC Application

6.1 Structured Computational Polymers

Smart materials are designed materials that have one or more properties that can be significantly changed in a controlled fashion by external stimuli, such as stress, temperature, moisture, pH, electric or magnetic fields. Such highly engineered, typically polymer materials are emerging as the basis for adaptive, soft robots (Ahn et al., 2012; Cho et al., 2009; Shepherd et al., 2011; Trivedi, Rahn, Kier, & Walker, 2008). The shift from rigid, precise mechanisms controlled through rigorous kinematics to soft, conformable mechanisms that dynamically interact with their environment represents a radical departure from the status quo. It also presents a challenge for the type of information processing used, with the current largely serial central processing not well suited for such a task. Therefore, smart materials require a truly and massively distributed form of information processing, such as the demonstrated Polymer Neuromorphic Circuitry.



(a)



(b)

Figure 64. Examples of highly engineered, smart materials: (a) liquid terminator from the movie Terminator 2 (image from Wikipedia.org), (b) concept of smart material used as an elbow brace or a glove (image from Nick Dragotta).

Structured Computational Polymers (SCP) is a new class of intelligent meta-materials. These materials will possess the ability to sense the environment and then intelligently react to changing conditions. Distributing the sensing, cognition, and actuation throughout the entirety of the material will, depending on the application, allow for all of the functionalities to be either local or global in nature. SCP is envisioned as a new class of intelligent materials that will be mass produced from in-bulk manufacturing

processes. For instance a 2-D form of SCP would be produced as a continuous sheet of material using roll-to-roll processes (Sondergaard, et al., 2013). Users would then simply cut out a piece of material and configure it according to their own specific needs. This places a requirement on the SCP to have all of its functionalities, namely sensing, cognition, and actuation, to be truly distributed throughout the entirety of the material. It also necessitates re-thinking of the physical layout and information processing as fabrication paradigms.

A vast majority of today's computation is performed at a central location. This computational model clearly violates the design criteria of distributed nature of SCP. However, the distributed nature of the Polymer Neuromorphic Circuitry makes it perfectly suitable for the task of distributed data processing needed for such a smart material.

SCP is envisioned to be conformal or affecting to its environment, with the ability to contract, expend, bend, or bulge when needed. As such, all of the functionalities, namely sensing, cognition, and actuation, need to be implemented with physically flexible components.

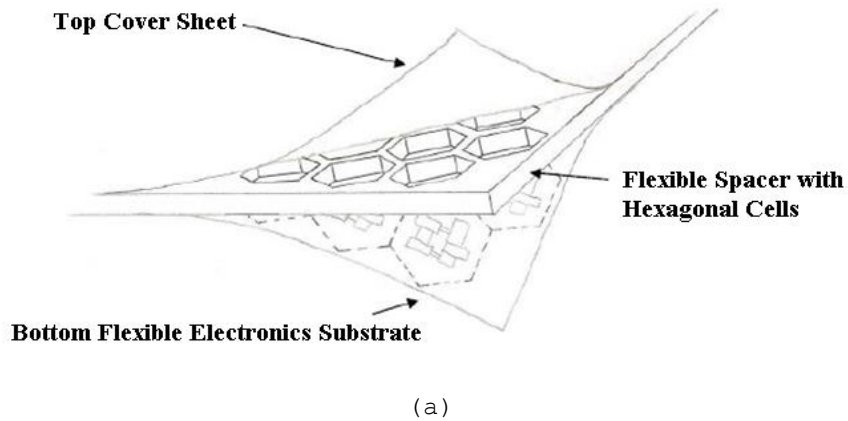
Semiconducting, conducting, and ferroelectric polymers have been used as piezoelectric sensors for strain gauges as well as actuators for contraction and expansion (Barisci, Wallace, Andrews, Partridge, & Harris, 2002; Ikushima, John, Yokoyama, & Nagamitsu, 2009; Maeda, Hara, Yoshida, & Hashimoto, 2008; Osada & De Rossi, 1999). The physical flexibility and distributed nature of the PNC makes it perfectly suitable to realize the cognitive functionalities of the SCP.

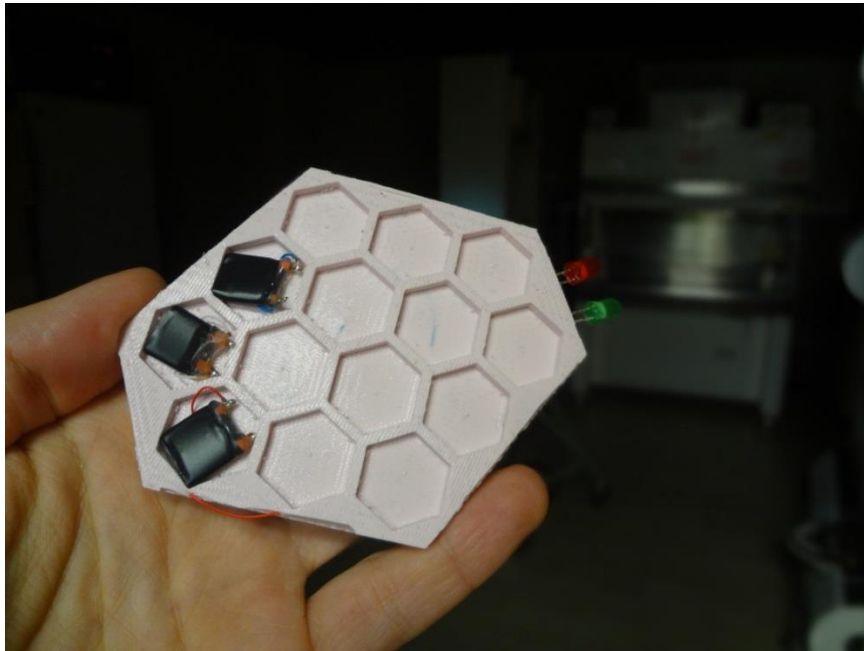
Figure 65(a) demonstrates a concept of an SCP prototype with fourteen hexagonal cells. Figure 65(b-g) shows a small scale implementation of the SCP prototype. The material (light pink seen in Figure 65(b-g)), formed inside a cast, is a two part polymer called SmoothSil 930, which is comprised of an A compound and a B compound (Smooth-Sil, 2013a, 2013b). These are mixed together with a 100:10 weight ratio respectively and the casting takes roughly 24 hours to set. The cast (dark blue seen in Figure 65(f-g)) is a plastic form that is formed inside of the rapid prototype machine (RPM). The geometry is formed by importing a solid model into the RPM, which it then can print in three dimensions.

The prototype features all the necessary functionalities, namely sensing, actuation, and cognition. Sensing is implemented in a form of three custom-made pressure/bending sensors placed inside separate SCP cells. Two conventional LEDs, protruding on a side of the prototype, are serving as the outputs. The choice of inorganic electronics over organic electronics for this early stage prototype was facilitated by the need to demonstrate the efficacy of the PNC to perform function mapping. The ability to build smart material with embedded organic electronics is shown in the next section.

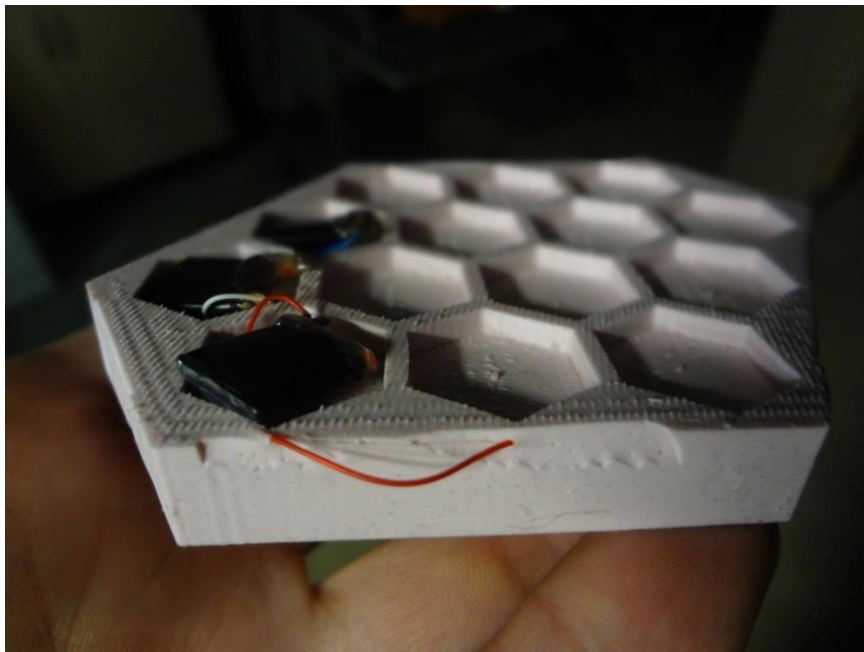
Information processing was implemented using conventional, inorganic electronics components, connected according to the PNC layout (Figure 1(b)), with the 3x3x2 neural topology (three input neurons, three hidden neurons, and two output neurons). Inorganic FETs were used in lieu of organic FETs. Conventional, inorganic resistors were used for the synaptic functionality, with two resistors (with low resistance

for $R_{MEM} = \text{ON}$ and high resistance for $R_{MEM} = \text{OFF}$, see Figure 3) used per synapse, along with a switch. The resistors were embedded inside the material while a series of dip switches are on the bottom surface of the SCP (Figure 65(e) and Figure 65(g)). The transistors, resistor, switches and LED wires were placed inside the cast when the SmoothSil 930 was being poured, making sure that switches and LEDs would extend outside of the poured polymer, while the pressure sensors were connected after the polymer has hardened. The dip switches were positioned just above the electronic components ensuring that they would not be covered during the casting. In this early concept of SCP prototype, the power is provided from an external battery.

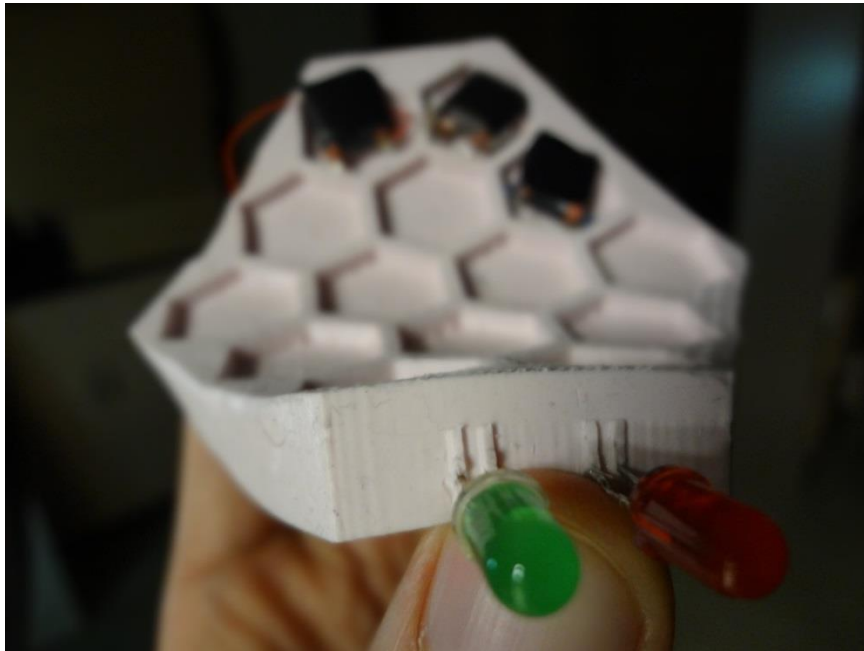




(b)



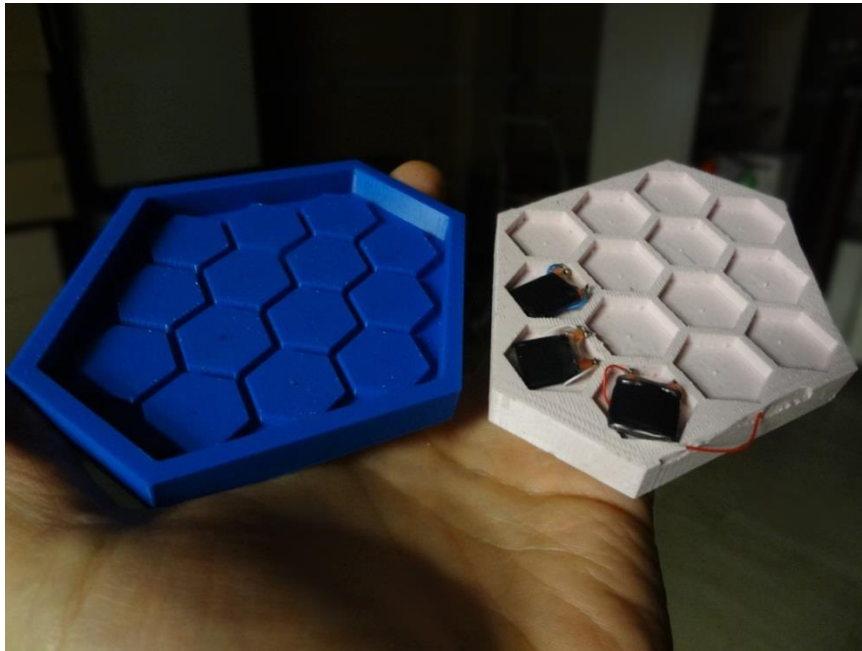
(c)



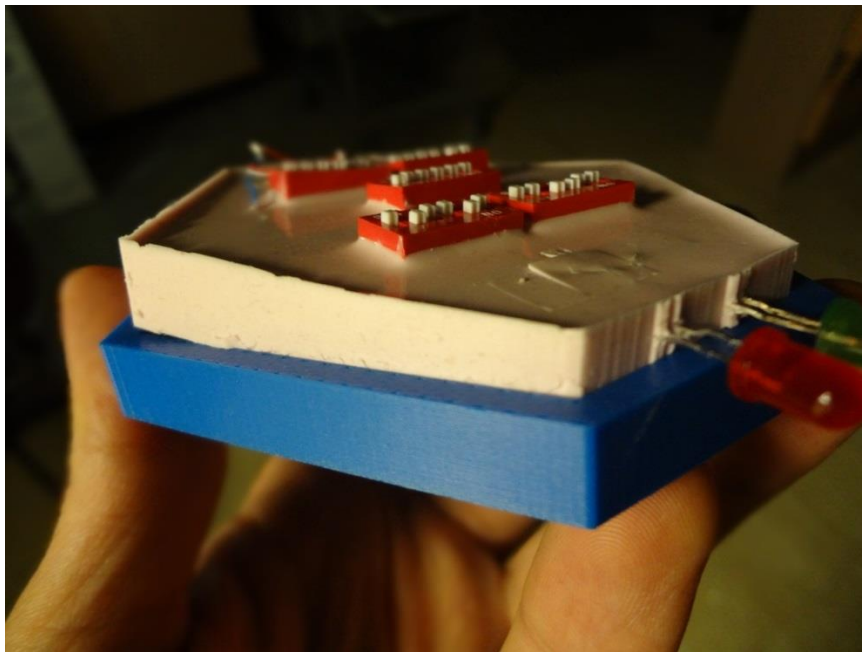
(d)



(e)



(f)



(g)

Figure 65. Concept of a prototype of Structured Computational Polymers. (a) Proposed concept of the design. (b-g) Small scale implementation of the prototype. The prototype features sensing functionality in a form of three, custom-made pressure sensors placed inside separate cells. Two conventional LEDs, protruding

on a side of the prototype, are serving as the outputs. Information processing, implemented using conventional, inorganic electronics components connected according to the PNC layout, is embedded inside the material.

Table 5 demonstrates the truth table of the three-input-two-output cognition of the SCP prototype. The training was performed off-line (as outlined in section 2.4 *Learning versus Programming*), and the connection weights were then manually exported by setting the individual dip switches.

Input 1	Input 2	Input 3	Output Left	Output Right
OFF	OFF	OFF	OFF	OFF
OFF	OFF	ON	OFF	OFF
OFF	ON	OFF	OFF	OFF
OFF	ON	ON	OFF	ON
ON	OFF	OFF	OFF	ON
ON	OFF	ON	OFF	ON
ON	ON	OFF	OFF	ON
ON	ON	ON	ON	ON

Table 5. A truth table of the SCP prototype with three pressure/bend sensors acting as neuronal inputs, and two LEDs functioning as neuronal outputs, as shown in Figure 65(b).

6.2 PaperBots

Robots, including both soft and hard robots, have historically taken a long time, and with a significant financial investment, to engineer. Rapid prototyping technologies are reducing the development cycle, and cost, allowing for greater innovation. Foldable structures can be printed in minutes for pennies, allowing even inexperienced individuals to experiment with robotic designs (Hoover & Fearing, 2008; Wood, Avadhanula, Sahai, Steltz, & Fearing, 2008).

Rapidly prototyped, low-cost, printed, mini- or micro-size mechanical devices with embedded intelligence cannot rely on conventional, central, heavy and power-hungry microprocessor based information processing. They require distributed, lightweight, damage resistant, printable information processing, such as the Polymer Neuromorphic Circuitry.

At the Collaborative Mechatronics Laboratory (CML) at University of Denver (Voyles, 2013), we have partnered with Biomimetic Millisystems Lab at University of California, Berkley to develop rapid prototyped, foldable / printable robots with printable, physically flexible electronics, to achieve low-cost, accessible, and bio-inspired robots. Figure 66 shows an example of bio-inspired, rapidly prototyped foldable hexapod design, termed PaperBot due to the material choice. The prototype design consists of three structural pieces, top, middle, and bottom, with three legs being attached to hinges at the top and bottom pieces. Akin to an arthropod locomotion, the PaperBot movement is based on three top legs, and three bottom legs, being fixed together, but moveable with respect to the other set. Such a design allows the hexapod to be always in a stable position (three legs are always in contact with the ground) as compared to quad- or bipeds (human walking is often compared to a controllable fall). The PaperBot moves by means of a small movement of the top-piece, or bottom-piece legs being thrust forward due to inward and outward movement of the middle piece attached to the leg hinges. At present the PaperBot does not incorporate any type of "intelligence". However, in the future the

information processing will be provided from physically flexible PNC embedded in the material itself.



Figure 66. A prototype of a foldable design, termed PaperBot, inspired by an arthropod locomotion.

Figure 67 demonstrates an example of a sheet of physically flexible material, PEN, with a fabricated array of organic transistors (more information on physically flexible OFETs can be found in section 3.3.2.3 *Physically Flexible OFETs*), used as a building block for a prototype of a smart material, shown in Figure 68 and Figure 69(c), used to create the foldable, rapidly prototyped PaperBots, Figure 69(g). At present, in this early prototype of the smart material, the organic electronics is not used to perform any cognitive functionalities, but rather serves as a demonstration of the ability to fabricate a type of designed, smart and physically flexible material with embedded physically flexible electronics. In the future, we envision to extend the electronic design to include the cognitive PNC as well as a small array of OPVs serving as the

neural input sensors, and allowing for PaperBots to be controlled remotely, for instance with a small laser pointer.

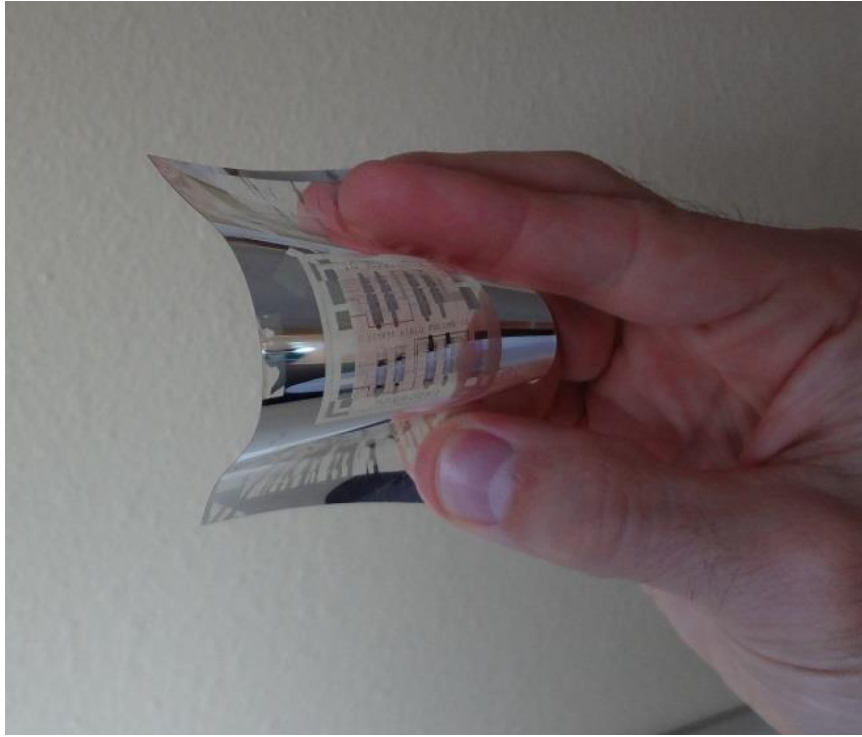


Figure 67. A physically flexible sheet of PEN, with a fabricated array of organic transistors, used to create a prototype of smart material, shown in Figure 69(c).

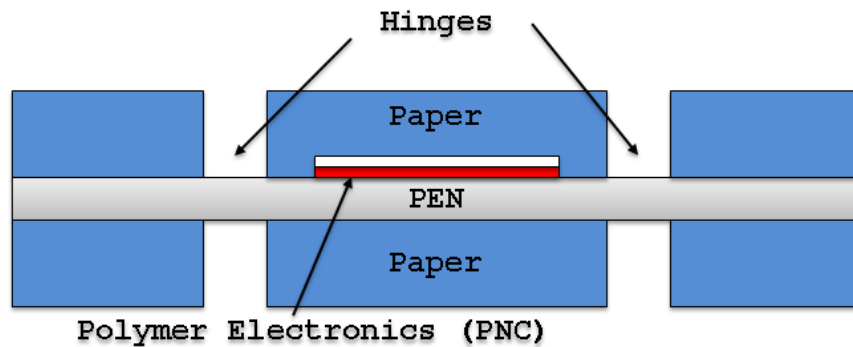
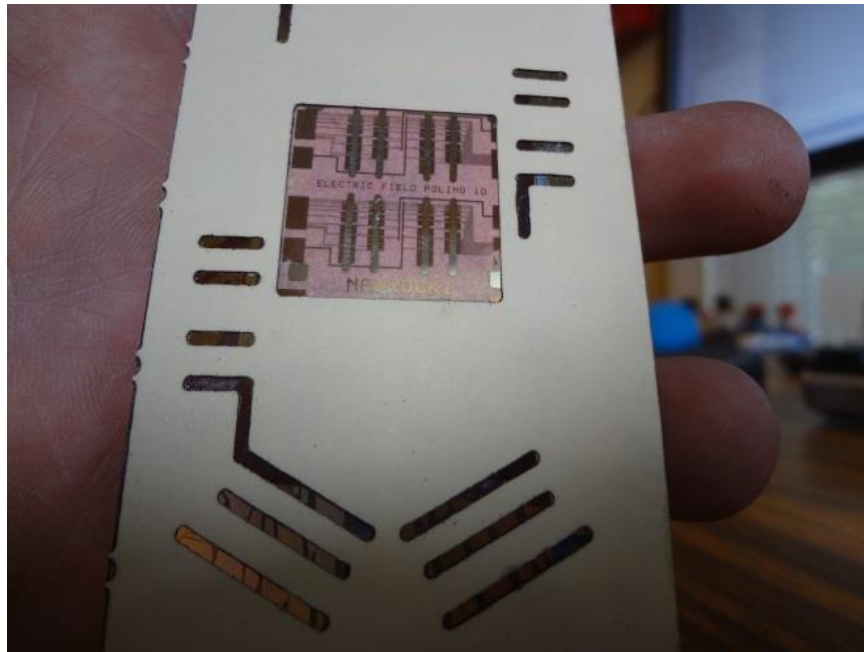
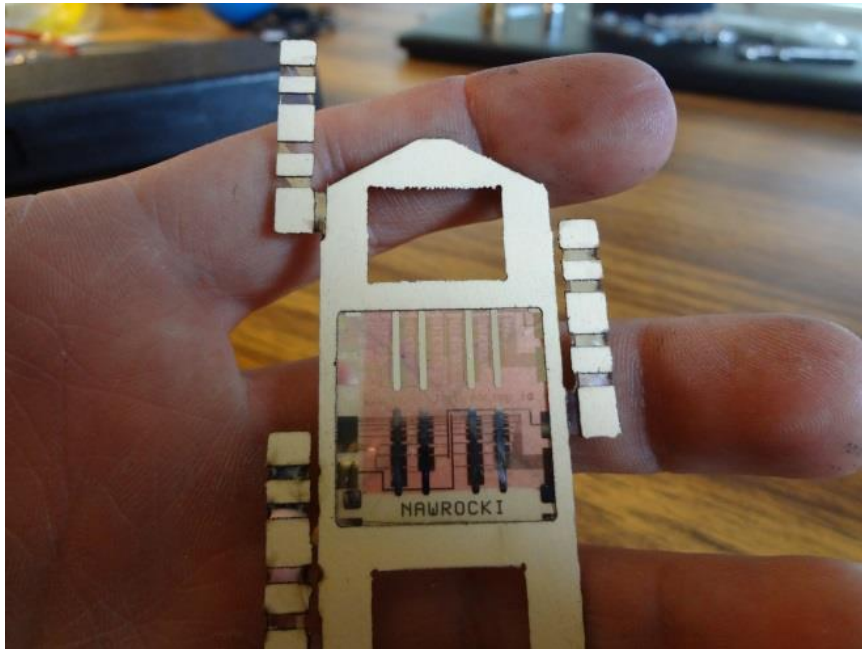


Figure 68. Structure of a smart material used for foldable PaperBots. Physically flexible PEN, with organic electronics fabricated on, is sandwiched between two sheets of paper. Cuts in the paper, performed with a laser cutter before the lamination step, are used as hinges of the PaperBot.

Figure 69 demonstrates fabrication steps necessary to create the early prototype of smart material with embedded physically flexible cognition, used to construct a small scale robot: Figure 69(a) shows the smart material itself, while Figure 69(b-d) depict various stages of the robot assembly, culminating with the final design featuring a motor, shown in Figure 69(e).



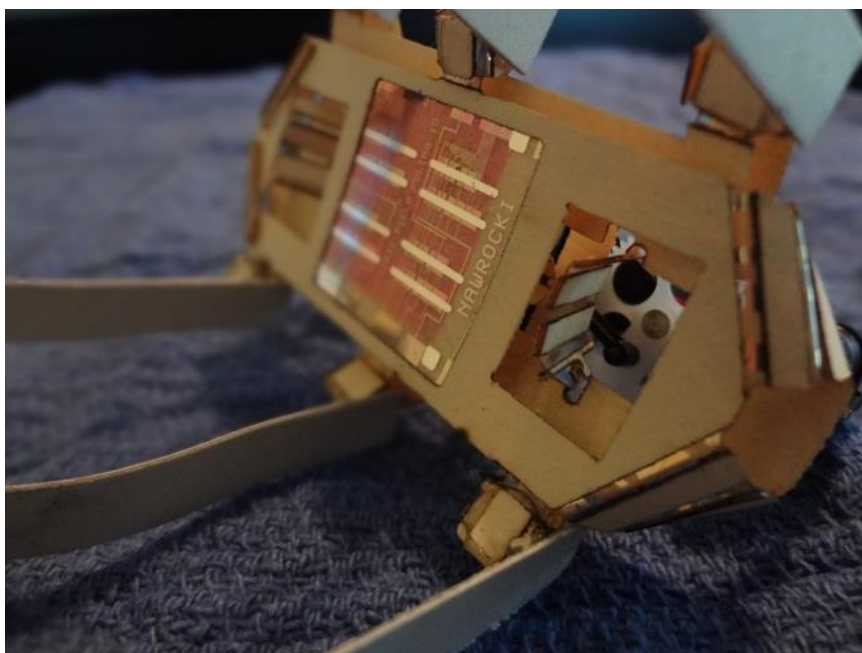
(a)



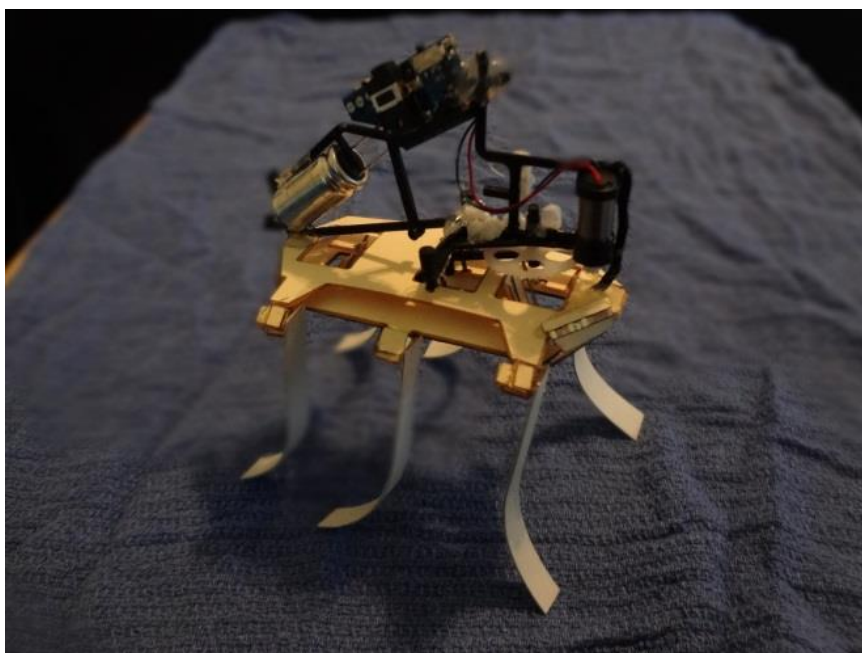
(b)



(c)



(d)



(e)

Figure 69. Step-by-step process of a prototype of a smart material, with embedded physically flexible organic electronics, used to manufacture a foldable, rapidly prototyped hexapod, termed PaperBot.

Development of web-based design tools, coupled with reduction of the cost of equipment, such as 3-D printers, and tailored elementary to high school education, should enable an explosion of print-at-home, intelligent, inexpensive, and rapidly prototyped and implemented robots, such as the foldable, PaperBot shown here.



(a)



(b)



(c)

Figure 70. Inexperienced high school students are guided in the assembly process of rapidly prototyped PaperBots.

Chapter 7: Summary and Future Work

Neuromorphic engineering is a new interdisciplinary conception that takes inspiration from biology, physics, mathematics, computer science and engineering to design artificial neural systems, to perform functions such as perception, motor control, sensory integration, and artificial intelligence, with physical configuration and design principles based on those of biological nervous systems.

Having previously shown a simplistic circuit design that approximates the neural functionalities commonly associated with the McCulloch-Pitts neuron, I have shown here a first demonstration of a fully functioning neuron, along with a network of such neurons, termed Polymer Neuromorphic Circuitry. The synaptic multiplicative functionality was accomplished with the use of memristive devices while the somatic summing, along with the activation, was obtained from a prudent design of a circuit based on a single transistor. All of the necessary electrical elements, namely memristive devices, transistors, and resistors, were manufactured using organic electronics, a new branch of electronics based on electrically conductive and semi-conductive polymers.

I have shown two possible fabrication paradigms that allow for the assembly of an entire neuron made with disparate electrical

elements. In the separate-substrate approach, all of the necessary elements were created on separate substrates with a subsequent external, inter-chip connections, according to the neural architecture. In an alternative, common-substrate fabrication methodology, all of the components were fabricated on the same substrate, with inter-element connections being designed as a part of the fabrication process. While the separate-substrate fabrication is much simpler to implement, it is not feasible for a large-scale implementation. The common-substrate fabrication process was validated by fabricating a small network of three neurons with demonstrated cascading capabilities.

I have corroborated the efficacy of the Polymer Neuromorphic Circuitry by demonstrating that the activation function of an individual neuron approximates the sigmoidal function commonly associated with artificial neural networks. I have also shown that a single neuron, as well as a network of such neurons, are capable of performing elementary linear classification.

Finally, I have demonstrated an intended application of the PNC in a form of a smart material, a material that, due to the embedded sensing, cognitive and actuating capabilities, can intelligently react to its changing environment. Such a material can be used to build large volumes of inexpensive robotics systems.

7.1 Future Work

Even though the currently manufactured Polymer Neuromorphic Circuitry is fully functioning and capable of elementary linear classification, there are still a number of issues that need to be implemented, corrected, or investigated as possible alternatives.

As already mentioned, the currently implemented neuromorphic circuit is essentially a linear amplifier that allows for the sigmoidal approximation by balancing the linear and saturation regimes of the organic transistor. In order to obtain a true neuronal behavior, the circuit will have to be modified. In one such alternative, the single transistor somatic sub-circuit would be replaced with a circuit that realizes a true sigmoidal activation function, such as the one proposed by Gupta and Bhat (Gupta & Bhat, 2005). In another possible alternative, the current single transistor circuit would be replaced with an operational amplifier circuit, such as the one presented in Figure 72(a) with the corresponding activation function shown in Figure 72(b). Both of these proposals would result in a much larger circuit that would necessitate a much more complicated manufacturing process. However, in biological neurons the size of the soma is significantly greater compared to the synapse as an individual can be connected to as many as 10,000 neurons, resulting in the synapse-to-soma ratio of 10,000/1 (Kandel, et al., 2000). As such, the use of an operational amplifier could be a viable alternative.

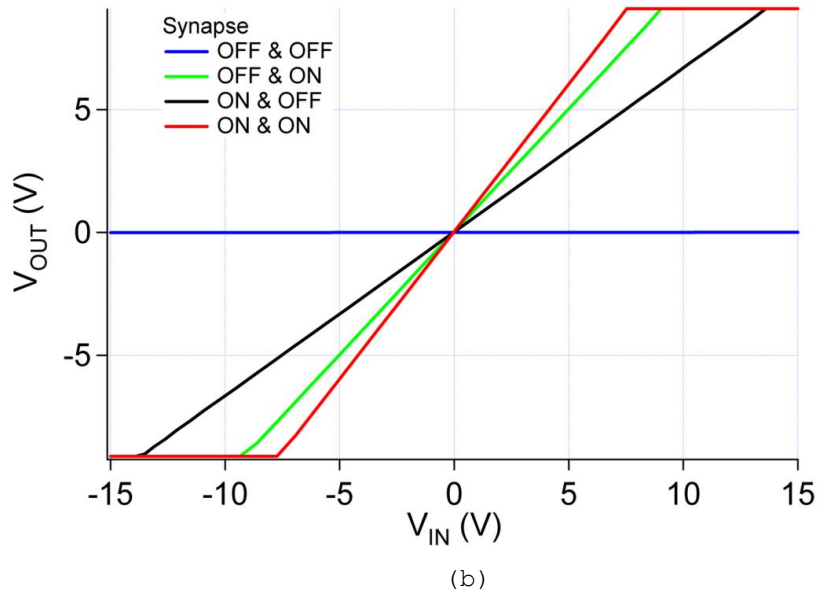
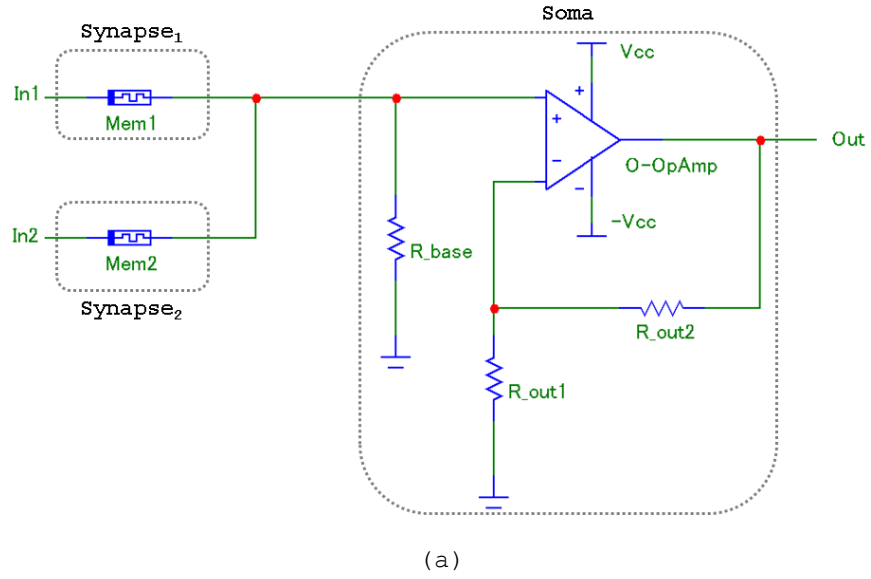


Figure 71. (a) Proposed neural circuit to realize the neuronal activation with the soma being realized by an organic operational amplifier (O-OpAmp). (b) Activation function of the O-OpAmp-based neuronal circuit with four memristive synaptic functionalities. The "ON & OFF" and "OFF & ON" cases produced two different curves by utilizing different *Mem1* and *Mem2* resistances.

For the purposes of simplicity, the current circuit design, based on synaptic multiplication as well as somatic summing, does not provide

any training or programming functionalities. This limitation could be addressed with an addition of a supplementary circuitry with the only purposes of adjusting the synaptic weights. This, however, would most likely require the use of non-permanent memristive devices, namely OM-RAMs instead of OM-PROMs. In my group, we have made a progress in fabricating OM-RAM devices with fabrication processes more compatible with printing or plotting techniques. Figure 72 displays an I - V characteristics curve of an OM-RAM device fabricated based on an insulating PS-*b*-PMMA copolymer doped with a highly conductive C_{60} , inspired by (H. Jo, Ko, Lim, Chang, & Kim, 2013).

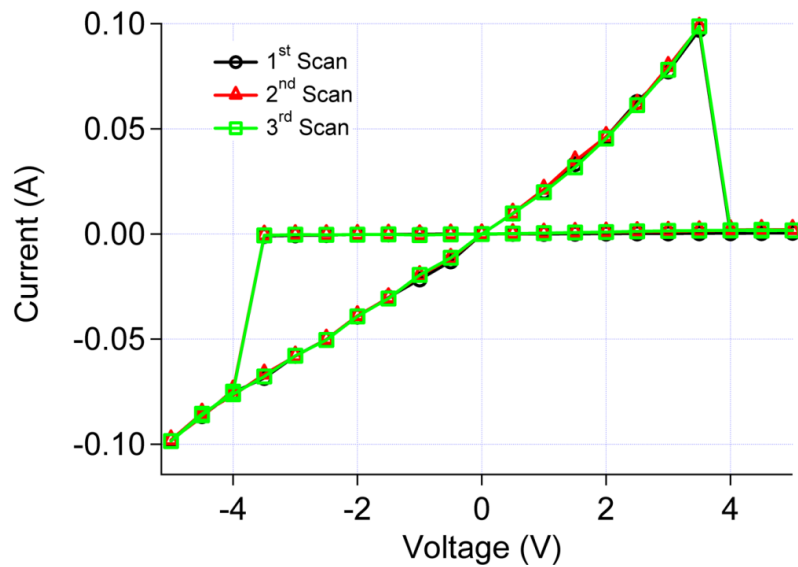


Figure 72. Example of I - V characteristics scan of an OM-RAM device fabricated based on insulating copolymer PS-*b*-PMMA doped with conductive C_{60} .

In a likely alternative, binary memristive devices could be replaced with analog memristive devices, with characteristics more akin to biological synapses, resulting in spiking neural behavior with intrinsic learning capabilities based on history of the input signal.

Figure 73 displays an I - V characteristics curve of an analog memristive device fabricated in my laboratory.

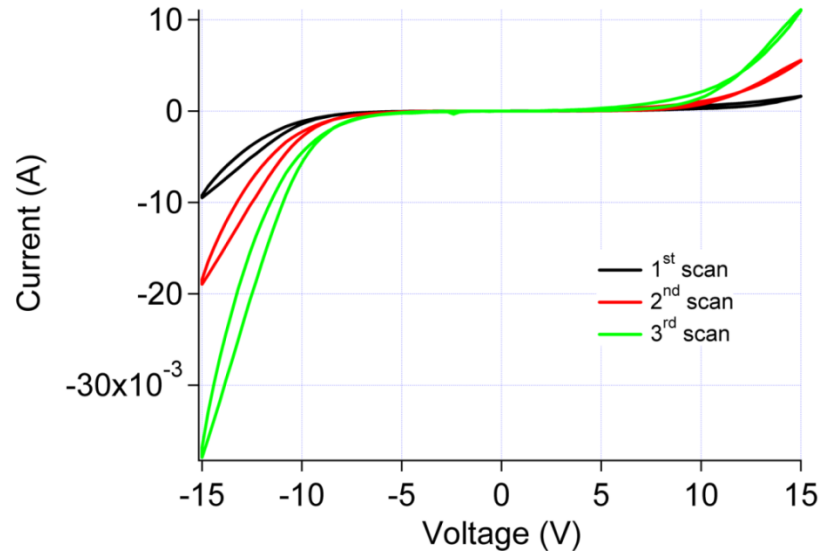


Figure 73. I - V characteristics scan of an analog memristive device that could be used as a spiking synapse in a spiking neural network.

Finally, with the large-scale physical separation of the individual devices, because of a relatively large number of device interconnects, that span the entire width of the substrate, the presently employed fabrication techniques allow only for manufacturing of small number of neurons on a single substrate. In order to produce truly distributed form of information processing, with individually grouped neurons, an alternative means of manufacturing would need to be investigated. Perhaps the most promising such technique is printing, such as inkjet printing, or plotting, such as the liquid-dispensing sonoplot (Sonoplot, 2013), that allows for precision deposition of individual materials at explicitly defined regions instead of indiscriminately covering the entirety of the substrate. The

aforementioned, PEDOT:PSS-based plotted resistors show a great promise of this technology.

References

- Ahn, S. H., Lee, K. T., Kim, H. J., Wu, R., Kim, J. S., & Song, S. H. (2012). Smart Soft Composite: An Integrated 3D Soft Morphing Structure Using Bend-Twist Coupling of Anisotropic Materials. [Article]. *International Journal of Precision Engineering and Manufacturing*, 13(4), 631-634.
- Aisa, B., Mingus, B., & O'Reilly, R. (2008). The Emergent neural modeling system. *Neural Networks*, 21(8), 1146-1152.
- Alibart, F., Pleutin, S., Guerin, D., Novembre, C., Lenfant, S., Lmimouni, K., . . . Vuillaume, D. (2010). An Organic Nanoparticle Transistor Behaving as a Biological Spiking Synapse. *Advanced Functional Materials*, 20(2), 330-337.
- Almeida, V. R., & Lipson, M. (2004). Optical bistability on a silicon chip. *Optics Letters*, 29(20), 2387-2389.
- Ananthanarayanan, R., Esser, S. K., Simon, H. D., & Modha, D. S. (2009, 14-20 Nov. 2009). *The cat is out of the bag: cortical simulations with 109 neurons, 1013 synapses*. Paper presented at the High Performance Computing Networking, Storage and Analysis, Proceedings of the Conference on.
- Apte, P., Bottoms, W. R., Chen, W., & Scalise, G. (2011). Advanced Chip Packaging Satisfies Smartphone Needs. *IEEE Spectrum*.
- Arthur, J. V., & Boahen, K. (2004, 25-29 July 2004). *Recurrently connected silicon neurons with active dendrites for one-shot learning*. Paper presented at the Neural Networks, 2004. Proceedings. 2004 IEEE International Joint Conference on.
- Baeg, K. J., Khim, D., Jung, S. W., Koo, J. B., You, I. K., Nah, Y. C., . . . Noh, Y. Y. (2011). Polymer Dielectrics and Orthogonal Solvent Effects for High-Performance Inkjet-Printed Top-Gated P-Channel Polymer Field-Effect Transistors. *Etri Journal*, 33(6), 887-896.
- Bailey, B. A., Reese, M. O., Olson, D. C., Shaheen, S. E., & Kopidakis, N. (2011). Air-processed organic photovoltaic devices fabricated with hot press lamination. *Organic Electronics*, 12(1), 108-112.
- Bao, Z., & Locklin, J. (2007). *Organic Field-Effect Transistors*: Taylor & Francis.
- Barisci, J. N., Wallace, G. G., Andrews, M. K., Partridge, A. C., & Harris, P. D. (2002). Conducting polymer sensors for monitoring aromatic hydrocarbons using an electronic nose. *Sensors and Actuators B-Chemical*, 84(2-3), 252-257.

- Bartolozzi, C., & Indiveri, G. (2007). Synaptic dynamics in analog VLSI. [Article]. *Neural Computation*, 19(10), 2581-2603.
- Berni, A., Mennig, M., & Schmidt, H. (2004). Doctor Blade. In M. Aegerter & M. Mennig (Eds.), *Sol-Gel Technologies for Glass Producers and Users* (pp. 89-92): Springer US.
- Blom, P. W. M., Smit, C., Haverkort, J. E. M., & Wolter, J. H. (1993). Carrier capture into a semiconductor quantum well. *Physical Review B*, 47(4), 2072-2081.
- Boahen, K. (2005). Neuromorphic Microchips. *Scientific American*, 56-63.
- Brabec, C., Scherf, U., & Dyakonov, V. (2008). *Organic Photovoltaics: Materials, Device Physics, and Manufacturing Technologies*: Wiley-VCH.
- Burroughes, J. H., Bradley, D. D. C., Brown, A. R., Marks, R. N., Mackay, K., Friend, R. H., . . . Holmes, A. B. (1990). Light-emitting diodes based on conjugated polymers. *Nature*, 347(6293), 539-541.
- Calamia, J. (2011). The Plastic Processor. *IEEE Spectrum*, 2.
- Charrier, D. S. H., Janssen, R. A. J., & Kemerink, M. (2010). Large Electrically Induced Height and Volume Changes in Poly(3,4-ethylenedioxythiophene)/Poly(styrenesulfonate) Thin Films. *Chemistry of Materials*, 22(12), 3670-3677. doi: 10.1021/cm100452a
- Chen, L., Li, C. D., Wang, X., & Duan, S. K. (2013). Associate learning and correcting in a memristive neural network. [Article]. *Neural Computing & Applications*, 22(6), 1071-1076.
- Chiang, C. K., Fincher, C. R., Jr., Park, Y. W., Heeger, A. J., Shirakawa, H., Louis, E. J., . . . MacDiarmid, A. G. (1977). Electrical Conductivity in Doped Polyacetylene. *Physical Review Letters*, 39(17), 1098-1101.
- Cho, K. J., Koh, J. S., Kim, S., Chu, W. S., Hong, Y., & Ahn, S. H. (2009). Review of manufacturing processes for soft biomimetic robots. [Article]. *International Journal of Precision Engineering and Manufacturing*, 10(3), 171-181.
- Chua, L. (1971). Memristor-The missing circuit element. *Circuit Theory, IEEE Transactions on*, 18(5), 507-519.
- Clevios. (2013). Conductive Polymers Retrieved 9 September 2013, from <http://clevios.com/en/downloads/heraeus-conductive-polymers-downloads.aspx>

- Coehoorn, R., Pasveer, W. F., Bobbert, P. A., & Michels, M. A. J. (2005). Charge-carrier concentration dependence of the hopping mobility in organic materials with Gaussian disorder. *Physical Review B*, 72(15).
- Corning, I. (2013). Gorilla Glass Retrieved 3 October 2013, 2013, from <http://www.corninggorillaglass.com/faqs/all?page=1>
- Coskun, Y., Cirpan, A., & Toppare, L. (2007). Construction of electrochromic devices using thiophene based conducting polymers. [Article]. *Journal of Materials Science*, 42(1), 368-372.
- Cragon, H. G. (2000). *Computer Architecture and Implementation*. Cambridge: Cambridge University Press.
- Crispin, X., Jakobsson, F. L. E., Crispin, A., Grim, P. C. M., Andersson, P., Volodin, A., . . . Berggren, M. (2006). The Origin of the High Conductivity of Poly(3,4-ethylenedioxythiophene)-Poly(styrenesulfonate) (PEDOT-PSS) Plastic Electrodes. *Chemistry of Materials*, 18(18), 4354-4360.
- DARPA. (2013). Systems Of Neuromorphic Adaptive Plastic Scalable Electronics (SyNAPSE), 2013, from [http://www.darpa.mil/Our Work/DSO/Programs/Systems of Neuromorphic Adaptive Plastic Scalable Electronics \(SYNAPSE\).aspx](http://www.darpa.mil/Our_Work/DSO/Programs/Systems_of_Neuromorphic_Adaptive_Plastic_Scalable_Electronics_(SYNAPSE).aspx)
- Das, S., & Appenzeller, J. (2011). FETRAM. An Organic Ferroelectric Material Based Novel Random Access Memory Cell. *Nano Letters*, 11(9), 4003-4007.
- David, M., Ranasinghe, D. C., & Larsen, T. (2011, 12-14 April 2011). A2U2: A stream cipher for printed electronics RFID tags. Paper presented at the RFID (RFID), 2011 IEEE International Conference on.
- de Kok, M. M., Buechel, M., Vulto, S. I. E., van de Weijer, P., Meulen Kamp, E. A., de Winter, S. H. P. M., . . . van Elsbergen, V. (2006). Modification of PEDOT:PSS As Hole Injection Layer in Polymer LEDs *Physics of Organic Semiconductors* (pp. 451-473): Wiley-VCH Verlag GmbH & Co. KGaA.
- Dearnaley, G., Morgan, D. V., & Stoneham, A. M. (1970). A model for filament growth and switching in amorphous oxide films. *Journal of Non-Crystalline Solids*, 4(0), 593-612.
- Deshmukh, A., Morghade, J., Khera, A., & Bajaj, P. (2005). Binary Neural Networks - A CMOS Design Approach. In R. Khosla, R. Howlett & L. Jain (Eds.), *Knowledge-Based Intelligent Information and Engineering Systems* (Vol. 3681, pp. 1291-1296): Springer Berlin Heidelberg.

- Dias, F. M., Antunes, A., & Mota, A. M. (2004). Artificial neural networks: a review of commercial hardware. *Engineering Applications of Artificial Intelligence*, 17(8), 945-952.
- Diller, A. (2010). Why AI and Robotics are going nowhere fast. In J. Vallverdu (Ed.), *Thinking Machines and the Philosophy of Computer Science: Concepts and Principles* (pp. 328-343): IGI Global.
- Drakakis, E. M., Payne, A. J., & Toumazou, C. (1997). Bernoulli operator: a low-level approach to log-domain processing. *Electronics Letters*, 33(12), 1008-1009.
- Ebisawa, F., Kurokawa, T., & Nara, S. (1983). Electrical properties of polyacetylene/polysiloxane interface. *Journal of Applied Physics*, 54(6), 3255-3259.
- Edwards, R. T., & Cauwenberghs, G. (2000). Synthesis of Log-Domain Filters from First-Order Building Blocks. *Analog Integrated Circuits and Signal Processing*, 22(2-3), 177-186.
- EPFL. (2013). The Blue Brain Project, 2013, from <http://bluebrain.epfl.ch/>
- Erokhin, V., Berzina, T., Smerieri, A., Camorani, P., Erokhina, S., & Fontana, M. P. (2010). Bio-inspired adaptive networks based on organic memristors. *Nano Communication Networks*, 1(2), 108-117.
- Ferguson, A. J., Kopidakis, N., Shaheen, S. E., & Rumbles, G. (2011). Dark Carriers, Trapping, and Activation Control of Carrier Recombination in Neat P3HT and P3HT:PCBM Blends. [Article]. *Journal of Physical Chemistry C*, 115(46), 23134-23148. doi: 10.1021/jp208014v
- Fox, D. (2009). Brain-Like Chip May Solve Computers' Big Problem: Energy. *Discover*, (October 2009). Retrieved from <http://discovermagazine.com/2009/oct/06-brain-like-chip-may-solve-computers-big-problem-energy>
- Futurrex. (2013). NR71 Retrieved 3 Oct 2013, 2013, from <http://futurrex.com/en/products/negative-photoresists/negative-etch-resists.html>
- Gaba, S., Sheridan, P., Zhou, J. T., Choi, S., & Lu, W. (2013). Stochastic memristive devices for computing and neuromorphic applications. [Article]. *Nanoscale*, 5(13), 5872-5878.
- Gao, P. R., Benjamin, B. V., & Boahen, K. (2012). Dynamical System Guided Mapping of Quantitative Neuronal Models Onto Neuromorphic Hardware. [Article]. *Ieee Transactions on Circuits and Systems I- Regular Papers*, 59(10), 2383-2394.

- Garnier, F., Horowitz, G., Peng, X., & Fichou, D. (1990). An all-organic "soft" thin film transistor with very high carrier mobility. *Advanced Materials*, 2(12), 592-594.
- Gburek, B., & Wagner, V. (2010). Influence of the semiconductor thickness on the charge carrier mobility in P3HT organic field-effect transistors in top-gate architecture on flexible substrates. *Organic Electronics*, 11(5), 814-819.
- Gergel-Hackett, N., Hamadani, B., Dunlap, B., Suehle, J., Richter, C., Hacker, C., & Gundlach, D. (2009). A Flexible Solution-Processed Memristor. *Electron Device Letters, IEEE*, 30(7), 706-708.
- Ghai, L. (2013). Polyethylene naphthalate Retrieved 19 Nov 2013, 2013, from <http://www.polymerupdate.com/general/special-features/articles/lekhraj/lekhrajghai-14072012-101926.pdf>
- Green, R., Morfa, A., Ferguson, A. J., Kopidakis, N., Rumbles, G., & Shaheen, S. E. (2008). Performance of bulk heterojunction photovoltaic devices prepared by airbrush spray deposition. *Applied Physics Letters*, 92(3).
- Gregg, B. A., Chen, S. G., & Branz, H. M. (2004). On the superlinear increase in conductivity with dopant concentration in excitonic semiconductors. *Applied Physics Letters*, 84(10), 1707-1709.
- Gupta, A. K., & Bhat, N. (2005). Asymmetric cross-coupled differential pair configuration to realize neuron activation function and its derivative. *Circuits and Systems II: Express Briefs, IEEE Transactions on*, 52(1), 10-13.
- Ha, H., & Kim, O. (2008). Bipolar switching characteristics of nonvolatile memory devices based on poly(3,4-ethylenedioxythiophene): poly(styrenesulfonate) thin film. *Applied Physics Letters*, 93(3), 033309.
- Haykin, S. (1998). *Neural Networks: A Comprehensive Foundation*: Pearson Education.
- Heonjun, H., & Ohyun, K. (2010). Electrode-Material-Dependent Switching Characteristics of Organic Nonvolatile Memory Devices Based on Poly(3,4-ethylenedioxythiophene):poly(styrenesulfonate) Film. *Electron Device Letters, IEEE*, 31(4), 368-370.
- Heremans, P., Gelinck, G. H., Muller, R., Baeg, K.-J., Kim, D.-Y., & Noh, Y.-Y. (2011). Polymer and Organic Nonvolatile Memory Devices. *Chemistry of Materials*, 23(3), 341-358.
- Herlogsson, L., Coelle, M., Tierney, S., Crispin, X., & Berggren, M. (2010). Low-Voltage Ring Oscillators Based on Polyelectrolyte-

- Gated Polymer Thin-Film Transistors. *Advanced Materials*, 22(1), 72.
- Hodgkin, A. L., & Huxley, A. F. (1952). A Quantitative Description Of Membrane Current And Its Application To Conduction And Excitation In Nerve. [Article]. *Journal of Physiology-London*, 117(4), 500-544.
- Hoover, A. M., & Fearing, R. S. (2008, 19-23 May 2008). *Fast scale prototyping for folded millirobots*. Paper presented at the Robotics and Automation, 2008. ICRA 2008. IEEE International Conference on.
- Horowitz, G. (2010a). Interfaces in Organic Field-Effect Transistors. In T. Grasser & G. Meller (Eds.), *Advances in Polymer Science* (Vol. 223): Springer-Verlag Berlin Heidelberg.
- Horowitz, G. (2010b). Interfaces in Organic Field-Effect Transistors *Organic Electronics* (Vol. 223, pp. 113-153).
- Houili, H., Tutis, E., & Izquierdo, R. (2010). Modeling nanoparticle embedded organic memory devices. *Organic Electronics*, 11(4), 514-520.
- Howatt, G. N., Breckenridge, R. G., & Brownlow, J. M. (1947). FABRICATION OF THIN CERAMIC SHEETS FOR CAPACITORS*. *Journal of the American Ceramic Society*, 30(8), 237-242.
- HRL. (2013). Center for Neural and Emergent Systems, 2013, from http://www.hrl.com/laboratories/cnes/cnes_main.html
- Hui, W., Hai, L., & Pino, R. E. (2012, 10-15 June 2012). *Memristor-based synapse design and training scheme for neuromorphic computing architecture*. Paper presented at the Neural Networks (IJCNN), The 2012 International Joint Conference on.
- Hwang, Y.-J., Murari, N. M., & Jenekhe, S. A. (2013). New n-type polymer semiconductors based on naphthalene diimide and selenophene derivatives for organic field-effect transistors. *Polymer Chemistry*, 4(11), 3187-3195.
- IBM. (2013). Cognitive Computing, 2013, from <http://www.research.ibm.com/cognitive-computing/>
- Ikushima, K., John, S., Yokoyama, K., & Nagamitsu, S. (2009). A practical multilayered conducting polymer actuator with scalable work output. *Smart Materials & Structures*, 18(9).
- Indiveri, G., Linares-Barranco, B., Hamilton, T. J., van Schaik, A., Etienne-Cummings, R., Delbruck, T., . . . Boahen, K. (2011).

- Neuromorphic silicon neuron circuits. [Review]. *Frontiers in Neuroscience*, 5.
- Indiveri, G., Linares-Barranco, B., Legenstein, R., Deligeorgis, G., & Prodromakis, T. (2013). Integration of nanoscale memristor synapses in neuromorphic computing architectures. *Nanotechnology*, 24(384010).
- Islam, M. S., Johns, C., Long, D., Ohlberg, D. A. A., Shih-Yuan, W., & Williams, R. S. (2010, 18-20 Dec. 2010). *Memristors based on an organic monolayer of molecules and a thin film of solid electrolytes*. Paper presented at the Electrical and Computer Engineering (ICECE), 2010 International Conference on.
- Jackson, P. C. (2013). *Introduction to Artificial Intelligence*: Dover.
- Jeong, H. Y., Kim, J. Y., Yoon, T. H., & Choi, S. Y. (2010). Bipolar resistive switching characteristics of poly(3,4-ethylene-dioxythiophene): Poly(styrenesulfonate) thin film. [Article; Proceedings Paper]. *Current Applied Physics*, 10(1), E46-E49.
- Jo, H., Ko, J., Lim, J. A., Chang, H. J., & Kim, Y. S. (2013). Organic Nonvolatile Resistive Switching Memory Based on Molecularly Entrapped Fullerene Derivative within a Diblock Copolymer Nanostructure. [Article]. *Macromolecular Rapid Communications*, 34(4), 355-361.
- Jo, S. H., Chang, T., Ebong, I., Bhadviya, B. B., Mazumder, P., & Lu, W. (2010). Nanoscale Memristor Device as Synapse in Neuromorphic Systems. [Article]. *Nano Letters*, 10(4), 1297-1301.
- Jung, J. H., & Kim, T. W. (2011). The effect of the trap density and depth on the current bistability in organic bistable devices. *Journal of Applied Physics*, 110(4).
- Kandel, E. R., Schwartz, J. H., & Jessell, T. M. (2000). *Principles of neural science*: McGraw-Hill, Health Professions Division.
- Kim, B. C., Too, C. O., Kwon, J. S., Bo, J. M., & Wallace, G. G. (2011). A flexible capacitor based on conducting polymer electrodes. *Synthetic Metals*, 161(11-12), 1130-1132.
- Kim, C.-J., Choi, S.-J., Kim, S., Han, J.-W., Kim, H., Yoo, S., & Choi, Y.-K. (2011). Photoinduced Memory with Hybrid Integration of an Organic Fullerene Derivative and an Inorganic Nanogap-Embedded Field-Effect Transistor for Low-Voltage Operation. *Advanced Materials*, 23(29), 3326.
- Kim, K. H., Gaba, S., Wheeler, D., Cruz-Albrecht, J. M., Hussain, T., Srinivasa, N., & Lu, W. (2012). A Functional Hybrid Memristor

- Crossbar-Array/CMOS System for Data Storage and Neuromorphic Applications. [Article]. *Nano Letters*, 12(1), 389-395.
- Kim, M., Park, B., & Kim, O. (2009). Unipolar Memory Operation of Resistance Random-Access Memory Using Compliance Current Controller. [Article; Proceedings Paper]. *Japanese Journal of Applied Physics*, 48(4).
- Kittel, C. (1996). *Introduction to solid state physics*: Wiley.
- Kopola, P., Tuomikoski, M., Suhonen, R., & Maaninen, A. (2009). Gravure printed organic light emitting diodes for lighting applications. *Thin Solid Films*, 517(19), 5757-5762.
- Krebs, F. C., Gevorgyan, S. A., & Alstrup, J. (2009). A roll-to-roll process to flexible polymer solar cells: model studies, manufacture and operational stability studies. *Journal of Materials Chemistry*, 19(30), 5442-5451.
- Kuang, Y., Huang, R., Tang, Y., Ding, W., Zhang, L., & Wang, Y. (2010). Flexible Single-Component-Polymer Resistive Memory for Ultrafast and Highly Compatible Nonvolatile Memory Applications. *IEEE Electron Device Letters*, 31(7), 758-760.
- Kuhnle, A. (2009). Self-assembly of organic molecules at metal surfaces. *Current Opinion in Colloid & Interface Science*, 14(2), 157-168. doi: 10.1016/j.cocis.2008.01.001
- Kushto, G. P., Kim, W. H., & Kafafi, Z. H. (2005). Flexible organic photovoltaics using conducting polymer electrodes. *Applied Physics Letters*, 86(9).
- Lampert, M. A., & Mark, P. (1970). *Current injection in solids*: Academic Press.
- Lee, J., Hong, W. G., & Lee, H. (2011). Non-volatile organic memory effect with thickness control of the insulating LiF charge trap layer. *Organic Electronics*, 12(6), 988-992.
- Lee, J. H., & Likharev, K. K. (2007). Defect-tolerant nanoelectronic pattern classifiers. [Article]. *International Journal of Circuit Theory and Applications*, 35(3), 239-264.
- Lehtonen, E., Poikonen, J. H., & Laiho, M. (2010). Two memristors suffice to compute all Boolean functions. *Electronics Letters*, 46(3), 230-230.
- Likharev, K. K., Mayr, A., Muckra, I., & Turel, O. (2003). CrossNets - High-performance neuromorphic architectures for CMOL circuits. In J. R. Reimers, C. A. Picconatto, J. C. Ellenbogen & R. Shashidhar

- (Eds.), *Molecular Electronics Iii* (Vol. 1006, pp. 146-163). New York: New York Acad Sciences.
- Lim, J. A., Cho, J. H., Park, Y. D., Kim, D. H., Hwang, M., & Cho, K. (2006). Solvent effect of inkjet printed source/drain electrodes on electrical properties of polymer thin-film transistors. *Applied Physics Letters*, 88(8), 082102-082102-082103.
- Lin, C. W., Wang, D. Y., Tai, Y., Jiang, Y. T., Chen, M. C., Chen, C. C., . . . Chen, Y. F. (2011). Type-II heterojunction organic/inorganic hybrid non-volatile memory based on FeS(2) nanocrystals embedded in poly(3-hexylthiophene). *Journal of Physics D-Applied Physics*, 44(29).
- Lin, H.-T., Pei, Z., & Chan, Y.-J. (2007). Carrier transport mechanism in a nanoparticle-incorporated organic bistable memory device. *IEEE Electron Device Letters*, 28(7), 569-571.
- Liu, B., Hu, M., Li, H., Mao, Z.-H., Chen, Y., Huang, T., & Zhang, W. (2013). *Digital-assisted noise-eliminating training for memristor crossbar-based analog neuromorphic computing engine*. Paper presented at the Proceedings of the 50th Annual Design Automation Conference, Austin, Texas.
- Liu, Y., Cui, T. H., & Varahramyan, K. (2003). All-polymer capacitor fabricated with inkjet printing technique. *Solid-State Electronics*, 47(9), 1543-1548.
- Lloyd, M. T., Olson, D. C., Lu, P., Fang, E., Moore, D. L., White, M. S., . . . Hsu, J. W. P. (2009). Impact of contact evolution on the shelf life of organic solar cells. *Journal of Materials Chemistry*, 19(41), 7638-7642.
- Lopez, M. A., Sanchez, J. C., & Estrada, M. (2008, 28-30 April 2008). *Characterization of PEDOT:PSS dilutions for inkjet printing applied to OLED fabrication*. Paper presented at the Devices, Circuits and Systems, 2008. ICCDCS 2008. 7th International Caribbean Conference on.
- Ma, H., Yip, H.-L., Huang, F., & Jen, A. K. Y. (2010). Interface Engineering for Organic Electronics. *Advanced Functional Materials*, 20(9), 1371-1388.
- Ma, L. P., Liu, J., & Yang, Y. (2002). Organic electrical bistable devices and rewritable memory cells. *Applied Physics Letters*, 80(16), 2997-2999.
- Ma, L. P., Xu, Q. F., & Yang, Y. (2004). Organic nonvolatile memory by controlling the dynamic copper-ion concentration within organic layer. *Applied Physics Letters*, 84(24), 4908-4910.

- Maass, W., Legenstein, R., & Markram, H. (2002). A new approach towards vision suggested by biologically realistic neural microcircuit models. In H. H. Bulthoff, S. W. Lee, T. A. Poggio & C. Wallraven (Eds.), *Biologically Motivated Computer Vision, Proceedings* (Vol. 2525, pp. 282-293). Berlin: Springer-Verlag Berlin.
- Maeda, S., Hara, Y., Yoshida, R., & Hashimoto, S. (2008). Self-Oscillating Gel Actuator for Chemical Robotics. *Advanced Robotics*, 22(12), 1329-1342.
- Mamo, M. A., Machado, W. S., van Otterlo, W. A. L., Coville, N. J., & Huemmelgen, I. A. (2010). Simple write-once-read-many-times memory device based on a carbon sphere-poly(vinylphenol) composite. *Organic Electronics*, 11(11), 1858-1863.
- Manuelli, A., Knobloch, A., Berndt, A., & Clemens, W. (2002, 2002). *Applicability of coating techniques for the production of organic field effect transistors*. Paper presented at the Polymers and Adhesives in Microelectronics and Photonics, 2002. POLYTRONIC 2002. 2nd International IEEE Conference on.
- Marks, P. (2012). Online spat over who joins memristor club. Retrieved from <http://www.newscientist.com/article/mg21328535.200-online-spat-over-who-joins-memristor-club.html#.UjnmzcZMnVU>
- Mathworks. (2013). Neural Network Toolbox, from <http://www.mathworks.com/help/nnet/index.html>
- McGimpsey, W. G., Samaniego, W. N., Chen, L., & Wang, F. (1998). Singlet-Singlet, Triplet-Triplet, and "Optically-Controlled" Energy Transfer in Polychromophores. Preliminary Models for a Molecular Scale Shift Register. *The Journal of Physical Chemistry A*, 102(45), 8679-8689.
- Mead, C. (1989). *Analog VLSI and neural systems*: Addison-Wesley.
- Mead, C. (1990). Neuromorphic electronic systems. *Proceedings of the IEEE*, 78(10), 1629-1636.
- Meuffels, P., & Schroeder, H. (2011). Comment on "Exponential ionic drift: fast switching and low volatility of thin-film memristors" by D.B. Strukov and R.S. Williams in Appl. Phys. A (2009) 94: 515-519. *Applied Physics A*, 105(1), 65-67.
- Meuffels, P., & Soni, R. (2012). Fundamental Issues and Problems in the Realization of Memristors. Retrieved from <http://arxiv.org/ftp/arxiv/papers/1207/1207.7319.pdf>
- Moller, S., Perlov, C., Jackson, W., Taussig, C., & Forrest, S. R. (2003). A polymer/semiconductor write-once read-many-times memory. *Nature*, 426(6963), 166-169.

- Mu, H., Li, W., Jones, R., Steckl, A., & Klotzkin, D. (2007). A comparative study of electrode effects on the electrical and luminescent characteristics of Alq3/TPD OLED: Improvements due to conductive polymer (PEDOT) anode. *Journal of Luminescence*, 126(1), 225-229.
- Myny, K., Beenhakkers, M. J., van Aerle, N. A. J. M., Gelinck, G. H., Genoe, J., Dehaene, W., & Heremans, P. (2009, 8-12 Feb. 2009). A 128b organic RFID transponder chip, including Manchester encoding and ALOHA anti-collision protocol, operating with a data rate of 1529b/s. Paper presented at the Solid-State Circuits Conference - Digest of Technical Papers, 2009. ISSCC 2009. IEEE International.
- Naarmann, H. (2000). *Polymers, Electrically Conducting Ullmann's Encyclopedia of Industrial Chemistry*: Wiley-VCH Verlag GmbH & Co. KGaA.
- Naber, R. C. G., Asadi, K., Blom, P. W. M., de Leeuw, D. M., & de Boer, B. (2010). Organic Nonvolatile Memory Devices Based on Ferroelectricity. *Advanced Materials*, 22(9), 933-945.
- Nalwa, H. S. (1997). *Handbook of Organic Conductive Molecules and Polymers: Conductive polymers : spectroscopy and physical properties*: Wiley.
- Nardes, A. M. (2007). *On the conductivity of PEDOT:PSS thin films*. Doctoral degree, Technische Universiteit Eindhoven, Eindhoven.
- Nardes, A. M., Kemerink, M., de Kok, M. M., Vinken, E., Maturova, K., & Janssen, R. A. J. (2008). Conductivity, work function, and environmental stability of PEDOT : PSS thin films treated with sorbitol. *Organic Electronics*, 9(5), 727-734.
- Nawrocki, R., Voyles, R., & Shaheen, S. (2012). Polymer and Nanoparticle-Composite Bistable Devices: Physics of Operation and Initial Applications. In R. Kozma, R. E. Pino & G. E. Pazienza (Eds.), *Advances in Neuromorphic Memristor Science and Applications* (Vol. 4, pp. 291-314): Springer Netherlands.
- Nawrocki, R. A., Galiger, E. M., Bailey, B. A., Jiang, X., Voyles, R. M., Kopidakis, N., . . . Shaheen, S. E. (2013). An Inverted, Organic WORM Device Based on PEDOT:PSS with Very Low Turn-On Voltage. *under review in Organic Electronics*.
- Nawrocki, R. A., Shaheen, S. E., & Voyles, R. M. (2011, July 31 2011-Aug. 5 2011). A neuromorphic architecture from single transistor neurons with organic bistable devices for weights. Paper presented at the Neural Networks (IJCNN), The 2011 International Joint Conference on.

- Nawrocki, R. A., Shaheen, S. E., Yang, X., & Voyles, R. M. (2009). *Towards an All-Polymer Robot for Search and Rescue*. Paper presented at the IEEE International Workshop on Safety, Security and Rescue Robots, Denver, CO.
- Nawrocki, R. A., Xiaoting, Y., Shaheen, S. E., & Voyles, R. M. (2011, 9-13 May 2011). *Structured Computational Polymers for a soft robot: Actuation and cognition*. Paper presented at the Robotics and Automation (ICRA), 2011 IEEE International Conference on.
- Neamen, D. (2009). *Microelectronics Circuit Analysis and Design*: McGraw-Hill Education.
- Ortiz, R. P., Facchetti, A., & Marks, T. J. (2010). High-k Organic, Inorganic, and Hybrid Dielectrics for Low-Voltage Organic Field-Effect Transistors. [Review]. *Chemical Reviews*, 110(1), 205-239.
- Osada, Y., & De Rossi, D. E. (1999). *Polymer Sensors and Actuators*: Springer.
- Ouyang, J., Chu, C. W., Chen, F. C., Xu, Q., & Yang, Y. (2005). High-Conductivity Poly(3,4-ethylenedioxythiophene):Poly(styrene sulfonate) Film and Its Application in Polymer Optoelectronic Devices. *Advanced Functional Materials*, 15(2), 203-208.
- Ouyang, J., Xu, Q., Chu, C.-W., Yang, Y., Li, G., & Shinar, J. (2004). On the mechanism of conductivity enhancement in poly(3,4-ethylenedioxythiophene):poly(styrene sulfonate) film through solvent treatment. *Polymer*, 45(25), 8443-8450.
- Owens, R. M., & Malliaras, G. G. (2010). Organic Electronics at the Interface with Biology. *Mrs Bulletin*, 35(6), 449-456. doi: 10.1557/mrs2010.583
- Padinger, F., Brabec, C. J., Fromherz, T., Hummelen, J. C., & Sariciftci, N. S. (2000). Fabrication large area photovoltaic devices containing. *Opto-Electronics Review*, 8(4), 4.
- Padinger, F., Brabec, C. J., Fromherz, T., Hummelen, J. C., & Sariciftci, N. S. (2000). Fabrication of large area photovoltaic devices containing various blends of polymer and fullerene derivatives by using the doctor blade technique. [Article]. *Opto-Electronics Review*, 8(4), 280-283.
- Peierls, R. E. (1955). *Quantum Theory of Solids*: Clarendon Press.
- Perrin, D. P., Know, A., & Howel, R. R. (2004). *A Novel Actuated Tethered Design for Rescue Robots Using Hydraulic Transients*. Paper presented at the IEEE International Conference on Robotics and Automation.

- Pershin, Y. V., & Di Ventra, M. (2010). Experimental demonstration of associative memory with memristive neural networks. *Neural Networks*, 23(7), 881-886.
- Potember, R. S., Poehler, T. O., & Cowan, D. O. (1979). Electrical switching and memory phenomena in Cu-TCNQ thin films. *Applied Physics Letters*, 34(6), 405-407.
- Reimann, M. W., Anastassiou, C. A., Perin, R., Hill, S. L., Markram, H., & Koch, C. (2013). A Biophysically Detailed Model of Neocortical Local Field Potentials Predicts the Critical Role of Active Membrane Currents. [Article]. *Neuron*, 79(2), 375-390.
- Renaud, S., Tomas, J., Bornat, Y., Daouzli, A., & Saighi, S. (2007, 27-30 May 2007). *Neuromimetic ICs with analog cores: an alternative for simulating spiking neural networks*. Paper presented at the Circuits and Systems, 2007. ISCAS 2007. IEEE International Symposium on.
- Ro, H. W., Popova, V., Chen, L., Forster, A. M., Ding, Y., Alvine, K. J., . . . Soles, C. L. (2011). Cubic Silsesquioxanes as a Green, High-Performance Mold Material for Nanoimprint Lithography. *Advanced Materials*, 23(3), 414-420.
- Rose, G. S., Pino, R., & Qing, W. (2011, July 31 2011-Aug. 5 2011). *A low-power memristive neuromorphic circuit utilizing a global/local training mechanism*. Paper presented at the Neural Networks (IJCNN), The 2011 International Joint Conference on.
- Salinga, M., & Wuttig, M. (2011). Phase-Change Memories on a Diet. *Science*, 332(6029), 543-544.
- Sansen, W. M. C. (2007). *Analog Design Essentials*: Springer.
- Schaefer, M., Holtkamp, J., & Gillner, A. (2011). Ablation of PEDOT/PSS with excimer lasers for micro structuring of organic electronic devices. *Synthetic Metals*, 161(11-12), 1051-1057. doi: <http://dx.doi.org/10.1016/j.synthmet.2011.03.014>
- Sekitani, T., Noguchi, Y., Zschieschang, U., Klauk, H., & Someya, T. (2008). Organic transistors manufactured using inkjet technology with subfemtoliter accuracy. *Proceedings of the National Academy of Sciences of the United States of America*, 105(13), 4976-4980.
- Senturia, S. D. (2001). *Microsystem Design*: Kluwer Academic Publishers.
- Seo, J., Brezzo, B., Yong, L., Parker, B. D., Esser, S. K., Montoye, R. K., . . . Friedman, D. J. (2011, 19-21 Sept. 2011). *A 45nm CMOS neuromorphic chip with a scalable architecture for learning in networks of spiking neurons*. Paper presented at the Custom Integrated Circuits Conference (CICC), 2011 IEEE.

- Serrano-Gotarredona, T., Masquelier, T., Prodromakis, T., Indiveri, G., & Linares-Barranco, B. (2013). STDP and STDP Variations with Memristors for Spiking Neuromorphic Learning Systems. [Focused Review]. *Frontiers in neuroscience*, 7.
- Shaheen, S. E., Ginley, D. S., & Jabbour, G. E. (2005). Organic-based photovoltaics. toward low-cost power generation. *Mrs Bulletin*, 30(1), 10-19.
- Shaheen, S. E., Radspinner, R., Peyghambarian, N., & Jabbour, G. E. (2001). Fabrication of bulk heterojunction plastic solar cells by screen printing. *Applied Physics Letters*, 79(18), 2996-2998.
- Sharad, M., Augustine, C., Panagopoulos, G., & Roy, K. (2012). Proposal For Neuromorphic Hardware Using Spin Devices. Retrieved from <http://arxiv.org/ftp/arxiv/papers/1206/1206.3227.pdf>
- Sharp, T., Galluppi, F., Rast, A., & Furber, S. (2012). Power-efficient simulation of detailed cortical microcircuits on SpiNNaker. *Journal of Neuroscience Methods*, 210(1), 110-118.
- Shepherd, R. F., Ilievski, F., Choi, W., Morin, S. A., Stokes, A. A., Mazzeo, A. D., . . . Whitesides, G. M. (2011). Multigait soft robot. *Proceedings of the National Academy of Sciences of the United States of America*, 108(51), 20400-20403.
- Sigma-Aldrich. (2013). NR71 Retrieved 3 October 2013, 2013, from <http://www.sigmaaldrich.com/catalog/product/aldrich/651796?lang=en®ion=US>
- Silver, R., Boahen, K., Grillner, S., Kopell, N., & Olsen, K. L. (2007). Neurotech for neuroscience: Unifying concepts, organizing principles, and emerging tools. [Article]. *Journal of Neuroscience*, 27(44), 11807-11819.
- Skotheim, T. A., Elsenbaumer, R. L., & Reynolds, J. R. (1998). *Handbook of Conducting Polymers*: M. Dekker.
- Smooth-Sil. (2013a). MSDS Retrieved 3 October 2013, from http://www.smooth-on.com/msds/files/SMOOTH-SIL_930_935_940.pdf
- Smooth-Sil. (2013b). Product Information Retrieved 3 October 2013, from http://www.smooth-on.com/tb/files/SMOOTH-SIL_SERIES_TB.pdf
- Snider, G. S. (2007). Self-organized computation with unreliable, memristive nanodevices. *Nanotechnology*, 18(36).
- So, F. (2010). *Organic Electronics: Materials, Processing, Devices and Applications*: CRC Press.

- Son, D. I., Kim, T. W., Shim, J. H., Jung, J. H., Lee, D. U., Lee, J. M., . . . Choi, W. K. (2010). Flexible Organic Bistable Devices Based on Graphene Embedded in an Insulating Poly(methyl methacrylate) Polymer Layer. *Nano Letters*, 10(7), 2441-2447.
- Son, D. I., Shim, J. H., Park, D. H., Jung, J. H., Lee, J. M., Park, W. I., . . . Choi, W. K. (2011). Polymer-ultrathin graphite sheet-polymer composite structured flexible nonvolatile bistable organic memory devices. *Nanotechnology*, 22(29), 295203.
- Son, D. I., You, C. H., Kim, W. T., Jung, J. H., & Kim, T. W. (2009). Electrical bistabilities and memory mechanisms of organic bistable devices based on colloidal ZnO quantum dot-polymethylmethacrylate polymer nanocomposites. *Applied Physics Letters*, 94(13).
- Sondergaard, R. R., Hosel, M., & Krebs, F. C. (2013). Roll-to-Roll fabrication of large area functional organic materials. [Review]. *Journal of Polymer Science Part B-Polymer Physics*, 51(1), 16-34.
- Sonoplot. (2013). GIX Microplotter II Retrieved 24 September 2013, from <http://www.sonoplot.com/products/gix-microplotter-ii>
- Storace, M., Julian, P., & Parodi, M. (2001, 6-9 May 2001). *Towards the circuit implementation of the Hodgkin-Huxley neuron model: A PWL approach*. Paper presented at the Circuits and Systems, 2001. ISCAS 2001. The 2001 IEEE International Symposium on.
- Strukov, D. B., & Likharev, K. K. (2012). Reconfigurable Nano-Crossbar Architectures. In R. Waser (Ed.), *Nanoelectronics and Information Technology* (3rd ed.): Wiley-VCH.
- Strukov, D. B., Snider, G. S., Stewart, D. R., & Williams, R. S. (2008). The missing memristor found. *Nature*, 453(7191), 80-83.
- Sun, S. S., & Dalton, L. R. (2008). *Introduction to Organic Electronic and Optoelectronic Materials and Devices*: CRC Press.
- Sze, S. M., & Ng, K. K. (2006). *Physics of Semiconductor Devices*: Wiley.
- Teijin. (2013). Q65F Retrieved 3 Oct 2013, 2013, from http://www.teijindupontfilms.jp/english/pdf/teonex_q65f.pdf
- Tinivella, R., Shen, S., Pirola, M., Ghione, G., & Camarchia, V. (2010, 23-28 May 2010). *A device-level analog and digital subsystem SPICE library for the design of low-cost pentacene OFET RFIDs*. Paper presented at the Microwave Symposium Digest (MTT), 2010 IEEE MTT-S International.

- Trivedi, D., Rahn, C. D., Kier, W. M., & Walker, I. D. (2008). Soft robotics: Biological inspiration, state of the art, and future research. *Applied Bionics and Biomechanics*, 5(3), 99-117.
- Türel, Ö., Lee, J. H., Ma, X., & Likharev, K. K. (2004). Neuromorphic architectures for nanoelectronic circuits. *International Journal of Circuit Theory and Applications*, 32(5), 277-302.
- van Schaik, A. (2001). Building blocks for electronic spiking neural networks. *Neural Networks*, 14(6-7), 617-628.
- Velu, G., Legrand, C., Tharaud, O., Chapoton, A., Remiens, D., & Horowitz, G. (2001). Low driving voltages and memory effect in organic thin-film transistors with a ferroelectric gate insulator. *Applied Physics Letters*, 79(5), 659-661.
- Voyles, R. M. (2013). Collaborative Mechatronics Laboratory Retrieved 3 October 2013, 2013, from <http://mysite.du.edu/~rvoyles/>
- Wallis, W. E. (1972). United States Patent No. 3689810. U. S. Patent.
- Wang, J., Cheng, X., Caironi, M., Gao, F., Yang, X., & Greenham, N. C. (2011). Entirely solution-processed write-once-read-many-times memory devices and their operation mechanism. *Organic Electronics*, 12(7), 1271-1274.
- Wang, J., Sun, B., Gao, F., & Greenham, N. C. (2010). Memristive devices based on solution-processed ZnO nanocrystals. *physica status solidi (a)*, 207(2), 484-487.
- Wood, R. J., Avadhanula, S., Sahai, R., Steltz, E., & Fearing, R. S. (2008). Microrobot Design Using Fiber Reinforced Composites. *Journal of Mechanical Design*, 130(5), 052304-052304.
- Xia, Y., & Ouyang, J. (2010). Anion effect on salt-induced conductivity enhancement of poly(3,4-ethylenedioxythiophene):poly(styrenesulfonate) films. *Organic Electronics*, 11(6), 1129-1135.
- Xia, Y., Zhang, H., & Ouyang, J. (2010). Highly conductive PEDOT:PSS films prepared through a treatment with zwitterions and their application in polymer photovoltaic cells. [10.1039/C0JM01593H]. *Journal of Materials Chemistry*, 20(43), 9740-9747.
- Xia, Y. J., & Ouyang, J. Y. (2009). Salt-Induced Charge Screening and Significant Conductivity Enhancement of Conducting Poly(3,4-ethylenedioxythiophene):Poly(styrenesulfonate). [Article]. *Macromolecules*, 42(12), 4141-4147.
- Xia, Y. J., & Ouyang, J. Y. (2010). Significant Conductivity Enhancement of Conductive Poly(3,4-ethylenedioxythiophene):

- Poly(styrenesulfonate) Films through a Treatment with Organic Carboxylic Acids and Inorganic Acids. [Article]. *Acs Applied Materials & Interfaces*, 2(2), 474-483.
- Yang, X. (2010). *Toward a Distributed Actuation and Cognition Means for a Miniature Soft Robot*. Master of Science, Univeresity of Denver, Denver.
- Yang, X., Voyles, R. M., Kang, L., & Povilus, S. (2009, 3-6 Nov. 2009). *Experimental comparison of robotics locomotion with passive tether and active tether*. Paper presented at the Safety, Security & Rescue Robotics (SSRR), 2009 IEEE International Workshop on.
- Yoo, B., Madgavkar, A., Jones, B. A., Nadkarni, S., Facchetti, A., Dimmler, K., . . . Dodabalapur, A. (2006). Organic Complementary D Flip-Flops Enabled by Perylene Diimides and Pentacene. *Electron Device Letters, IEEE*, 27(9), 737-739.
- Yu, T., & Cauwenberghs, G. (2010). Analog VLSI Biophysical Neurons and Synapses With Programmable Membrane Channel Kinetics. *Biomedical Circuits and Systems, IEEE Transactions on*, 4(3), 139-148.
- Zhang, D., Ryu, K., Liu, X., Polikarpov, E., Ly, J., Tompson, M. E., & Zhou, C. (2006). Transparent, conductive, and flexible carbon nanotube films and their application in organic light-emitting diodes. *Nano Letters*, 6(9), 1880-1886.
- Zhang, J., Li, C. M., Chan-Park, M. B., Zhou, Q., Gan, Y., Qin, F., . . . Chen, T. (2007). Fabrication of thin-film organic transistor on flexible substrate via ultraviolet transfer embossing. *Applied Physics Letters*, 90(24).

Appendix A: List of Publications

- Nawrocki, R.A., Voyles, R.M., Shaheen, S.E., "New Fabrication Processes For Polymer Neuromorphic Engineering", in progress, 2014**
- Nawrocki, R.A., Voyles, R.M., Yang, X., Shaheen, S.E., "Pushing on a Rope: 1-Dimensional Structured Computational Polymers for an All-Polymer Urban Search and Rescue Robot", in progress, *IEEE Transactions on Electron Devices*, 2014**
- Nawrocki, R.A., Voyles, R.M., Shaheen, S.E., "Improved Carrier Mobilities in OFET Due to In Situ Application of Electric Field Poling", in progress, *Advanced Materials*, 2014**
- Nava, A., Barkeloo, J.T., Nawrocki, R.A., ray, S., Ghosh, K., Taylor, R.P., Shaheen, S.E., "Modulation of Fractal Structure in P. Dendritiformis Bacterial Colonies via Nutrient Modification", in progress, *New Journal of Physics*, 2014**
- Nawrocki, R.A., Voyles, R.M., Shaheen, S.E., "Neurons in Polymer: Hardware Neural Unites based on Polymer Memristive Devices and Transistors", under review in *IEEE Transactions on Electron Devices*, 2013**
- Nawrocki, R.A., Galiger, E.M., Ostrowski, D., Bailey, B.A., Jiang, X., Voyles, R.M., Kopidakis, N., Olson, D.C., Shaheen, S.E., "An Inverted, Organic WORM Device Based on PEDOT:PSS with Very Low Turn-On Voltage", under review in *Organic Electronics*, 2013**
- Cui, Y., Voyles, R.M., Nawrocki, R.A., Jiang, G., "The Morphing Bus: A New Paradigm in Peripheral Interconnect Bus", *IEEE Transactions on Components, Packaging and Manufacturing Technology*, 2013**
- Nawrocki, R.A., Voyles, R.M., Shaheen, S.E., "Polymer and Nanoparticle-Composite Bistable Devices: Physics of Operation and Initial Applications", *Advances in Neuromorphic Memristor Science and Applications* (Book chapter), 2012**
- Nawrocki, R.A., Shalaan, M., Shaheen, S. E., Lorenzon, N.M., "Monitoring Performance Degradation of Cerebellar Functions Using Computational Neuroscience Methods: Implications on Neurological Diseases", *Public Library of Science*, 2012**
- Nawrocki, R.A., Frutiger, D. R., Voyles, R.M., Nelson, B. J., "Wireless Electrical Power to Sub-millimeter Robots", 2012 *IEEE***

International Conference on Intelligent Robotics and Automation, 2012

Nawrocki, R. A., "Simulation, Application, And Resilience of An Organic Neuromorphic Architecture, Made With Organic Bistable Devices And Organic Field Effect Transistors", Master of Science, University of Denver, 2011

Nawrocki, R.A., Yang, X., Shaheen, S.E., Voyles, R.M., "Structured Computational Polymers for a Soft Robot: Actuation and Cognition", 2011 *IEEE International Conference on Robotics and Automation, 2011*

Nawrocki, R.A., Shaheen, S.E., Voyles, R.M., "A Neuromorphic Architecture from Single Transistor Neurons With Organic Bistable Devices for Weights", 2011 *IEEE International Joint Conference on Neural Networks, 2011*

Nawrocki, R.A., Voyles, R.M., "Artificial Neural Network Performance Degradation Under Network Damage: Stuck-At Faults", 2011 *IEEE International Joint Conference on Neural Networks, 2011*

Nawrocki, R.A., Voyles, R.M., Shaheen, S.E., "Structured Computational Polymers for Safety, Security, and Rescue Robotics", *IEEE Workshop on Safety, Security and Rescue Robots, 2011*

Nawrocki, R.A., Voyles, R.M., Shaheen, S.E., "Simulating Hardware Neural Networks with Organic Memristors and Organic Field Effect Transistors", 2010 *Artificial Neural Networks In Engineering, 2010*

Nawrocki, R.A., Voyles, R.M., Shalaan, M., "Monitoring Artificial Neural Network Performance Degradation Under Network Damage", 2010 *Artificial Neural Networks In Engineering, 2010*

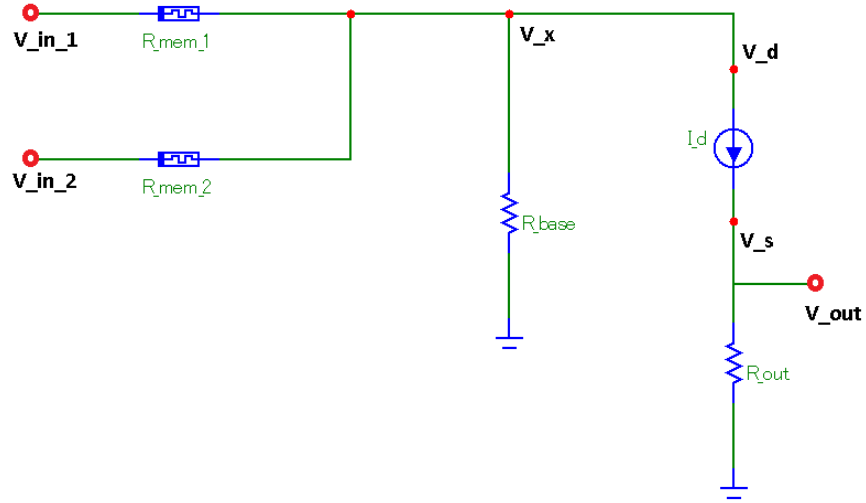
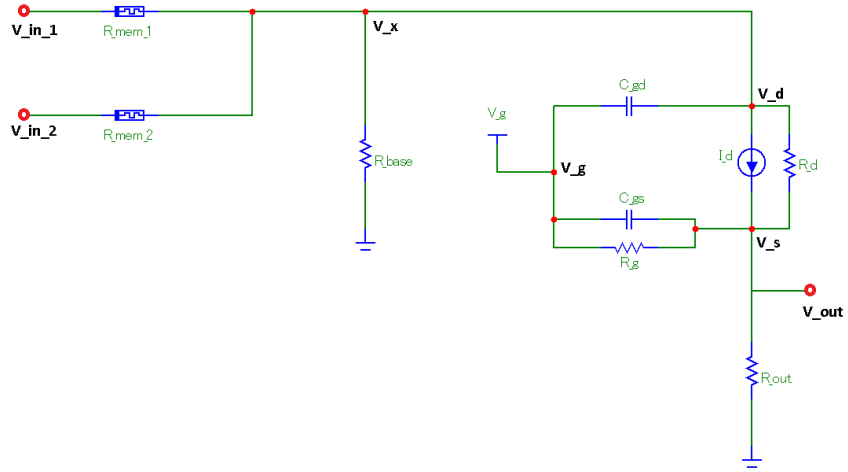
Nawrocki, R.A., Shaheen, S.E., Yang, X., Voyles, R.M., "Towards an All-Polymer Robot for Search and Rescue", 2009 *IEEE International Workshop on Safety, Security and Rescue Robotics, 2009*

Nawrocki, R.A., Abisaleh, D., Rojas-Cessa, R., "Implementation of Scheduling Algorithms for Input-Queued Packet Switches: an Undergraduate Senior Project Experience", *Proceedings of the X Workshop, Iberchip, 2004*

Appendix B: PNC Simulation

$$I_D = \begin{cases} \mu * C_x * \frac{W}{L} * \left(V_{GS} - V_T - \frac{V_{DS}}{2} \right) * V_{DS} & \text{for } V_{GS} < V_T, V_{DS} < V_{GS} - V_T \text{ (linear)} \\ \mu * C_x * \frac{W}{L} * \frac{(V_{GS} - V_T)^2}{2} (1 + \lambda V_{DS}) & \text{for } V_{GS} < V_T, V_{DS} \geq V_{GS} - V_T \text{ (saturation)} \\ I_{leakage} & \text{for } V_{GS} > V_T \text{ (OFF)} \end{cases}$$

$$\mu = \mu_0 * (-V_{GS} + V_T)^\gamma; \quad \lambda = \frac{1}{V_A}$$



Linear

$$i_D = \frac{V_S}{R_{OUT}} = \mu C_x \frac{W}{L} \left(V_{GS} - V_T - \frac{V_{DS}}{2} \right) V_{DS}$$

$$\frac{V_S}{R_{OUT}} = \mu_0 (-V_{GS} + V_T)^\gamma C_x \frac{W}{L} \left(V_{GS} - V_T - \frac{V_{DS}}{2} \right) V_{DS}$$

$$\text{Assumptions: } V_{GS} = V_G - V_S \ ; \quad V_{DS} = V_D - V_S \ ; \quad V_T = 0$$

$$\frac{V_S}{R_{OUT}} = \mu_0 (-V_G + V_S)^\gamma C_x \frac{W}{L} \left(V_G - V_S - \frac{V_D - V_S}{2} \right) (V_D - V_S)$$

$$\text{Substitution: } K = \mu_0 C_x \frac{W}{L}$$

$$\frac{2 V_S}{K R_{OUT}} = (-V_G + V_S)^\gamma (2V_G - 2V_S - V_D + V_S) (V_D - V_S)$$

$$\frac{2 V_S}{K R_{OUT}} = (-V_G + V_S)^\gamma (2V_G - V_S - V_D) (V_D - V_S)$$

$$\text{Substitution: } K_1 = \frac{1}{2} K = \frac{1}{2} \mu_0 C_x \frac{W}{L}$$

$$\frac{V_S}{K_1 R_{OUT}} = (-V_G + V_S)^\gamma (2V_G V_D - V_S V_D - V_D^2 - 2V_G V_S + V_S^2 + V_S V_D)$$

$$\frac{V_S}{K_1 R_{OUT}} = (-V_G + V_S)^\gamma (2V_G V_D - V_D^2 - 2V_G V_S + V_S^2)$$

$$\frac{V_S}{K_1 R_{OUT}} (-V_G + V_S)^{-\gamma} = 2V_G V_D - V_D^2 - 2V_G V_S + V_S^2$$

$$-V_S^2 + \left(\frac{(-V_G + V_S)^{-\gamma}}{K_1 * R_{OUT}} + 2V_G \right) V_S + (V_D^2 - 2V_G V_D) = 0$$

$$\text{Substitution: } V_S = V_{OUT}; \quad V_D = \frac{R_{BASE}}{R_{BASE} + R_{MEM}} V_{IN}$$

Solution:

$$-V_{OUT}^2 + \left(\frac{(-V_G + V_{OUT})^{-\gamma}}{K_1 R_{OUT}} + 2V_G \right) V_{OUT} + \left(\left(\frac{R_{BASE}}{R_{BASE} + R_{MEM}} V_{IN} \right)^2 - 2V_G \left(\frac{R_{BASE}}{R_{BASE} + R_{MEM}} V_{IN} \right) \right) = 0$$

$$-V_{OUT}^2 + \left(\frac{(-V_G + V_{OUT})^{-\gamma}}{\frac{1}{2} \mu_0 C_x \frac{W}{L} R_{OUT}} + 2V_G \right) V_{OUT} + \left(\left(\frac{R_{BASE}}{R_{BASE} + R_{MEM}} V_{IN} \right)^2 - 2V_G \left(\frac{R_{BASE}}{R_{BASE} + R_{MEM}} V_{IN} \right) \right) = 0$$

$$\text{Substitution: } K = \frac{1}{2} \mu_0 C_x \frac{W}{L} R_{OUT} \ ; \ V_X = \frac{R_{BASE}}{R_{BASE} + R_{MEM}}$$

$$-V_{OUT}^2 + \left(\frac{(-V_G + V_{OUT})^{-\gamma}}{K} + 2V_G \right) V_{OUT} + ((V_X V_{IN})^2 - 2V_G V_X V_{IN}) = 0$$

$$V_{OUT} \left(-V_{OUT} + \frac{(-V_G + V_{OUT})^{-\gamma}}{K} + 2V_G \right) = -V_X V_{IN} (V_X V_{IN} - 2V_G)$$

$$\frac{V_{OUT}}{V_{IN}} = \frac{-V_X (V_X V_{IN} - 2V_G)}{\left(-V_{OUT} + \frac{1}{K(-V_G + V_{OUT})^\gamma} + 2V_G \right)}$$

Large V_G

$$\frac{V_{OUT}}{V_{IN}} = \frac{-V_X (V_X V_{IN} - 2V_G)}{\left(-V_{OUT} + \frac{1}{K(-V_G + V_{OUT})^\gamma} + 2V_G \right)} = \frac{-V_X \left(\frac{V_X V_{IN}}{V_G} - 2 \right)}{\left(\frac{-V_{OUT}}{V_G} + \frac{1}{V_G K(-V_G + V_{OUT})^\gamma} + 2 \right)}$$

$$\frac{V_{OUT}}{V_{IN}} = \frac{-V_X \left(\frac{V_X V_{IN}}{V_G} - 2 \right)}{\left(\frac{-V_{OUT}}{V_G} + \frac{1}{V_G K(-V_G + V_{OUT})^\gamma} + 2 \right)} = \frac{2V_X}{2} = V_X$$

$$V_{OUT} = \frac{R_{BASE}}{R_{BASE} + R_{MEM}} V_{IN}$$

Small V_G

$$\frac{V_{OUT}}{V_{IN}} = \frac{-V_X(V_X V_{IN} - 2V_G)}{\left(-V_{OUT} + \frac{1}{K(-V_G + V_{OUT})^\gamma} + 2V_G\right)} = \frac{-V_X(V_X V_{IN} - 2V_G)}{\left(-V_{OUT} + \frac{1}{K(-V_G + V_{OUT})^\gamma} + 2V_G\right)}$$

$$\frac{V_{OUT}}{V_{IN}} = \frac{-V_X V_X V_{IN}}{\left(-V_{OUT} + \frac{1}{KV_{OUT}^\gamma}\right)}$$

$$V_{OUT} \left(\frac{1}{KV_{OUT}^\gamma} - V_{OUT} \right) = \frac{R_{BASE}}{R_{BASE} + R_{MEM}} V_{IN}^2$$

Saturation

$$i_D = \frac{V_S}{R_{OUT}} = \mu C_x \frac{W}{L} \frac{(V_{GS} - V_T)^2}{2} (1 + \lambda V_{DS})$$

$$\frac{V_S}{R_{OUT}} = \mu_0 (-V_{GS} + V_T)^\gamma C_x \frac{W}{L} \frac{(V_{GS} - V_T)^2}{2} (1 + \lambda V_{DS})$$

Assumptions: $V_{GS} = V_G - V_S$; $V_{DS} = V_D - V_S$; $V_T = 0$

$$\frac{V_S}{R_{OUT}} = \mu_0 (-V_G + V_S)^\gamma C_x \frac{W}{L} \frac{(V_G - V_S)^2}{2} (1 + \lambda V_D - \lambda V_S)$$

Substitution: $K = \frac{1}{2} \mu_0 C_x \frac{W}{L}$

$$\frac{V_S}{KR_{OUT}} = (-V_G + V_S)^\gamma (V_G^2 - 2V_G V_S + V_S^2) (1 + \lambda V_D - \lambda V_S)$$

$$\begin{aligned} \frac{V_S}{KR_{OUT}} (-V_G + V_S)^{-\gamma} \\ = (V_G^2 - 2V_G V_S + V_S^2 + \lambda V_G^2 V_D - 2\lambda V_G V_S V_D + \lambda V_S^2 V_D - \lambda V_G^2 V_S + 2\lambda V_G V_S^2 - \lambda V_S^3) \end{aligned}$$

$$\lambda V_S^3 - V_S^2 - \lambda V_S^2 V_D - 2\lambda V_G V_S^2 + \frac{V_S (-V_G + V_S)^{-\gamma}}{K * R_{OUT}} + 2V_G V_S + 2\lambda V_G V_S V_D + \lambda V_G^2 V_S - V_G^2 - \lambda V_G^2 V_D = 0$$

$$\lambda V_S^3 - (1 + \lambda V_D + 2\lambda V_G) V_S^2 + \left(\frac{(-V_G + V_S)^{-\gamma}}{KR_{OUT}} + 2V_G + 2\lambda V_G V_D + \lambda V_G^2 \right) V_S - (V_G^2 + \lambda V_G^2 V_D) = 0$$

Substitution: $V_S = V_{OUT}$; $V_D = \frac{R_{BASE}}{R_{BASE} + R_{MEM}} V_{IN}$

Solution:

$$\begin{aligned} \lambda V_{OUT}^3 - \left(1 + \lambda \frac{R_{BASE}}{R_{BASE} + R_{MEM}} V_{IN} + 2\lambda V_G \right) V_{OUT}^2 + \left(\frac{(-V_G + V_{OUT})^{-\gamma}}{KR_{OUT}} + 2V_G + 2\lambda V_G \frac{R_{BASE}}{R_{BASE} + R_{MEM}} V_{IN} \right. \\ \left. + \lambda V_G^2 \right) V_{OUT} - (V_G^2 + \lambda V_G^2 \frac{R_{BASE}}{R_{BASE} + R_{MEM}} V_{IN}) = 0 \end{aligned}$$

$$\lambda V_{\text{OUT}}^3 - (1 + \lambda \frac{R_{\text{BASE}}}{R_{\text{BASE}} + R_{\text{MEM}}} V_{\text{IN}} + 2\lambda V_{\text{G}}) V_{\text{OUT}}^2 + (\frac{(-V_{\text{G}} + V_{\text{OUT}})^{-\gamma}}{1/2 \mu_0 C_x \frac{W}{L} R_{\text{OUT}}} + 2V_{\text{G}} + 2\lambda V_{\text{G}} \frac{R_{\text{BASE}}}{R_{\text{BASE}} + R_{\text{MEM}}} V_{\text{IN}} + \lambda V_{\text{G}}^2) V_{\text{OUT}} - (V_{\text{G}}^2 + \lambda V_{\text{G}}^2 \frac{R_{\text{BASE}}}{R_{\text{BASE}} + R_{\text{MEM}}} V_{\text{IN}}) = 0$$

$$\text{Substitution: } K = 1/2 \mu_0 C_x \frac{W}{L} R_{\text{OUT}} \ ; \ V_{\text{X}} = \frac{R_{\text{BASE}}}{R_{\text{BASE}} + R_{\text{MEM}}}$$

$$\lambda = 0$$

$$-V_{\text{OUT}}^2 + \left(2V_{\text{G}} + \frac{(-V_{\text{G}} + V_{\text{OUT}})^{-\gamma}}{K} \right) V_{\text{OUT}} - V_{\text{G}}^2 = 0$$

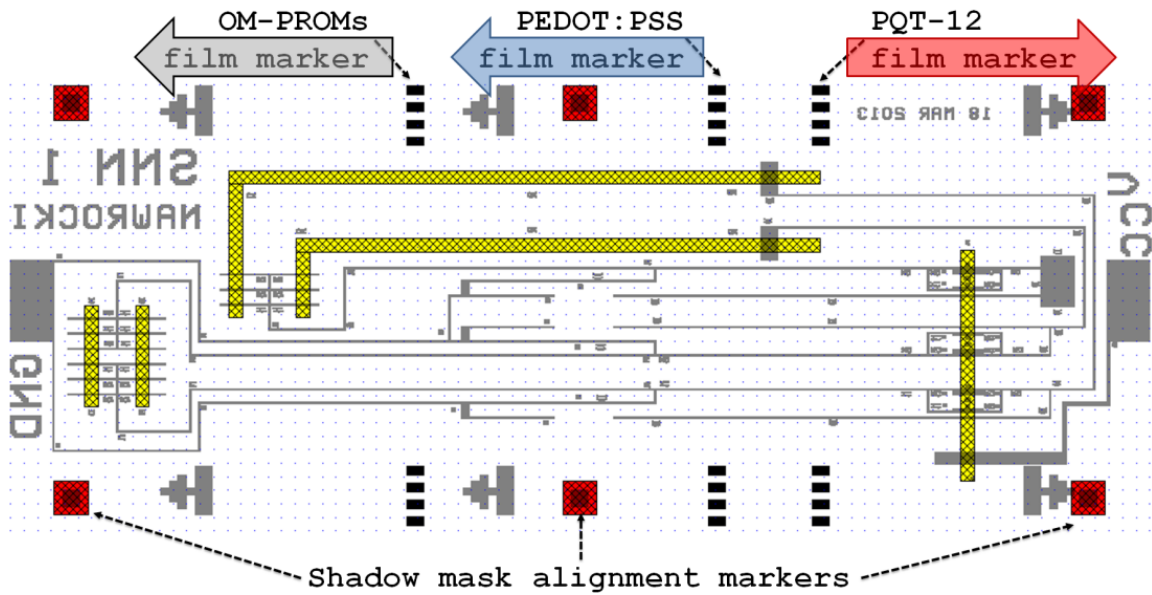
Large V_{G}

$$\lambda V_{\text{OUT}}^3 - (1 + \lambda V_{\text{X}} V_{\text{IN}} + 2\lambda V_{\text{G}}) V_{\text{OUT}}^2 + (\frac{(V_{\text{OUT}} - V_{\text{G}})^{-\gamma}}{K} + 2V_{\text{G}} + 2\lambda V_{\text{G}} V_{\text{X}} V_{\text{IN}} + \lambda V_{\text{G}}^2) V_{\text{OUT}} - (V_{\text{G}}^2 + \lambda V_{\text{G}}^2 V_{\text{X}} V_{\text{IN}}) = 0$$

Small V_{G}

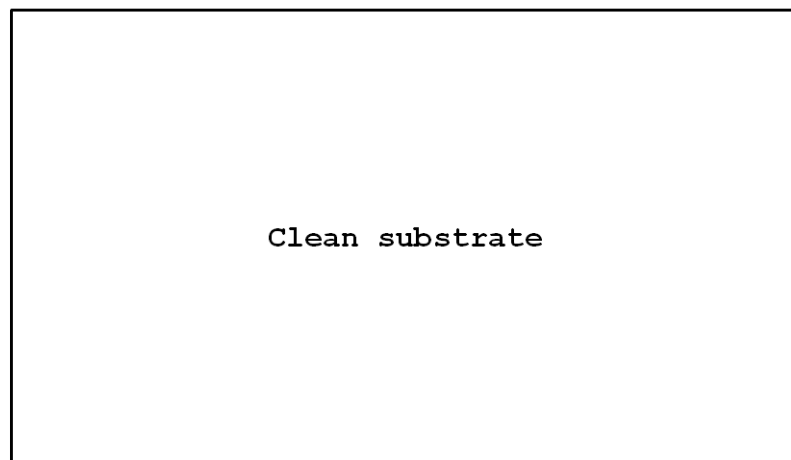
$$\lambda V_{\text{OUT}}^3 - (1 + \lambda V_{\text{X}} V_{\text{IN}}) V_{\text{OUT}}^2 + 1/K V_{\text{OUT}}^{1-\gamma} = 0$$

Appendix C: Manufacturing Process

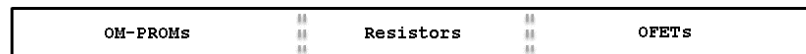


Alignment markers (dashed lines at the top and bottom of the design) used for aligning the polymer film-depositing blade and six markers (red squares, placed at the periphery of the design) used for aligning TE shadow mask.

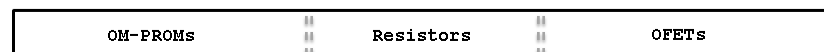
Common Structure Design



Separation of Elements

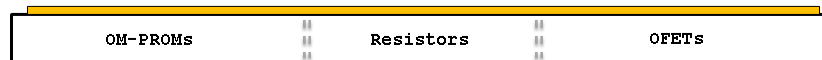
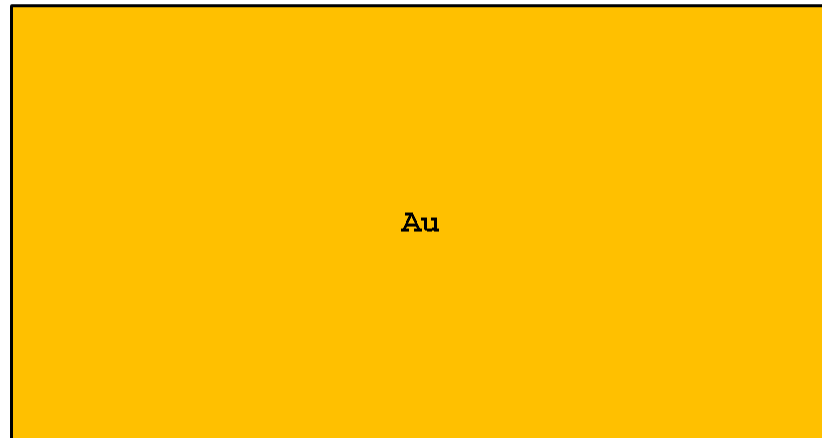


Photolithography

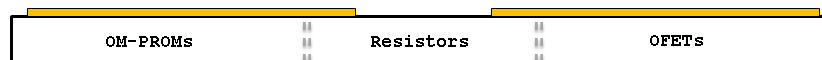
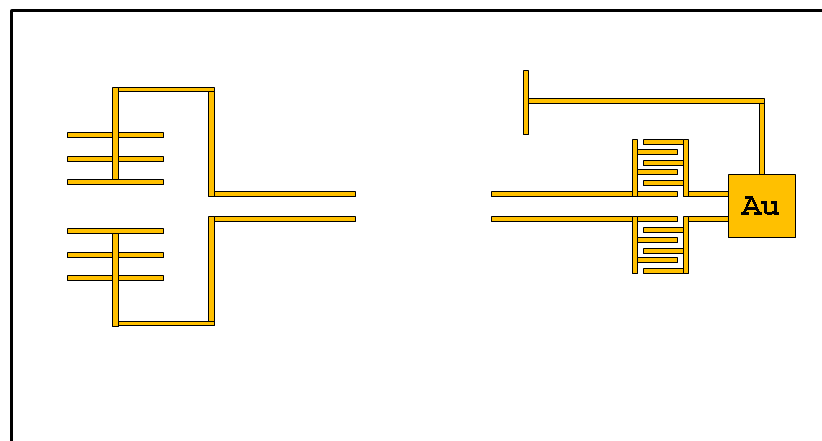


Metal evaporation

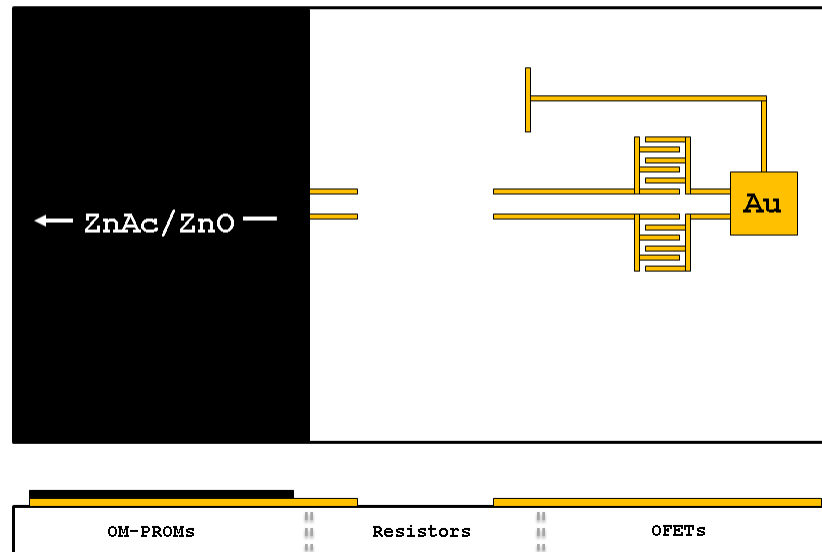
(Cr, Ag, Au)



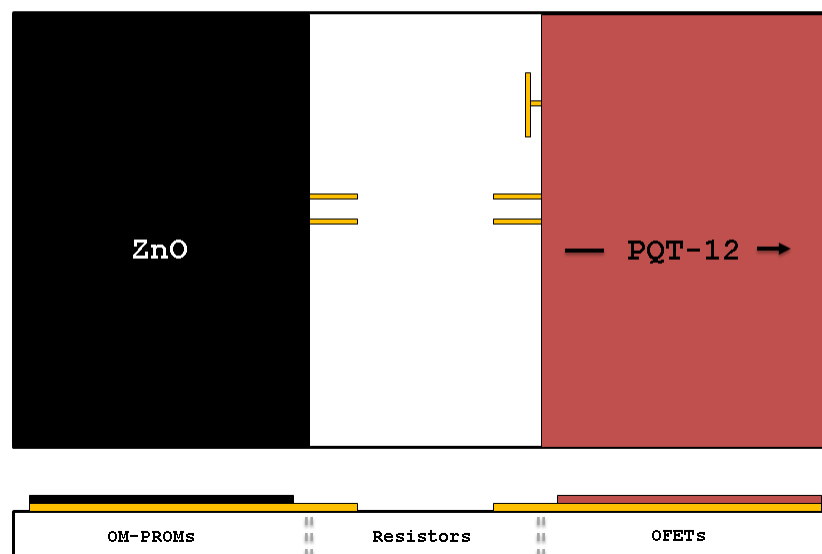
Liftoff



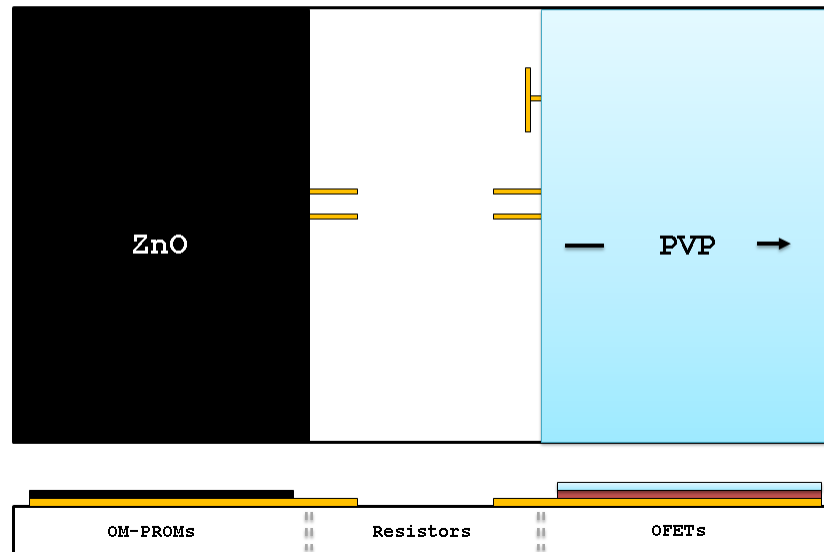
ZnAc / ZnO (OM-PROM)



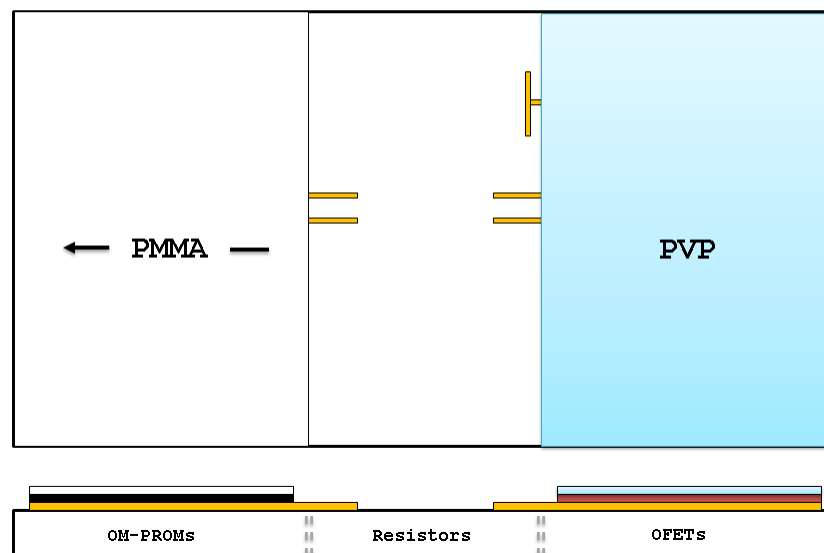
PQT-12 (OFET)



PVP (OFET)

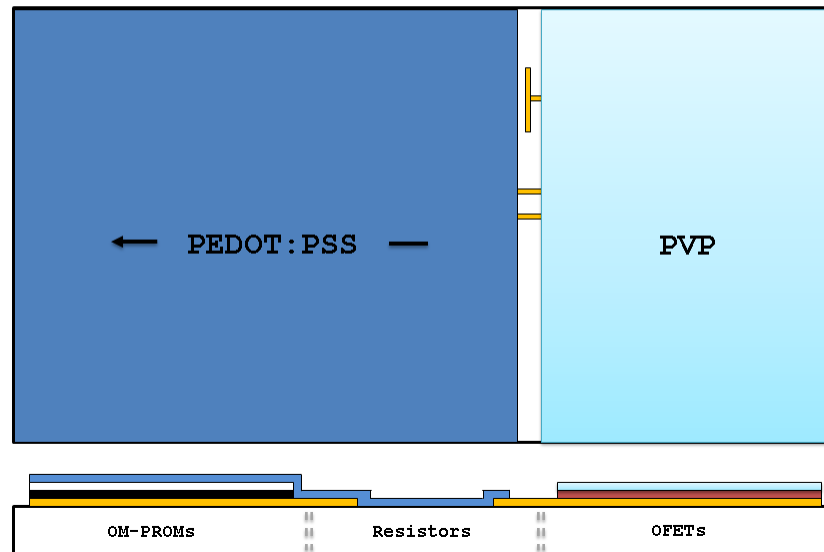


PMMA (OM-PROM)

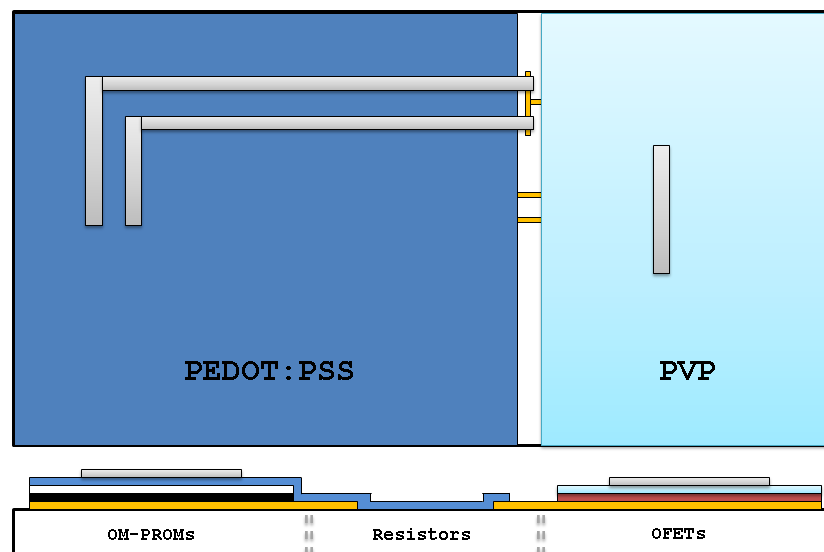


PEDOT:PSS

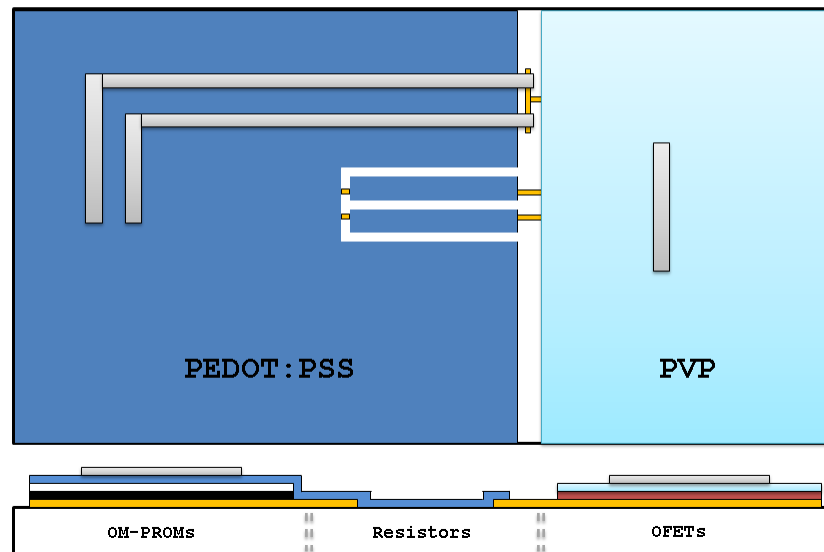
(OM-PROM, Resistor)



Ag (all devices)



PEDOT:PSS removal

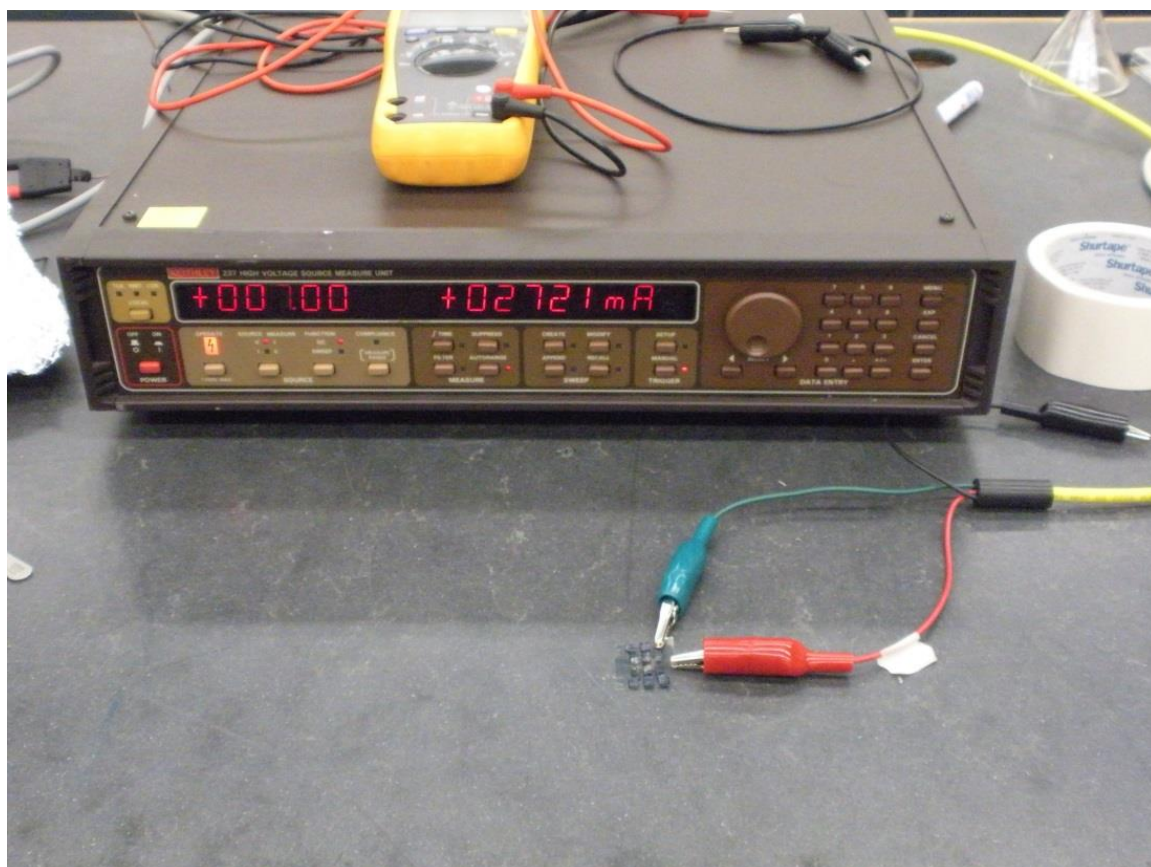


Step-by-step sequential **PNC fabrication process**, including photolithography steps, bladed coating of individual polymeric films, and thermal evaporation through shadow mask.

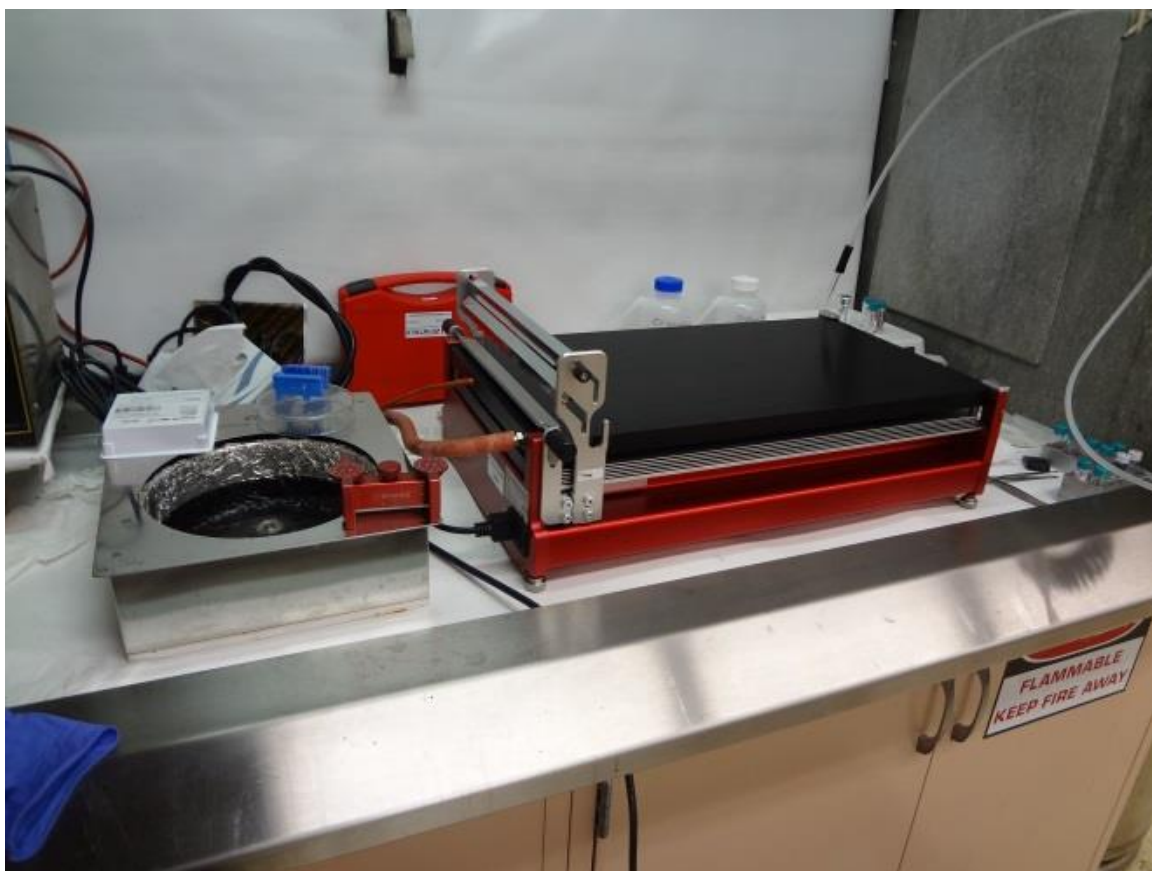
Appendix D: List of Equipment Used

- BYK-Gardner manual film applicator and Zehntner ZAA 2300 Automatic Film Applicator Coater were used to blade coat individual polymeric films
- *I-V* measurements of Memristive Devices were performed using Keithley 237
- *I-V* measurements of Organic Transistors were performed using Hewlett Packard 4145B Semiconductor Parameter Analyzer and Hewlett Packard 4142B Modular DC Source / Monitor
- Thicknesses of individual layers were measured with surface profiler Dektak 3030
- Thicknesses and surface morphology was characterized using Asylum Research MFP-3D AFM Atomic Force Microscope (AFM)
- Optical microscopy was conducted with Olympus Optical AX70TRF
- Metal evaporation was obtained with customized 3-boat CVC thermal evaporator with electronic rate deposition and thickness readout
- Karl Suss MJB3-HP/200W and Karl Suss MJB4 mask aligners were used for photolithography
- Photolithographic masks were generated using Heidelberg DWL 66FS Mask Generator
- Glass samples were cleaned using Branson 1510 sonicator followed by March Jupiter III RIE
- Impedance and capacitance was characterized using Hewlett Packard 4192A Impedance Analyzer
- Organic resistor was plotted using Sonoplot's GIX Microplotter II

Appendix E: Manufacturing Equipment



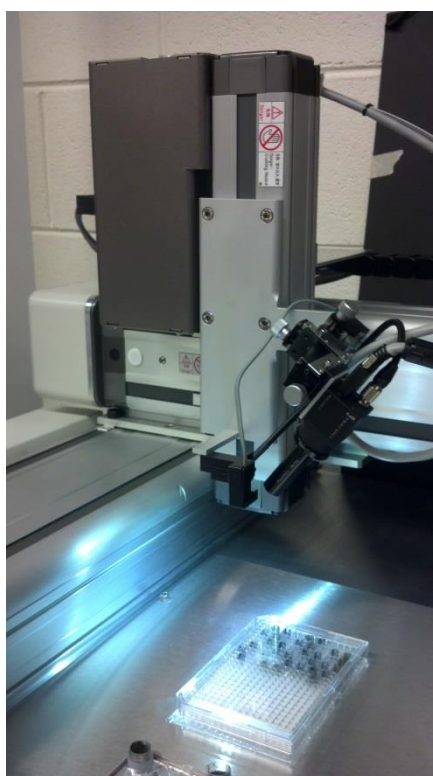
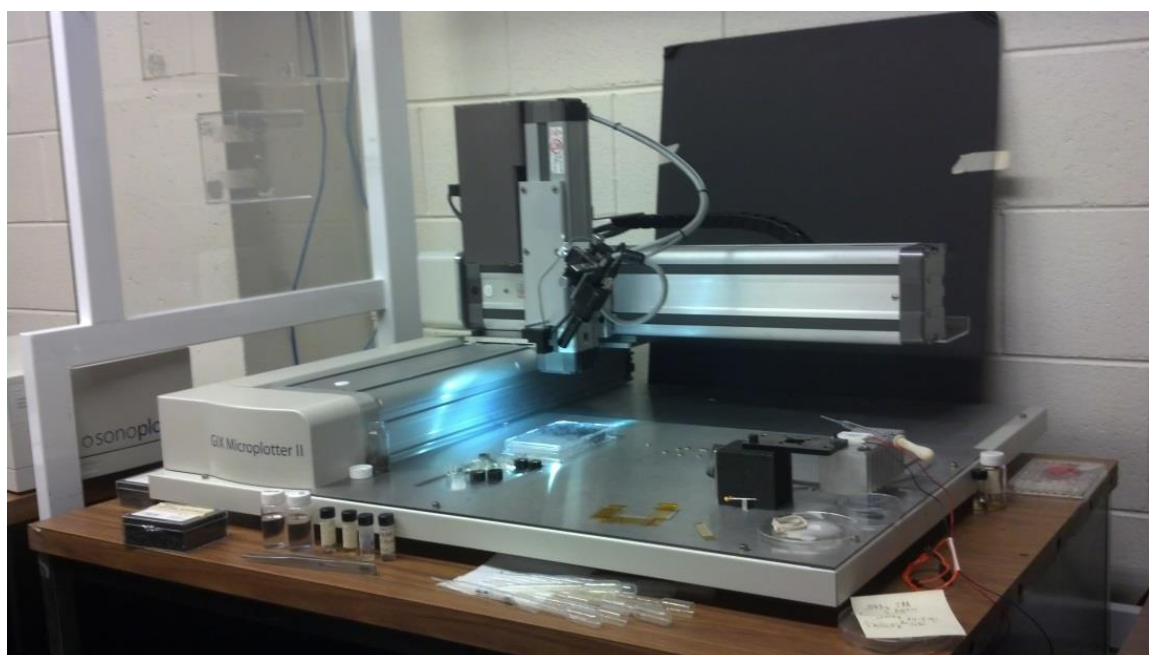
Keithley 237 used to characterize memristive devices.



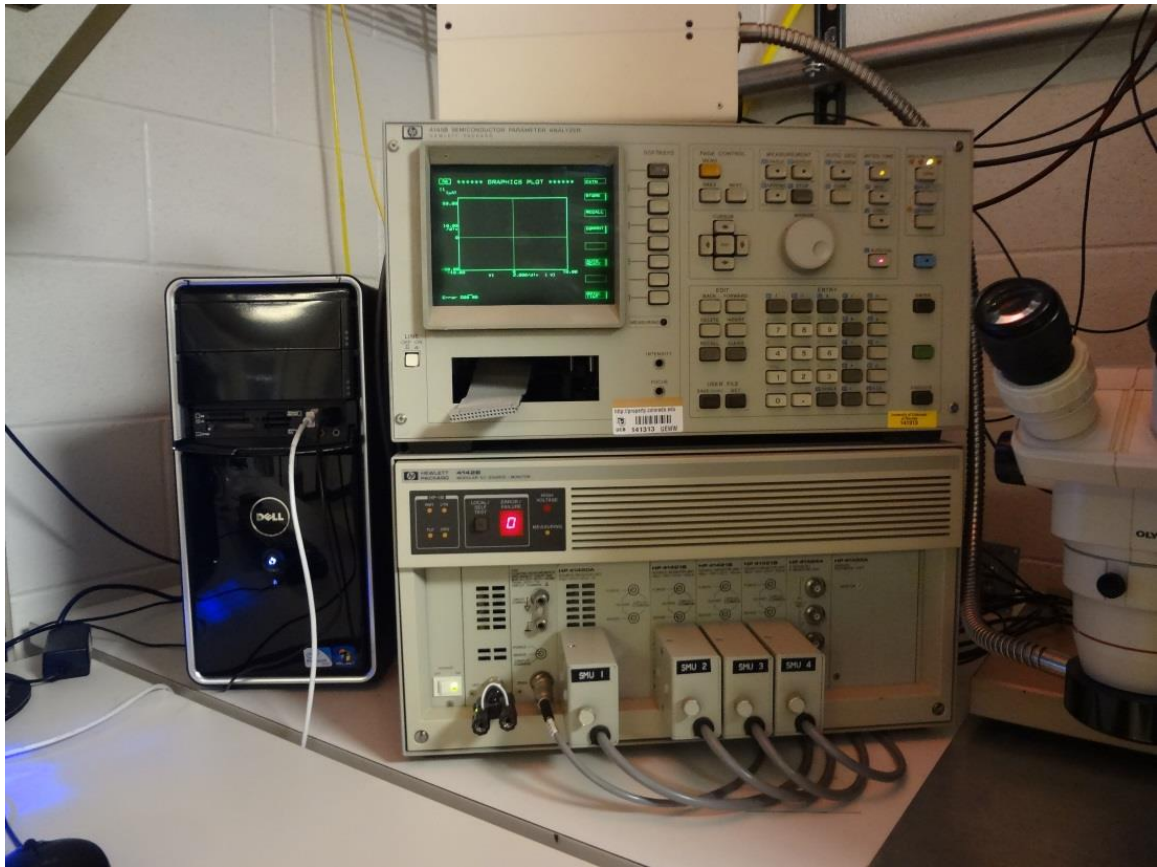
Zehntner ZAA 2300 used to apply polymeric materials.



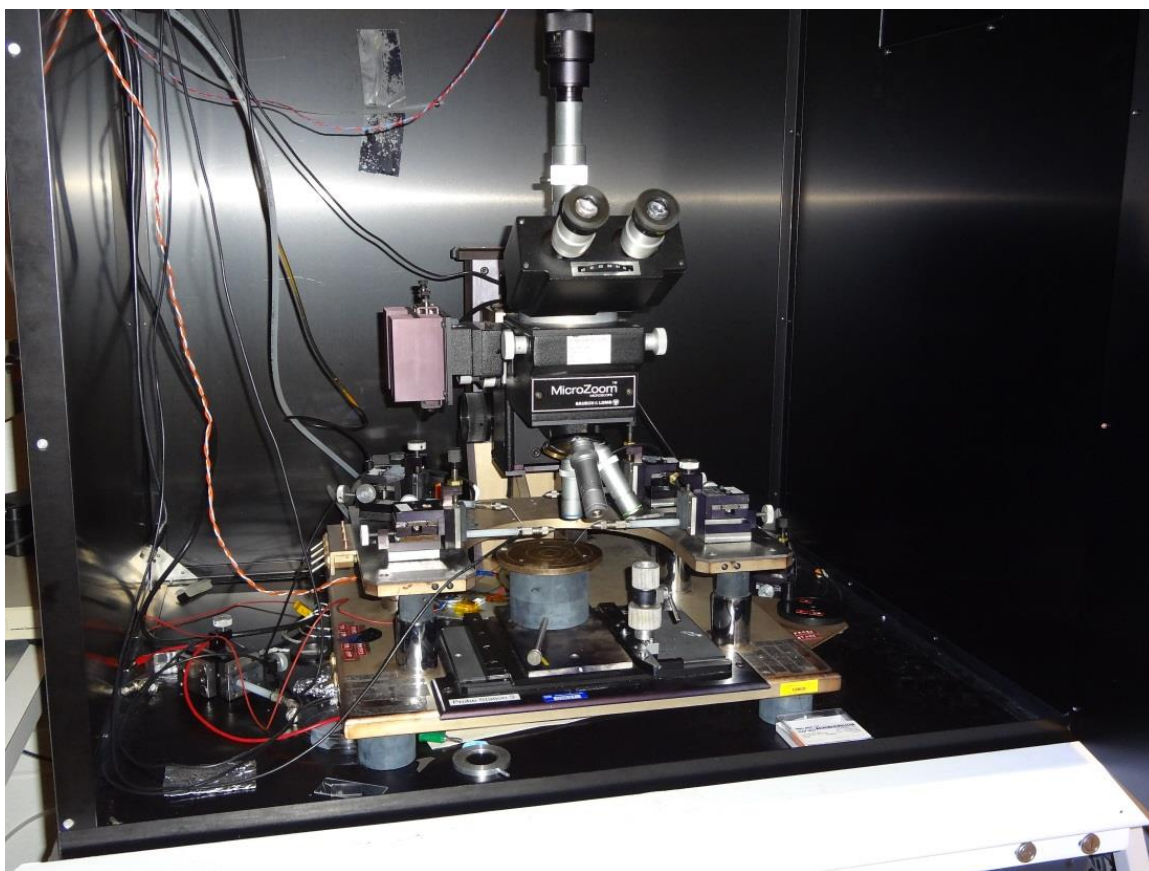
Fume hood with spin and blade coaters inside. Nitrogen tank, used to dust off samples immediately before film deposition, can be seen immediately to the right of the fume hood.



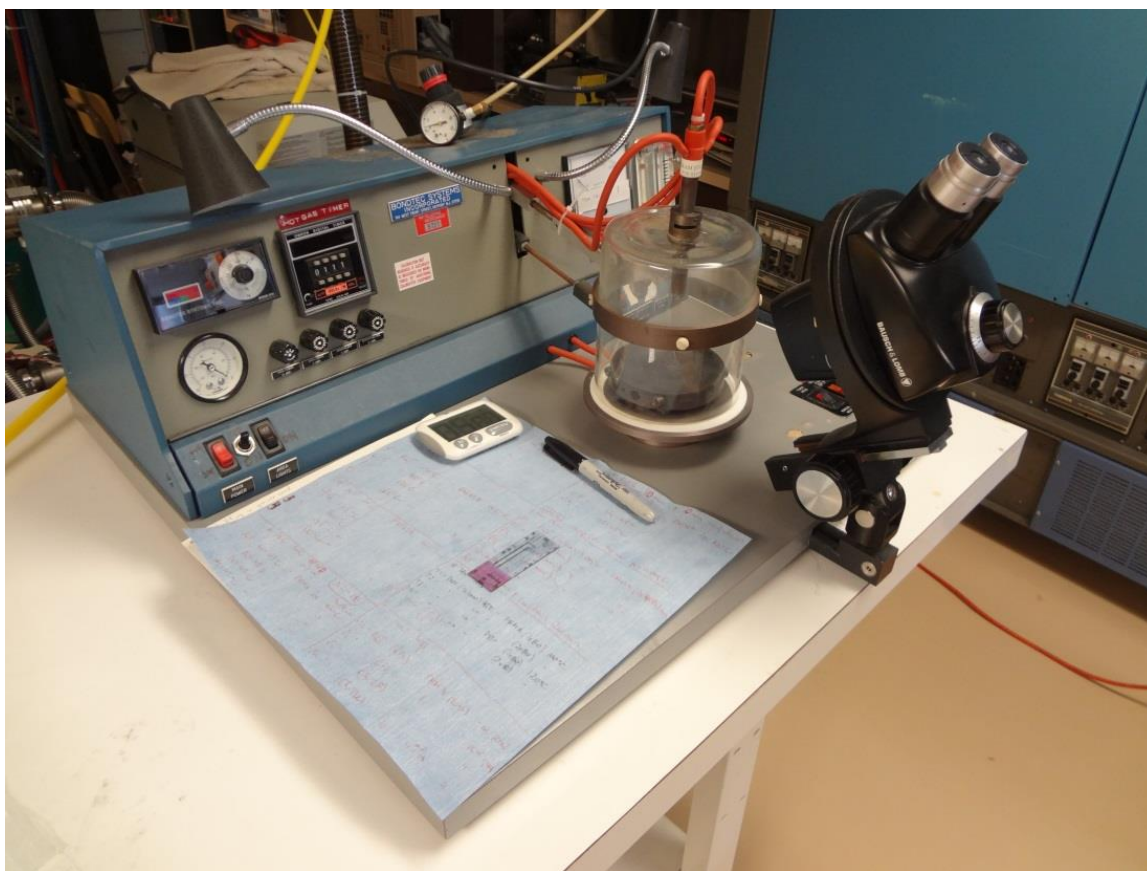
GIX Microplotter II used to plot polymer resistors from PEDOT:PSS.



Hewlett Packard 4145B Semiconductor Parameter Analyzer and **Hewlett Packard 4142B** Modular DC Source / Monitor used to characterize OFETs as well as PNC.



Probe station, with individual micromanipulators, used to connect to individual OFET and PNC electrodes. Station is placed inside a black box in order to avoid photointerference during measurements.



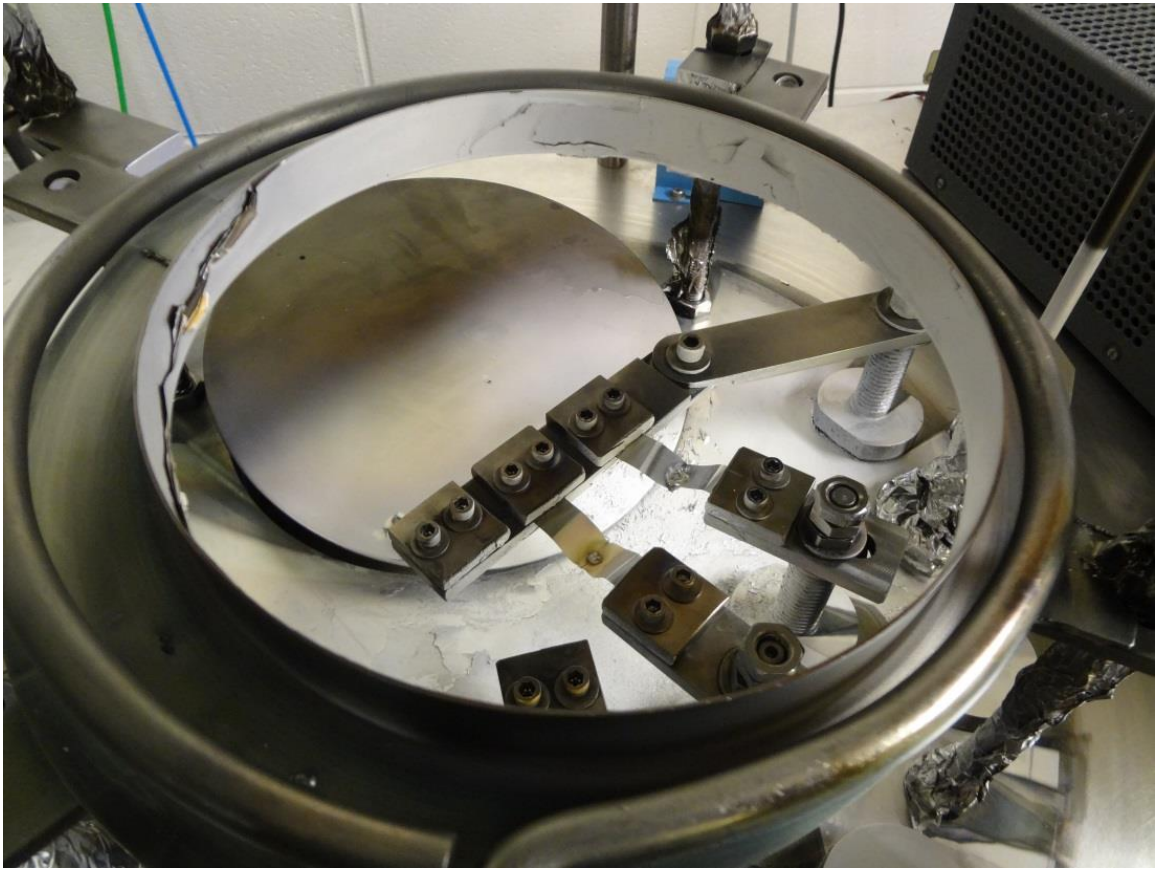
Hot plate with **N₂ chamber** used for annealing PEDOT:PSS films with reduced presence of O₂.



3-boat **CVC thermal evaporator** used to deposit metal.



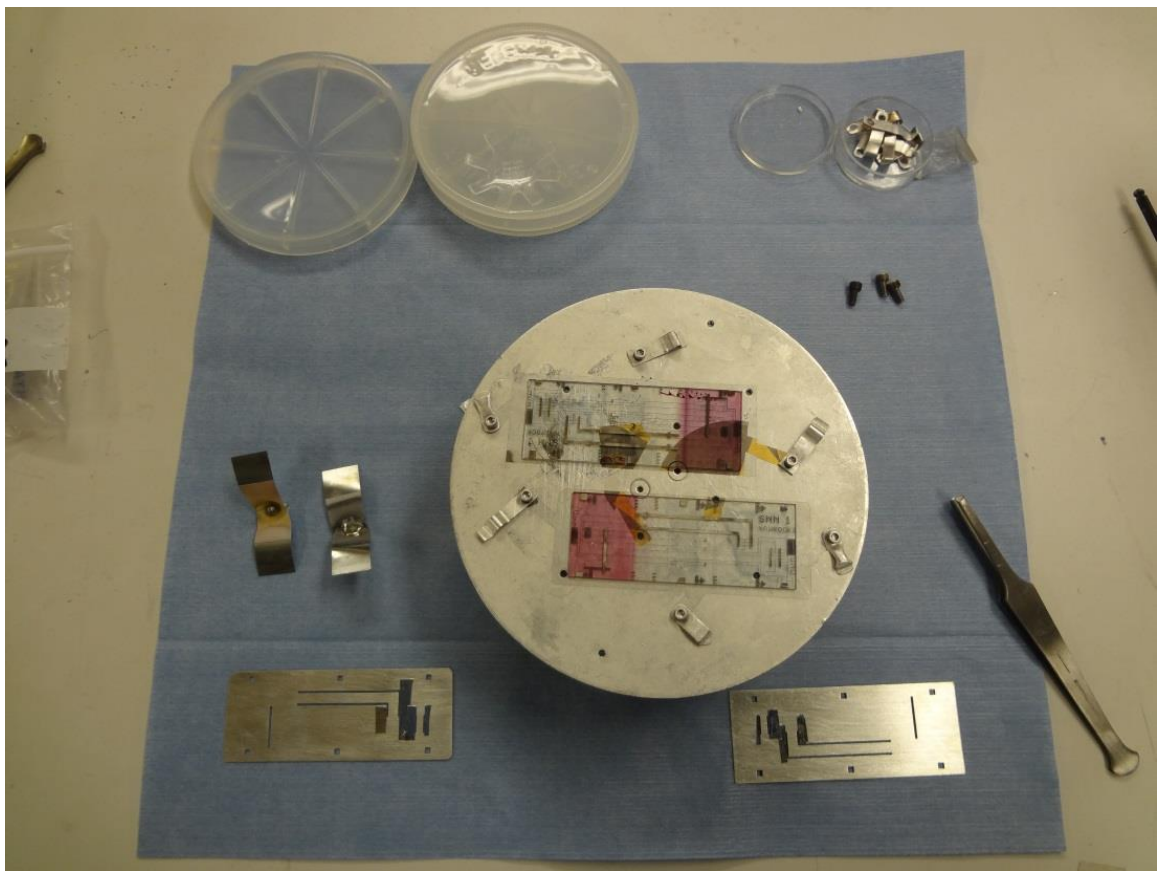
Inside of **CVC thermal evaporator chamber.**



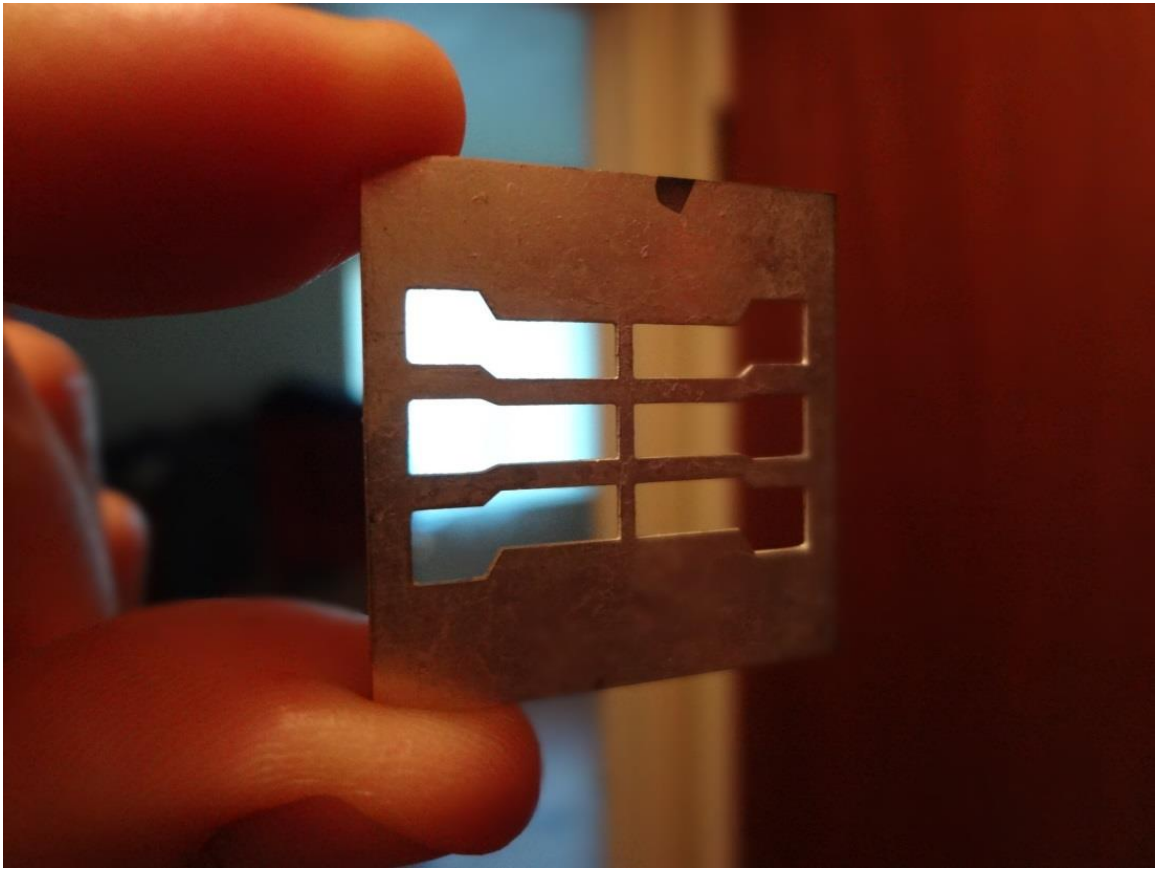
Three boats, inside of **CVC thermal evaporator chamber**, allow for deposition of three separate metals during a single evaporation, for instance chromium (Cr), silver (Ag), and gold (Au), without opening the chamber, prohibiting formation of oxides between individual materials.



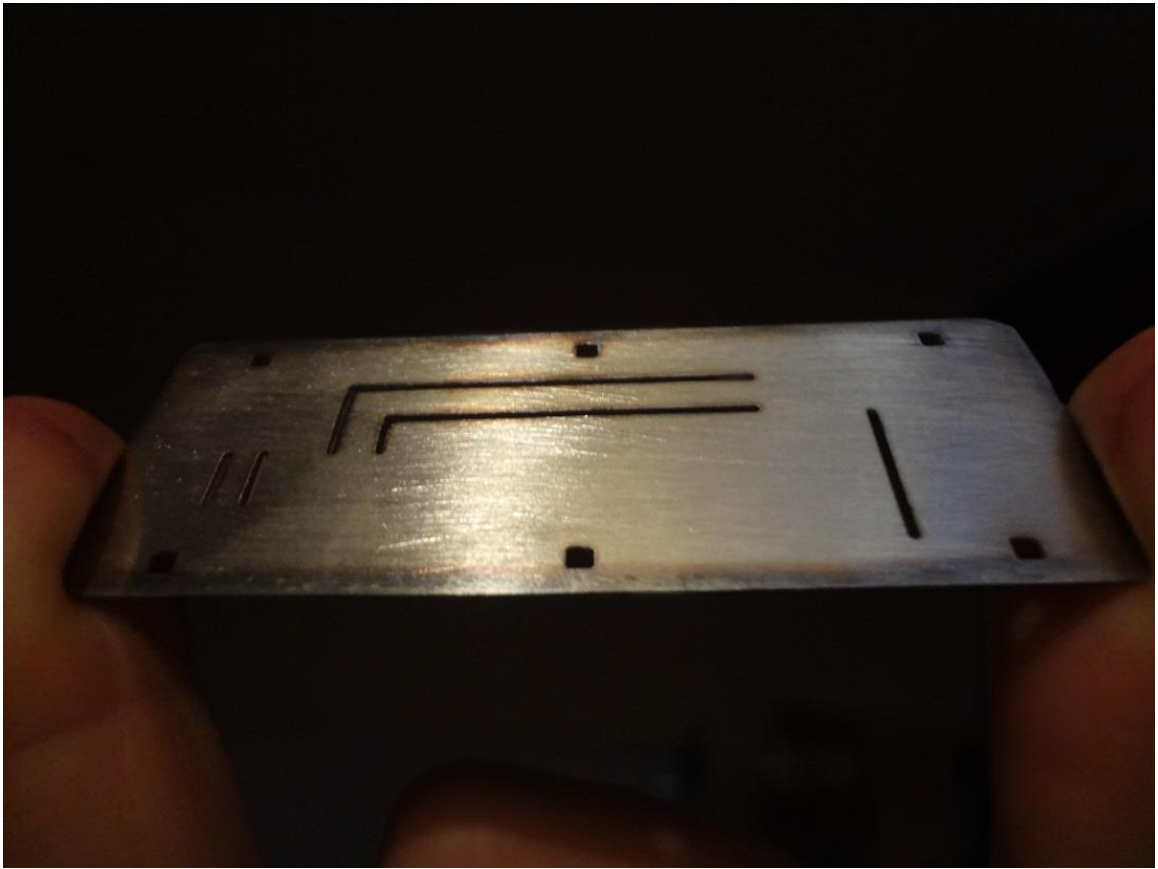
Inside **CVC thermal evaporator** samples are mounted to a **rotating chuck** providing for a uniform film deposition (no shadow effect).



Chuck removed from inside the CVC thermal evaporator, with two **PNC chips** visible and two **PNC shadow masks** placed on lint-free blue clean room paper, immediately adjacent to the chuck.



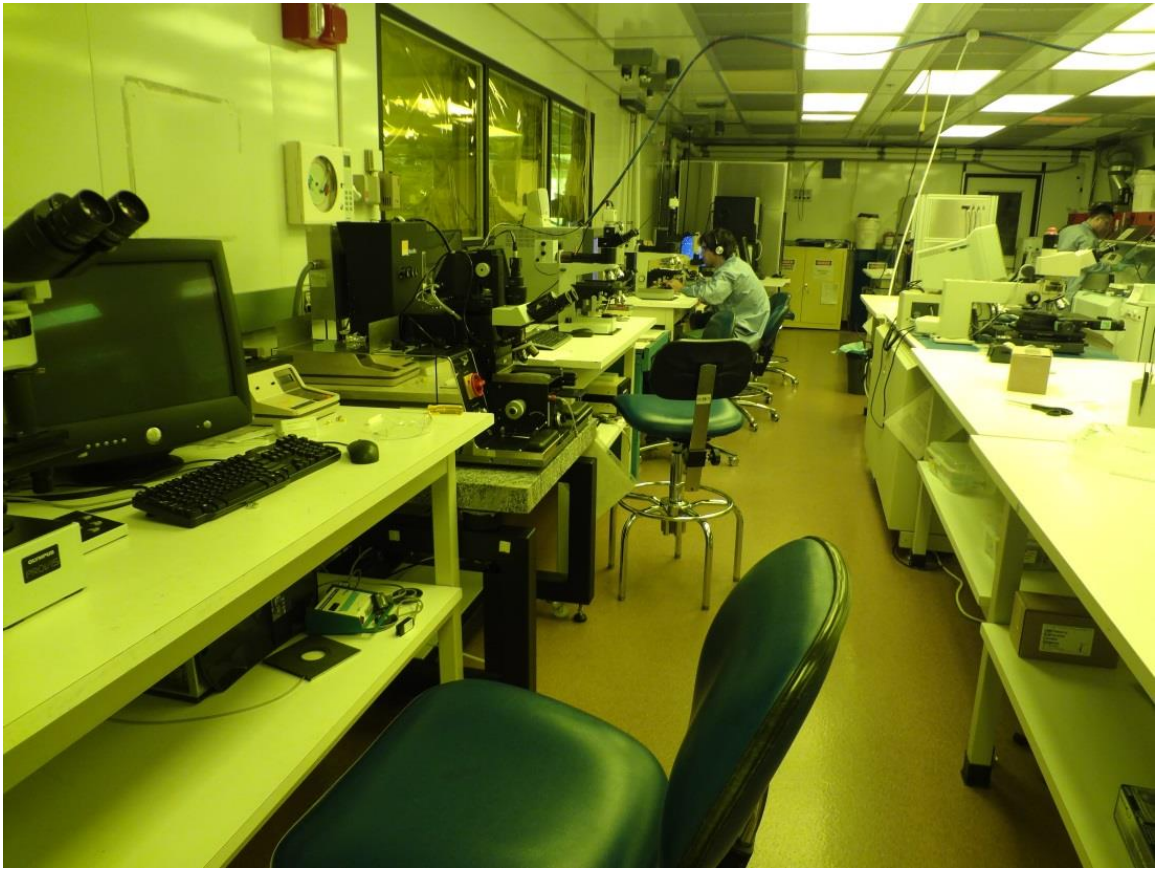
Metal shadow mask, approximately 1.2" x 1.2", used to define top electrodes of six **memristive devices** on a single 1" x 1" chip. Only metallic materials can be introduced inside a chamber as organic materials, such as wood or plastic, traps oxygen atoms slowing down the pumping down process (removal of air from the chamber).



Metal shadow mask, approximately 3" x 1.2", used to define top electrodes of a single, 2.8" x 1", **PNC** chip with three neurons arranged to form a neural network.



Olympus Optical AX70TRF, used for optical microscopy, allows for 5x, 10x, 20x, 50x, and 100x magnification. The yellow light is a result of the microscope residing inside "yellow cleanroom" - a room used to perform photolithography.



"Yellow cleanroom", with **mask aligners** clearly visible on the left hand side.



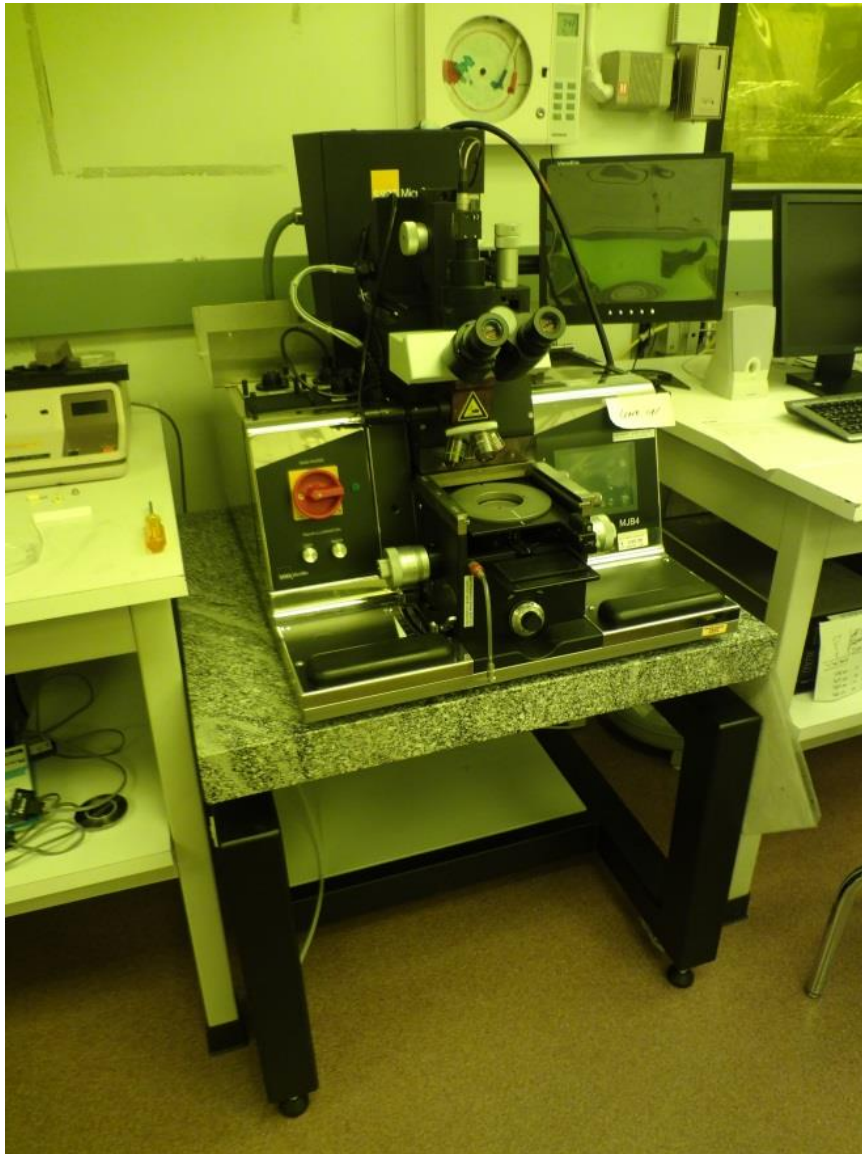
"Yellow cleanroom", with **fume hoods** (housing deionized water, used for cleaning surfaces) clearly visible on the right hand side.



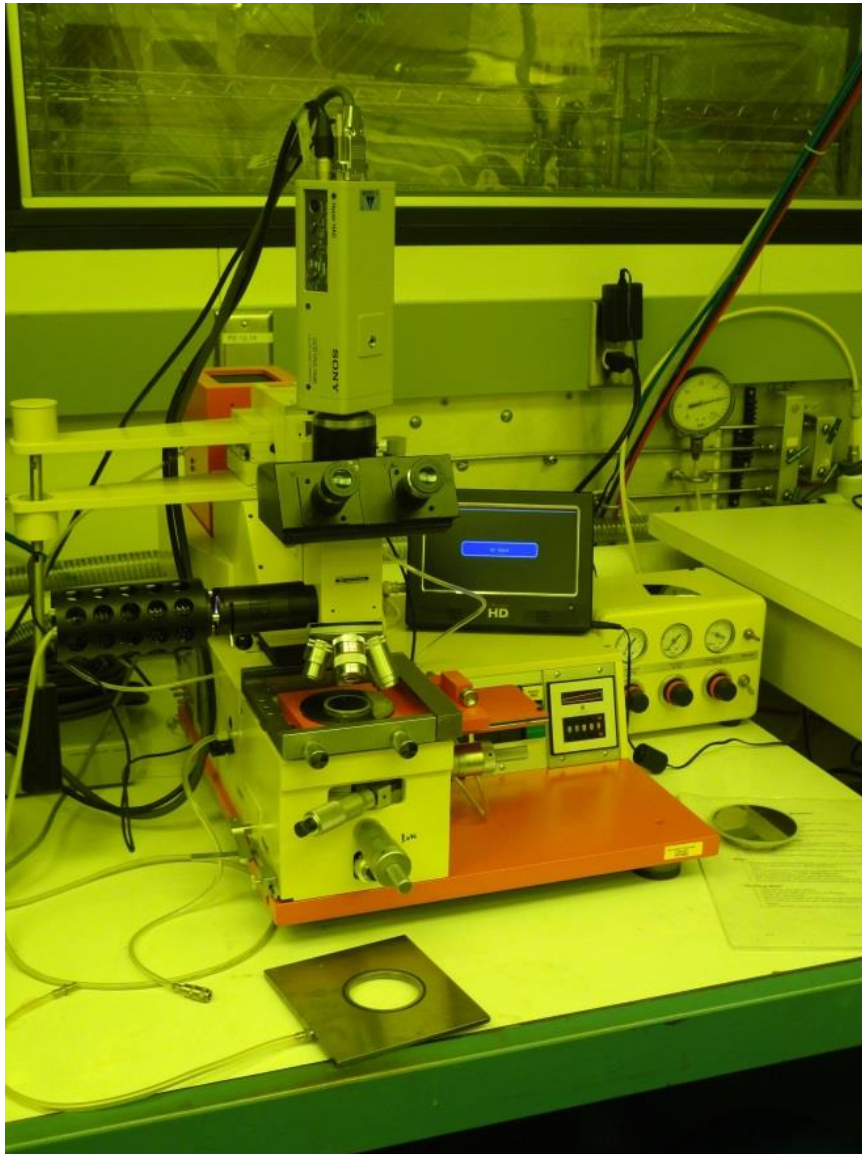
Fume hood housing two **spin coaters** used to deposit photoresists for photolithography.



Heidelberg DWL 66FS inside "yellow cleanroom", used to generate photolithographic masks with dimensions as small as 1 μm .



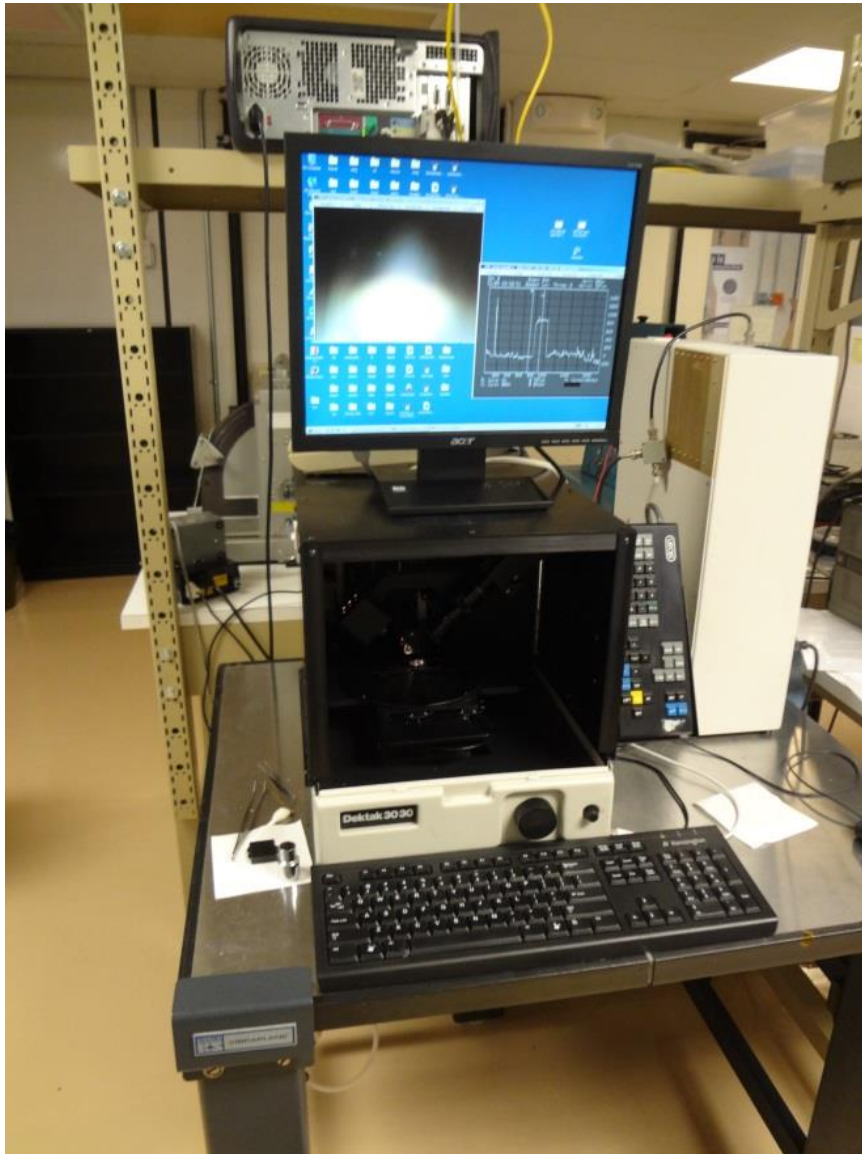
Karl Suss MJB4 mask aligner used for photolithography.



Karl Suss MJB3-HP/200W mask aligner used for photolithography.



March Jupiter III Reactive Ion Etching (REI) used to remove organic residue on glass samples immediately before applying NR71 photoresist.



Dektak 3030 surface profiler used to analyze the surface roughness as well as measure layer thicknesses.